

Ludwig-Maximilians-Universität München

Faculty of Physics

**Optimization and Calibration  
of the Drift-Tube Chambers for the  
ATLAS Muon Spectrometer**

Dissertation

submitted by

Mario Deile

from

Munich

supervised by

Prof. Dr. Arnold Staude

---

May 2000

Oceani finem iuxta solemque cadentem  
ultimus Aethiopum locus est, ubi maxumus ATLAS  
axem humero torquet stellis ardentibus aptum.

*On Ocean's bound and next the setting sun  
lies the last Aethiop land, where ATLAS tall  
lifts on his shoulder the wide wheel of heaven,  
studded with burning stars.*

P. Vergili Maronis Aeneidos Liber Quartus, 480–482

## Abstract

The final phase of preparations for the ATLAS experiment at the future Large Hadron Collider (LHC) has begun. In the last decade the collaboration has carried out various test-beam experiments to study and optimize prototypes of all subdetectors under more and more realistic conditions. To enhance the detector-physical understanding, these hardware activities were complemented by detailed simulations. In parallel the development of reconstruction software has made important progress.

The present work focusses on some advanced aspects of optimizing the Monitored Drift Tube Chambers (MDT) for operation as precision chambers in the Muon Spectrometer. It will be shown how this system has been tuned for maximum performance in order to meet the ambitious goals defined by the objectives of LHC particle physics (Chapter 2). After defining the basic detector parameters (Chapter 4), the tubes' capability of running in ATLAS's high-rate gamma radiation background was verified (Chapter 5). Both tasks necessitated several years of gathering experience in muon test beams to which the author has contributed together with colleagues from institutes spread over the entire globe. Although efforts have been made to concentrate on issues for which the writer bore the full responsibility, it was sometimes unavoidable – in view of a more coherent treatment of sophisticated contexts – to also display results contributed by other collaborators. This is particularly true for the analysis of the high-rate behaviour of drift tubes which was shared with M. Alekса (CERN), N. Hessey (LMU, now NIKHEF) and W. Riegler (Harvard, now CERN).

The employment of a silicon microstrip tracker (Chapter 3) in the test-beam experiments yielded an unprecedented precision in the understanding of the subtleties of drift-chamber physics. Chapter 6 presents an approach for taking advantage of this knowledge in the reconstruction of muon tracks through a multilayer of tubes.

The momentum resolution and the track reconstruction efficiency of the muon spectrometer achieved with the optimized detector system were investigated in a Monte Carlo simulation (Chapter 7). A central aspect of this study was the impact of the non-Gaussian errors in the drift-tube response near the anode wires on the spectrometer performance.

Finally, techniques for the calibration of the space-time relationship of drift tubes were developed (Chapter 8). Since in ATLAS no external reference detector will be available, the muon system has to be self-calibrating. This task will be accomplished by exploiting muon tracks from normal LHC operation. For each calibration method the attainable precision and the applicability for ATLAS MDT chambers are discussed. Here again, the results from the beam tests proved to be an indispensable input. Based on these insights a scenario for the in-situ calibration of all ATLAS MDT chambers is outlined. This includes a strategy for the definition of the spatial “autocalibration zones” in the spectrometer within which a calibration of the space-time relationship is valid. A simple estimate of the number of muons needed for a full calibration shows that approximately one day of normal data-taking is sufficient to collect the required statistics.

## Kurzfassung

Die Vorbereitungen für das ATLAS-Experiment am zukünftigen Hadronenbeschleuniger LHC befinden sich im Endstadium. In den letzten zehn Jahren führte die Kollaboration verschiedene Teststrahlexperimente durch, um Prototypen aller Teildetektoren unter immer realistischeren Bedingungen zu studieren und zu optimieren. Zur Verbesserung des detektorphysikalischen Verständnisses wurden die experimentellen Untersuchungen durch detaillierte Simulationen ergänzt. Inzwischen hat die Produktion von Detektorkomponenten begonnen. Fortschritte wurden auch in der Entwicklung der Datenanalyseprogramme erzielt.

Die vorliegende Arbeit konzentriert sich auf die Detektorphysik von Driftrohrkammern (Monitored Drift Tube Chambers MDT), die im ATLAS-Myonspektrometer als Präzisionskammern zum Einsatz kommen werden. Es wird gezeigt, wie dieses Detektorsystem im Hinblick auf die harten Anforderungen des LHC-Teilchenphysikprogramms (Kapitel 2) optimiert wurde. Nach Festlegung des Arbeitspunktes der Driftrohre (Kapitel 4) wurde ihre Tauglichkeit für den Betrieb im Hochratenstrahlungsuntergrund des ATLAS-Detektors überprüft (Kapitel 5). Beide Zielsetzungen erforderten mehrjährige Erfahrungen aus Myonen-Teststrahlexperimenten, zu denen der Autor zusammen mit Kollegen von Instituten aus der ganzen Welt beitrug. Wenn auch der Schwerpunkt des Textes auf diejenigen Sachverhalte gelegt wurde, für deren Erforschung der Verfasser persönlich verantwortlich zeichnete, war es manchmal zur vollständigen Darstellung der Zusammenhänge unverzichtbar, auch Teilergebnisse darzustellen, die von anderen Mitgliedern der Teststrahlgruppe erarbeitet wurden. Dies gilt hauptsächlich für die Analyse des Hochratenverhaltens von Driftrohren, die gemeinsam mit M. Aleksi (CERN), N. Hessey (LMU, jetzt am NIKHEF) und W. Riegler (Harvard, jetzt am CERN) durchgeführt wurde.

Der Einsatz eines Silizium-Mikrostreifen-Strahlteleskops (Kapitel 3) als externer Referenzdetektor in den Teststrahlexperimenten ergab eine bisher unerreichte Präzision bei der Vermessung von Feinheiten in der Auflösungsfunktion von Driftrohren. Kapitel 6 stellt einen Ansatz vor, mit dem diese Detailkenntnisse zur Verbesserung der Rekonstruktion von Myon-Spuren durch Multilagen von Rohren genutzt werden können.

Die mit dem optimierten Detektorsystem erreichte Impulsauflösung und Spurrekonstruktionseffizienz des Myonspektrometers wurden in einer Monte-Carlo-Simulation untersucht (Kapitel 7). Ein zentraler Aspekt dieser Studie war der Einfluß der nicht-gaußischen Fehler der Driftrohrauflösungsfunktion in der Nähe des Anodendrahtes.

Schließlich wurden Algorithmen für die Kalibration der Orts-Driftzeit-Beziehung entwickelt (Kapitel 8). Da in ATLAS kein externer Referenzdetektor verfügbar sein wird, muß das Myonsystem selbst-kalibrierbar sein. Dies wird unter Ausnutzung von Myonenspuren aus dem normalen LHC-Betrieb bewerkstelligt. Für jede der erörterten Methoden werden die erreichbare Präzision und die Anwendbarkeit für ATLAS-MDT-Kammern diskutiert. Auch in diesem Zusammenhang erwiesen sich die Ergebnisse der Präzisionsexperimente als sehr nützlich.

Auf der Grundlage dieser Erkenntnisse wird ein Szenario für die Kalibration aller MDT-Kammern in ATLAS skizziert. Dies beinhaltet eine Strategie für die Festlegung der räumlichen Zonen („Autokalibrationszonen“), innerhalb derer eine Kalibration der Orts-Driftzeit-Beziehung gültig ist. Eine einfache Abschätzung der Anzahl von Myonen, die für die vollständige Kalibration des Spektrometers notwendig ist, ergibt, daß die erforderliche Statistik innerhalb etwa eines Tages normaler Datennahme angesammelt werden kann.

# Contents

<b>1 The ATLAS Detector: An Experiment at the LHC</b>	<b>1</b>
1.1 The Large Hadron Collider . . . . .	1
1.2 Potential for New Physics at the LHC . . . . .	3
1.2.1 Particle Production Rates . . . . .	3
1.2.2 The Standard Model Higgs Boson . . . . .	4
1.2.2.1 Higgs Production at the LHC . . . . .	4
1.2.2.2 Higgs Decay . . . . .	5
1.2.3 Super-Symmetric Particles . . . . .	7
1.2.4 New Heavy Gauge Bosons $Z'$ , $W'$ . . . . .	9
1.2.5 Top and Beauty Physics . . . . .	9
1.2.6 Other Searches . . . . .	9
1.2.7 Heavy Ion Physics . . . . .	9
1.3 Experiments at the LHC . . . . .	10
1.4 Overview about the Layout of the ATLAS Detector . . . . .	11
1.4.1 The Inner Detector . . . . .	11
1.4.2 The Calorimeters . . . . .	13
1.4.2.1 The Electromagnetic Calorimeter . . . . .	13
1.4.2.2 The Hadronic Calorimeter . . . . .	14
<b>2 The Design of the ATLAS Muon Spectrometer</b>	<b>15</b>
2.1 The Basic Ideas . . . . .	15
2.2 Performance Requirements . . . . .	17
2.2.1 Physics Requirements . . . . .	17
2.2.2 The Radiation Background Environment . . . . .	19
2.3 The ATLAS Trigger Strategy . . . . .	21
2.4 Technical Realization of the Muon Precision Chambers . . . . .	22
2.4.1 The Single Drift Tube . . . . .	22
2.4.2 Monitored Drift Tube Chambers . . . . .	25
<b>3 ODYSSEUS – A Silicon Microstrip Tracker</b>	<b>27</b>
3.1 Set-up of the Silicon Microstrip Tracker . . . . .	27
3.2 System Performance . . . . .	30

<b>4 Optimization of the Operating Parameters of Drift Tubes</b>	<b>32</b>
4.1 Overview . . . . .	32
4.2 Choice of Gas Pressure and Gain . . . . .	35
4.3 Choice of the Gas Mixture . . . . .	36
4.4 Optimization of the Read-out Electronics . . . . .	38
4.4.1 Discriminator Threshold . . . . .	38
4.4.2 Pulse Shaping . . . . .	39
4.4.2.1 Peaking Time . . . . .	39
4.4.2.2 Tail Cancellation and Baseline Restoration . . . . .	40
4.5 Choice of the Anode Wire Diameter . . . . .	42
4.5.1 Experimental Set-up . . . . .	42
4.5.2 Tube Resolution . . . . .	43
4.5.3 Streamer-Pulse Probability . . . . .	48
4.6 Single Tube Performance at the Chosen Operating Point . . . . .	50
4.6.1 Spatial Resolution . . . . .	50
4.6.2 Efficiency . . . . .	51
4.6.2.1 Hit Efficiency . . . . .	51
4.6.2.2 $3\sigma$ -Efficiency . . . . .	52
<b>5 Drift-Tube Operation in a High-Rate Radiation Background</b>	<b>54</b>
5.1 Set-up of the Gamma Irradiation Facility in a Muon Test Beam . . . . .	54
5.1.1 The Experiments with Ar/N <sub>2</sub> /CH <sub>4</sub> (91/4/5) . . . . .	55
5.1.2 The Experiments with Ar/CO <sub>2</sub> Mixtures . . . . .	60
5.2 The Influence of a Radiation Background on the Tube Performance . . . . .	61
5.2.1 Resolution Deterioration . . . . .	61
5.2.1.1 Effects Related to the Electronics . . . . .	62
5.2.1.2 Space-Charge Effects . . . . .	66
5.2.1.3 Results from the Resolution Measurements . . . . .	68
5.2.1.4 Time-Slewing Corrections . . . . .	71
5.2.2 Efficiency Deterioration . . . . .	73
5.2.2.1 Deterioration of the Hit Efficiency . . . . .	73
5.2.2.2 Deterioration of the $3\sigma$ -Efficiency . . . . .	74
5.2.2.3 Double-Track Separation with a Second Threshold . . . . .	75
5.3 Conclusion about the Rate Capability of Drift Tubes . . . . .	81
<b>6 Track Reconstruction with the Maximum Likelihood Method</b>	<b>82</b>
6.1 The Least-Squares Track Reconstruction Technique . . . . .	82
6.2 Consequences of the Ionization Cluster Statistics . . . . .	83
6.3 Experimental Set-up . . . . .	85
6.4 Parametrization of the r-t Relationship . . . . .	86
6.5 The Maximum Likelihood Tracking Method . . . . .	93
6.5.1 Principle . . . . .	93
6.5.2 Technical Procedure . . . . .	93
6.6 Improvements with Respect to Least-Squares Tracking . . . . .	95
6.7 Conclusions about Maximum Likelihood Tracking . . . . .	101

<b>7 Tracking Performance of the ATLAS Muon Spectrometer</b>	<b>102</b>
7.1 The Simulation Chain . . . . .	102
7.2 Description of the MDT Response . . . . .	103
7.3 Momentum Resolution . . . . .	105
7.4 Reconstruction Efficiency and Fake-Track Probability . . . . .	109
7.5 Conclusion about the Consequences of Non-Gaussian Resolution . . . . .	112
<b>8 Calibration of the Space-Time Relationship</b>	<b>113</b>
8.1 Required Calibration Precision . . . . .	114
8.2 Determination of the r-t Relationship from the Drift-Time Spectrum . . . . .	115
8.2.1 The Composition of a Drift-Time Spectrum . . . . .	116
8.2.2 Integration Method . . . . .	117
8.2.3 Integration Method with $\delta$ -Ray Correction . . . . .	118
8.2.4 Unfolding the Detector Response . . . . .	119
8.2.4.1 Results for Test-Beam Data without Radiation Background . . . . .	122
8.2.4.2 Results for Test-Beam Data with Radiation Background . . . . .	124
8.2.5 Applicability in ATLAS . . . . .	127
8.3 Autocalibration Using Muon Tracks . . . . .	128
8.3.1 The Principle of Autocalibration . . . . .	128
8.3.2 An Algebraic Approach to Autocalibration . . . . .	129
8.3.2.1 The Matrix Equation of Autocalibration . . . . .	129
8.3.2.2 Autocalibration Constraints for a Given Track . . . . .	131
8.3.2.3 Autocalibration Constraints Combining Different Tracks . . . . .	147
8.3.3 Autocalibration Methods and their Performance . . . . .	153
8.3.3.1 The Conventional Autocalibration Technique . . . . .	153
8.3.3.2 Fitting the Global Matrix Equation . . . . .	156
8.3.4 Autocalibration Tests in Monte Carlo – The Procedure . . . . .	159
8.3.5 Comment on Autocalibration near the Wire . . . . .	159
8.3.6 Autocalibration at ATLAS . . . . .	161
8.3.6.1 Determination of the Angular Spread in ATLAS MDT Chambers	161
8.3.6.2 Precision of Autocalibration for all MDT Chambers . . . . .	161
8.3.6.3 Autocalibration Zones and the Time Required for a Calibration	167
<b>9 Summary</b>	<b>180</b>
<b>A Derivation of the Autocalibration Matrix Elements</b>	<b>183</b>
<b>B Proof of <math>\text{rank}(M) \leq \dim(M) - 2</math> for the Autocalibration Matrix <math>M</math></b>	<b>187</b>
<b>C The Distributions of Track Incidence Angles for ATLAS Chambers</b>	<b>189</b>
<b>Bibliography</b>	<b>207</b>



# Chapter 1

## The ATLAS Detector: An Experiment at the LHC

### 1.1 The Large Hadron Collider

In the year 2005 – if the ambitious schedule is realistic – the international scientific community will welcome a new era of experimental particle physics at CERN. After more than a decade of productive research at LEP and TEVATRON, whose highlights were the verification of the Standard Model up to an energy scale of about 200 GeV, the precision measurement of the W and Z masses and finally the discovery of the top-quark, the Large Hadron Collider (LHC) will open up an unprecedented range of collision energies. The acceleration of electrons and positrons in ring colliders like LEP is practically limited by energy loss through synchrotron radiation which increases with  $\gamma^4/r$  where  $\gamma$  is the Lorentz factor and  $r$  the radius of the storage ring. This effect is less important for hadrons which – due to their larger mass – acquire much more energy than electrons with the same  $\gamma$ . Thus the LHC, which will be installed in the same 27 km long ring tunnel as LEP, will be able to reach centre-of-mass energies up to 14 TeV in proton-proton collisions and up to about 1 PeV in Pb-Pb collisions. This is an increase of a factor 7 in centre-of-mass energy with respect to the TEVATRON, today's most powerful hadron collider, and a factor 70 compared to LEP2. At the TeV energy scale which will now be accessible, a large potential for new physics is expected by theorists. In Section 1.2 a brief summary of the most important predicted processes will be given.

Owing to the composite nature of the proton, only a fraction of the 14 TeV will be available for an elementary parton interaction. To enhance the observability of heavy particles originating from infrequent hard encounters where the colliding constituents take a large fraction of the total momentum, the LHC designers aim for a maximum luminosity as high as  $10^{34} \text{ cm}^{-2}\text{s}^{-1}$ . This design luminosity will be achieved by having a bunch of  $10^{11}$  protons every 25 ns in both colliding beams whose transverse radii will be  $15 \mu\text{m}$ .

The LHC will make maximum use of the existing accelerator infrastructure at CERN (Figure 1.1) to increase the proton energy step by step to 450 GeV before injecting them into the LHC. To accelerate particles of equal charge in opposite sense, two separate beam pipes are placed in a common cryostat with superconducting dipole magnets of 8.4 T strength and opposite field directions (Figure 1.2). At four positions along LHC the two proton beams will cross each other. Around these interaction points the four detectors will be built (see Section 1.3).

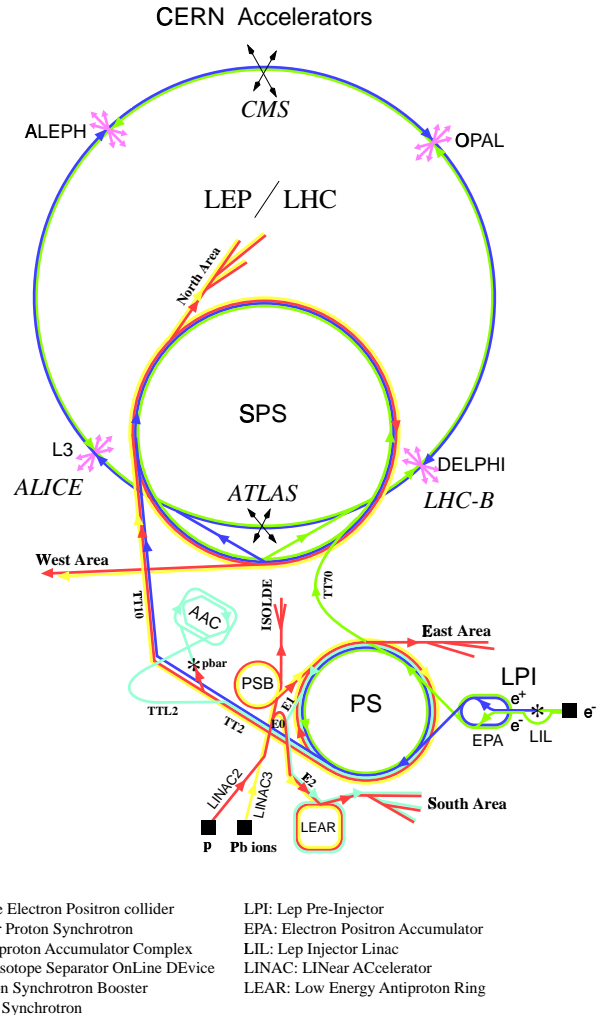


Figure 1.1: The particle accelerators at CERN.

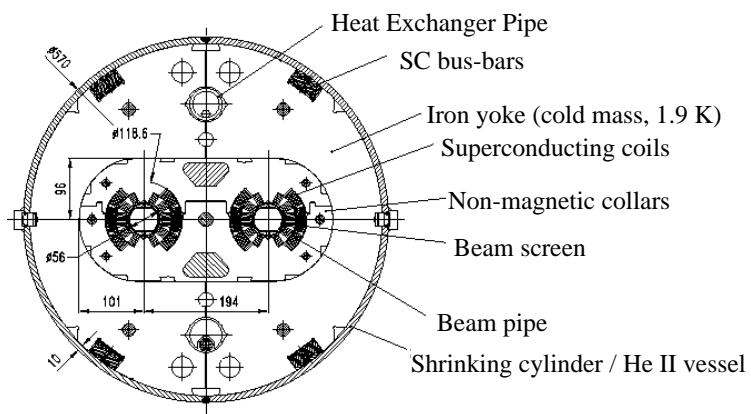


Figure 1.2: Cross-section of the LHC beam pipes with the dipole magnet system.

## 1.2 Potential for New Physics at the LHC

### 1.2.1 Particle Production Rates

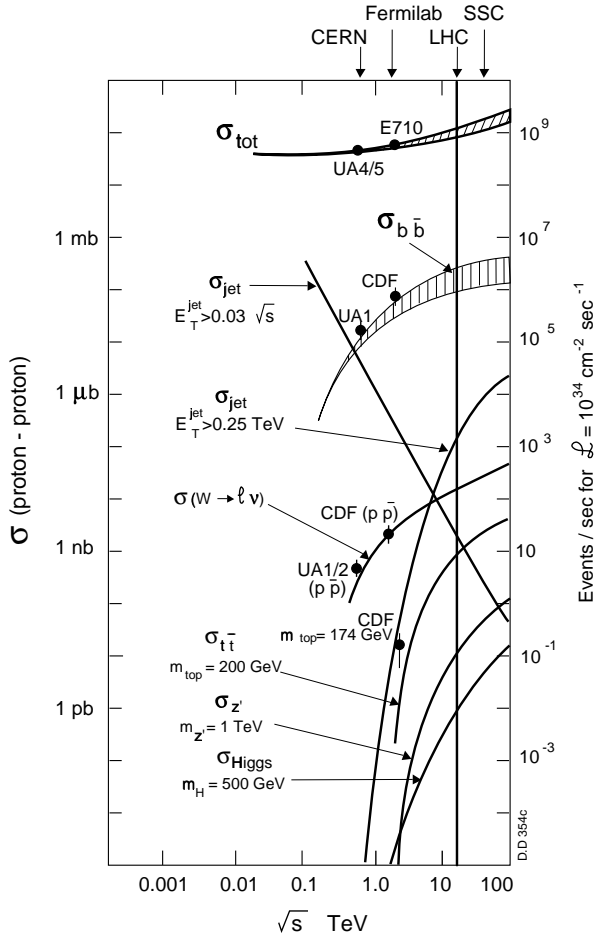


Figure 1.3: Energy dependence of some characteristic cross-sections, extrapolated to the LHC c.m. energy. The SSC project whose energy is also indicated, has been terminated.

At the LHC design luminosity of  $10^{34} \text{ cm}^{-2}\text{s}^{-1}$  there will be about 20 interactions per bunch crossing, i.e. every 25 ns, given the extrapolated total pp cross-section of about 100 mb at 14 TeV (Figure 1.3). Based on these numbers a total integrated luminosity of  $10^5 \text{ pb}^{-1}$  per year is expected. The total particle production rate will be dominated by soft proton-proton interactions. The cross-sections of the most interesting processes like Higgs production are up to 11 orders of magnitude smaller, which underlines the importance of high luminosity and efficient background rejection techniques.

In the following we shall give a short description of the most promising benchmark processes within the reach of LHC. Due to the particular importance of Higgs-boson searches for the LHC design, this issue will be discussed more in detail than the other perspectives.

## 1.2.2 The Standard Model Higgs Boson

The most famous goal of the LHC experiments is the detection of the Higgs boson which is the last missing member of the Standard Model's particle zoo. This boson owes its particular importance to the still missing definitive explanation for the masses of the fermions and the  $Z^0$  and  $W^\pm$  bosons. In the case of electroweak  $SU(2) \times U(1)$  symmetry these masses are required to vanish. However, assuming the existence of a complex isodoublet of scalar Higgs fields with a non-zero vacuum expectation value, the symmetry would be hidden in the vacuum state and at energies lower than the  $Z$  mass, where only the remaining electromagnetic  $U(1)_{\text{em}}$  symmetry is observable. This mechanism is called "spontaneous symmetry breaking". Three of the four degrees of freedom of the complex Higgs doublet are absorbed in the mass terms of the  $Z^0$  and  $W^\pm$  bosons, while the fourth corresponds to the real Higgs boson whose mass is predicted to range between 104 GeV and 1 TeV. The lower limit is due to the non-observation of the Higgs boson at LEP2, whereas the upper boundary is postulated by theorists in order to prevent a strong self-coupling of the Higgs leading to non-perturbativity already at the TeV scale [SPI 95].

For both the production and the decay of the Higgs boson it is important to know that the coupling between Higgs and fermions is proportional to the fermion mass (Yukawa coupling), while the coupling between Higgs and gauge bosons is proportional to the square of the boson mass. Therefore in Higgs physics preferentially heavy particles are involved.

### 1.2.2.1 Higgs Production at the LHC

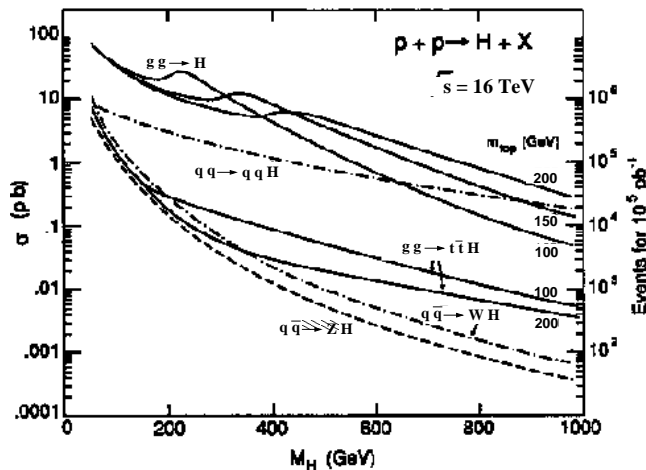


Figure 1.4: Higgs production cross-sections at LHC [DEN 90]. This plot was published before the top quark discovery.  $m_{\text{top}}$  was found to be 174 GeV. In this figure the  $WW(ZZ)$  fusion channel is labelled  $qq \rightarrow qqH$ .

The total Higgs production cross-section at LHC is predicted to range between 0.1 pb and 100 pb depending on the Higgs mass (Figure 1.4). Assuming a Higgs mass of 500 GeV, about  $10^5$  Higgs particles would be produced per year.

The dominant production mechanisms are gluon-gluon fusion, WW fusion and ZZ fusion (Figure 1.5). Other less important processes are  $t\bar{t}$  fusion and Higgs bremsstrahlung from W or Z.

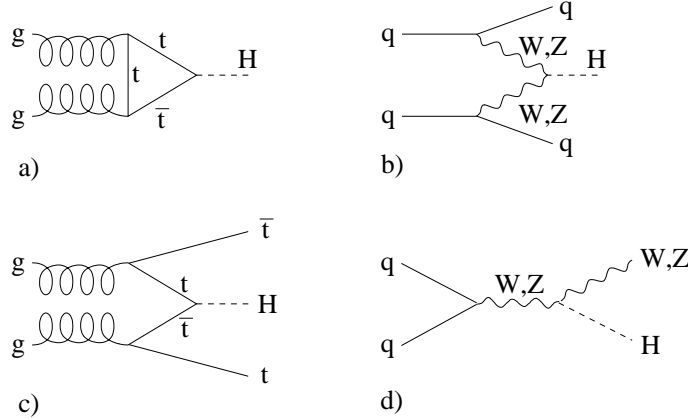


Figure 1.5: Channels for Higgs production at LHC: (a) gluon-gluon fusion, (b) WW(ZZ) fusion, (c)  $t\bar{t}$  fusion, (d) Higgs bremsstrahlung. (a) and (b) are dominant.

### 1.2.2.2 Higgs Decay

Figure 1.6 shows the branching ratios of Higgs decay channels. Depending on the Higgs mass different processes offer opportunities for observation:

- $80 \text{ GeV} < m_H < 120 \text{ GeV}$ :

Since in this mass range the b-quark is the heaviest accessible particle for pair production, the decay

$$H \rightarrow b\bar{b} \quad (1.1)$$

is dominant, but swamped by an enormous background because direct  $b\bar{b}$  production has a big cross-section (cf. Figure 1.3). However, if the Higgs stems from an associated production with W, Z or  $t\bar{t}$ , the background can be reduced by lepton tagging and the  $b\bar{b}$  pair be detected by looking for secondary vertices.

Another promising channel in this mass domain is

$$H \rightarrow \gamma\gamma \quad (1.2)$$

although it suffers from its low branching ratio and big background. The detection requires an electromagnetic calorimeter with high angular and mass resolution. As in the previously discussed channel, the associated production of a W can help reducing the background.

- $120 \text{ GeV} < m_H < 2m_Z \approx 180 \text{ GeV}$ :  
The channel

$$H \rightarrow Z Z^* \rightarrow 4\ell^\pm \quad (1.3)$$

offers a clean signature due to the high transverse momenta of the four leptons. Due to the low width of the Higgs in this mass range, a high mass resolution (about 1%) is required. The special cases where some of the leptons are muons is very relevant for the design of the muon spectrometer. The main background comes from direct  $Z Z^*$  or  $Z \gamma^*$  production.

- $2m_Z < m_H < 800 \text{ GeV}$ :  
Above the threshold for two real  $Z$ 's the “gold-plated” channel

$$H \rightarrow Z Z \rightarrow 4\ell^\pm \quad (1.4)$$

offers a large branching ratio and low background. In this mass range the natural width of the Higgs boson grows rapidly with increasing  $m_H$ , while the production rate decreases. Therefore at high masses the detection potential is determined by the available integrated luminosity. The signal from this process can be observed up to 800 GeV. For higher masses the rate becomes too low.

- $m_H > 800 \text{ GeV}$ :  
At these high masses the channel

$$H \rightarrow Z Z \rightarrow \ell^+ \ell^- \nu \nu \quad (1.5)$$

is six times more frequent than (1.4). It is characterized by the missing transverse energy due to the neutrinos and by two leptons with high transverse momenta. Other promising channels are

$$H \rightarrow Z Z \rightarrow 2\ell^\pm 2j \quad (1.6)$$

$$H \rightarrow W^+ W^- \rightarrow \ell^\pm \nu 2j \quad (1.7)$$

where the energy and angular distribution of the jets  $j$  have to be measured with a hadronic calorimeter.

At masses higher than 1 TeV the Higgs is wider than 500 GeV and thus very difficult to separate from the background.

- $150 \text{ GeV} < m_H < 190 \text{ GeV}$ :

For Higgs masses near  $2m_W \approx 160 \text{ GeV}$  the branching ratio of channel (1.3) is strongly reduced because the decay mode

$$H \rightarrow W W \rightarrow \ell^+ \nu \ell^- \nu \quad (1.8)$$

opens up. Like channel (1.6) this decay mode has the disadvantage that the Higgs peak cannot be reconstructed due to the escaping neutrinos. Thus one has to identify the kinematic characteristics of the two charged leptons and to measure precisely the missing energy.

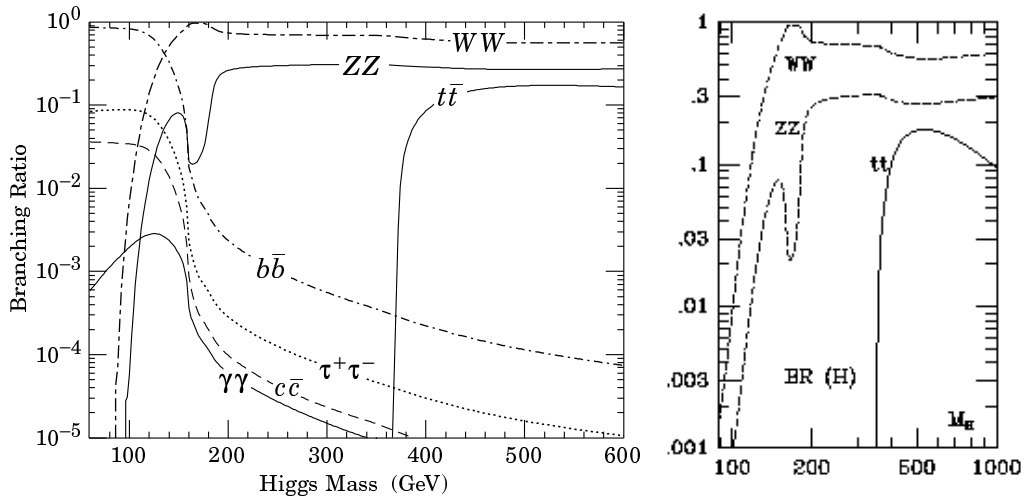


Figure 1.6: Branching ratios of the Higgs based on  $m_{top} = 174$  GeV. The mass interval between 600 GeV and 1 TeV which is missed out in the left hand plot, is covered by the right hand plot.

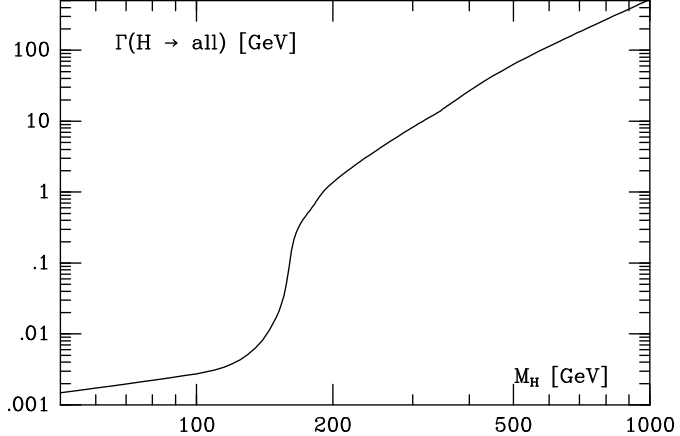


Figure 1.7: Natural width of the Higgs boson as a function of its mass [SPI 95].

### 1.2.3 Super-Symmetric Particles

In the minimal super-symmetric extension of the standard model MSSM (see e.g. [PDG 98], pp. 743ff) the super-partners of the known particles are expected to have masses at the TeV scale and thus to be observable at the LHC [TDR 99](chap. 20). Since super-symmetric particles can only be produced in pairs (assuming the conservation of R-parity), the lightest super-symmetric particle (LSP) must be stable. Since it is also expected to be electrically and colour neutral, it will escape detectors without being directly observed. In order to infer its presence from missing energy, detectors must have efficient calorimetry and high hermeticity.

The Higgs sector of the MSSM contains two isodoublets of complex fields:

$$\begin{pmatrix} H_u^+ \\ H_u^0 \end{pmatrix} \quad \text{and} \quad \begin{pmatrix} H_d^0 \\ H_d^- \end{pmatrix}.$$

Three out of the eight degrees of freedom cause the masses of the Z and  $W^\pm$  bosons. The remaining degrees of freedom give rise to five particles: a charged boson pair ( $H^\pm$ ), two CP-even neutral bosons ( $H^0, h$ ) and one CP-odd neutral boson (A). The current upper bound on the lightest Higgs boson  $h$  from theory is  $m_h < 125$  GeV.

The neutral MSSM Higgs bosons are predicted to be mainly produced by gluon-gluon fusion and Higgs radiation off W or Z. The charged Higgs bosons will be produced either by the top decay  $t \rightarrow H^+ b$  (if  $m_H < m_t - m_b$ ) or, if  $m_H > m_t - m_b$ , mainly by the processes  $g b \rightarrow H^+ t$  and  $g g \rightarrow H^+ b t$ .

Some decay channels of the Standard Model Higgs exist also for the neutral MSSM Higgs bosons (cf. Section 1.2.2.2):

$$h, H^0, A \rightarrow \gamma\gamma \tag{1.9}$$

$$h, H^0, A \rightarrow b\bar{b} \tag{1.10}$$

$$H^0 \rightarrow ZZ^{(*)} \rightarrow 4\ell \quad (\text{less than in the SM}) \tag{1.11}$$

$$H^0, A \rightarrow t\bar{t} \rightarrow W^+ b W^- \bar{b} \quad (\text{in the SM low branching ratio}) \tag{1.12}$$

$$H^0, A \rightarrow \tau^+ \tau^- \quad (\text{in the SM very low branching ratio}) \tag{1.13}$$

$$H^0, A \rightarrow \mu^+ \mu^- \quad (\text{in the SM very low branching ratio}). \tag{1.14}$$

For decay (1.13) an efficient  $\tau$ -identification algorithm involving secondary-vertex reconstruction is needed. The process (1.14) is one of the benchmark reactions for the designed momentum resolution of the ATLAS muon spectrometer (see Section 2.2.1).

On the other hand there are new processes like

$$H^0 \rightarrow h h \tag{1.15}$$

$$A \rightarrow Z h . \tag{1.16}$$

where the secondary h bosons decay according to (1.9) or (1.10).

In addition, if other super-symmetric particles are light enough, decay channels into these particles will compete with the ones mentioned above.

The most important decay channels for charged Higgs bosons are:

$$H^\pm \rightarrow \tau \nu_\tau \quad (\text{if } m_H < m_t) \tag{1.17}$$

$$H^\pm \rightarrow c s \quad (\text{if } m_H < m_t) \tag{1.18}$$

$$H^\pm \rightarrow t b \rightarrow W b b \quad (\text{if } m_H > m_t) \tag{1.19}$$

The cross-sections and branching ratios, hence the observability of channels in the MSSM Higgs sector, depend strongly on the super-symmetric parameters  $m_A$  and  $\tan \beta$ .<sup>1</sup> A detailed discussion of the decay channels and their observability as a function of these parameters would be beyond the scope of this work. It is fully explained in [TDR 99](19.3).

<sup>1</sup> $m_A$  is the mass of the CP-odd boson A;  $\tan \beta$  is the ratio of the vacuum expectation values of the neutral Higgs field components  $H_u^0$  and  $H_d^0$ .

### 1.2.4 New Heavy Gauge Bosons Z', W'

Several extensions of the Standard Model postulate the existence of additional heavy gauge bosons  $Z'$  and  $W'$ . They would be accessible to the LHC for masses up to 5 or 6 TeV. Assuming that the couplings of these bosons are similar to those of the Standard Model  $Z$  and  $W$ , the models predict the following leptonic decay channels which are expected to be observable at LHC experiments [SHA 97, PAU 90]:

$$Z' \rightarrow \ell^+ \ell^- \quad (1.20)$$

$$W'^\pm \rightarrow \ell^\pm \nu \quad (1.21)$$

For the detection a high resolution lepton measurement and charge identification up to transverse momenta of a few TeV are required. The special case where  $\ell = \mu$  defines the aims for the ATLAS muon spectrometer at muon momenta in the TeV range. In particular the charge identification becomes more and more difficult as  $p_T$  increases because the track curvature decreases and can be reconstructed with the wrong sign.

### 1.2.5 Top and Beauty Physics

As visible in Figure 1.3, the production cross-section for b-quarks at LHC will be very high. Thus precise measurements of the b-quark related elements of the CKM matrix and the verification of the predicted CP violation in the decays of  $B_d^0$  and  $B_s^0$  will be possible. For B-physics a dedicated detector, LHCb, will be built. The omni-purpose experiments ATLAS and CMS will do B-physics mainly during the initial low-luminosity period of LHC when secondary-vertex identification will not be impeded by outrageous particle rates.

Top quarks will also be abundant: at the design luminosity of  $10^{34} \text{ cm}^{-2}\text{s}^{-1}$  there will be 36000  $t\bar{t}$  pairs per hour. This will allow a precise measurement of the top quark mass and detailed studies of the decay channels.

### 1.2.6 Other Searches

The LHC experiments will also be able to investigate predictions of other extensions of the Standard Model, such as leptoquarks, magnetic monopoles or substructure of quarks and leptons. There will also be searches for signatures of technicolour models which could provide an alternative mechanism for electroweak symmetry breaking.

### 1.2.7 Heavy Ion Physics

The possibility to operate LHC as a Pb-Pb ion collider will offer the opportunity of studying matter at extreme energy densities. QCD thermodynamics predict that at sufficiently high densities hadronic matter shows a phase transition to a plasma state where quarks and gluons are no longer confined in colour singlets. Recently (Feb. 2000) the searches for this Quark Gluon Plasma found new encouragement when seven experiments of CERN's Heavy Ion programme reported about indications of a new state of matter at high densities. For heavy ion physics at LHC a specialized detector is constructed: ALICE.

### 1.3 Experiments at the LHC

Four experiments are being prepared for the LHC:

**ALICE** (**A** Large Ion Collider **E**xperiment) is an experiment specialized to heavy ion physics (mentioned in Section 1.2.7) in Pb-Pb collisions with centre-of-mass energies at the PeV scale. For details see [ALI 95].

**ATLAS** (**A** Toroidal LHC Apparatu**S**) is a general-purpose experiment for the physics of proton-proton collisions. The most characteristic feature of the detector is its magnet configuration: the inner detector will be placed inside a solenoid, whereas muon spectrometry in the outer detector will be done with a toroidal field. ATLAS is the detector on which this thesis is focussed. An introduction to the general layout of the detector will be given in the next section. The subsequent chapters are dedicated to the muon spectrometer and the detector physics of its precision chambers.

**CMS** (Compact Muon Solenoid) is the second general-purpose experiment at the LHC. Its basic design differs from ATLAS mainly in the uniform solenoidal magnetic field which covers the whole detector including the muon chambers. The strong field of 4 T allows a compact design for the muon spectrometer while preserving the necessary field integral  $\int B \, dl$ . For details see [CMS 94].

**LHCb** is an experiment specialized to B-physics. Since B mesons are most likely to emerge from collisions close to the beam direction, the LHCb detector is designed as a forward detector in order to catch low-angle particles. Its key elements will be its vertex detector, which will measure charged particle tracks, and its Ring-Imaging Cherenkov (RICH) detectors, that will identify particles. Details are described in [LHB 98].

## 1.4 Overview about the Layout of the ATLAS Detector

A three-dimensional view of the entire ATLAS Detector is shown in Figure 1.8.

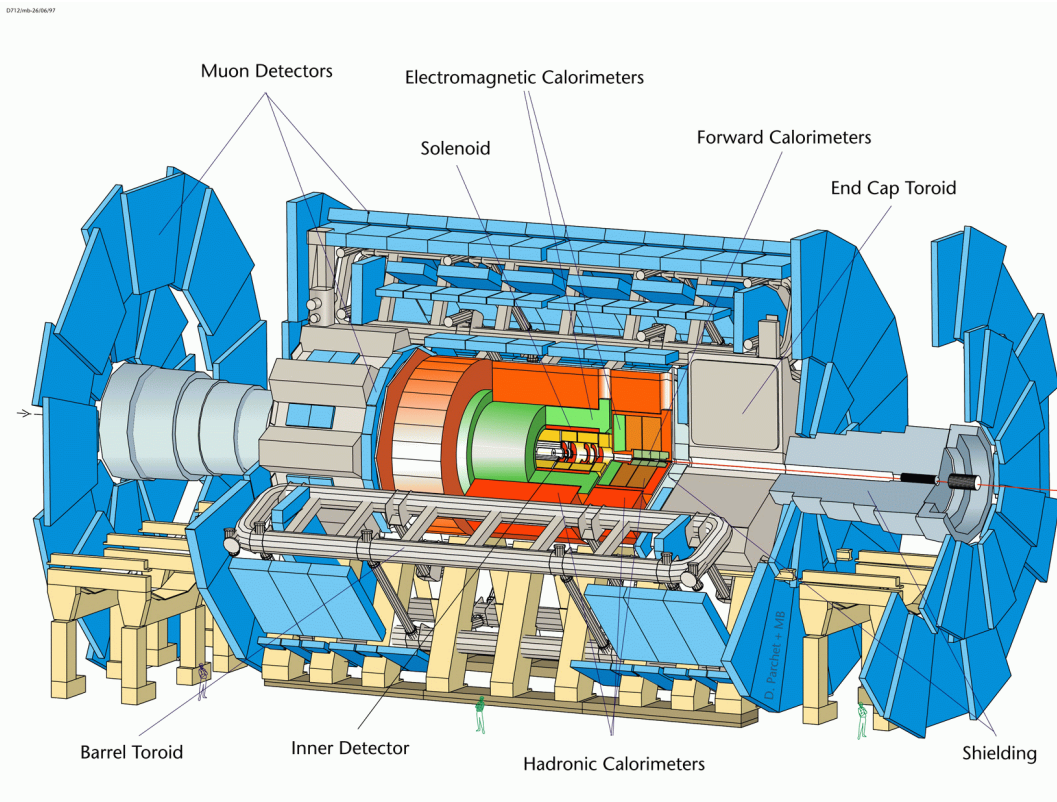


*Figure 1.8: Three-dimensional view of the ATLAS detector.*

Let us have a little tour through the detector subsystems starting in the centre.

### 1.4.1 The Inner Detector

The ATLAS Inner Detector [TDR 97a] covers the radial range from 4 cm to 1 m around the beam. Its task is a high precision tracking as close as possible to the primary vertex of a pp-interaction with the aim of finding secondary vertices and identifying particles. A solenoidal magnetic field of 2 T on average allows charge identification and momentum measurement.

Due to the intense particle background the development of detectors with sufficient radiation hardness is a particular challenge.

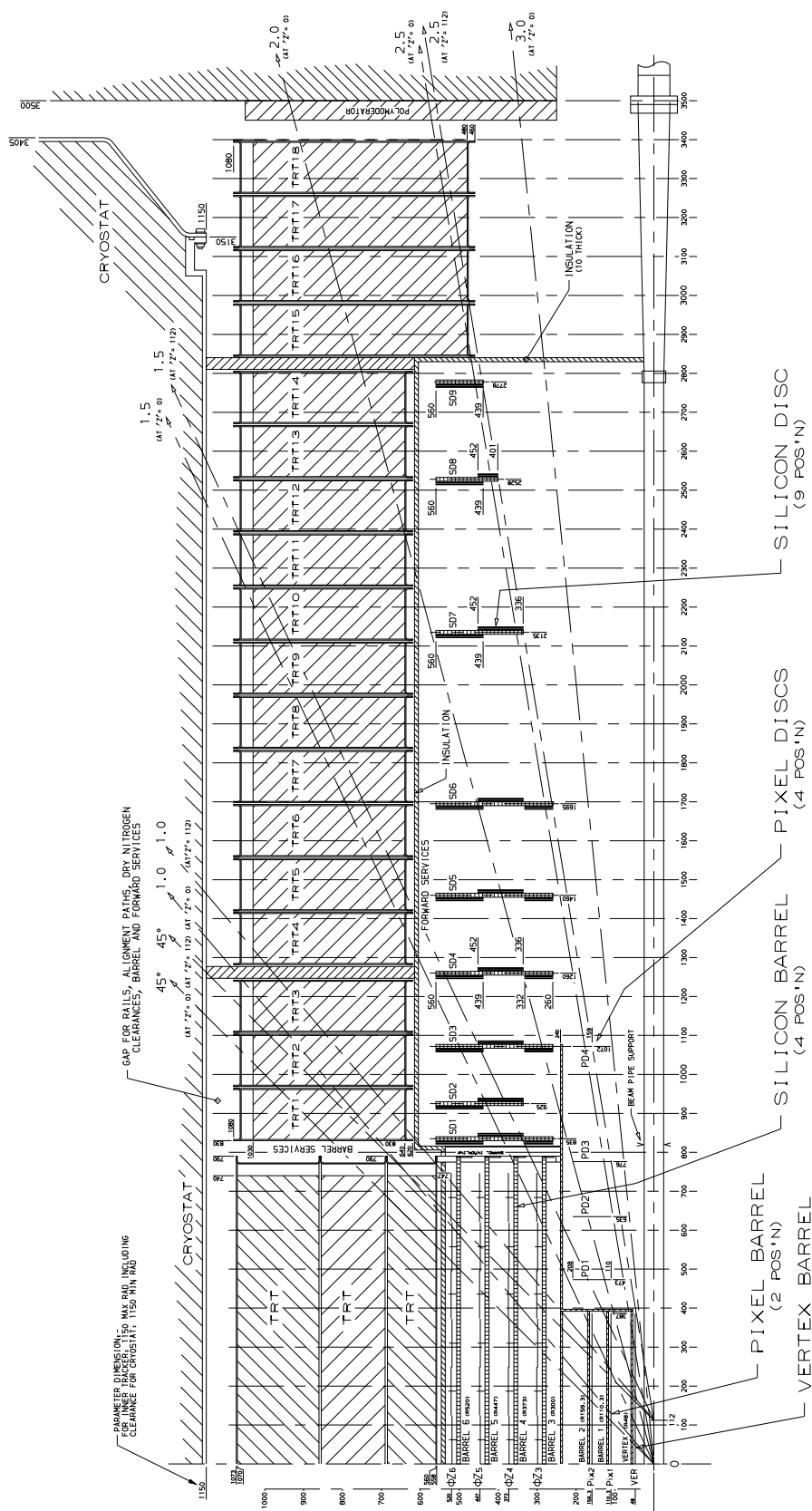


Figure 1.9: Longitudinal cross-section of the Inner Detector engineering layout.

The following detector technologies are applied (see Figure 1.9):

- **The Pixel Vertex Detector** is designed to provide a set of measurements with high granularity from 4 to 14 cm from the beam pipe. It consists of three barrel layers and four forward disks of silicon detectors segmented in pixels with a size of  $50\text{ }\mu\text{m} \times 300\text{ }\mu\text{m}$ . The finer segmentation is oriented in the bending direction of the solenoid, i.e. along  $\Phi$ . On this coordinate a resolution of  $12\text{ }\mu\text{m}$  will be achieved, while the second coordinate (along the beam in the barrel layers, radial in the forward disks) will be measured with  $70\text{ }\mu\text{m}$  precision.
- **The Semi Conductor Tracker (SCT)** has to contribute four measurements per track in the radial range between 30 and 55 cm. It will consist of silicon microstrip detectors with an  $80\text{ }\mu\text{m}$  pitch. The barrel part will have four double layers, while the forward domain will be equipped with nine double disks. The resolution in the azimuthal direction (perpendicular to the strips) will be  $16\text{ }\mu\text{m}$ . A second coordinate resolution of  $580\text{ }\mu\text{m}$  is obtained by tilting the two detector planes of each double layer by 40 mrad with respect to each other.
- **The Transition Radiation Tracker (TRT)** will cover the radial range from 55 cm to 1 m. Its components will be straw tubes with 4 mm diameter, filled with the gas mixture Xe/CF<sub>4</sub>/CO<sub>2</sub> (70/20/10). Their orientation will be axial in the barrel and radial in the forward detector. A typical track will cross about 40 tubes and be measured with  $170\text{ }\mu\text{m}$  by each of them. The transition radiation which gave the system its name, will be generated in polypropylene or polyethylene radiators between the straw tubes. Since it depends on the Lorentz factor  $\gamma$ , it provides information about the identity of a particle. A double-threshold read-out will allow the distinction between ionization signals from the particle tracks and the photon signals from the transition radiation.

## 1.4.2 The Calorimeters

We will now travel further away from the beam and enter the Calorimeter [TDR 96] whose global layout is shown in Figure 1.10. Its inner part, the Electromagnetic (EM) Calorimeter, is designed to stop electrons and photons and to measure their deposited energy with high angular resolution. It covers the pseudorapidity region  $|\eta| < 3.2$ . The outer part, the Hadronic Calorimeter, has the same task as the EM Calorimeter, but for hadrons. It extends from  $\eta = 0$  up to the very forward domain with  $\eta = 4.9$ . This design provides an excellent hermeticity.

### 1.4.2.1 The Electromagnetic Calorimeter

The EM Calorimeter is a detector made of accordion-shaped lead absorber plates alternating with copper read-out electrodes on Kapton carriers. The gaps between absorbers and electrodes are filled with liquid argon. The total thickness of the EM Calorimeter corresponds to more than 24 radiation lengths. With a granularity of  $\Delta\eta \times \Delta\Phi \approx 0.025 \times 0.025$  an angular resolution of  $50\text{ mrad} / \sqrt{E/\text{GeV}}$  will be obtained. The expected energy resolution is  $\Delta E/E = 10\% / \sqrt{E/\text{GeV}}$ .

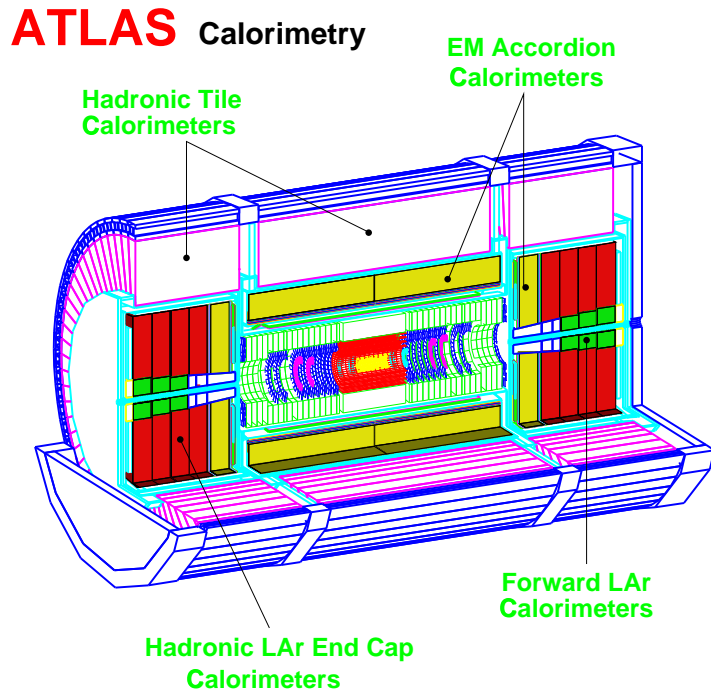


Figure 1.10: Three-dimensional view of the ATLAS calorimeter system.

#### 1.4.2.2 The Hadronic Calorimeter

The barrel hadron calorimeter (Tile Calorimeter) is a cylinder divided in three sections: the central barrel and two extended barrels. It uses iron plates as absorbers and scintillating tiles as active material. The tiles are read out by wavelength-shifting fibres leading the signal to photo-multipliers.

The end-cap and forward regions will have a liquid argon calorimeter with copper absorbers.

The granularity of the hadronic calorimeters will range between  $\Delta\eta \times \Delta\Phi \approx 0.1 \times 0.1$  ( $\eta < 2.5$ ) and  $\Delta\eta \times \Delta\Phi \approx 0.2 \times 0.2$  ( $\eta > 2.5$ ). It will provide an energy resolution  $\Delta E/E$  between 50 %/ $\sqrt{E}/\text{GeV}$  and 100 %/ $\sqrt{E}/\text{GeV}$ . The total thickness will be around 11 interaction lengths.

Leaving the calorimeters at their outer radius of 4.2 m, we finally arrive at the outermost subdetector which is the topic of this thesis: the Muon Spectrometer.

## Chapter 2

# The Design of the ATLAS Muon Spectrometer

### 2.1 The Basic Ideas

The Muon Spectrometer dominates ATLAS by its impressive dimensions of 22 m in diameter and 44 m in length. The overall layout is shown in Figures 2.1 and 2.2.

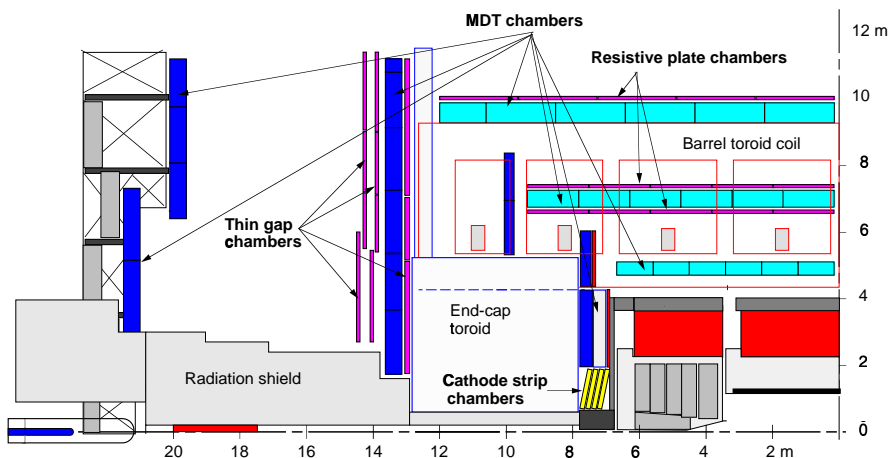
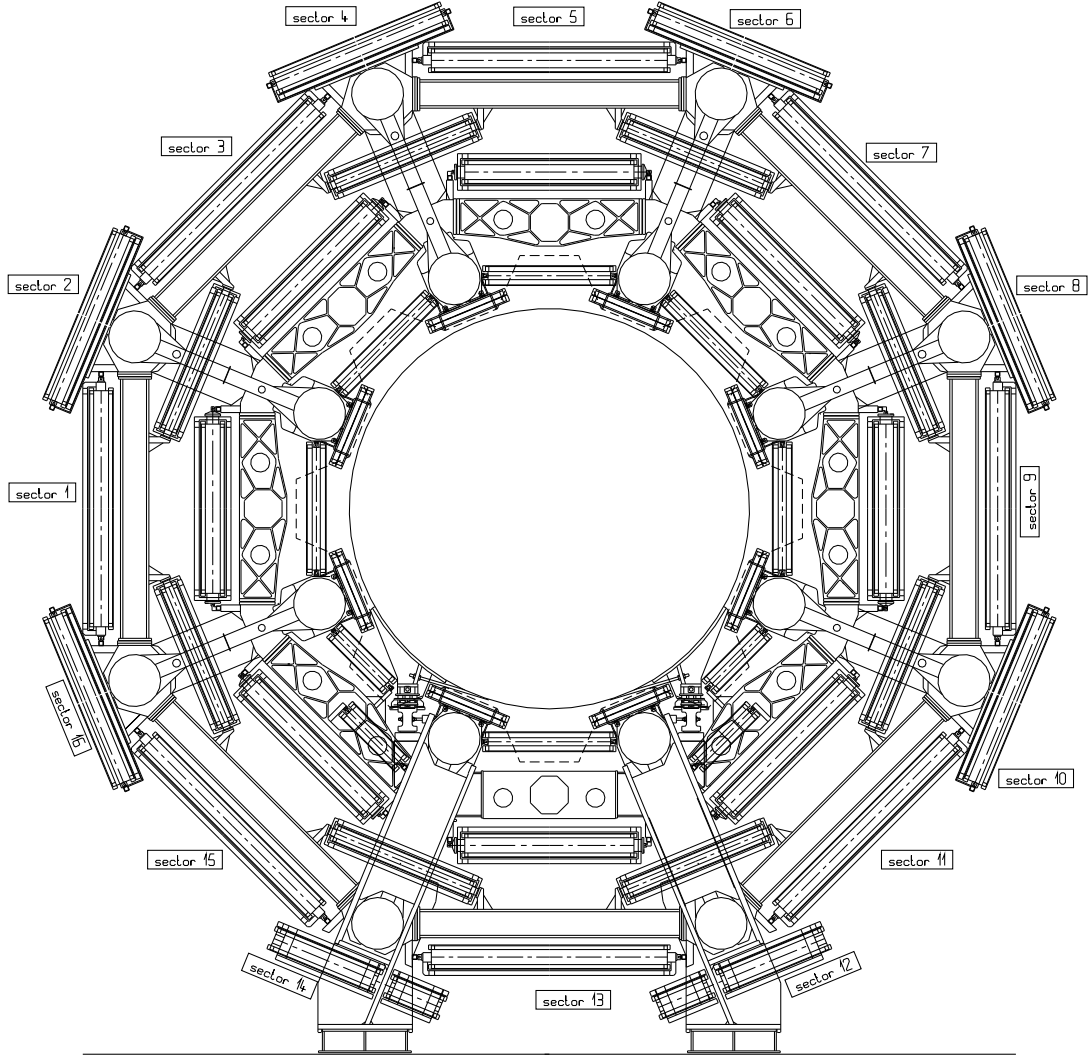


Figure 2.1: Longitudinal cut through a sector of the ATLAS muon spectrometer.

The idea underlying the design is to deflect the muon tracks with a toroidal magnetic field of 0.4 T on average, and to measure each track in at least three chambers. Knowing the magnetic field map one can infer the momentum from the sagitta of the track.

The magnet system consists of a barrel toroid and two smaller end-cap toroids (Figure 2.3). Each of them has eight superconducting coils with an air core in order to avoid resolution degradation by multiple scattering in a massive core.

The precision chambers – Monitored Drift Tube chambers and Cathode Strip Chambers (see Section 2.4) – will measure the bending coordinate: in the barrel (pseudorapidity  $\eta < 1$ ) this



*Figure 2.2: Transverse cut through the barrel of the ATLAS muon spectrometer.*

coordinate is oriented parallel to the beam line, whereas in the forward region ( $\eta > 1$ ) it is radial. The “second coordinate” (along the magnetic field lines) needs to be measured only with a precision of about 1 cm because it is mainly important for pattern recognition but not essential to the momentum measurement. The chambers measuring the second coordinate also serve as trigger chambers. In the barrel they are technically realized by Resistive Plate Chambers which are positioned below and above the middle MDT station and below the outer MDT station (see detailed view in Figure 2.7). In the forward region the same task is taken by Thin Gap Chambers behind and in front of the outer MDT station of the end-cap.

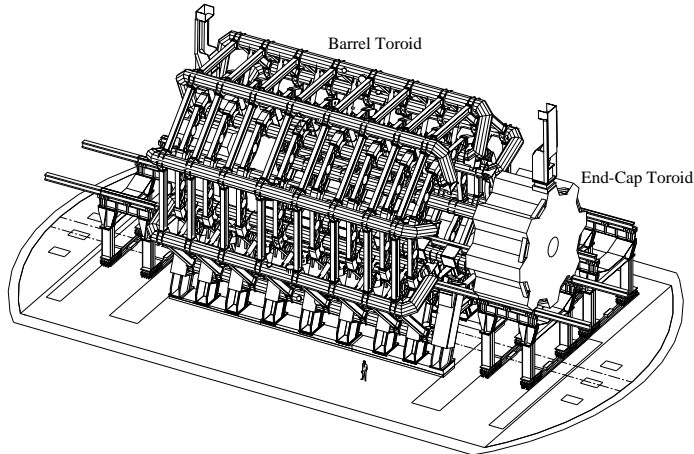


Figure 2.3: The super-conducting air-core toroid magnet.

## 2.2 Performance Requirements

Up to this point we have only presented the basic design principles. To decide on the details of the technical realization we have to define the performance requirements imposed on the chamber development.

### 2.2.1 Physics Requirements

The desired spectrometer performance was defined by the requirements of some important reactions [TDR 97b](2.1):

1.  $H \rightarrow Z Z^* \rightarrow \mu\mu\ell\ell$  : This process is important for Higgs masses between 120 and 180 GeV where the natural width is below 1 GeV (Figure 1.7). Given this small width and the high background it was found that for an adequate signal sensitivity the mass resolution should be of the order 1 %. Thus the aim for the momentum resolution of the Higgs decay muons with typical transverse momenta between 5 and 50 GeV is  $dpt/pT \leq 2\%$ . In this low momentum region resolution is dominated by energy loss fluctuations (up to 20 GeV) and multiple scattering. Limitation of the latter contribution was the decisive argument for choosing an air core magnet system with the lowest possible amount of matter. As demonstrated in Figure 2.4a, the muon spectrometer achieves a momentum resolution between 2 % and 3.5 % in the considered momentum range. Combining the tracks reconstructed in the muon spectrometer with those found in the inner detector, the performance at low momenta strongly improves (Figure 2.4b). In the range from 5 to 50 GeV the 2 % requirement is met.
2.  $H^0, A \rightarrow \mu^+ \mu^-$  : This MSSM process which plays a role for  $H^0$  or  $A$  masses between 100 and 200 GeV and  $\tan\beta > 10$ , defines similar requirements on the muon momentum resolution as the previously discussed Standard Model channel.

3.  **$Z' \rightarrow \mu\mu$  and muonic decays of heavy supersymmetric particles:** New heavy vector bosons with masses up to 5 TeV have decay channels with muons in the TeV range. The resolution in this momentum range should be on the 10 % scale. It is dominated by the spatial resolution of the precision chambers and by the alignment (Figure 2.4a). Given that the sagitta of a 1 TeV muon track in the toroidal magnetic field is typically 0.5 mm, a resolution of 10 % is equivalent to a spatial resolution of  $50 \mu\text{m}$  on the sagitta. This requires a single tube resolution of  $80 \mu\text{m}$ .
4. **Beauty physics:** The typical momentum of muons from b-decays lies below 30 GeV. In that range the resolution of the inner detector is better than that of the muon spectrometer. Therefore in b-physics the muon chambers are mainly used as a level 1 trigger (for the ATLAS trigger strategy see Section 2.3). The implication for the muon system is that pattern recognition should work down to the softest muons which reach the spectrometer, i.e. about 3 GeV.

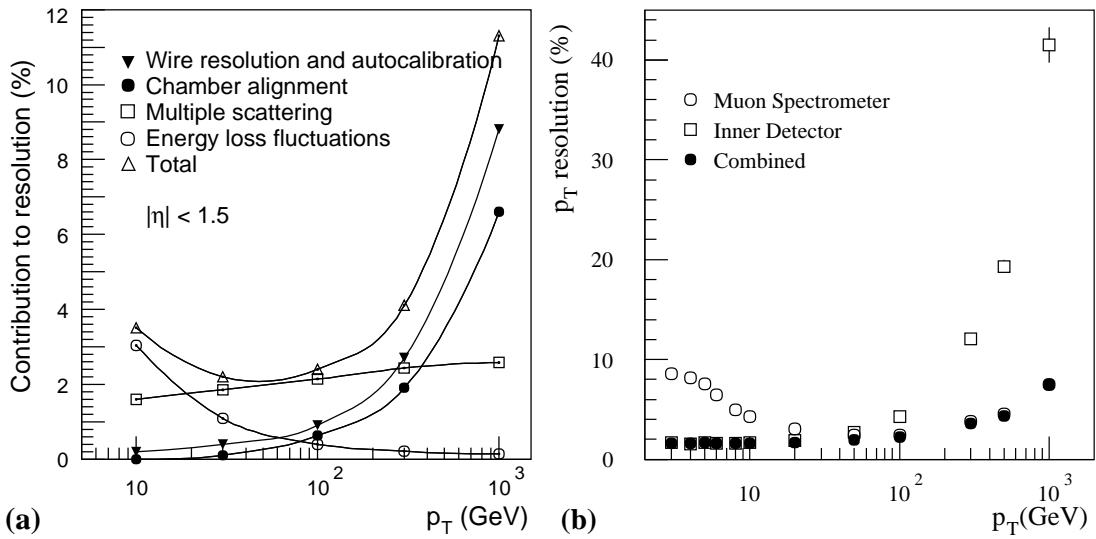


Figure 2.4: (a) Contributions to the standalone muon momentum resolution as a function of  $p_T$  assuming a single tube resolution of  $80 \mu\text{m}$ . (b) Muon momentum resolution of a combined track fit in the muon spectrometer and the inner detector compared with the individual resolutions.

Furthermore the detection efficiency of all the processes mentioned above is enhanced by a good geometrical acceptance, i.e. a high coverage in  $\eta$ . This is particularly important for the Higgs decay process (1), which due to the low transverse muon momenta requires a good hermeticity in the forward region. The actual rapidity coverage  $|\eta| < 2.7$  yields an acceptance of 62 % for the Higgs boson. Extending the coverage up to  $|\eta| = 3$  would only improve this acceptance to 68 %, but would increase the rates in the forward chambers because the radiation shield would have to be reduced in thickness to make space for the additional chambers.

The high hermeticity is also important to avoid fake missing energy which might suggest the escape of neutrinos or stable super-symmetric particles.

Of course a very high intrinsic detector efficiency is desirable. This wish is well complied with by using pressurized drift tubes which have an efficiency of more than 99.9 % (Section 4.6.2.1). The resulting muon tracking efficiency will be discussed in Chapter 7.

### 2.2.2 The Radiation Background Environment

The ambitious performance requirements discussed in the previous section will have to be met in an environment with high particle fluxes. The radiation conditions define the specifications for rate capability and ageing robustness of the muon chambers.

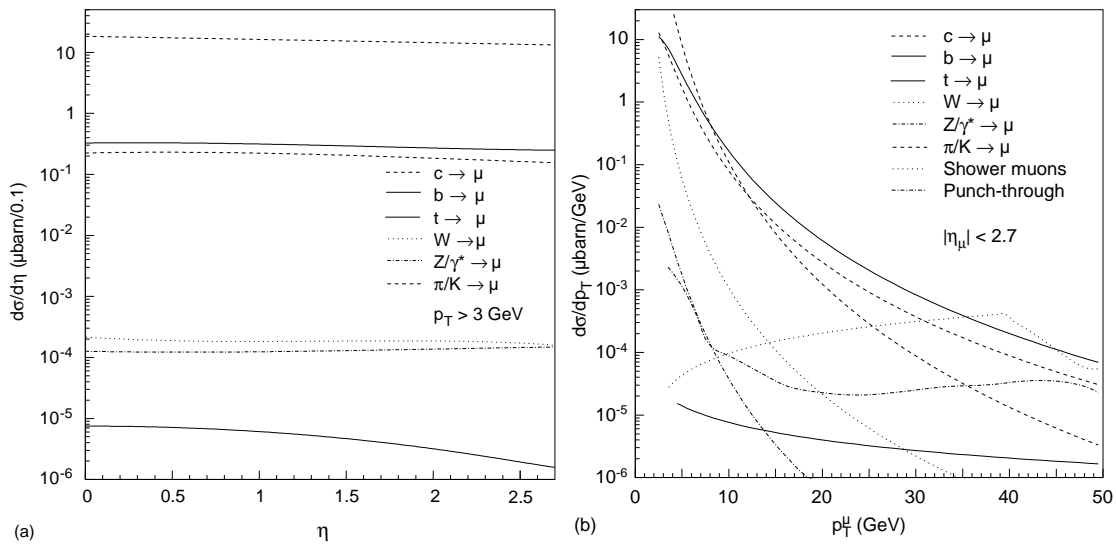


*Figure 2.5: Simulated inclusive cross-section for primary collision products [CHE 93]: (a) as a function of the rapidity, integrated over  $3 < p_T < 50 \text{ GeV}$ ; (b) as a function of  $p_T$ , integrated over  $|\eta| < 2.7$ .*

One can distinguish two categories of background:

1. **Primary collision products** are still associated in time with a p-p interaction. Only muons and hadrons with momenta above 3 GeV can contribute to this correlated background. Softer particles are stopped before the spectrometer. As we can see in Figure 2.5a, the primary background is dominated by muons from the decay of low- $p_T$  pions and kaons in the inner detector and the calorimeter. The second most important contribution comes from prompt muons produced in the decay of hadrons with b and c quarks. For  $p_T > 8 \text{ GeV}$  they even dominate the inclusive muon cross-section (Figure 2.5b).

Less important are muons from gauge boson and t quark decay.

Finally there is a contribution from “punch-through” hadrons, i.e. hadrons which do not interact in the calorimeters and penetrate into the muon spectrometer. However, the absorptive power of the calorimeter system is sufficient to suppress this hadronic debris down to a negligible amount.

From the point of view of particle rate the primary background is negligible compared to the uncorrelated radiation which will be discussed next. The maximum expected flux is at the scale of  $10\text{ Hz/cm}^2$  in the innermost precision chambers.

In Chapter 8 we shall see that the background muons with  $p_T > 6\text{ GeV}$  are not a nuisance at all: they are even essential for the autocalibration of the Monitored Drift Tube chambers. Note that the background muon cross-section is almost flat in rapidity, which is important for calibrating the entire spectrometer.

- Radiation background:** In interactions of primary collision products with various detector and machine elements huge quantities of low-energy photons and neutrons are produced. By frequent rescattering these particles lose any correlation with the initial p-p collision and form a permanent background with energies mainly between 0.1 and 10 MeV (Figure 2.6a). Although the photon and neutron sensitivities of MDTs are only 0.45 % and 0.1 % respectively [BAR 94a, CHL 93], counting rates up to  $100\text{ Hz/cm}^2$  are expected (Figure 2.6b), corresponding to 300 Hz per centimeter tube length. In the inner station the region  $\eta > 2$  will be equipped with Cathode Strip Chambers which can operate at higher rates than MDTs. They will have to cope with up to  $1\text{ kHz/cm}^2$  near the beam pipe.

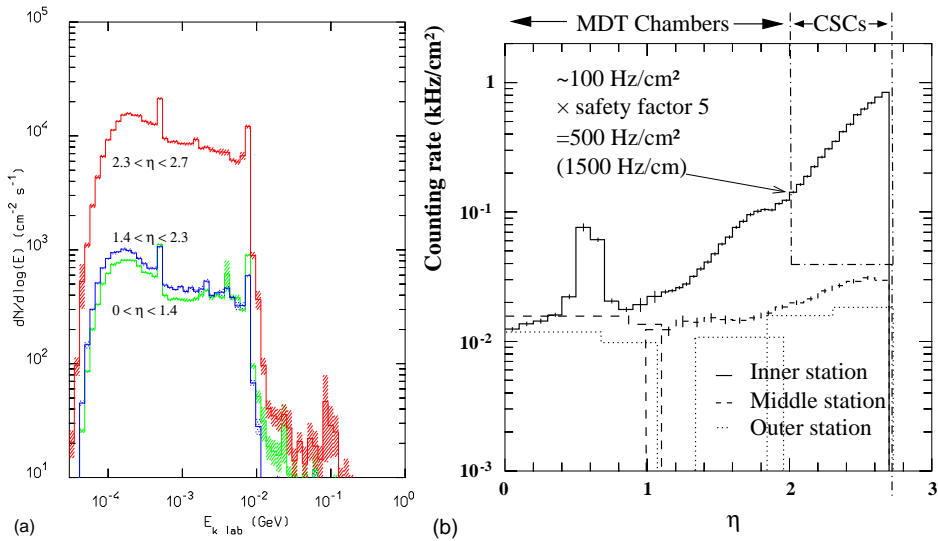


Figure 2.6: (a) Simulated background photon energy spectrum for three pseudo-rapidity ranges. (b) Pseudo-rapidity dependence of the total counting rate in the three precision-chamber stations at the nominal LHC luminosity of  $10^{34}\text{ cm}^{-2}\text{ s}^{-1}$  [TDR 97b]. The dash-dotted line represents the boundary between MDT and CSC chambers in the inner station.

Presently the background counting rate is still subject to uncertainties: due to a limited knowledge of the shower processes in the calorimeters and of the  $(n,\gamma)$  cross-section, the simulated photon and neutron fluxes might be wrong by a factor up to 2.5. Furthermore the chamber sensitivities are uncertain by a factor up to 1.5. To minimize the risk of underestimating the background rates, the ATLAS collaboration decided to design the

muon system for a five times higher background than expected. Thus MDTs must be able to operate at rates up to  $500 \text{ Hz/cm}^2$  or  $1500 \text{ Hz}$  per centimeter tube length which means total count rates up to  $300 \text{ kHz}$  for the most irradiated EIL1 chambers with tube lengths up to  $2 \text{ m}$ .

To study the effects of the high-rate radiation background on drift chamber operation, a dedicated test-beam experiment with a strong gamma source was carried out. It will be discussed in Chapter 5.

## 2.3 The ATLAS Trigger Strategy

The ATLAS trigger algorithm has three levels which successively reduce the event rate starting from the bunch-crossing rate of  $40 \text{ MHz}$  to about  $100 \text{ Hz}$  which can be recorded.

- **The Level 1 trigger (LVL1)** searches for basic signatures of interesting physics in the data. Criteria of this preselection are the multiplicities of muons, electromagnetic clusters and jets as well as global information like missing transverse energy. Only events accepted by LVL1 will be investigated further. After this trigger step the event rate is reduced to  $75 \text{ kHz}$ .

For the special case of the Level 1 muon trigger the decision scheme is sketched in Figure 2.7:

When LHC will run on high luminosity ( $10^{34} \text{ cm}^{-2} \text{ s}^{-1}$ ), the amount of data can only be coped with if a sufficiently high muon threshold is chosen: therefore the so-called high- $p_T$  trigger is set to  $20 \text{ GeV}$ . For low luminosity ( $10^{33} \text{ cm}^{-2} \text{ s}^{-1}$ ) on the other hand, muons down to  $6 \text{ GeV}$  can be accepted. This is called the low- $p_T$  trigger.

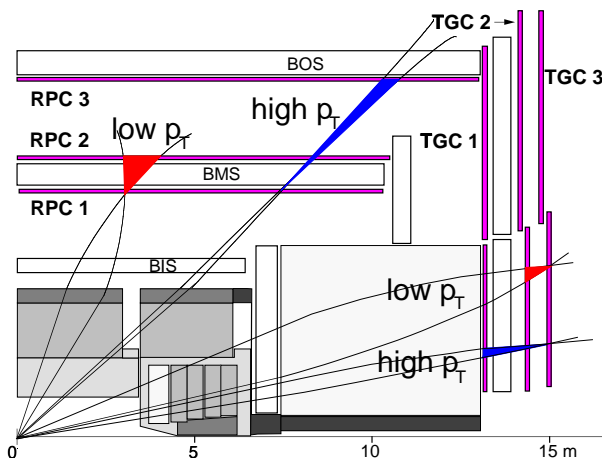


*Figure 2.7: The positions of the muon trigger chambers. Also shown is the scheme of the level 1 muon trigger (see text).*

In the barrel region the low- $p_T$  trigger is satisfied if in the stations RPC1 and RPC2 a combination of hits in both coordinates can be found which fulfill the condition that the hits in RPC2 lie within a tolerance window from the straight line defined by the interaction point and the hit in RPC1. Since low energy muons are likely to be stopped before the outer station or to be strongly deflected, no hit is required in RPC3. For the end-cap low- $p_T$  trigger an analogous hit combination is required in TGC3 and TGC2. For the high- $p_T$  trigger an additional hit is required in RPC3 (barrel) or TGC1 (end-cap), again within a coincidence window.

- **The Level 2 trigger (LVL2)** focuses on regions of interest (RoI) identified by LVL1. While these RoI are further analyzed in more detail, the full event information is kept in a buffer. If LVL2 confirms the event, the data are passed on to LVL3. At this stage the event rate is about 1 kHz.
- **The Level 3 trigger (LVL3) or Event Filter (EF)** performs a global analysis combining the information from the different subsystems. Events which satisfy the final criteria are stored.

## 2.4 Technical Realization of the Muon Precision Chambers

In the major part of the muon spectrometer the technology of Monitored Drift Tube (MDT) chambers was adopted for the precision chambers. Only for a very small forward domain ( $\eta > 2$ ), where the background rate is beyond the capability of MDTs, the technology of Cathode Strip Chambers was chosen [POL 94, GOR 00].

In this work we shall focus on the MDT chambers. We start the discussion with their smallest element, the single drift tube.

### 2.4.1 The Single Drift Tube

This section will give a short introduction to the operation principles of drift tubes. The parameter values mentioned here, will be justified in Chapter 4.

ATLAS drift tubes have a diameter of 3 cm and a length between 1 and 6 m. They are made of an Al/Mn alloy. In the centre they have a 50  $\mu\text{m}$  thick gold-plated W/Re anode wire which is connected to positive high voltage (Figure 2.8). Through the tubes there will be a gas flow with one volume exchange per day. The gas will have an absolute pressure of 3 bar.

A muon crossing a drift tube (Figure 2.9) ionizes the detector gas. The charge produced along the track is stochastically distributed [BLU 93]:

- The interactions of the muon with gas particles being independent, the number of ionization clusters per unit length is governed by a Poisson distribution. In Argon at 3 bar the mean number of clusters per cm of track is about 105 corresponding to a mean cluster distance of 95  $\mu\text{m}$ .
- The number of electrons in a cluster depends on the details of the various contributing ionization mechanisms and cannot be expressed in a closed form. It can however be simulated with HEED [SMI 97], a programme for computing energy loss of particles in gases,

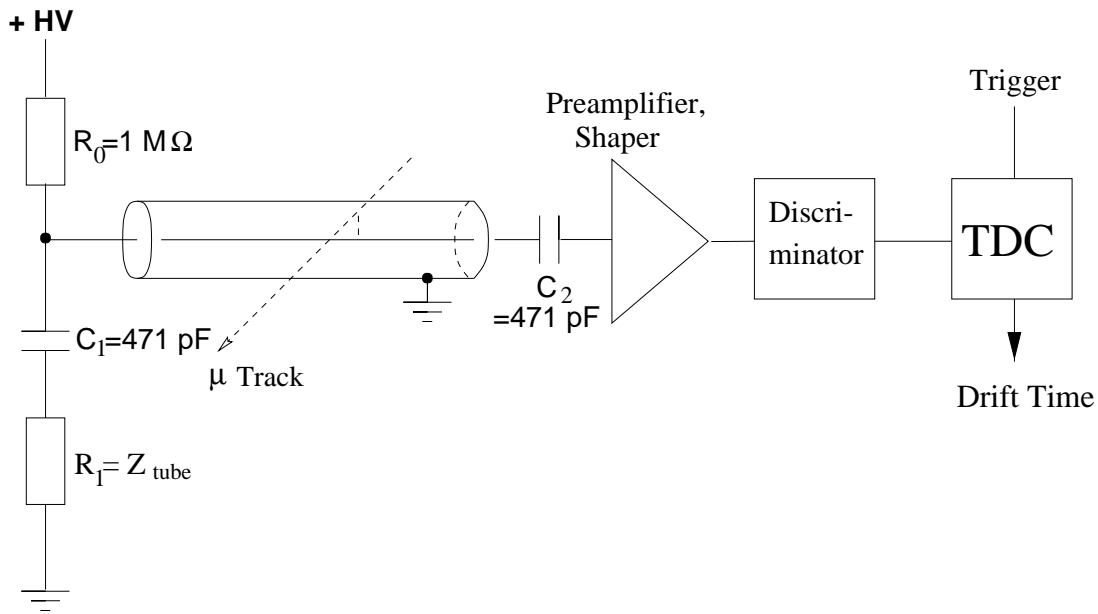


Figure 2.8: Electric circuitry of a drift tube. The termination resistor  $R$  matches the tube impedance  $Z_{\text{tube}}$  to avoid reflections. For a wire diameter of  $50 \mu\text{m}$  and a tube diameter of  $3 \text{ cm}$  we have  $Z_{\text{tube}} = 382 \Omega$  (see Equation (4.4)).

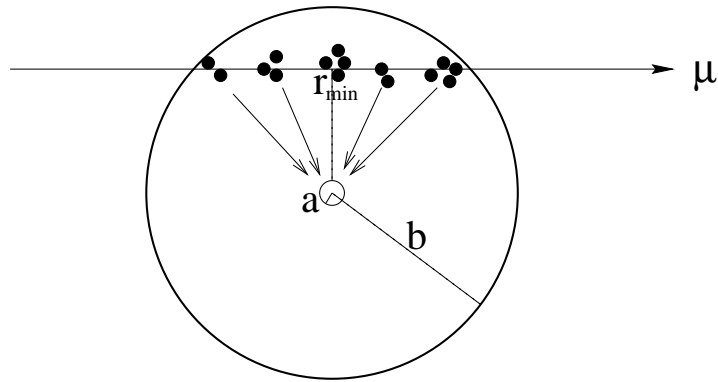


Figure 2.9: Ionization of the gas along a muon track crossing a drift tube.

which not only involves the cross-sections for muon collisions with gas atoms, but also takes into account secondary ionization processes and delta-ray production. Figure 2.10 shows the cluster-size distribution for Ar/N<sub>2</sub>/CH<sub>4</sub> (91/4/5) [RIE 97a]. Ignoring clusters above 500 e the mean number of electrons per cluster is about 3.

In Section 6.2 we shall see that this statistical behaviour has consequences for the drift-time distributions if a particle track approaches the wire closer than 2 mm.

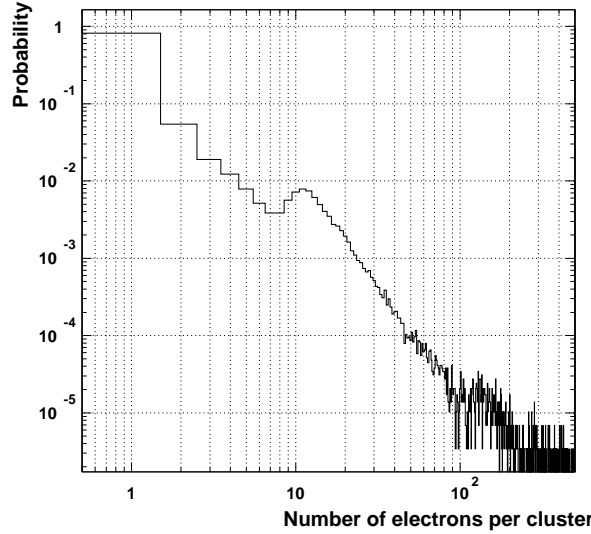


Figure 2.10: Cluster-size distribution for  $\text{Ar}/\text{N}_2/\text{CH}_4$  (91/4/5) at 3 bar calculated with HEED

The clusters of ionization electrons will now drift towards the anode wire, guided by the radial electric field

$$E(r) = \frac{V}{r \ln \frac{b}{a}} , \quad (2.1)$$

where  $a$  is the wire radius,  $b$  the inner cathode radius and  $V$  the high voltage applied to the anode. In the high-field region near the wire the charge is multiplied in an avalanche process creating new electron-ion pairs. The anode voltage is chosen such that the avalanche amplification factor (gas gain) is  $2 \times 10^4$ . Typically this voltage is about 3 kV. The precise value depends on the detector gas (Section 4.3) and the wire diameter (Section 4.5).

The positive ion cloud moves from the avalanche zone towards the cathode, inducing a current signal in the anode wire. There is also a signal induced by the drifting electrons. However, since the drift distance of the electron avalanche is only as big as the amplification zone near the wire (i.e. about  $150 \mu\text{m}$ ) the electron signal is a sharp spike of only about 100 ps length containing very little charge. Therefore this electron pulse is negligible compared to the ion signal.

The pulse of a single ion is given by

$$I(t) = \begin{cases} \frac{e}{2 \ln \frac{b}{a}} \cdot \frac{1}{t+t_0} & \text{for } 0 \leq t \leq t_{max} \\ 0 & \text{otherwise.} \end{cases} \quad (2.2)$$

with the decay time constant

$$t_0 \equiv \frac{a^2}{2 \mu V} \ln \frac{b}{a} . \quad (2.3)$$

$t_{max}$  is the arrival time of the ion at the cathode (some ms):

$$t_{max} \equiv \int_a^b \frac{dr'}{\mu E(r')} = \frac{b^2 - a^2}{2 \mu V} \ln \frac{b}{a} . \quad (2.4)$$

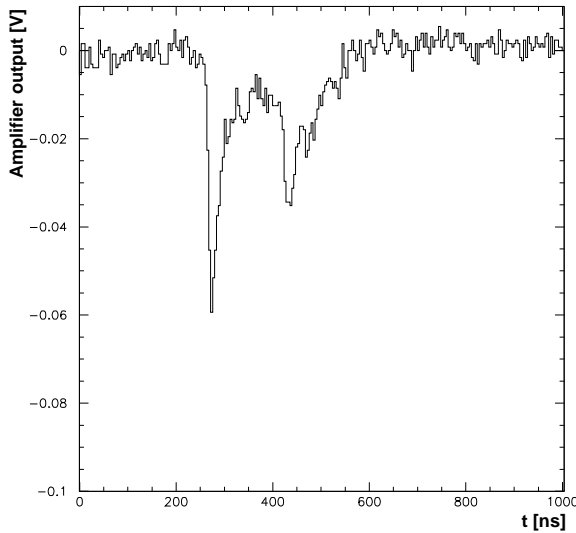


Figure 2.11: Typical muon pulse measured with a fast preamplifier [REW 86] (4 ns peaking time) and a Flash ADC.

The ion mobility  $\mu$  is approximated to be constant which is justified outside the avalanche region. A solution taking into account the field dependence of  $\mu$  can be found in [DEI 96b].

A typical muon signal with two dominant cluster spikes is shown in Figure 2.11.

The current signal is read out on one side of the tube, amplified and shaped, then presented to a discriminator. The logical output pulse of the discriminator is given to a TDC which measures the time difference between the muon pulse and a trigger signal. This time difference is the drift time plus a constant offset due to the signal propagation time in the electronics.

Now the drift time is converted into the radius of closest approach of the track using the space-time relationship ( $r$ - $t$  relationship) obtained by autocalibration (Chapter 8). Thus a single tube can only determine the circle to which the muon track was tangent. For reconstructing tracks the tubes are arranged in multilayers as it will be shown in the next section.

#### 2.4.2 Monitored Drift Tube Chambers

An MDT chamber consists of two close-packed multilayers of tubes with a support structure between them (Figure 2.12).

Depending on the position in the muon spectrometer, a multilayer has three or four layers of tubes: The four-layer chambers are located in the inner stations where the gamma and neutron radiation rates are highest and thus the background hits most frequent. By adding another layer of tubes the difficult pattern recognition in these regions is made more reliable.

To cover the whole spectrometer area of  $5500 \text{ m}^2$ , 1194 MDT chambers with 370000 tubes are needed.

Given the large scale of the spectrometer and the big number of chambers, it would be extremely difficult or even impossible to keep the geometry of the chambers and their positions stable on the scale of the tracking accuracy of  $50 \mu\text{m}$ . Therefore a different approach was chosen

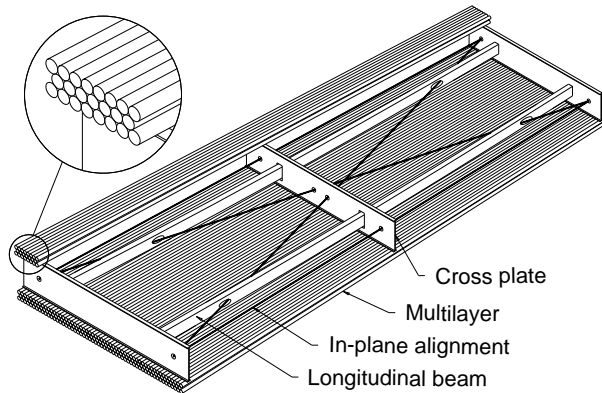


*Figure 2.12: To build an MDT chamber two multilayers of drift tubes are glued to a spacer structure.*

for alignment: the chambers will be positioned only with low precision, i.e. on the millimeter scale. Instead, the chamber movements and deformations will be continuously monitored<sup>1</sup> with an optical alignment system [TDR 97b] to a precision of better than  $20\text{ }\mu\text{m}$ . Then the measured deviations from the ideal geometry can be used as corrections for the muon tracking procedure.

---

<sup>1</sup>This geometry monitoring is the origin of the name “Monitored Drift Tube Chambers”.

## Chapter 3

# ODYSSEUS – A Silicon Microstrip Tracker for Test-Beam Experiments

For reliable measurements of drift tube resolution and efficiency and for unambiguous verification of reconstructed tracks through chamber prototypes a state-of-the-art reference tracker with well understood detector technology is indispensable. Given the typical drift tube resolution of  $80 \mu\text{m}$ , the reference system ought to have a precision of the order of  $10 \mu\text{m}$ .

Our group's choice was to use silicon microstrip detectors. In this chapter we shall briefly present the Silicon Microstrip Tracker "ODYSSEUS" – a tool which was used in all our test-beam experiments as external reference detector. More details can be found in [DEI 99, DUB 96].

### 3.1 Set-up of the Silicon Microstrip Tracker

Our beam telescope consists of six silicon microstrip detectors<sup>1</sup> and two trigger scintillators aligned along the beam axis (Figure 3.1).

x: Second Coordinate  
y: Precision Coordinate  
z: Beam Direction

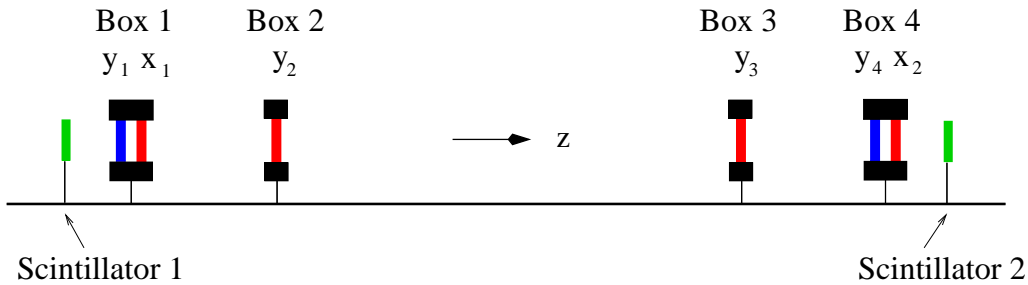


Figure 3.1: Set-up of the silicon telescope ODYSSEUS.

<sup>1</sup>donated by the MPI Semiconductor Laboratory in Munich

Each detector has 996 strips with a pitch of  $50 \mu\text{m}$  and covers an area of  $51 \times 51 \text{ mm}^2$ . Figure 3.2 shows a simplified drawing of the detector cross-section. For the detector physics of semiconductor microstrip detectors the reader is asked to consult the literature, e.g. [LEO 94, HYA 83, BEL 83].

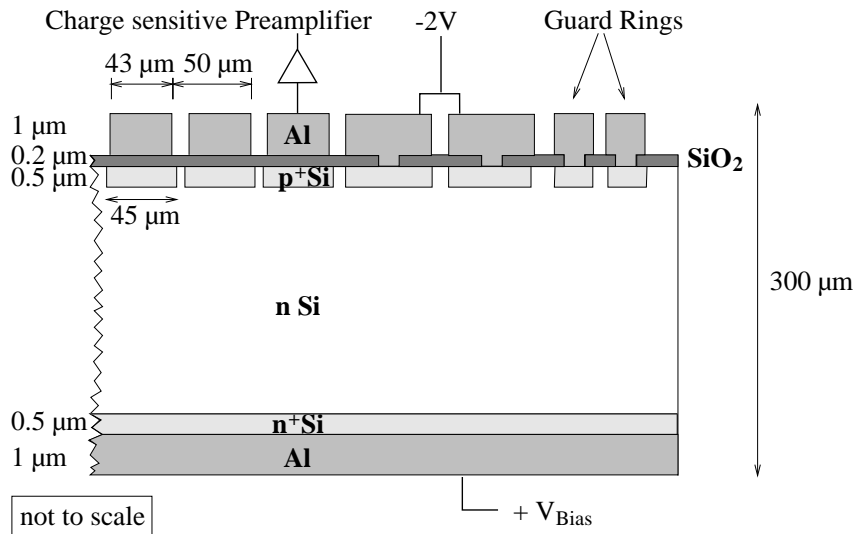


Figure 3.2: Schematic cut through a Silicon microstrip detector. In our system all strips are read out.

Four planes measure the precision coordinate of particle tracks (called “y”) while the two remaining detectors measure the second coordinate (called “x”). In test-beam experiments with drift tube chambers the precision coordinate is oriented perpendicular to the anode wires, whereas the second coordinate is parallel to them.

The six detectors are arranged in four frames (Figure 3.3) covered with light-tight lids. These boxes are mounted on a support plate with a precision of  $10 \mu\text{m}$ . The boxes 1 and 4 contain one x- and one y-plane each, whereas in the boxes 2 and 3 there is only a y-plane. The physical orientation of the (x-y) coordinate system (x horizontal, y vertical or vice versa) can be changed by turning the detector boxes around the z-axis (beam direction). This possibility is convenient because the reference tracker can be easily adapted to the wire direction of the MDT chambers which is in some cases vertical, in others horizontal.

In the front-end electronics (VA-chips [IDE 94]) the signal pulses of all individual strips are amplified and shaped with a time constant of about  $2 \mu\text{s}$ . At the peaking time the signal values of all channels are simultaneously sampled and held constant (sample & hold circuit) while waiting for being sequentially read out. The multiplexed signal values of all strips in a box (one or two detectors) are fed into an FADC (CRAMS<sup>2</sup>). Each CRAMS can consecutively read 2016 channels, which is sufficient for a box with two detectors. The full readout chain is drawn in Figure 3.4.

If the signal value of a CRAMS channel exceeds a certain threshold, the pedestal of that channel (measured and stored in a CRAMS memory before data taking) is subtracted from the

<sup>2</sup>Caen Readout of Analog Multiplexed Signals [CAE 94]

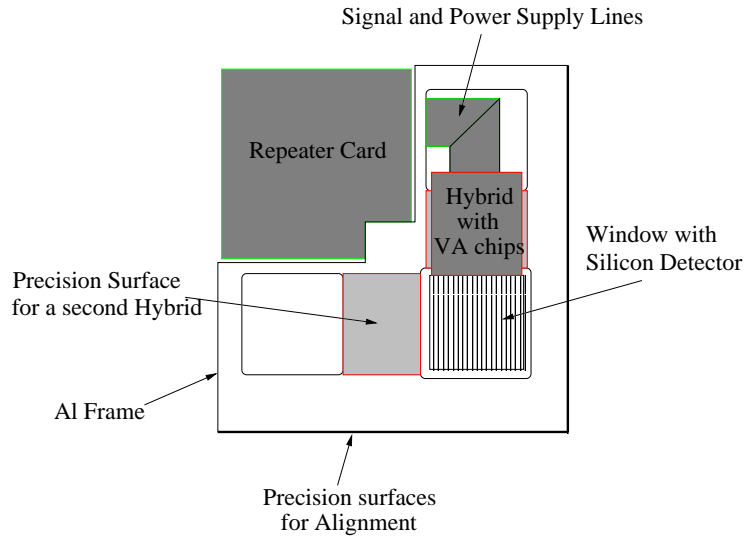


Figure 3.3: Frame with Silicon microstrip detector and the front-end electronics.

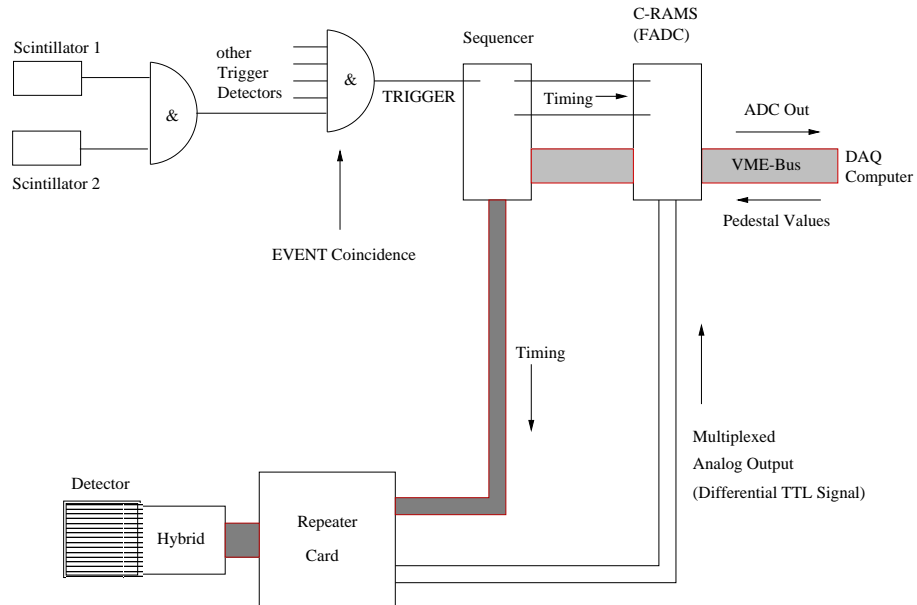


Figure 3.4: The Silicon telescope read-out.

signal. Finally the pedestal-subtracted signal value is given to the VME bus and recorded by the DAQ.

## 3.2 System Performance

The performance of the reference tracker can be characterized by three quantities: the spatial resolution, the signal/noise ratio and the efficiency.

The passage of an ionizing particle through a silicon microstrip detector creates signals in a cluster of 1 to 5 adjacent strips. Our detectors have a mean cluster size of about 3 strips. The most pessimistic number for the spatial resolution is obtained by just using the centre of the strip with the highest deposited charge as the track position. This worst-case resolution is given by

$$\sigma_{\text{worst}} = \frac{\text{pitch}}{\sqrt{12}} = \frac{50 \mu\text{m}}{\sqrt{12}} = 14.4 \mu\text{m} \quad (3.1)$$

By determining the particle hit position as the centre of mass of the charge deposited on the strips near the track, a single detector resolution of 7  $\mu\text{m}$  is obtained.

Without multiple scattering a linear track fit through the 4 y-planes would yield a tracking precision of

$$\sqrt{\frac{\sigma^2}{4}} = \frac{7 \mu\text{m}}{2} = 3.5 \mu\text{m}. \quad (3.2)$$

in the centre of the detector set-up (between the boxes 2 and 3). With multiple scattering however it is limited to 5  $\mu\text{m}$  for muons with energies of the order 100 GeV.

The main contribution to the noise of a semiconductor detector is caused by the leakage current which is a strong function of the temperature:

$$I_{\text{leak}} \sim T^{3/2} e^{-\frac{E_{\text{gap}}}{2kT}} \quad (3.3)$$

High leakage currents have to be avoided not only to limit the noise, but also to prevent detector damage. In order to compensate the heat produced by the readout chips and components on the repeater cards, we added a Peltier cooling system which stabilizes the detector temperature at about 20°C. Thus the leakage current is kept below 100 nA per detector. The achieved signal-to-noise ratio, defined as

$$S/N \equiv \frac{\text{maximum of pulse-height spectrum}}{\text{rms spread of pedestal spectrum}} , \quad (3.4)$$

is  $62 \pm 1$  averaged over all strips in all detectors.

The efficiency of the total reference system has several components:

- The intrinsic efficiency of semiconductor detectors is very close to 100 % [LEO 94].
- The geometrical acceptance is given by the ratio

$$\frac{\text{detector surface}}{\text{trigger scintillator surface}} = \frac{51\text{mm} \times 51\text{mm}}{51\text{mm} \times 53\text{mm}} = 96 \% ,$$

provided that the scintillators and the silicon detectors are perfectly aligned with respect to each other and parallel to the beam.

- An important contribution to inefficiencies comes from dead or noisy channels, mostly caused by broken or damaged bonds or preamplifiers. Very noisy channels which produce hits in almost every event must be discarded from the analysis and therefore have to be considered as dead.

Figure 3.5 shows a typical efficiency plot for “ODYSSEUS”.

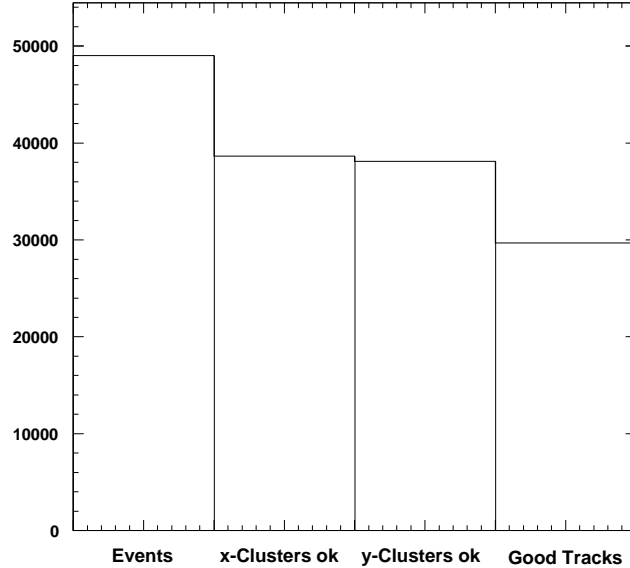


Figure 3.5: Efficiency plot for “ODYSSEUS” (see text).

The first bin contains the total number of events, i.e. scintillator triggers.

In the second bin only those events enter which have exactly one good hit cluster in both planes measuring the second coordinate. This selection cut is necessary because through two planes a unique track can only be determined if each plane has one measured track position. Even after elimination of generally noisy channels, 20 % of all events have more than one valid cluster in an x-plane, which explains the strong drop from the first to the second bin in the figure.

The third bin requires in addition at least one good cluster in at least three of the four planes measuring the precision coordinate. These three points are necessary to fit a track by least-squares minimization. Only very few events fail this selection test.

To be considered a “good track” (fourth bin in Figure 3.5), a track has to pass a cut on  $\chi^2$ . This cut is chosen such that the confidence level of the measured  $\chi^2$  (upper tail probability of the  $\chi^2$ -distribution for 2 degrees of freedom) is greater than 0.05. By applying this cut we discard mainly events whose real hit positions coincide with bad strips and remain undetected, while the track fit uses noise hits, resulting in a bad  $\chi^2$ . Another contribution to losses at this cut is made by acceptance inefficiencies, i.e. tracks passing through the scintillators but not through the slightly smaller detectors.

Finally the silicon telescope has a typical yield of 60 % good tracks relative to the total number of events.

## Chapter 4

# Optimization of the Operating Parameters of Drift Tubes

To meet the ambitious performance specifications for the ATLAS drift tubes, detailed studies of the operating parameters had to be performed. In Section 4.1 we shall give a brief description of the chosen operating point. The subsequent sections will treat the most important parameters in more detail.

### 4.1 Overview

The working point of MDTs chosen by the ATLAS collaboration is the result of a multidimensional optimization which was done during the last four years. These studies include test-beam measurements as well as detector simulations. Table 4.1 shows the qualitative influence of the operating parameters on the quantities characterizing the performance:

- **The Mechanical stability** is determined by the anode wire diameter and the wall thickness.
- **Low ageing:** ATLAS drift tubes have to survive ten years of operation. Since they are glued together in the chambers, it is impossible to replace single tubes. Replacing entire chambers is possible, but has to be avoided for financial reasons. Therefore the minimization of ageing effects has the highest priority in the optimization process. This concerns mainly the choice of the gas mixture, where detector-physical desires had to be subordinated to a long life time (Section 4.3). Ageing depends strongly on the total charge accumulated in a tube during its life time, which sets an upper limit on the product of pressure and gas gain (Section 4.2). The total charge is also a function of the tube volume per unit length which is exposed to the radiation. Therefore the tube radius should not be too big.
- **Good spatial resolution** is necessary to achieve the required momentum resolution. The dependence on pressure and gas gain will be discussed in Section 4.2. Section 4.4 will treat the optimization of read-out aspects like shaping time and trigger electron. The impact of the wire diameter will be thoroughly investigated in Section 4.5. A slight improvement of

	mechanical stability	low ageing	good resolution	small L-effect	noise hit suppression	low hit multiplicity	high efficiency	low dead time	linear $r(t)$	value chosen
<b>Wire diameter</b>	↗	—	↗	—	—	↗	—	—	—	<b>50 <math>\mu\text{m}</math></b>
<b>Tube diameter</b>	—	↗	↗	—	—	↗	—	—	—	<b>3 cm</b>
<b>Wall thickness</b>	↗	—	—	↗	—	—	↗	—	—	<b>400 <math>\mu\text{m}</math></b>
<b>Pressure</b>	—	↗	↗	↗	—	↗	—	—	—	<b>3 bar</b>
<b>Gas gain</b>	—	↗	↗	—	—	—	—	—	—	<b><math>2 \times 10^4</math></b>
<b>Trigger <math>e^-</math></b>	—	—	opt. @ 4	—	↗	↗	—	—	—	<b>16 - 25 e (5 <math>\times</math> noise)</b>
<b>Shaping time</b>	—	—	—	↗	—	↗	↗	—	—	<b>15 ns</b>
<b>Gas</b>	—	$\text{Ar}/\text{CO}_2$ (93/7)	—	$\text{Ar}/\text{CO}_2$ (93/7)	—	$\text{Ar}/\text{N}_2/\text{CH}_4$ (91/4/5)	—	$\text{Ar}/\text{N}_2/\text{CH}_4$ (91/4/5)	—	<b><math>\text{Ar}/\text{CO}_2</math> (93/7)</b>

↗ for better performance increase this value  
↘ for better performance reduce this value

Table 4.1: Qualitative dependence of drift tube performance on the operating parameters.

resolution with increasing tube diameter is due to the fact that near the anode wire the resolution is much worse than far from the wire (see Figure 4.13). Since for a bigger tube diameter the average distance of tracks from the wires will be longer than for a smaller diameter, the typical resolution will be better.

For a detailed description of all the effects contributing to tube resolution see [RIE 99a].

- **Small Lorentz Effect:** In the presence of a magnetic field parallel to the anode wire the drifting electrons are deflected from the radial direction by the Lorentz angle

$$\alpha_L = \arctan(\mu_e B) ,$$

where  $\mu_e$  is the electron mobility. Thus the drift time for a given radius increases, which means that the r-t relationship changes. In ATLAS MDT chambers the magnetic field component parallel to the wires will range between 0 and 1 Tesla. To limit the variations of the r-t relationship within a chamber, the Lorentz angle has to be kept small. This requires a low electron mobility which can be achieved by choosing a slower gas mixture (Section 4.3) and by increasing the pressure (Section 4.2). On the other hand, with regard to a minimized dead time the drift velocity should not be too small.

The tube diameter also has an impact on tube operation in a magnetic field. Ionization electrons originating from distant tracks are subject to a bigger drift time change than those from tracks passing near a wire. This provides an argument in favour of a smaller tube diameter because the average distance of tracks from the wire decreases.

- **Suppression of noise hits** requires a sufficiently high discriminator threshold. Furthermore a longer shaping time is advantageous because the integration removes short noise spikes. More details about read-out optimization are given in Section 4.4.
- **Low hit multiplicity:** The ionization along a particle track is not continuous but distributed in clusters (Section 2.4.1). Each electron cluster produces a spike in the signal pulse (see Figure 2.11). This can result in several threshold crossings for one muon pulse which would increase the amount of (unnecessary) data and slow down the read-out. The number of hits per pulse depends crucially on the pulse shape which is a function of many parameters:

By increasing the wire diameter we would broaden the individual electron pulse (see Equation (2.3)), thereby avoiding that the signal dives below the threshold between cluster spikes.

Another way of preventing the pulse going below threshold is to reduce the separation between the arrival times of individual clusters by either choosing a higher pressure (higher ionization density) or by choosing a gas with a bigger drift velocity.

Reducing the threshold would also help keeping the signal above threshold between clusters.

By geometry the clusters from distant tracks arrive all within a short time interval, which reduces the spikiness of the pulse. Consequently a bigger tube diameter with more tracks at big radii would help reducing the number of signal spikes.

Finally we could keep the number of spikes small by smoothing the pulse with a longer shaping time.

- **High efficiency:** The most obvious way of maximizing the efficiency is to increase the primary ionization and thus the pulse height by increasing the pressure. Another possibility would be to reduce the discriminator threshold, which is however constrained by the need of good noise rejection. As we shall show in Section 4.6, for the chosen threshold and pressure a significant inefficiency is only measured in and near the tube walls. Therefore the walls should be as thin as tolerable from the mechanical point of view. Furthermore the tube diameter should not be too small in order to limit the number of tubes per chamber volume and thus the fraction of space filled with wall material. There is also a slight dependence of efficiency on the pulse shape: A longer shaping time helps to sum up the charge of individual clusters which would not exceed the threshold on their own.
- **Low dead time:** The read-out electronics for ATLAS MDTs will have a fixed artificial dead time starting with the leading edge of the pulse and ending after the maximum drift time (Section 4.4). The maximum drift time decreases with increasing drift velocity which is specific to the gas mixture, and increases with the maximum drift distance, i.e. the tube radius.
- **Linear r-t relationship:** The linearity of the r-t relationship is a property of the drift gas and will be discussed in Section 4.3.

The following sections will focus on those operating parameters for whose optimization more detailed studies had to be performed.

## 4.2 Choice of Gas Pressure and Gain

Aiming for an excellent spatial resolution we would like to operate drift tubes at a high gas gain and a high pressure [RIE 99a, RIE 97a]:

A higher gas gain increases the pulse height allowing to trigger on an earlier primary electron while keeping the absolute discriminator threshold constant at the level required for noise rejection. Triggering on a low primary electron is advantageous in view of reducing time slewing effects which deteriorate the resolution (Section 4.4).

Strictly speaking the detector-physical properties depend on the gas density rather than on the pressure. If we still define our working point in terms of pressure for a temperature of 293 K, this is done with the purpose of a more intuitive number. For ATLAS practice it is envisaged to keep the density constant, not the pressure. We have shown that this compensates variations of the temperature [DEI 97].

A higher gas pressure has several advantages: It enhances the primary ionization which improves the efficiency, reduces the hit multiplicity and improves the resolution near the wire by reducing cluster position fluctuations. Another consequence of higher pressure is the shorter mean free path which reduces the Lorentz angle and – most important – improves the resolution by impeding the diffusion of the drifting electron cloud.

However, to keep ageing problems small, the total amount of charge per unit tube length accumulated during the 10 years of operation has to be limited to at most 0.6 C/cm. For the

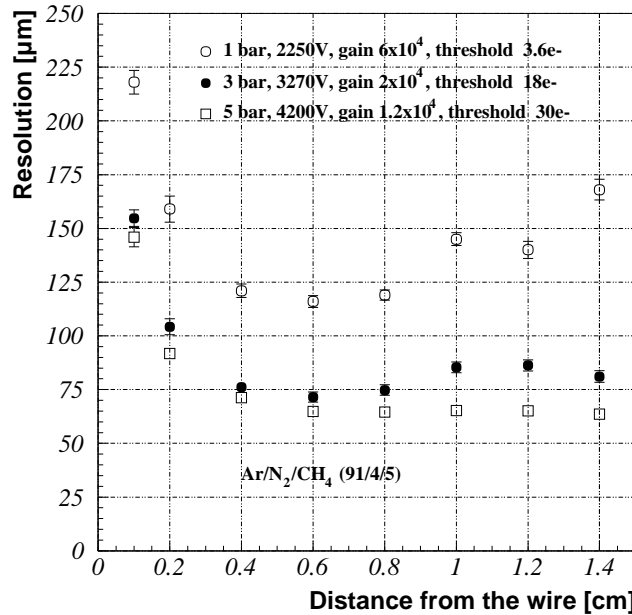


Figure 4.1: Simulated resolution for different gas pressures and the same amount of charge deposit [RIE 99a].

inner regions of the muon spectrometer with radiation background rates up to 100 Hz/cm (see Section 2.2.2) this charge limit translates into a maximum value of  $6 \times 10^4$  bar for the product of gain and pressure. Another reason for keeping the total charge low is the build-up of space charge which deteriorates the resolution (Section 5.2.1.2). Keeping this constraint in mind, we have to optimize gas gain and pressure for constant deposited charge. Figure 4.1 shows the simulated resolution for different gas pressures and gains, but with their product kept constant. One notices a major improvement from 1 to 3 bar but only a slight change for the step from 3 to 5 bar [RIE 99a].

Based on this result the gas gain of ATLAS drift tubes was set to  $2 \times 10^4$  and the pressure to 3 bar.

### 4.3 Choice of the Gas Mixture

The choice of a drift gas is subject to several – sometimes contradictory – detector-physical desires:

- First of all the set of possible gas mixtures is strongly restricted by the safety requirement of non-flammability.
- For the drift velocity a compromise has to be made: on one hand the maximum drift time should be smaller than  $1 \mu\text{s}$  to keep the occupancy lower than 25 %. On the other hand fast gases suffer from big Lorentz angles.
- Low diffusion is desired to enhance the resolution.

- Since streamer pulses have up to 100 times the charge of proportional pulses, their fraction must not exceed the 1 % level.
- Afterpulsing also contributes to a higher occupancy and has to be avoided [DEI 96a].
- To ensure stability of the r-t relationship against slight changes of pressure, temperature and voltage, the drift velocity should not show a strong dependence on the reduced electric field  $E/p$ . A constant drift velocity is equivalent to a linear r-t relationship.
- The decisive selection criterion which has priority over all the mentioned aims is low ageing. This problem strongly concerns gases with hydrocarbonic quenchers [KAD 91].

With these criteria in mind, several gas mixtures were studied in test beams [DEI 96c]. The favourite candidate was Ar/N<sub>2</sub>/CH<sub>4</sub> (91/4/5). It is appreciated due to the very linear r-t relationship (see Figure 4.2a), the high drift velocity (maximum drift time = 480 ns) and the good spatial resolution of typically 80 µm (see Section 4.6). This gas was used for all further test beam experiments until summer 1998. However, at the time when the decision for this gas was taken, the ageing studies had not been completed yet. Finally those lifetime investigations yielded the disappointing result that already after an accumulated charge of about 0.1 C/cm some tubes showed strong damage, i.e. a dramatic gain drop due to hydrocarbonic polymere deposits on the wires [SPE 98].

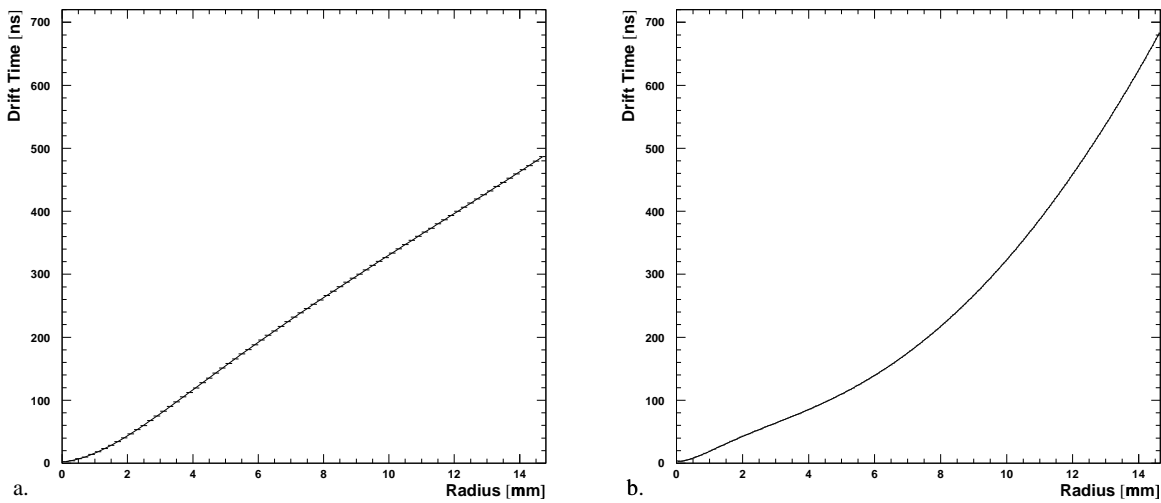


Figure 4.2: Measured r-t relationships (a) for Ar/N<sub>2</sub>/CH<sub>4</sub> (91/4/5) and (b) for Ar/CO<sub>2</sub> (93/7) at  $B = 0$  T and a gain of  $2 \times 10^4$ .

As replacement for the old baseline gas different mixtures without hydrocarbons were considered [KOL 97, PAS 00]. Finally Ar/CO<sub>2</sub> (93/7) – a gas which doesn't show any ageing even at 0.7 C/cm – was found to be a viable solution, despite its strongly non-linear r-t relationship

(Figure 4.2b) and the longer drift times (up to 680 ns) [ALE 98b]. The lower drift velocity leads to a higher occupancy, but reduces the Lorentz angle.

Due to the very low diffusion the resolution is better than that of Ar/N<sub>2</sub>/CH<sub>4</sub> (see Section 4.6). However, as we shall see in Section 5.2.1.2, the strong E-field dependence of the drift velocity makes the r-t relationship very susceptible to space-charge effects which finally deteriorates the resolution in a high-rate background. The resulting resolution in a background ends up at a level comparable to the old linear gas.

Table 4.2 summarizes the central properties of the old and the new MDT gas.

Property	Ar/N <sub>2</sub> /CH <sub>4</sub> (91/4/5)	Ar/CO <sub>2</sub> (93/7)
Maximum drift time at B = 0	480 ns	680 ns
Occupancy at the rate 300 kHz/tube	14 %	19 %
Lorentz angle averaged over r at B = 0.5 T	19.0°	9.3°
Linearity	good	poor
Operating voltage for the gain $2 \times 10^4$	3280 V	3080 V

Table 4.2: Properties of the old and the new ATLAS MDT gas.

## 4.4 Optimization of the Read-out Electronics

This section will give a brief overview about the design of the MDT read-out electronics. More details have been published in [RIE 99b, RIE 99c].

### 4.4.1 Discriminator Threshold

The discriminator threshold influences the resolution as well as the suppression of noise hits.

The former criterion would imply a rather low threshold level. There is an optimum at a level equivalent to the charge induced by the avalanche of about 4 primary electrons. Triggering on an earlier electron would make us more susceptible to cluster-size and cluster-distance fluctuations resulting in a resolution deterioration. For a later trigger electron the resolution would suffer more from diffusion and from time slewing due to gain variations.

The latter criterion pushes us towards a higher threshold. As a compromise the ATLAS collaboration opted for a threshold level of five times the rms of the intrinsic electronics noise which is mainly determined by the termination resistor at the high-voltage end of the tube (Figure 2.8 and Equation (4.3)). Given that this intrinsic noise is equivalent to about 3.3 primary electrons, the chosen threshold corresponds ideally to about 16.5 primary electrons. However, in real life there are additional noise contributions from all stages of the read-out electronics. Therefore the trigger threshold corresponding to five times the actual noise is usually at 20 to 25 primary electrons. In the final ATLAS electronics one will try to push the noise down to the intrinsic limit.

### 4.4.2 Pulse Shaping

The shaping of a signal pulse in a drift tube has two major aspects: the peaking time which determines the steepness of the pulse's leading edge, and the treatment of the long tail of the ion signal which decays only according to a  $(t + t_0)^{-1}$  law (see Equation (2.2)).

#### 4.4.2.1 Peaking Time

The peaking time affects the resolution through the time slewing effect: ionization charge fluctuations entail variations of the leading edge slope of the pulse resulting in a jitter on the threshold crossing time and thus in a resolution degradation. This jitter is further enhanced by longer shaping times (Figure 4.3).

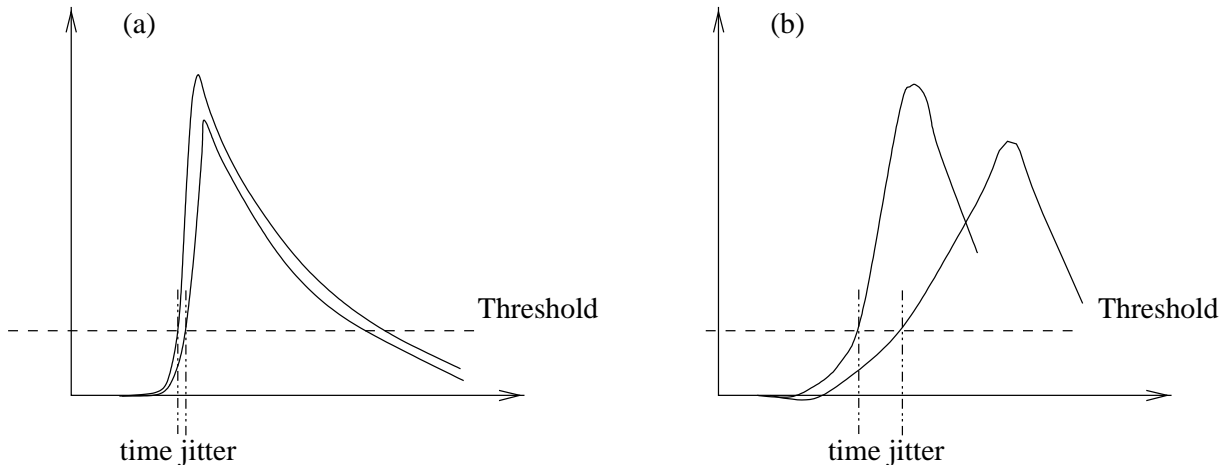


*Figure 4.3: Resolution degradation by the time slewing effect: (a) for short peaking times, (b) for long peaking times. The consequence of varying pulse slopes is a jitter on the threshold crossing time.*

Apparently this mechanism provides an argument in favour of a fast shaping. However, short shaping times also increase the sensitivity to pick-up noise. Furthermore, longer shaping times can help reducing the hit multiplicity of a pulse by integrating over the spikes of the individual ionization clusters.

The resolution deterioration by time slewing can partly be compensated by measuring the charge contained in the leading edge of every pulse. Then one can work out a correction for the threshold crossing time using the correlation between the charge and the time: large pulses shift the crossing towards earlier times, while small pulses shift it to later times. Details of this technique are given in [ALE 98a]. The MDT electronics in ATLAS will provide the necessary charge information using ADCs with short gates (length up to  $2 \times$  peaking time).

#### 4.4.2.2 Tail Cancellation and Baseline Restoration

Every signal pulse has a long tail due to the slow ion drift to the cathode. Leaving this tail untreated would cause signal pile-up and thus increase the dead time. In addition – as we shall further discuss in Section 5.2.1.1 – high background rates produce shifts and fluctuations of the signal baseline which aggravate resolution degradation by time slewing. To avoid this, there are two techniques of baseline restoration (Figure 4.4), which have both their advantages [RIE 99c]:

- **Unipolar pulse shaping with an active baseline restoration circuit:** This shaping scheme was favoured at the time when Ar/N<sub>2</sub>/CH<sub>4</sub> was the baseline gas. The reasons were the following:

- The trailing edge of the signal is resolved with a precision of about 25 ns. This time doesn't depend on the track distance from the anode wire because it is given by the last arriving ionization electrons which are always created at the tube wall and thus have a fixed drift distance. Therefore at ATLAS the trailing edge will be the same for all tracks belonging to a given pp-bunch crossing. This time information can be used by pattern recognition to correlate the event to the correct bunch crossing and to eliminate out-of-time background events.
- A second threshold at 100 - 150 electrons can be used to separate pile-up pulses (double-track separation; see Section 5.2.2.3). This threshold has to be carefully chosen in order to avoid counting late spikes of the first pulse.
- A hit multiplicity close to 1 can be achieved by an appropriate adjustment of the circuit's filter time constants and by introducing a threshold hysteresis<sup>1</sup>.

- **Bipolar pulse shaping:** At the time of the old gas Ar/N<sub>2</sub>/CH<sub>4</sub> the bipolar shaping scheme was considered to be less advantageous:

- The trailing-edge information is lost.
- The separation of pile-up pulses with a second threshold has a lower efficiency than for unipolar shaping because the second pulse can sit in the undershoot of the first pulse and remain undetected.
- Since each spike of the signal is bipolar, the hit multiplicity is greater than 1.

The main advantage of this shaping scheme is its simplicity: it doesn't need the complicated active baseline restoration circuit nor adjustable filter constants nor threshold hysteresis. The only way to achieve a hit multiplicity of 1 is the introduction of an artificial dead time which has to be as long as the maximum pulse length, i.e. the maximum drift time.

---

<sup>1</sup>Hysteresis: A new hit is only counted if the signal falls below the 12th electron after the preceding hit.

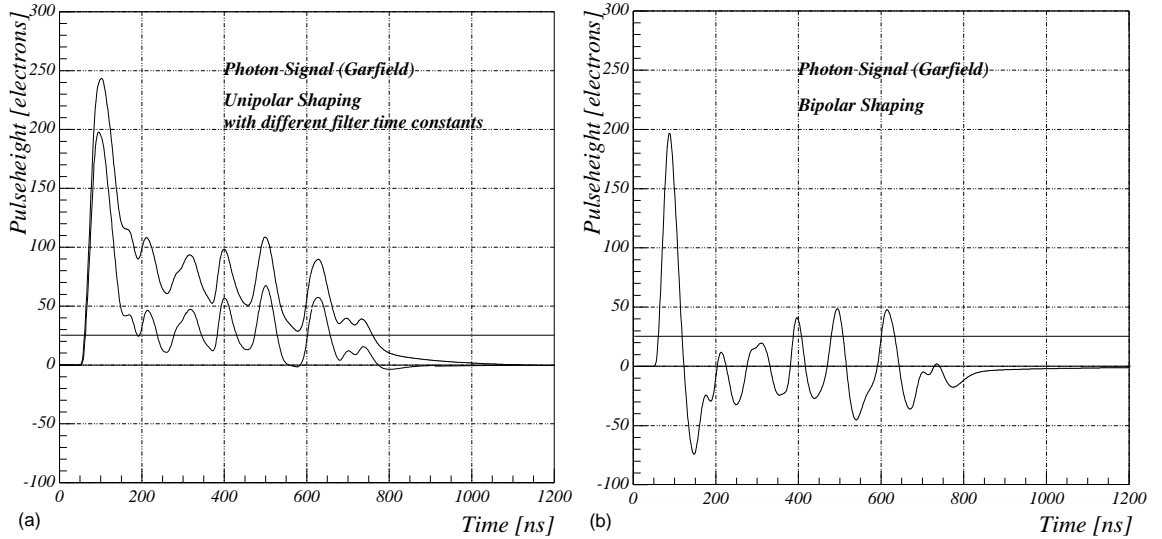


Figure 4.4: Photon signal in Ar/CO<sub>2</sub>: (a) for unipolar shaping with different filter time constants; (b) for bipolar shaping [RIE 99c]. An example threshold at 25 e is also shown.

When the ageing problems with Ar/N<sub>2</sub>/CH<sub>4</sub> forced the collaboration to choose Ar/CO<sub>2</sub> as MDT gas, the situation of pulse shaping was found to have changed:

- Due to the very low drift velocity near the wall, the trailing-edge resolution for unipolar shaping is only 80 ns which is not very useful.
- The longer drift time makes the adjustment of the filter time constants for a low hit multiplicity more difficult.
- Double-track separation turned out not to be very helpful for pattern recognition due to the low separation efficiency (60 %) and the bad resolution at the high threshold (170 μm at 100 e). It can even deteriorate pattern recognition if a late spike of the first pulse is interpreted as a pile-up pulse.

For these reasons it was decided to use bipolar shaping with a constant artificial dead time of 700 ns.

## 4.5 Choice of the Anode Wire Diameter

This section will describe the measurement of spatial resolution and the fraction of streamer signals for drift tubes with different anode wire diameters (see also [DEI 00a]).

The choice of the anode wire diameter is not only driven by performance considerations, but also by the need for good mechanical strength. Therefore the decision was in favour of the thickest wire diameter which still complies with the physics requirements.

### 4.5.1 Experimental Set-up

The measurement set-up is shown in Figure 4.5.

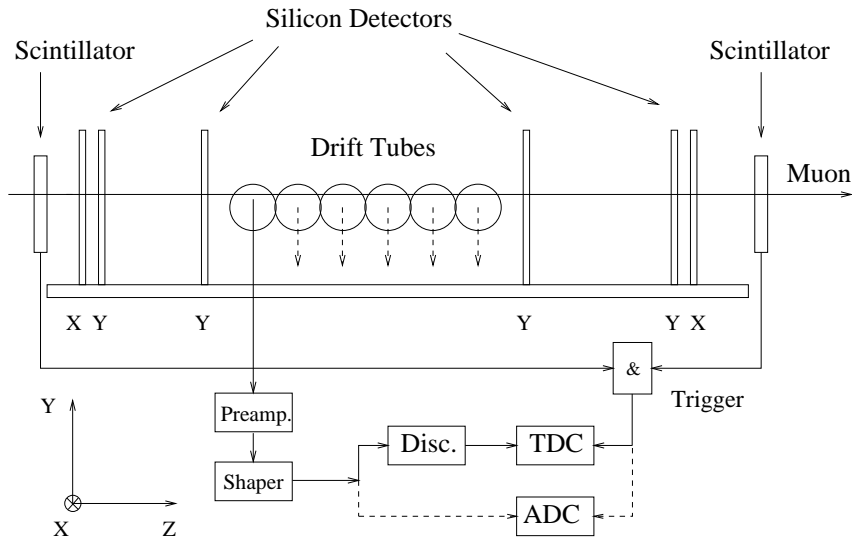


Figure 4.5: Experimental set-up in the M2 muon test beam at CERN.

Five drift tubes with different wire diameters were operated in the halo of the SPS beamline M2 at CERN. The muon energy was about 170 GeV. Table 4.3 shows a summary of the fundamental properties and operating conditions of these drift tubes. Parameters specific to the wire diameter are given in Table 4.4.

Since the measurements were made before the final decision on the drift gas for ATLAS MDTs, the old baseline gas Ar/N<sub>2</sub>/CH<sub>4</sub> (91/4/5) was used. Also the anode wire material was different from the one now chosen (gold-plated W/Re 97/3). We assume however that our conclusions about the dependence of drift-tube performance on the wire diameter will not be affected by these changes.

For the resolution measurements an amplifier/shaper combination [BNL 73] with 15 ns peaking time and a unipolar shaping scheme was used. With the same set-up the tube efficiency was measured. It doesn't depend on the wire diameter and will be presented in Section 4.6.

The streamer rate was measured with a slightly different set-up which had also served for the calibration of the relationship between voltage and gas gain [DEI 96a]. Here a preamplifier with

Tube length	1 m
Anode wire material	Cu/Be (50, 70, 100, 150 $\mu\text{m}$ ) INOX (30 $\mu\text{m}$ )
Gas	Ar/N <sub>2</sub> /CH <sub>4</sub> (91/4/5)
Pressure	3 bar absolute
Gas gain	(1, 2, 6) $\times 10^4$
Maximum drift time	480 ns
Peaking time of the shaper	15 ns
Discriminator threshold	5 $\times$ rms noise

Table 4.3: General parameters of the drift tubes in the test set-up

Wire diameter [ $\mu\text{m}$ ]	Tube impedance [ $\Omega$ ]	Voltage [V] for $G = 2 \times 10^4$	Threshold [p.e.]
30	413	2750	10.5
50	382	3280	16.3
70	362	3760	20.6
100	340	4335	27.2
150	316	4960	42.2

Table 4.4: Tube and operating parameters depending on the wire diameter. The voltages for a gain of  $2 \times 10^4$  are taken from [DEI 96a]. The discriminator threshold always corresponds to five times the noise level which is a function of the wire diameter (see Equation (4.5)).

4 ns shaping time [REW 86] and a charge sensitive ADC were used. The set of tubes contained a 160  $\mu\text{m}$  wire instead of the 150  $\mu\text{m}$  wire; no 100  $\mu\text{m}$  wire was available.

As external reference system the silicon microstrip tracker (Chapter 3) was employed.

#### 4.5.2 Tube Resolution

Figure 4.6 shows the space-time distribution for the tube with the 50  $\mu\text{m}$  wire. The space coordinate  $r$  is the minimum distance of the muon track from the anode wire as given by the silicon tracker. The drift time  $t$  is measured by the TDC. The entries below the “V”-shaped band correspond to electromagnetic secondaries (mainly delta-rays) produced by the muon: if a delta-ray is emitted towards the anode wire of the tube, its own ionization signal can hide the muon pulse, and the measured drift time is too short.

The r-t relationship which is used for reconstructing track radii, is defined as the centre of the band in Figure 4.6. The resolution corresponds to the width of this band. It is determined together with the r-t relationship in the following iterative way: We start with a first-guess r-t relationship  $\rho_0(t)$  and plot the residuals  $\Delta r = \rho_0(t_{\text{drift}}) - r_{\text{silicon}}$  as a function of the drift time  $t_{\text{drift}}$ , where  $r_{\text{silicon}}$  is the track radius given by the silicon tracker. Then we project time slices of this two-dimensional distribution onto the  $\Delta r$  axis and fit them with Gaussians. The means of these Gaussian fits are used as corrections to  $\rho_0(t)$  which yields a better estimate  $\rho_1(t)$ . After about five iterations the centre of the residual distribution converges at zero (Figure 4.7). Its

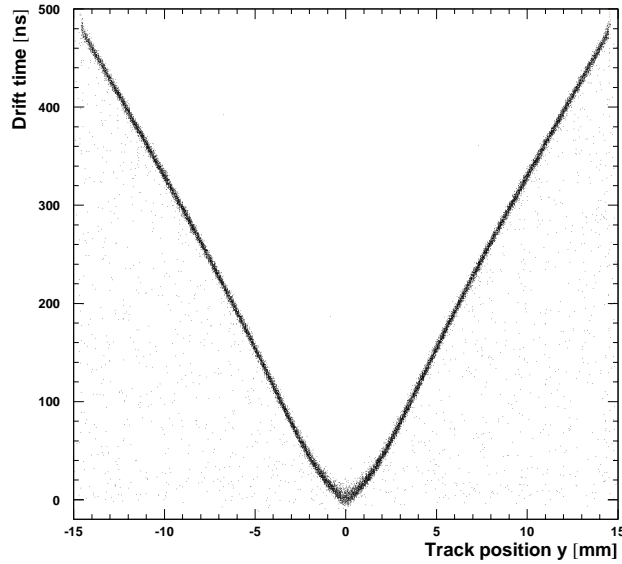


Figure 4.6: Drift time measured with the TDC versus track distance from the anode wire given by the silicon tracker.

Gaussian width is defined as the resolution. Far from the wire this Gaussian approximation is quite good whereas for  $r < 2$  mm the cross-sections of the r-t-distribution have considerable non-gaussian tails due to the cluster statistics of the ionization process (Section 6.2). Deviations from the Gaussian shape are the main contribution to the error of the resolution measurement because the width of the Gaussian fit depends on the range around the maximum in which the fit is done. It was found empirically that acceptable fits are obtained for a range of two standard deviations around the peak.

Figure 4.9 shows the resolution as a function of the track radius for each wire diameter studied. In addition to the measurements a simulation with the program GARFIELD [VEE 99] is displayed. At every millimeter of radial distance from the wire 2000 muon tracks were simulated. The ionization of the muons was generated according to the exponential cluster-distance distribution and the cluster-size distribution calculated with the program HEED [SMI 97] which is interfaced to GARFIELD. Then the drift of the ionization electrons was simulated using the transport properties of the gas calculated with MAGBOLTZ [BIA] which is also interfaced to GARFIELD. The charge amplification process near the anode wire was modelled with a Polya distribution. Then the signal induced on the wire by the drift of the positive ions from the wire to the wall was calculated. Finally the signal was convoluted with the delta-response of the read-out electronics, and the threshold-crossing time was determined.

For the ion drift the field-dependent mobility of  $\text{Ar}^+$  in Ar was used. This is a simplification because in reality charge transfer processes take place, and not only  $\text{Ar}^+$  ions but also other ions like  $[\text{CH}_4]^+$  are drifting. Their mobility might be different. Also not taken into account are the sharp electron pulse before the ion pulse and the fact that the ions are not produced exactly on the wire surface but in the whole avalanche region. The details of the amplification process

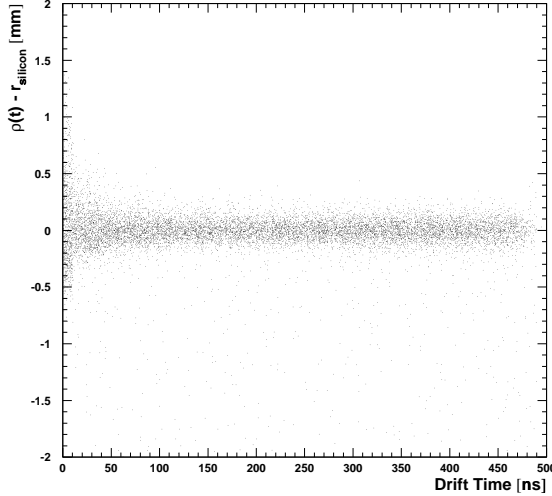


Figure 4.7: Residuals  $\rho(t_{\text{drift}}) - r_{\text{silicon}}$  versus drift time at the end of the iterative determination of the  $r$ - $t$  relationship  $\rho(t)$ .

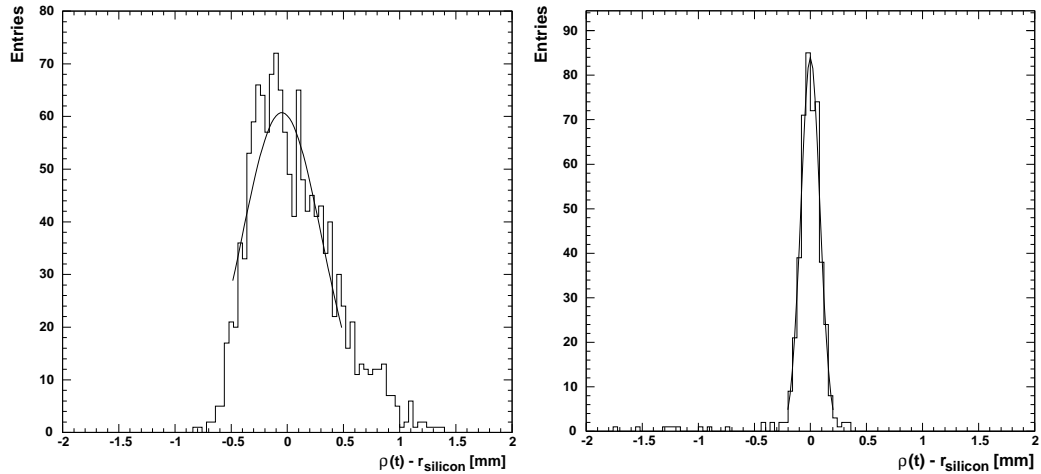


Figure 4.8: Projections of time slices of Figure 4.7. Left:  $0 < t < 10$  ns; right:  $100 < t < 110$  ns. Superimposed are Gaussian fits to a range of two standard deviations around the peak.

are very difficult to simulate. Nevertheless the simulation is in fairly good agreement with the measurements.

To facilitate the resolution comparison of the wires with different diameters, we calculate the quadratic mean resolution

$$\langle \sigma \rangle \equiv \sqrt{\frac{1}{R} \int_{1\text{mm}}^R [\sigma(r)]^2 dr} . \quad (4.1)$$

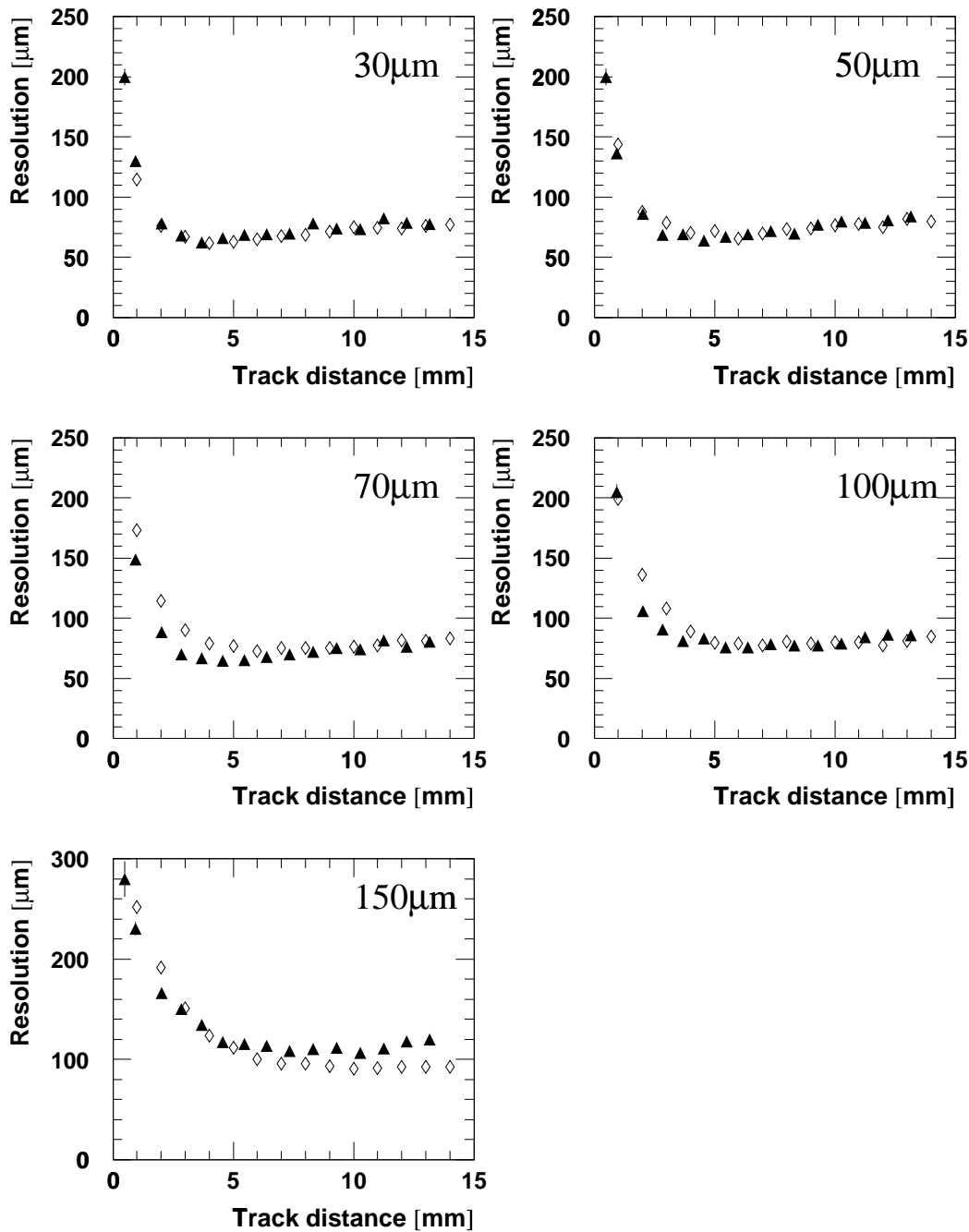


Figure 4.9: Spatial resolution as a function of the distance of the muon track from the wire for different wire diameters. The gas gain was  $2 \times 10^4$ . The triangles represent the measurements, the diamonds show a simulation using GARFIELD [VEE 99]. The errors are typically between 5 μm (far from the wire) and 10 μm (near the wire, where the resolution is non-Gaussian).

Following the convention in [TDR 97b], the first millimeter is excluded from the average because near the wire the resolution is so bad that hits in this range will often not be taken into account by track fits through an MDT chamber. Furthermore, the quadratic average would be dominated by the large  $\sigma(r)$  in this small interval and would not be a representative number. The results are presented in Figure 4.10. In addition to our measurements (solid markers) the Garfield simulation is shown.

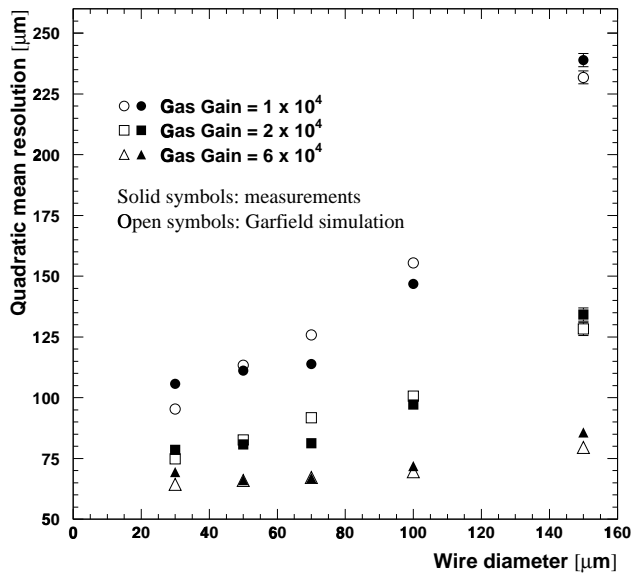


Figure 4.10: Dependence of the quadratic mean resolution as defined in (4.1) on the wire diameter for different gas gains.

The resolution deterioration with increasing wire diameter is a consequence of the higher threshold in terms of primary electrons (see Table 4.4): In [RIE 99a] we have shown that the resolution is approximately proportional to the trigger electron  $n_{thr}$  which is given by

$$n_{thr} = \frac{V_{thr}}{V_{1e}} \quad , \quad (4.2)$$

where  $V_{thr}$  is the threshold voltage and  $V_{1e}$  the height of a single primary electron pulse at the output of the shaper. To avoid noise hits,  $V_{thr}$  is required to be five times the rms noise voltage, which is dominated by the Thermal Equivalent Noise Charge (ENC) of the termination resistor  $R_t = Z_{\text{tube}}$  at the high-voltage end of the tube:

$$ENC = \sqrt{\frac{kT}{R_t} \tau} \quad , \quad (4.3)$$

where  $k$  is the Boltzmann constant,  $T$  the temperature and  $\tau = 15$  ns the preamplifier peaking time [RIE 99a]. The tube impedance  $Z_{\text{tube}}$  and thus  $R_t$  depends on the wire diameter:

$$R_t = Z_{\text{tube}} = \sqrt{\frac{L}{C}} = \frac{1}{2\pi} \sqrt{\frac{\mu}{\epsilon}} \ln \frac{b}{a} \quad , \quad (4.4)$$

where  $L$  and  $C$  are the inductance and capacitance per unit tube length,  $\mu$  the magnetic permeability and  $\varepsilon$  the permittivity of the gas. From (4.3) and (4.4) follows

$$ENC \sim \frac{1}{\sqrt{\ln \frac{b}{a}}} \quad , \quad (4.5)$$

i.e. the noise decreases slowly with decreasing wire diameter  $a$ .

The height  $V_{1e}$  of the pulse created by a single ionization electron is proportional to

$$I_{1e} = \frac{G e \mu V}{a^2 (\ln \frac{b}{a})^2} \quad (4.6)$$

with the gas gain  $G$ , the anode voltage  $V$  and the ion mobility  $\mu$  which is approximated to be independent of the electric field [BLU 93]. Thus the signal height increases with decreasing wire diameter  $a$ .

From (4.2), (4.5) and (4.6) follows

$$n_{thr} \sim \frac{a^2}{G} \cdot \frac{(\ln \frac{b}{a})^{\frac{3}{2}}}{V(G, a)} \quad . \quad (4.7)$$

The dependence of the operation voltage  $V(G, a)$  on both the gain and the wire radius is less than linear. Therefore one expects the trigger electron and thus the resolution to have approximately a quadratic dependence on the wire radius  $a$  and an inverse proportionality to the gain  $G$ , which is in qualitative agreement with the measurements and the simulation. However, the saturation of the resolution for decreasing wire diameter is more accentuated in the measurements than in the simulation.

The important conclusion for the development of ATLAS drift tubes is that from the point of view of resolution optimization there is no significant advantage in choosing a wire diameter thinner than  $50 \mu\text{m}$ .

#### 4.5.3 Streamer-Pulse Probability

To minimize ageing, ATLAS drift tubes have to be operated in proportional mode. Since streamer pulses deposit up to 100 times the charge of a proportional pulse, a streamer fraction of 1 % could double the total deposited charge. The ATLAS collaboration defined 1 % as the upper limit [ATL 94].

To distinguish streamer pulses from events in the Landau tail of signals in proportional mode, a feature of our read-out electronics was used (Figure 4.11): Generally the charge of a streamer pulse is far beyond the range of our ADC, and their entries in the ADC spectrum lie in the overflow together with events belonging to the Landau tail. However, the gate of the ADC was only 600 ns long. Thus signals with long drift times are not integrated over the whole gate length, and even streamers remain in the range of the ADC. In Figure 4.11 this mechanism produces, for drift times greater than about 270 ns, a clear gap between proportional and streamer signals, the latter visible as a narrow band due to amplifier saturation. Therefore the streamer-pulse probability was determined by counting the entries above and below the cut line for drift times  $> 270$  ns. This limit biases us to tracks far from the wire for which the charge density in the

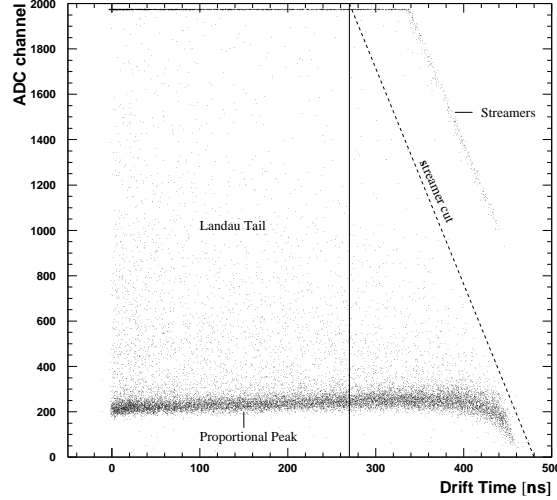


Figure 4.11: ADC channel (proportional to the charge) versus drift time for the  $70\text{ }\mu\text{m}$  wire at  $4.2\text{ kV}$ .

amplification region is higher than for tracks near the wire. Measurements with gamma-sources of different energy ( $^{55}\text{Fe}$ :  $5.9\text{ keV}$ ,  $^{241}\text{Am}/\text{Mo}$ :  $17\text{ keV}$ ) showed that the streamer probability increases with this charge density [DEI 96a]. Therefore the streamer fractions measured for distant tracks can be considered as an upper limit for all tracks.

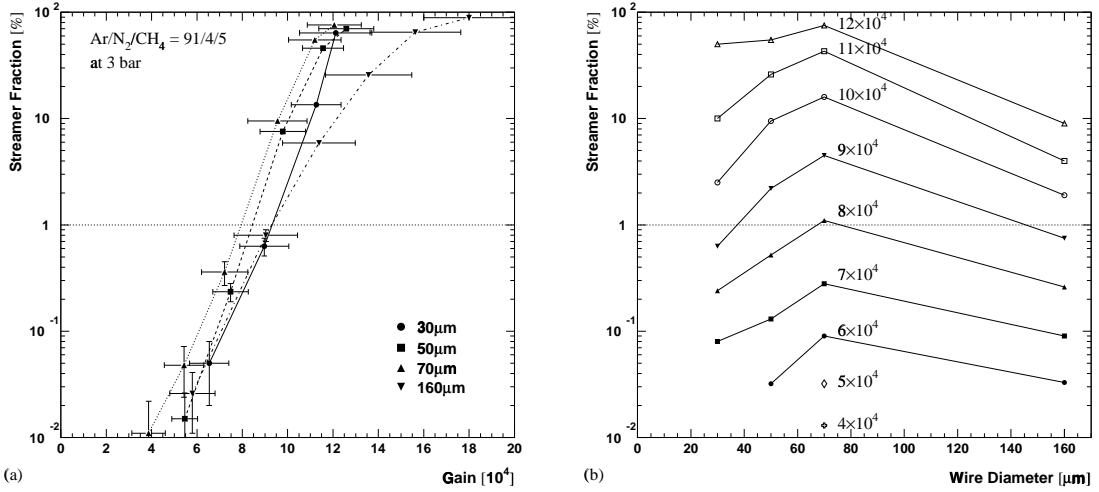


Figure 4.12: (a) Fraction of streamer pulses as a function of the gas gain for different wire diameters.  
(b) Fraction of streamer pulses as a function of the wire diameter for different gas gains. The values have been interpolated from the measurements shown in (a). The connecting lines are drawn to guide the eye.

Figure 4.12a shows the fraction of streamer pulses as a function of the gas gain for different wire diameters. Figure 4.12b shows the variation of streamer rate with wire diameter. For the three thinner wires there is a tendency to an increase of streamer fraction with increasing wire diameter, which was also reported by other groups about other gases (e.g. [BOY 95]); for the  $160\text{ }\mu\text{m}$  wire however this tendency seems not to hold anymore. We have no explanation why the streamer probability has a maximum at a wire diameter somewhere between  $70\text{ }\mu\text{m}$  and  $160\text{ }\mu\text{m}$ .

The important conclusion for our purpose is that streamer tendency does not provide a strong selection argument for the wire diameter. At gas gains below  $4 \times 10^4$  – the relevant domain for ATLAS drift tubes – no streamers were observed at all. Given our statistics, at  $2 \times 10^4$  the upper limit for the streamer rate is  $10^{-4}$  with a confidence level of 90 % for all wire diameters.

Based on the results presented above the ATLAS Muon Collaboration has decided to use wires with  $50\text{ }\mu\text{m}$  diameter in the MDT chambers.

## 4.6 Single Tube Performance at the Chosen Operating Point

In the preceding sections we have explained how an appropriate operation point for ATLAS MDTs was determined. In the following the tube performance for the chosen parameter settings (Table 4.1) will be summarized. In addition to the resolution for the old and the new MDT gas, we shall show the measured efficiency.

### 4.6.1 Spatial Resolution

Figure 4.13 shows the resolution as a function of the distance from the wire; part (a) represents the old gas  $\text{Ar}/\text{N}_2/\text{CH}_4$  (91/4/5), part (b) the new gas  $\text{Ar}/\text{CO}_2$  (93/7) [ALE 99a].

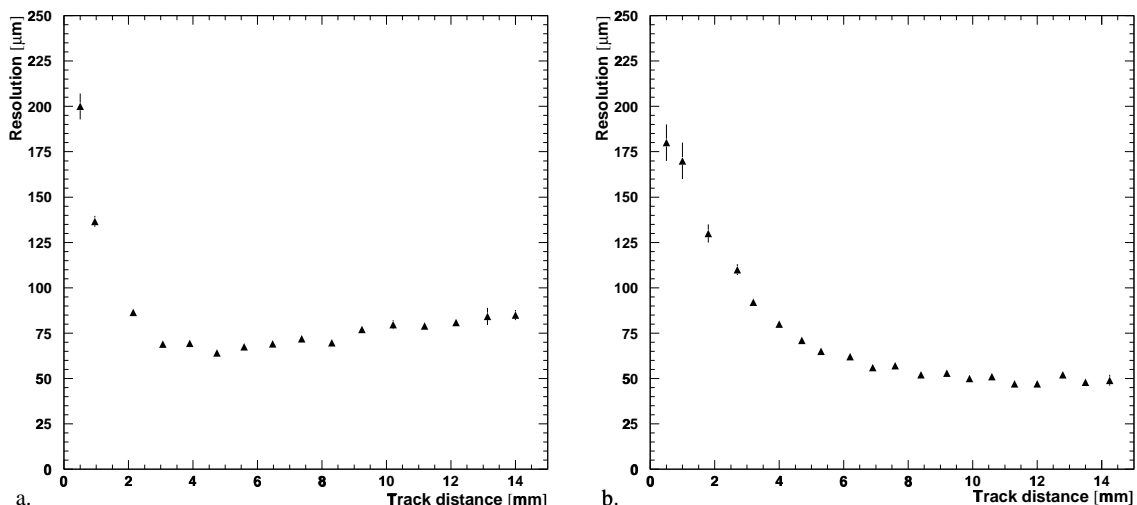


Figure 4.13: Resolution as a function of the distance  $r$  from the wire: (a) for  $\text{Ar}/\text{N}_2/\text{CH}_4$  (91/4/5), (b) for  $\text{Ar}/\text{CO}_2$  (93/7).

The main reason for the qualitatively different radial dependence of the resolution for the two gases is the higher diffusion in Ar/N<sub>2</sub>/CH<sub>4</sub> which causes the deterioration for  $r > 4\text{ mm}$  [RIE 99a]. In the quadratic mean defined in Eq. (4.1) the resolution of Ar/CO<sub>2</sub> is  $69\text{ }\mu\text{m}$  compared to  $80\text{ }\mu\text{m}$  for Ar/N<sub>2</sub>/CH<sub>4</sub>. However, note that these numbers refer to operation without radiation background. The influence of a high-rate environment as it is expected for ATLAS, will be investigated in Chapter 5.

#### 4.6.2 Efficiency

Drift tube efficiency has two aspects: The first one is the simple probability for detecting a crossing particle at all; we call it the hit efficiency which is described in Section 4.6.2.1. For pattern recognition in a high-rate background it is important to have a very high hit efficiency.

To get a relevant efficiency for track reconstruction it is appropriate to apply a quality cut on the detected hits, because a reconstructed hit radius which is far from the true impact radius doesn't provide any information for the track fit. Therefore we introduce the so-called  $3\sigma$ -efficiency which is discussed in Section 4.6.2.2.

The efficiency measurements were made with the same set-up as the study of resolution as a function of wire diameter, described in Section 4.5 (see in particular Figure 4.5).

##### 4.6.2.1 Hit Efficiency

The hit efficiency  $\eta_{hit}$  is defined as the fraction of events with a hit registered in the total drift-time window, when the silicon tracker indicates that a track has passed through the tube.

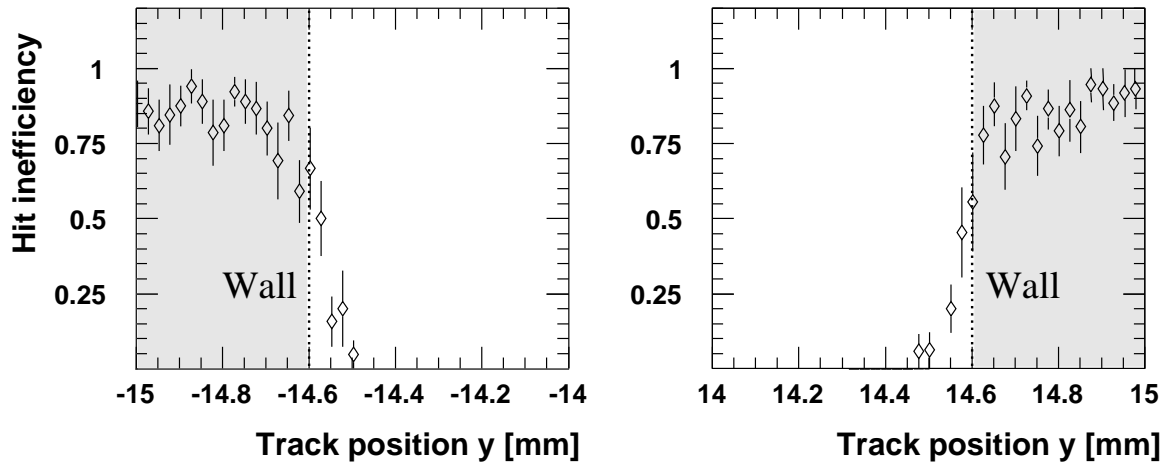


Figure 4.14: Hit inefficiency at the tube walls for a gas gain of  $2 \times 10^4$  and a pressure of 3 bar.

The measurement showed for all tubes that the inefficiency is only significant for tracks within  $200\text{ }\mu\text{m}$  of the wall (Figure 4.14). This is due to the fact that near the wall the track length within the gas volume becomes short and in some cases the primary ionization is too small for obtaining a pulse greater than the discriminator threshold. The figure also demonstrates that even some tracks passing only through the aluminium wall without entering the gas volume are

detected, leading to an inefficiency  $< 1$  for  $r > 14.6$  mm. This effect is caused by delta-rays knocked out of the aluminium and flying into the gas volume where they create an ionization signal.

In order to separate the geometry-related inefficiency at the tube walls from the inefficiency of the gas volume, we apply a cut at  $r = 14.4$  mm and consider only the efficiency inside this radius. The resulting hit inefficiency is only

$$1 - \eta_{hit} = (4.30 \pm 4.28) \times 10^{-5} \quad (4.8)$$

i.e. one missed hit in 23000 events. The almost perfect efficiency can be understood taking into consideration the high primary ionization of about 700 electrons in our argon-based gas mixture at a pressure of 3 bar absolute and the low discriminator threshold of less than 50 electrons for all wires.

#### 4.6.2.2 $3\sigma$ -Efficiency

For track reconstruction only hits within typically three times the spatial resolution will be used. The amount of successfully reconstructed hits can be quantified by the  $3\sigma$ -efficiency defined as

$$\eta_{3\sigma} = \frac{\text{number of hits reconstructed with } \rho(t) - r_{silicon} < 3\sigma(r_{silicon})}{\text{number of tracks through the tube at a radius } r_{silicon}}. \quad (4.9)$$

Again the silicon tracker is used as external reference. Since  $\sigma(r_{silicon})$  is the Gaussian approximation to the spatial resolution of the tube at the distance  $r_{silicon}$  from the wire,  $\eta_{3\sigma}$  quantifies the importance of non-Gaussian tails in the drift-time distribution for a given radius. Figure 4.15 shows  $\eta_{3\sigma}$  as a function of  $r$ .

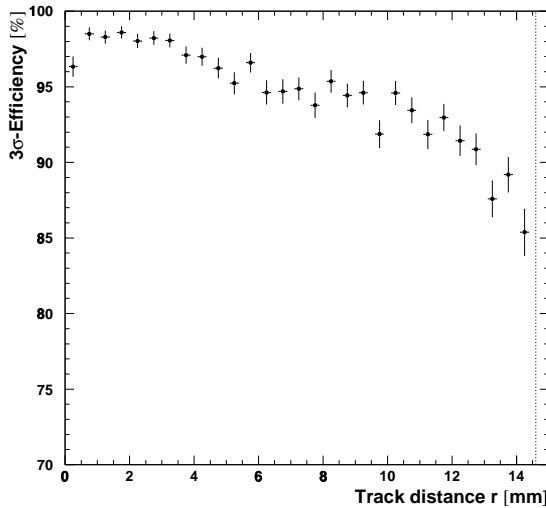


Figure 4.15:  $3\sigma$ -Efficiency for a gas gain of  $2 \times 10^4$  and a pressure of 3 bar.

The decrease of  $\eta_{3\sigma}$  from the tube centre towards the wall can be explained by the increasing probability for the muon being hidden by a delta-ray (see Figure 4.2) creating a hit outside  $3\sigma$ . Note that this result applies to the case where only the first hit in the tube within the total drift-time window is considered. For multihit electronics one can try to recover the muon hits after preceding delta-ray hits.

The little hollow near the wire is a consequence of the non-Gaussian errors due to clustering effects which are important in that domain (see Figure 4.8b and Section 6.2).

## Chapter 5

# Drift-Tube Operation in a High-Rate Radiation Background

In the previous chapter we have shown that with pressurized drift tubes adequate spatial resolution and efficiency can be achieved in test-beam conditions. However, up to this point our studies neglected an important factor characterizing the chamber environment in ATLAS: the high-rate radiation background with rates up to  $100 \text{ Hz/cm}^2$  or  $300 \text{ Hz}$  per centimeter tube length (see Figure 2.6b). From this background various detector-physical complications are to be expected, such as chamber ageing (which is not subject of this work), high occupancies and resolution deterioration via space charge effects and problems related to the read-out electronics. To improve the understanding of those effects and to test and optimize drift tubes in a realistic environment, an area around a muon beam line was equipped with a strong gamma source simulating ATLAS conditions.

### 5.1 Set-up of the Gamma Irradiation Facility in a Muon Test Beam

To study the effects of a high-rate radiation background on chamber performance, the collaborations ATLAS and CMS created the common Gamma Irradiation Facility (GIF) in the SPS beam line X5 at CERN (Figure 5.1).

In addition to the  $100 \text{ GeV}$  muon beam, the GIF has a  $^{137}\text{Cs}$  source with an activity of  $740 \text{ GBq}$  emitting  $662 \text{ keV}$  Gammas, which deposit on average an energy of about  $36 \text{ keV}$  in our tubes [BOY 97], simulating well the photon background in ATLAS. The actual gamma rate can be adjusted by choosing an appropriate combination of several lead filters. In addition there is a convex lead filter (“collimator”) permanently fixed in front of the source. It has the task to flatten the planes of equal gamma flux perpendicular to the beam axis.

Figure 5.2a shows the full gamma spectrum of the source with only the collimator filter in place [VIT 98]. The dominant contribution is the primordial  $662 \text{ keV}$  Cs line at the upper edge of the spectrum. At lower energies one sees a continuum due to Compton scattering in the collimator and in the lead walls of the source box. This continuum extends down to the Compton edge at a gamma energy of  $184.3 \text{ keV}$  where the photons are back-scattered. At  $72.1 \text{ keV}$  we see a characteristic Pb peak.

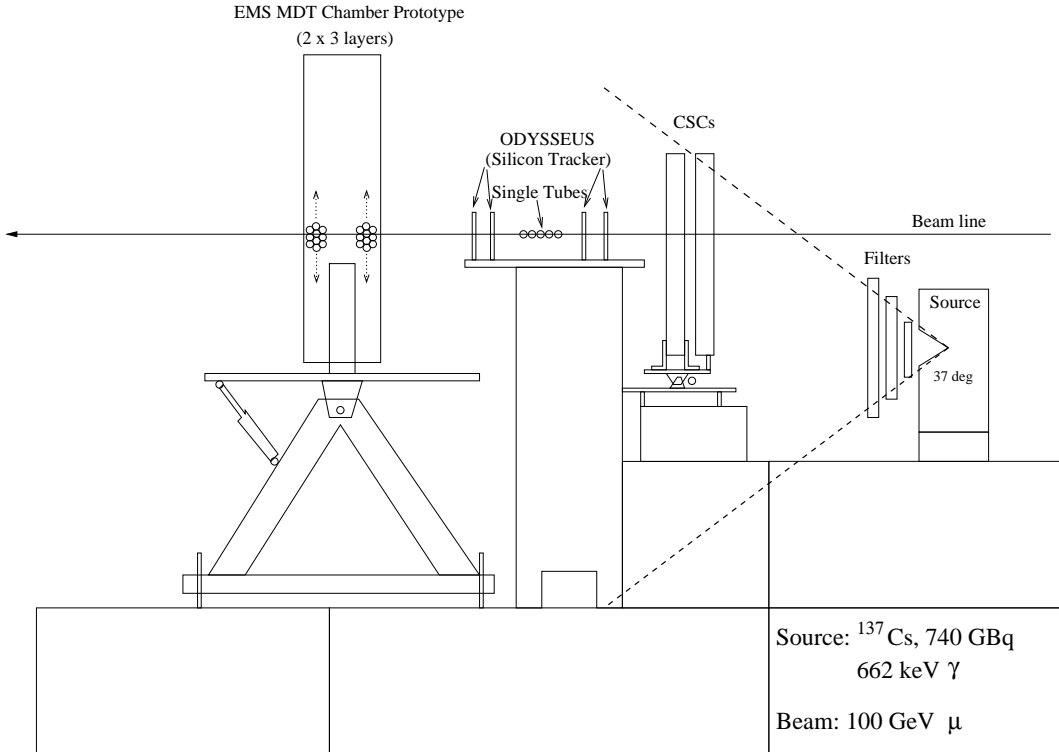


*Figure 5.1: The set-up in the X5-GIF zone. Our studies were based on an End-Cap (station EMS) MDT chamber prototype with two triple layers of horizontal tubes and on single tubes between the planes of a silicon tracker. The CSC chamber shown in the picture is not subject of this work.*

Putting more filters in front of the source not only attenuates the emission but also smears the spectrum to lower energies by Compton scattering (Figure 5.2b).

Two series of experiments have been carried out in the GIF; the first one with the old MDT gas Ar/N<sub>2</sub>/CH<sub>4</sub> (91/4/5), the second one with different Ar/CO<sub>2</sub> mixtures and a slightly modified set-up. In the following two sections the experimental layouts of both measurement series will be described. The results will be treated afterwards in common.

### 5.1.1 The Experiments with Ar/N<sub>2</sub>/CH<sub>4</sub> (91/4/5)

The tubes that we used for our investigations with the old MDT gas Ar/N<sub>2</sub>/CH<sub>4</sub> (91/4/5) were part of an EMS End-Cap chamber prototype built by the universities of Seattle and Boston. The chamber consists of two triple layers of horizontal drift tubes with a typical length of 2 m. The operating parameters were the standard ones as explained in Chapter 4. The noise level was such that the discriminator threshold (five times rms of the noise) corresponded to the 25<sup>th</sup> primary electron.

The external reference system for the resolution and efficiency measurements was the silicon tracker ODYSSEUS, described in Chapter 3. By extrapolation of the silicon telescope track to the chamber we get a prediction accuracy of 15  $\mu\text{m}$ . The  $5.1 \times 5.1 \text{ cm}^2$  window defined by the

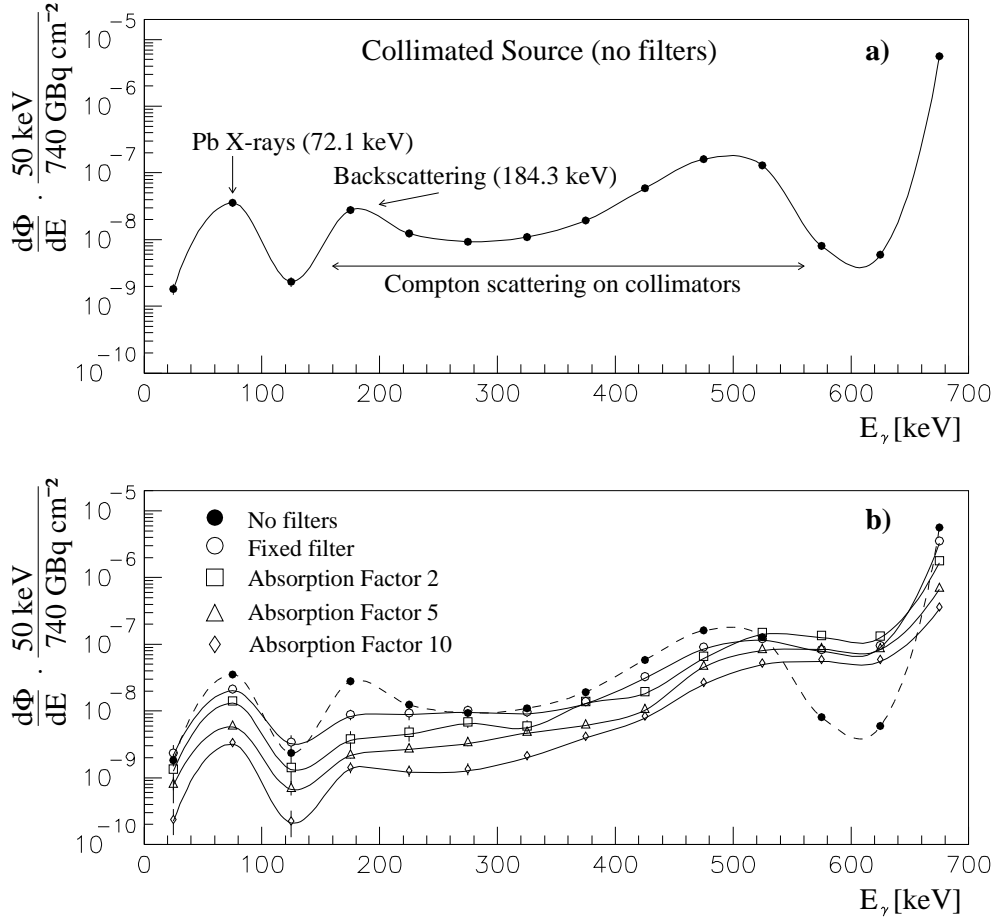


Figure 5.2: Gamma spectrum at 117.4 cm from the source in free air [VIT 98]: (a) Spectral contributions with collimators but without filters. (b) Spectra for different filter configurations. The spectra were determined in bins of 50 keV width. The connecting lines between the points are only drawn to guide the eye.

silicon detectors was centred on the beam. It covered in each multilayer of the MDT chamber seven tubes, three of them fully, the other four only partly (Figure 5.3). For our purposes we only used the downstream multilayer.

As front-end electronics (Figure 5.4) we used BNL preamplifiers [BNL 73] and different kinds of shapers which will be discussed in Section 5.2.1.1 together with rate effects related to the read-out electronics.

The signals from tubes n° 1, 3, 4, 6 and 7 were split and discriminated with two different thresholds (25 and 100 primary electrons) before being registered by TDCs. The high threshold was used for time-slewing corrections [ALE 98a] and double-track separation studies (Section 5.2.2.3).

The signals from tubes n° 2 and 5 were also split, but here the second signal half was fed into a FADC allowing us to look at pulse shapes.

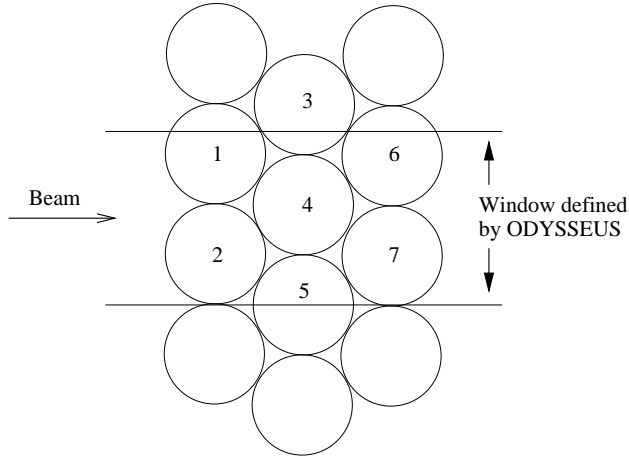


Figure 5.3: The “flower” of the seven drift tubes in the downstream multi-layer of the MDT chamber which were covered by ODYSSEUS.

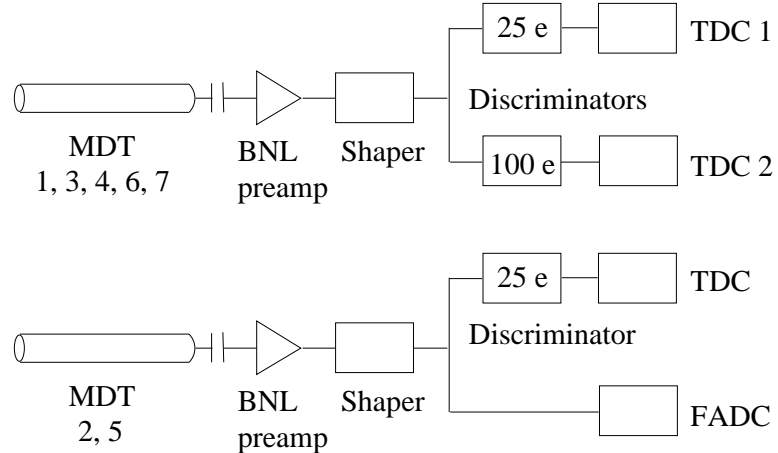


Figure 5.4: The read-out chain of the seven tubes analyzed in this study.

The following paragraphs are dedicated to the rate environment created by the Cs source.

The total gamma count rate of a tube as a function of the attenuation factor adjusted by using appropriate combinations of the lead filters is shown in Figure 5.5 (right scale). This total rate per tube is the relevant number for electronics effects (see Section 5.2.1.1).

We also wanted to study space charge effects (Section 5.2.1.2) which depend on the local rate per unit tube length at the position of the silicon tracker (i.e. in the centre of the beam). By dividing the total count rate by the tube length we only get the average rate per tube length (left scale of Figure 5.5). To get knowledge about the local rate we need to measure the variation of the gamma flux along the tube, e.g. by moving a scintillator along the line [A,B] in Figure 5.6a. The flux profile  $\Phi(x)$  can then be used to calculate the local count rate  $R_C$  of the tube in the

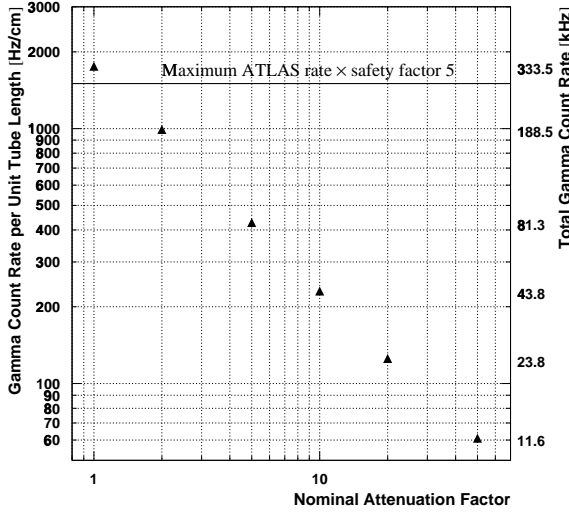


Figure 5.5: Average gamma count rate per unit tube length (left scale) and total count rate of a 1.90 m long tube (right scale) as a function of the nominal attenuation factor. For this measurement tube 4 (see Figure 5.3) in the downstream multilayer was used. The maximum rate, for which ATLAS drift tubes have to be designed, is 1500 Hz/cm (horizontal line) or 300 kHz per tube including a safety factor 5 due to uncertainties in the knowledge of the ATLAS background as explained in Section 2.2.2. This maximum rate is well within the scope of the X5 set-up.

centre of the beam:

$$R_C = \langle R \rangle_{[A,B]} \cdot \frac{\Phi_C}{\langle \Phi \rangle_{[A,B]}} \quad (5.1)$$

where  $\langle R \rangle_{[A,B]}$  is the measured average count rate per unit tube length and

$$\langle \Phi \rangle_{[A,B]} = \frac{1}{AB} \int_A^B \Phi(x) dx \quad (5.2)$$

the average over the flux profile measured with the scintillator.

Due to space problems in the test zone the profile measurement could not be done immediately at the chamber, but only at a distance of 1.70 m, i.e. along the horizontal line [A',B']. The fact that the rate varies along [A',B'] (Figure 5.6b) shows that the collimator filter in front of the source is not perfect.

The relative intensities of the profile along [A,B] follow from the measured profile along [A',B'] by projection:

$$\frac{\Phi_C}{\langle \Phi \rangle_{[A,B]}} = \frac{\Phi_{C'}}{\langle \Phi \rangle_{[A',B']}} \quad (5.3)$$

Analogous equations apply to the other interesting points along the tube: the ends A and B and the position of maximum rate, D. Calculating the ratios (5.3) for all attenuation factors we get Figure 5.7.

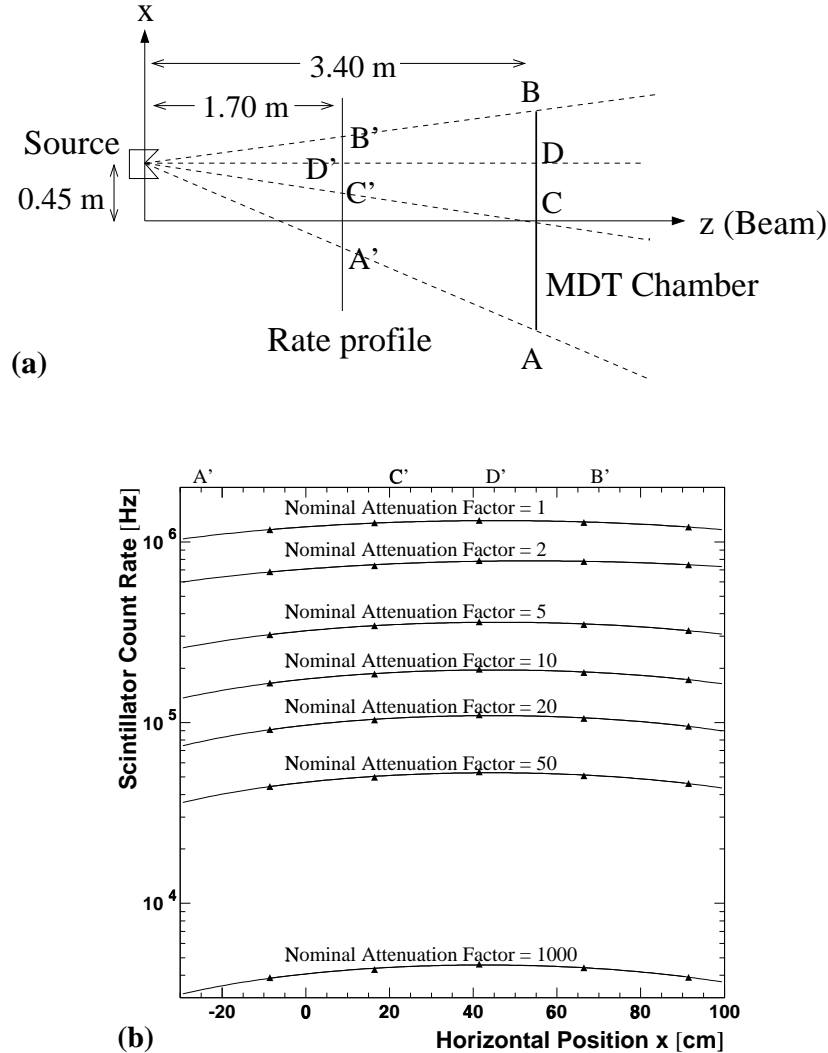


Figure 5.6: Measurement of the rate profile. (a) Schematic view of the set-up from the top. The profile was measured along [A'B']. (b) Profile measured with a  $6 \times 6 \text{ cm}^2$  scintillator. The solid lines represent quadratic fits to the measured points.

Since the source is not centred on the beam, the rates at the tube ends A and B are different by almost 30 %. The centre of the beam (point C) which is the most important position for us, is still in the flat part around the maximum of the profile (point D). The rate in C differs from the mean rate by less than 5 %.

The strong dependence of the rate ratio in A on the attenuation factor can be explained by the fact that the absorption filters disturb the flattening effect of the collimator filter. Adding another absorption layer causes a stronger increase of attenuation for big emission angles (e.g. tube end A) than for small angles.

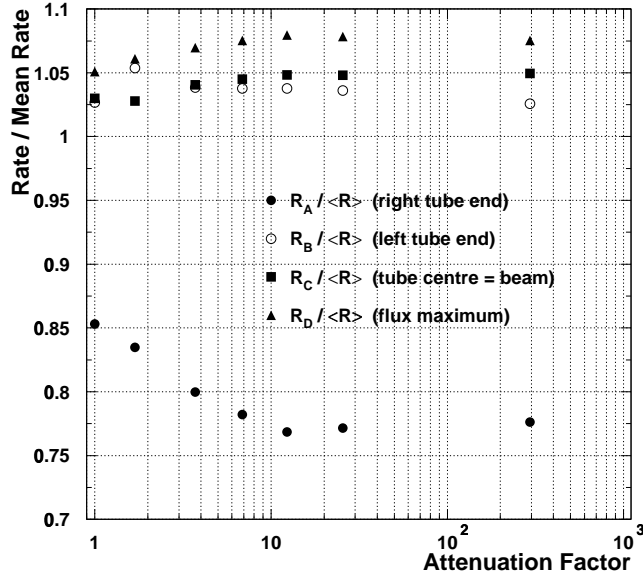


Figure 5.7: Rates at the points A, B, C, D (see Figure 5.6a) in relation to the mean rate as a function of the nominal attenuation factor.

### 5.1.2 The Experiments with Ar/CO<sub>2</sub> Mixtures

By the time when the above measurements with the old MDT gas had been finished, the ATLAS community became aware of the ageing problems with that gas and started to evaluate different Ar/CO<sub>2</sub> mixtures which were known to be ageing resistent. Consequently the rate behaviour of these new gas candidates had to be investigated.

For the new measurements single tubes in the middle of ODYSSEUS were used instead of the EMS prototype chamber. Since electronics-related effects were already covered by the previous experiment, the set-up was adapted to isolate space charge effects which are expected to have a major impact on Ar/CO<sub>2</sub> due to the strong non-linearity. To avoid the electronics effects, the total count rate was kept low by shielding the tubes almost entirely with lead blocks; only 10 cm around the beam centre were exposed to the radiation.

The single tubes were closer to the source than the EMS chamber, which explains that for a given attenuation factor the rate in the tube was higher than in the previous experiment (Figure 5.8).

The read-out chain is drawn in the lower sketch of Figure 5.4. Due to lower noise the discriminator threshold in this experiment corresponded to 20 primary electrons.

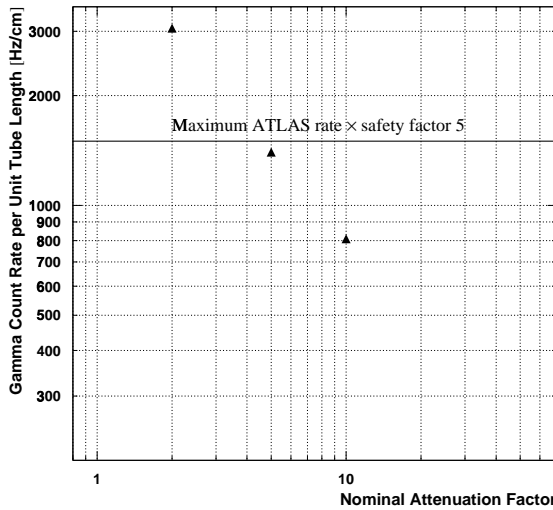


*Figure 5.8: Gamma count rate per unit tube length in the irradiated portion of the tube (10 cm) as a function of the nominal attenuation factor [ALE 98b]. For this measurement one of the single tubes in the centre of ODYSSEUS was used.*

## 5.2 The Influence of a Radiation Background on the Tube Performance

This section is dedicated to the degradation of drift-tube performance by a high-rate background. We shall discuss two aspects: resolution and efficiency.

### 5.2.1 Resolution Deterioration

The resolution of drift tubes suffers from two groups of high-rate effects:

- Electronics effects:  
The high-rate behaviour is significantly affected by the pulse shaping scheme of the front-end electronics. In Section 5.2.1.1 we shall see that high count rates can cause shifts and fluctuations of the signal baseline. Since for the read-out the distribution of the hit positions along the tube is irrelevant, these electronics effects depend on the total counting rate of the tube.
- Space-charge effects: At high local rates the space charge of the ion cloud drifting to the cathode changes the electric field and thus reduces the gas gain. Furthermore, for non-linear drift gases the r-t relationship changes because the drift velocity depends on the electric field. These effects are discussed in Section 5.2.1.2.

Finally in Section 5.2.1.3 the measured resolution deterioration will be presented. It is a combination of the two classes of effects.

### 5.2.1.1 Effects Related to the Electronics

The impact of the shaping scheme on high rate MDT performance is mainly determined by the amount of baseline shift. Therefore we shall first give an outline of the mechanism which affects the baseline of signal pulses in presence of high counting rates.

#### a. Baseline Shift

In the introductory section 2.4.1 we mentioned that every raw signal pulse ends in a very long tail caused by the slow drift of the ions to the tube wall (Equations (2.2)ff). However, this is not the whole story. Due to the AC coupling between the tube anode and the read-out the net charge flow into the preamplifier integrates to zero within a time which is of the same order as the time constant  $\tau = R_0 \cdot (C_1 + C_2) \approx 1 \text{ ms}$  (using the symbols of Figure 2.8) for the restoration of the charge on the wire by the high voltage supply. Therefore the ion tail of the pulse goes into a long and shallow undershoot. If the total count rate of the tube is large compared to  $1/\tau$ , subsequent pulses sit on the undershoot of the preceding pulses (Figure 5.9), and the undershoot builds up to a permanent negative shift of the baseline.

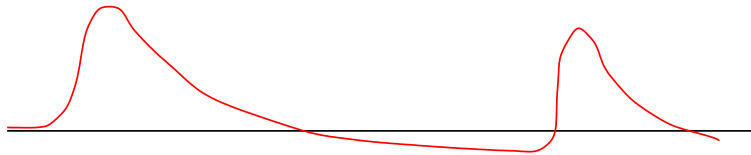


Figure 5.9: The origin of the baseline shift for a shaping without tail cancellation.

A negative baseline shift is equivalent to a higher effective discriminator threshold and therefore deteriorates the resolution by time slewing.

#### b. Baseline Fluctuations

In addition to the permanent baseline shift there are fluctuations of the baseline because the time distances between background pulses as well as the deposited charge are statistically distributed. This effect introduces additional time jitter, again deteriorating the resolution (Figure 5.10).

We have now shown the basic mechanism of baseline shift and fluctuations. In the following we shall focus on the influence of the pulse shaping scheme on these effects.

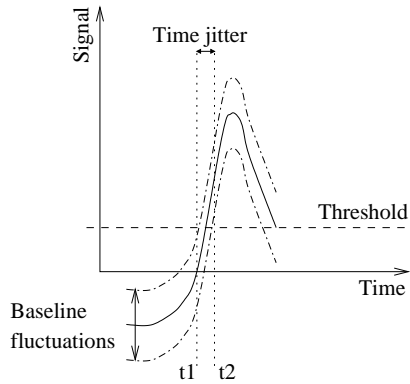


Figure 5.10: Baseline fluctuations introduce time jitter and hence deteriorate the resolution.

### c. Shaping Schemes applied in the Test-Beam Experiments

In the test-beam experiments three different shaping schemes were tested (see Figure 5.11):

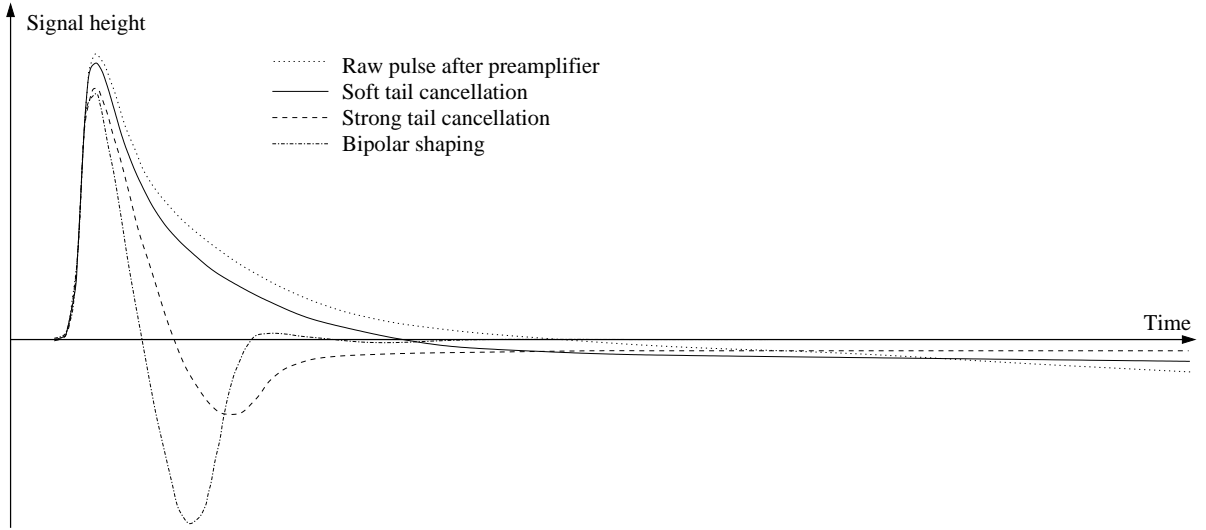


Figure 5.11: Schematic drawing of an example muon pulse without any shaping (dotted line) and for each of the three shaping schemes applied in the experiment. In order to show the principle more clearly, neither the time nor the signal height are to scale: In reality the undershoots of the raw pulse and of the pulse with soft tail cancellation set in later. The magnitudes of the late stages of all undershoots are exaggerated.

- **Soft tail cancellation:** This shaping scheme was realized with the BNL shapers [BNL 73]. Two pole/zero filters in series with adjustable time constants shorten the pulse by partly compensating the tail. Although this shaping scheme is intrinsically unipolar (the delta-response is positive at all times), the output pulse has a long shallow undershoot in the

late stages of the ion tail. This undershoot is inherited from the raw pulse and cannot be avoided with passive shaping circuits. However, the partial cancellation of the early tail reduces the magnitude of the undershoot.

- **Strong tail cancellation:** Technically this scheme is very similar to the soft tail cancellation. It was also realized with the BNL shapers. The only difference lay in the settings of the pole/zero time constants. They were chosen such that the early signal tail was overcompensated resulting in a big undershoot immediately after the pulse. This early undershoot compensated already about 20 % of the charge contained in the positive part of the pulse. Thus the magnitude of the late flat part of the undershoot was smaller than with soft tail cancellation. We chose the early undershoot as deep as possible with the BNL shapers.
- **Bipolar shaping:** This shaping scheme where the full charge of the muon signal is compensated immediately after the pulse, provides the strongest tail cancellation. Since a perfectly bipolar shaping was not within the range of the potentiometers in the BNL shapers, a separate bipolar shaping amplifier was used. Unfortunately the available device had twice the desired shaping time for the leading edge, leading to a deterioration of the resolution without and with radiation background. But this did not affect the main objectives of studying bipolar shaping, namely baseline shift and fluctuations.

For the measurements with Ar/N<sub>2</sub>/CH<sub>4</sub> (91/4/5) all three shaping schemes were used to investigate the electronics effects. The Ar/CO<sub>2</sub> studies on the other hand were fully dedicated to space charge effects. Electronics effects could not contribute to the resolution deterioration because the total counting rate was kept low (about 4.5 kHz) by irradiating only 3 cm along the tube with photons (cf. Section 5.1.2). Therefore it was not necessary to compare different shapers; we chose the BNL shapers with strong tail cancellation.

#### d. Measurements of Baseline Shift and Fluctuations

Figure 5.12 shows the distributions of baseline positions averaged over the last 500 ns before a muon pulse. They were measured with an FADC for the soft tail cancellation scheme.

The background rates are 0 for distribution (a) and 188.5 kHz for (b). We define the means of these distributions as the baseline shifts. The rms of the distributions characterize the baseline fluctuations.

Figure 5.13 shows the rate dependence of baseline shift (plot a) and fluctuations (plot b). In Figure 5.13b only the contribution of the background rate to the baseline fluctuations is shown. For this purpose the noise contribution, i.e. the rms width of the baseline position distribution without rate (Figure 5.12a), was subtracted in quadrature from the rms width of the distribution with rate (Figure 5.12b). On the first glance it is surprising that the reduction of baseline shift from soft to strong tail cancellation is rather small whereas the fluctuations are significantly suppressed. This behaviour can be understood from the baseline distribution in Figure 5.12b: This distribution has a significant portion at positive baseline positions because many muon pulses are sitting on the early part of the preceding ion tail, i.e. before the start of the undershoot (cf. Figure 5.11). Thus the mean does not well characterize this asymmetric distribution. The huge tail in the negative part is better visible in the rms, i.e. in the fluctuations.

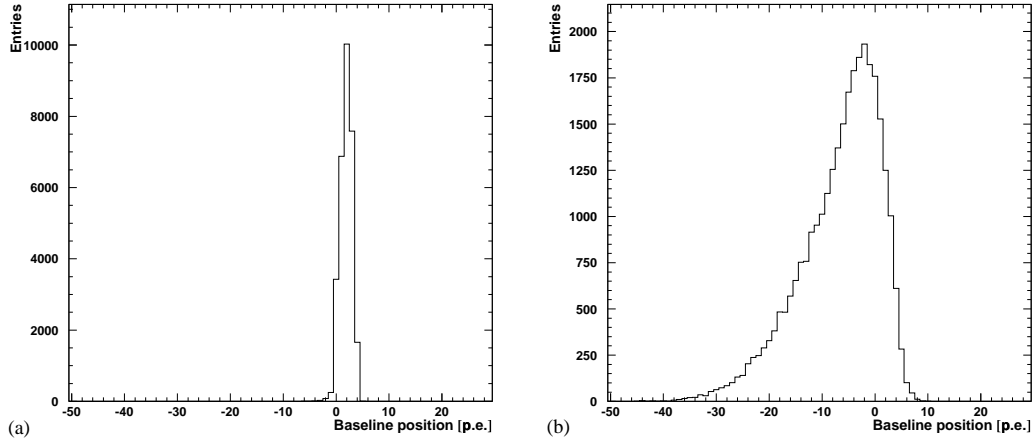


Figure 5.12: Distribution of the baseline position averaged over the last 500 ns before a muon pulse, measured with an FADC. (a) Soft tail cancellation without background; (b) Soft tail cancellation with 188.5 kHz background.

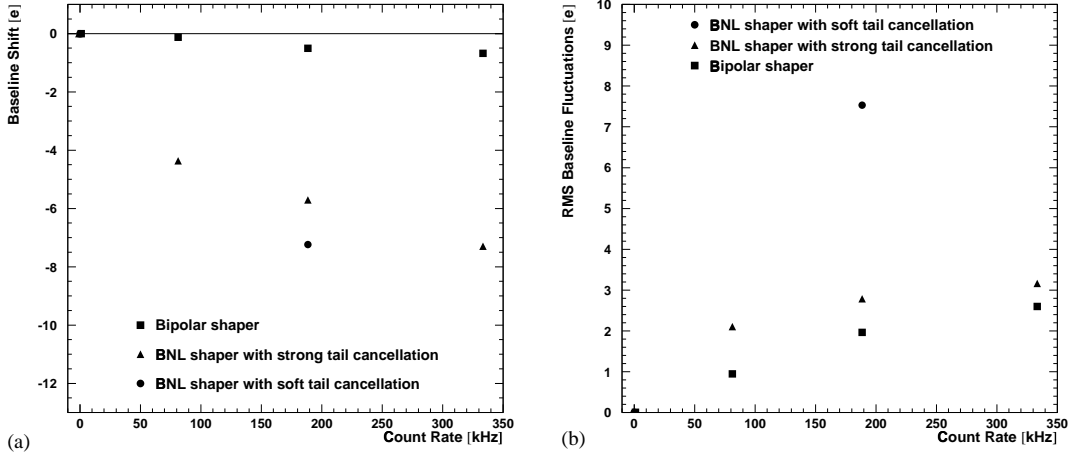


Figure 5.13: Comparison of (a) the measured baseline shifts and (b) the rms baseline fluctuations for the three shaping schemes used in the test-beam experiment. For the shaping with soft tail cancellation data were taken only at 0 and 188.5 kHz. In (a) the mean baseline position at zero rate was subtracted as a constant offset. In (b) the width at zero rate was subtracted in quadrature.

The undershoot produced by the strong tail cancellation has a deep part immediately after the positive pulse and then becomes flat and shallow very early. Thus the baseline for the following pulse has no strong variations.

Bipolar shaping finally avoids the long shallow undershoot and pushes the baseline shift under the level of one primary electron even at a rate of 330 kHz. Also the fluctuations are further reduced with this shaping scheme.

### 5.2.1.2 Space-Charge Effects

For our tube geometry and working point, the ions created in the avalanche near the wire take about 4 ms to drift to the tube wall. Their presence in the drift region creates a space charge which modifies the electric field for subsequent events. The consequences are a reduction of the gas gain and fluctuations of the drift velocity. We shall explain that both effects deteriorate the resolution.

#### a. Gain Drop

Due to the decreased electric field at the anode wire the electron multiplication close to the wire is reduced and the gas gain drops. This gain drop was measured by comparing the signal charges with and without rate (Figure 5.14). In Figure 5.15 the measurements are compared with an analytical model [ALE 98a] and show good agreement. The ratio  $G/G_0$  of the gas gain at the maximum background rate for the MDT design (1500 Hz/cm) and the gas gain without space charge is about 0.87 at a gas gain of  $G_0 = 2 \times 10^4$ .

The impact of a gain drop on the resolution can be understood in the following way: the signals are scaled down whereas the threshold remains fixed. Consequently the threshold gets effectively shifted to a larger number of primary ionization electrons, which deteriorates the resolution.

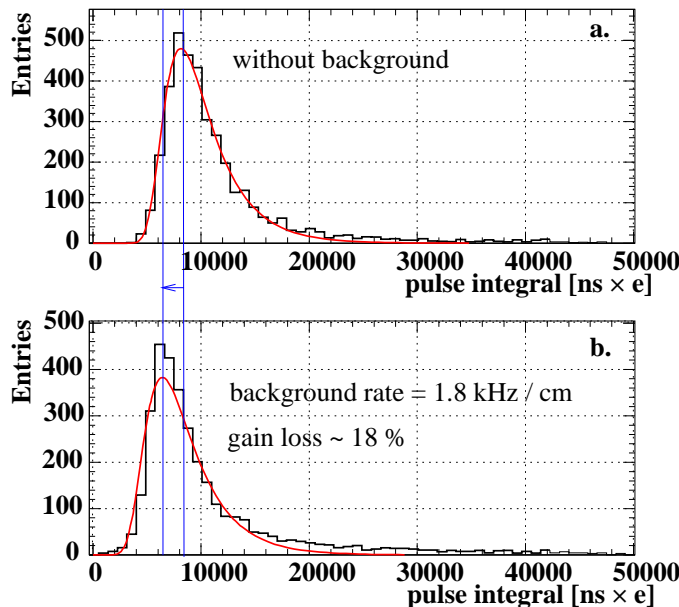


Figure 5.14: Distributions of the integrated pulse charge (a) without background and (b) with a rate of 1.8 kHz per centimeter tube length. The charge was measured with an FADC.

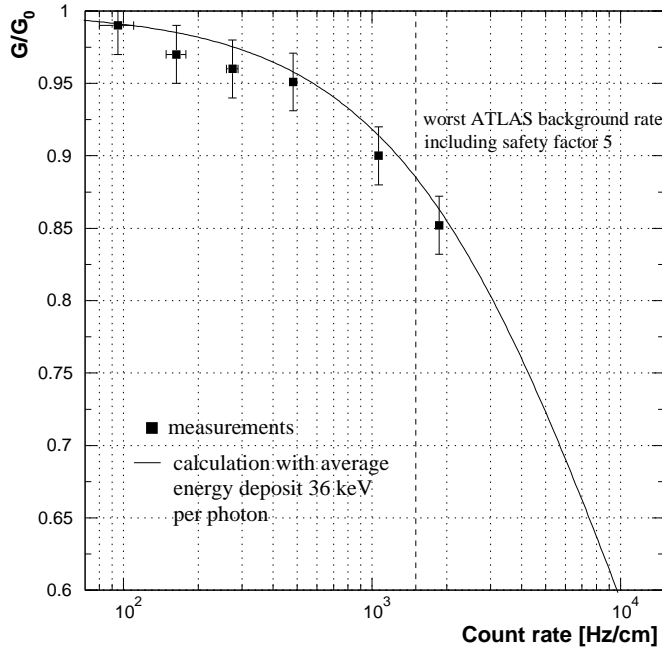


Figure 5.15: Gain drop versus background rate for a gas gain of  $G_0 = 2 \times 10^4$ . The solid line represents a calculation using an analytical model for the space charge [ALE 98a].

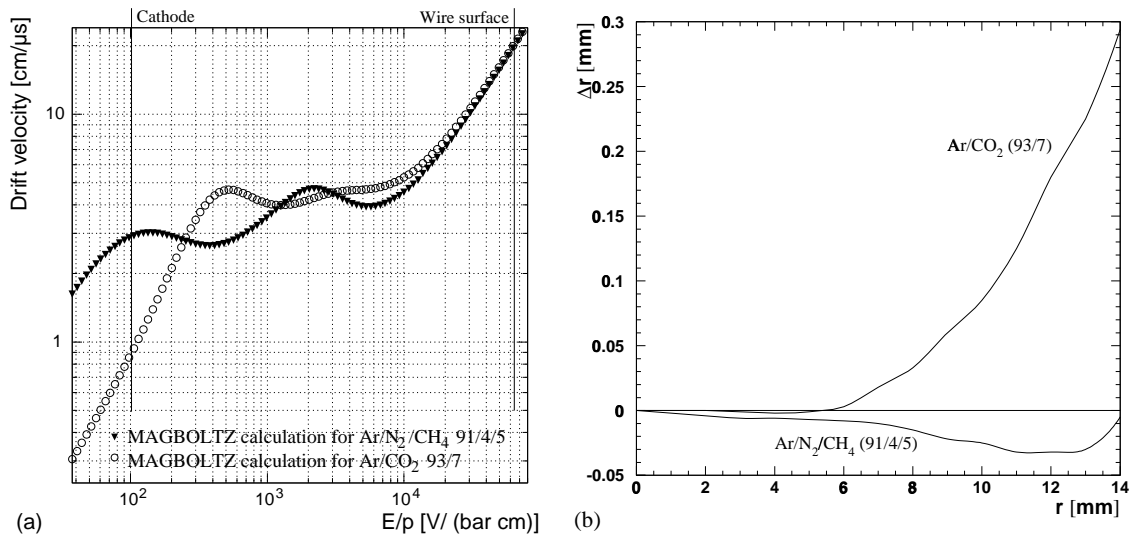


Figure 5.16: (a) Drift velocity as a function of the reduced electric field  $E/p$  for the old and the new MDT gas (calculation with MAGBOLTZ). (b) Change of  $r(t)$  from 0 to 1500  $\text{Hz}/\text{cm}$  background rate for both gases (GARFIELD simulation).

### b. Fluctuations of the Drift Field

The space charge changes the drift field and hence the space-time relationship. If this space charge were constant for a given hit rate, the drift field would be globally changed and there would be no deterioration of resolution. However, the electrons drifting towards the wire are affected only by the charge within approximately 1 cm along the tube, and at a rate of 1500 Hz/cm there are on average only six ion clouds in such a slice. Since the actual number  $n$  of ion clouds is Poisson distributed, the drift field varies and the resolution deteriorates. This effect is rather small for linear gases such as Ar/N<sub>2</sub>/CH<sub>4</sub> (91/4/5), where the drift velocity depends only weakly on the electric field, but becomes an important effect for non-linear gas mixtures like Ar/CO<sub>2</sub> where  $r(t)$  changes by up to 300  $\mu$ m for a rate of 1500 Hz/cm (Figure 5.16).

#### 5.2.1.3 Results from the Resolution Measurements

In this section we shall show the measured deterioration of tube resolution with increasing background rate and compare the results with simulations in order to identify and understand the individual rate effects. We concentrate on the gases Ar/N<sub>2</sub>/CH<sub>4</sub> (91/4/5) and Ar/CO<sub>2</sub> (93/7). Other Ar/CO<sub>2</sub> mixtures were also studied. They are discussed in [ALE 99b].

The technique for determining the resolution with the silicon tracker as reference system was already described in Section 4.5. The resolution simulation using GARFIELD was also similar to the procedure explained in the same context. The only difference were the rate effects which were modelled in the following way:

Since it is difficult to implement a full description of the read-out electronics into GARFIELD, the electronics effects were modelled by modifying the discriminator threshold instead of introducing real baseline shifts and fluctuations. To simulate the effect of a negative baseline shift the threshold was raised. In addition a threshold smearing was applied to account for the baseline fluctuations. The drift-field fluctuations were introduced by modifying the electric field according to a calculation given in [ALE 98a]. A gain drop corresponding to the measurements was also taken into account.

We shall first present the results for the BNL shaper with strong tail cancellation. Afterwards the differences to the soft tail cancellation will be demonstrated.

The data taken with the bipolar shaper will not be discussed in the context of resolution. The device which was available for the test beam had a higher noise level than the other shapers, twice the nominal peaking time and smaller output pulses. Hence the resolution was very bad and not instructive for this comparison. This shaper was only useful to study baseline shift and fluctuations.

### a. Resolution for Strong Tail Cancellation

Figure 5.17 shows the resolution as a function of the distance from the wire. Part (a) compares the behaviour of Ar/N<sub>2</sub>/CH<sub>4</sub> (91/4/5) without background and at a rate of 1850 Hz/cm (333 kHz per tube); part (b) is the corresponding plot for Ar/CO<sub>2</sub> (93/7) at the rates 0 Hz/cm and 1400 Hz/cm (4.5 kHz per tube). For both gases measurements and simulation are in acceptable agreement.

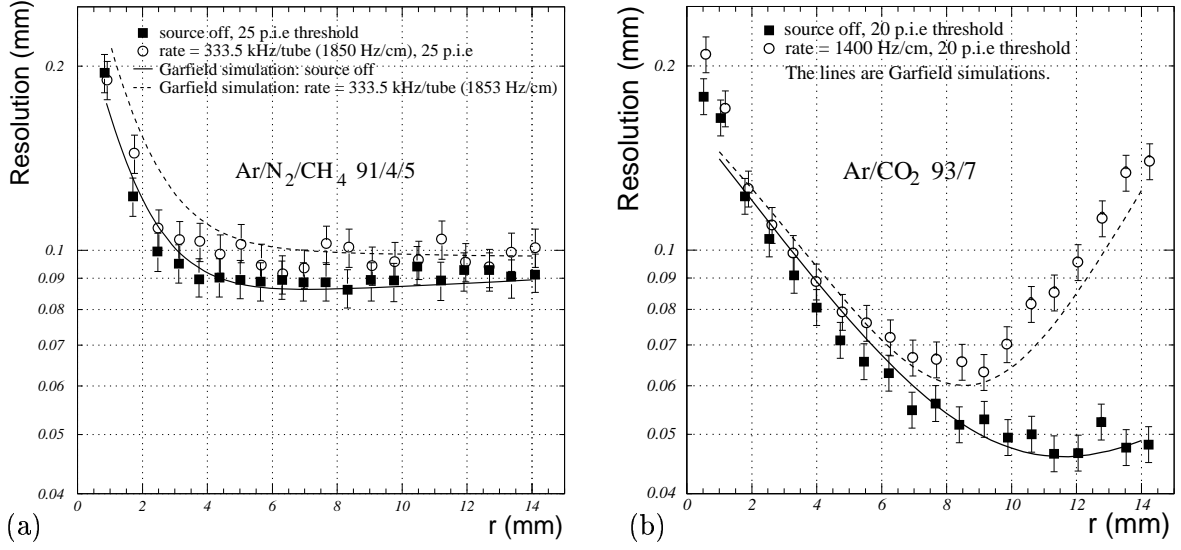


Figure 5.17: Measured and simulated resolution for BNL shapers with strong tail cancellation: (a) for Ar/N<sub>2</sub>/CH<sub>4</sub> (91/4/5) without background rate and at 1850 Hz/cm (333 kHz per tube); (b) for Ar/CO<sub>2</sub> (93/7) without background rate and at 1400 Hz/cm (4.5 kHz per tube).

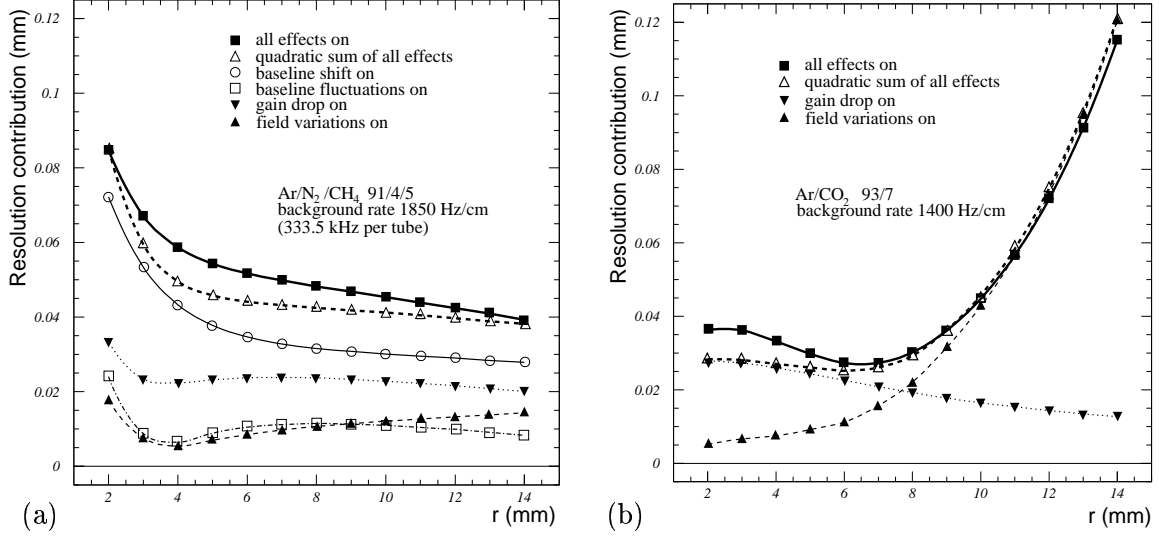


Figure 5.18: Simulated contributions to resolution deterioration with background: The individual rate effects were separately switched on. For each effect the curve represents the quantity  $\sqrt{\sigma_{\text{with this rate effect}}^2 - \sigma_{\text{no rate effects}}^2}$ . The lines are drawn to guide the eye. (a) Ar/N<sub>2</sub>/CH<sub>4</sub> (91/4/5) at 1850 Hz/cm (333 kHz per tube); (b) Ar/CO<sub>2</sub> (93/7) at 1400 Hz/cm (4.5 kHz per tube).

Figure 5.18 separates the different simulated contributions to resolution deterioration at high background rates for the strong tail cancellation scheme. The first 2 mm are omitted,

because in this domain the resolution function is non-Gaussian which leads to problems in the determination of the width with a Gaussian fit (cf. Section 4.5.2). Therefore the separation of the different effects in this region is technically difficult. From Figure 5.18 we can draw the following conclusions:

- The contribution of the field fluctuations is rather small for the linear gas (plot a). Since the drift velocity has only a weak dependence on  $E/p$  (Figure 5.16a), variations of the drift field translate only into small variations of the drift time. For the non-linear gas mixture (plot b) this contribution dominates.
- The baseline shift dominates the resolution deterioration of the linear gas by shifting the effective threshold from the 25<sup>th</sup> to the 33<sup>rd</sup> primary electron. We remind that in our test with Ar/CO<sub>2</sub> the baseline shift could not contribute to the resolution because the total rate per tube was kept low. Therefore this effect was also switched off in the simulation.
- The contribution of the gain drop ( $G/G_0 = 0.87$ ) is smaller than the one of the baseline shift since the effective threshold shifts only to  $G_0/G \cdot 25$  p.e. = 28.4 p.e.
- The baseline fluctuations of 3 p.e. rms have only a small direct impact on the resolution. However, we have to consider that these fluctuations are a contribution to the noise. According to the ATLAS policy we would have to set the threshold to  $5 \times \sigma_{\text{noise+fluct}}$  instead of  $5 \times \sigma_{\text{noise}}$ . For a noise of 5 p.e. without background the baseline fluctuations of 3 p.e. would raise the threshold from 25 p.e. to 29 p.e. which would result in a resolution deterioration comparable to the contribution of the gain drop.
- The significance difference between “all effects on” and the quadratic sum of all effects in plot (a) shows that there is a correlation between individual contributions. The quadratic sum underestimates the resolution deterioration because a baseline shift amplifies the effect of the gain drop: The baseline shift moves the threshold from 25 p.e. to 34 p.e. Multiplying this with  $G_0/G$  yields a threshold of 39 p.e. which is higher than the 37 p.e. which we obtain by summing up the two individual effects.

### b. Resolution Comparison between Strong and Soft Tail Cancellation

In the last paragraph we have given a detailed analysis of the resolution with strong tail cancellation. We shall now compare it with the performance of the soft tail cancellation which was already shown to suffer more from baseline shifts and fluctuations. Therefore we expect a faster deterioration of resolution with higher rates for soft tail cancellation. Figure 5.19 demonstrates that this happens indeed. Part (a) of the figure shows the radial dependence of resolution for both shaping schemes and two different rates. To facilitate the quantitative comparison of resolution as a function of the rate for the soft and strong tail cancellation, we calculate the quadratic mean resolution as defined in (4.1). The result is presented in Figure 5.19b.

The big resolution improvement from soft to strong tail cancellation underlines the importance of choosing the right shaping scheme. With properly adjusted bipolar shaping (which was not available for the tests) we would expect an even smaller deterioration with background rate

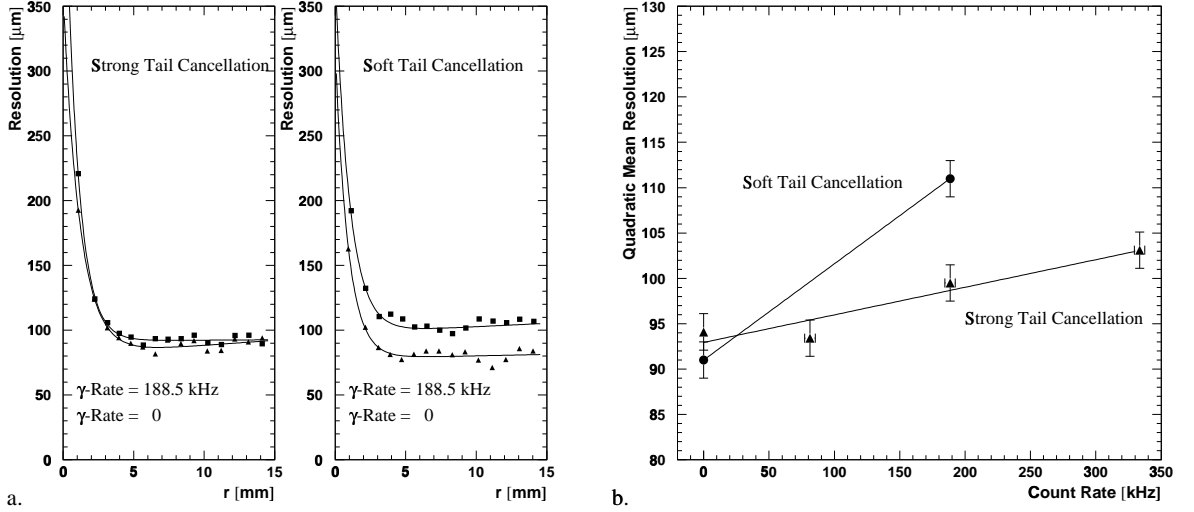


*Figure 5.19: (a) Measured resolution for strong and soft tail cancellation at the rates 0 Hz and 188.5 kHz. (b) Quadratic mean resolution of Ar/N<sub>2</sub>/CH<sub>4</sub> (91/4/5) as a function of the count rate for soft and strong tail cancellation. The tube which had the shaper with strong tail cancellation showed a higher noise level than the tube with soft tail cancellation. Therefore its resolution at zero rate is worse.*

than for the other shaping schemes since baseline shift and baseline fluctuations are suppressed (as shown in Section 5.2.1.1).

#### 5.2.1.4 Time-Slewing Corrections

A part of the resolution deterioration can be compensated by a time-slewing correction. This technique takes advantage of the correlation between the leading edge charge of a pulse and the threshold crossing time. Details of the method are described in [ALE 98a] and [ALE 99b]. For the completeness of this discussion we show the improvement in Figure 5.20 where the resolution with and without time slewing correction is displayed for the cases without background and at a count rate of 333.5 kHz. Unfortunately the tube which was used for this study, had a high noise level and hence a bad resolution of about 100 μm without rate.

A more quantitative comparison of the resolution with and without time-slewing correction is given in Table 5.1 for both MDT gases. Here the resolution is characterized by a new figure of merit: the Inverse Quadratic Average IQA defined by

$$\bar{\sigma}_{\text{IQA}} \equiv \frac{1}{\sqrt{\left\langle \frac{1}{\sigma^2} \right\rangle}} \quad \text{with} \quad \left\langle \frac{1}{\sigma^2} \right\rangle = \frac{1}{b-a} \int_a^b \frac{1}{\sigma^2(r)} dr . \quad (5.4)$$

The motivation for this definition is the stronger accentuation of the radial regions with better resolution, which has some relevance for tracking where hits are weighted by  $\frac{1}{\sigma^2(r)}$ . For

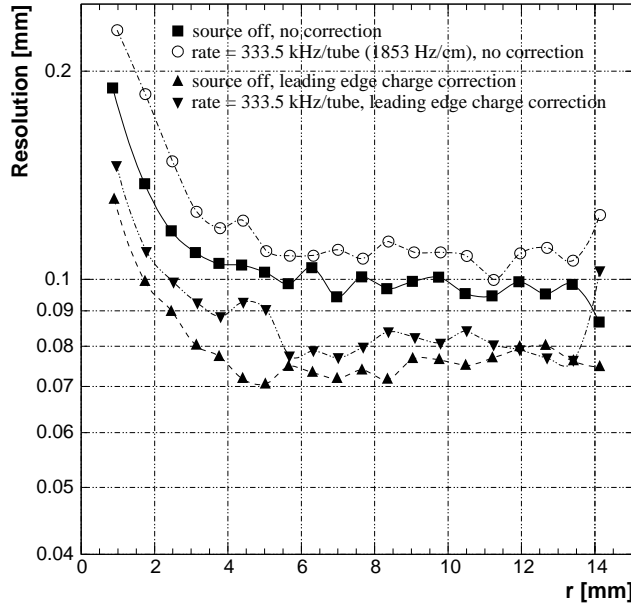


Figure 5.20: Improvement of the resolution with leading-edge charge correction for Ar/N<sub>2</sub>/CH<sub>4</sub> (91/4/5).

Ar/N<sub>2</sub>/CH<sub>4</sub> (91/4/5) the IQA coincides with our familiar quadratic mean within about 3 μm; for Ar/CO<sub>2</sub> it gives lower numbers (without rate: quadr. mean = 69 μm,  $\bar{\sigma}_{\text{IQA}} = 60 \mu\text{m}$ ).

As conclusion we can point out that even at the maximum rate a typical resolution around 80 μm is achievable.

gas	IQA $\bar{\sigma}$ (all values in μm)			
	without background rate		with background rate	
	without correction	with correction	Ar/N <sub>2</sub> /CH <sub>4</sub> : 1853 Hz/cm, 333.5 kHz	Ar/CO <sub>2</sub> : 1400 Hz/cm, 4.5 kHz
Ar/N <sub>2</sub> /CH <sub>4</sub> 91/4/5	104	79	119	87
Ar/CO <sub>2</sub> 93/7	60	56	87	82

Table 5.1: IQA resolution with and without leading-edge charge correction (taken from [ALE 99b]). The tube which was used for the study with Ar/N<sub>2</sub>/CH<sub>4</sub> (91/4/5) was noisy; therefore the resolution was untypically bad. However, the important fact is the improvement with time-slewing correction.

### 5.2.2 Efficiency Deterioration

This section discusses the dependence of the MDT efficiency on the background rate and the shaping scheme. We distinguish two different efficiencies:

- The hit efficiency indicates the probability that a muon going through a tube is registered at all. No quality criterion is applied to the reconstructed hit radius.
- The  $3\sigma$ -efficiency indicates the probability that a muon passing through a tube is detected and the reconstructed hit radius is within  $3\sigma$  from the true value, where  $\sigma$  is the spatial resolution at the respective track radius. This efficiency definition characterizes the importance of the tails in a residual distribution.

Both efficiencies have been measured using the information of ODYSSEUS as an external tracker.

#### 5.2.2.1 Deterioration of the Hit Efficiency

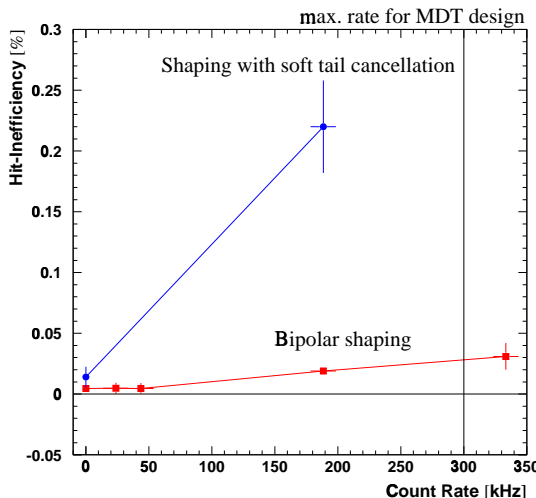


Figure 5.21: Hit inefficiency as a function of the gamma rate for unipolar and bipolar shaping.

The hit efficiency remains very high even with a radiation background. Figure 5.21 shows the rate dependence of the hit inefficiency averaged over hit radii between 0 and 14 mm for the unipolar and the bipolar shaping. In our average we exclude the 0.6 mm near the wall because in this domain the MDT starts becoming inefficient anyway (cf. Section 4.6.2.1), and efficiency fluctuations as well as systematic errors due to wire displacements are bigger than the tiny rate effect we are looking for.

The efficiency deterioration depends on the shaping: It is most accentuated for the soft tail cancellation due to its important negative baseline shift which increases the effective threshold. Therefore with a background it is more likely that a muon pulse stays below the threshold than without background. This effect however is very small: the maximum inefficiency is a few per-mille.

For the bipolar shaping there is no baseline shift. The tiny increase of inefficiency can be explained with the gain loss due to space charge effects which – in a similar way as a baseline shift – is equivalent to a higher effective threshold.

### 5.2.2.2 Deterioration of the $3\sigma$ -Efficiency

In Section 4.6.2.2 the  $3\sigma$ -efficiency  $\eta_{3\sigma}$  was introduced as a criterion quantifying the importance of non-Gaussian tails in the drift-time distribution for a given radius.

Figure 5.22 shows the rate dependence of the  $3\sigma$ -efficiency for Ar/N<sub>2</sub>/CH<sub>4</sub> (91/4/5).

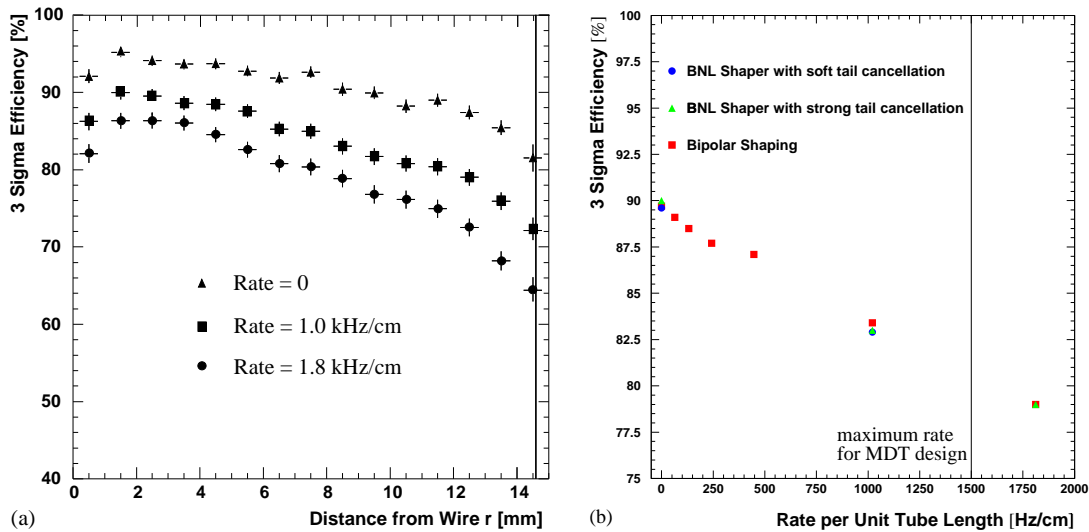


Figure 5.22: (a)  $3\sigma$ -efficiency as a function of the track radius for different gamma rates. For this plot the shaping with strong tail cancellation was used. (b)  $3\sigma$ -efficiency averaged over  $r$  as a function of the gamma rate for the three shaping schemes studied.

Since the probability for a delta ray arriving earlier than the muon increases with the track radius, the  $3\sigma$ -efficiency decreases from the wire to the wall. For an analogous reason the distance between two curves for different rates grows with increasing radius: the longer the drift time corresponding to the muon track, the bigger is the probability to have a background hit before the muon hit. Delta rays alone push the averaged  $3\sigma$ -efficiency below 90 %. This is about 5 % lower than the value found in the M2 test-beam experiment described in Section 4.6.2.2. The reason is a 20 cm thick chamber support bar (Aluminium) immediately in front of the tubes under study, which produced shower particles leading to a reduced  $3\sigma$ -efficiency. The magnitude of the effect is well in agreement with a dedicated study of additional hits due to matter in the beam [KOR 99].

Taking the average  $3\sigma$ -efficiency over all radii  $r$  and plotting it versus the rate we obtain Figure 5.22b. At the maximum rate for MDT design only 80 % of the muon hits would be reconstructed within  $3\sigma$ . Taking into account the 5 % additional shower background due to the Aluminium cross bar yields a slightly more optimistic  $3\sigma$ -efficiency of 85 % at the maximum rate relevant for the MDTs.

Interpreting these numbers we have to keep in mind that with increasing rate also  $3\sigma$  becomes bigger. Therefore an increase in the number of hits outside the increased  $3\sigma$  limit implies that the effect of the background rate on the fraction of events with big deviations is even stronger than indicated by  $\eta_{3\sigma}$ .

Unlike the hit efficiency, the  $3\sigma$ -efficiency does not depend on the shaping scheme. This is reasonable because background hits and delta rays mask signal hits whichever electronics we use. As long as only the first hit within the total drift-time window is considered, every muon hit which is preceded by a background hit, is lost. In principle one could imagine a slight difference in  $\eta_{3\sigma}$  between the shaping schemes because the underlying  $\sigma$  are slightly different. However,  $\eta_{3\sigma}$  is dominated by delta- and gamma-ray hits whose typical excursions from the track are much bigger than the little resolution differences from one shaping scheme to the other.

In the next section a technique will be demonstrated which allows us to recover some of the hidden muon hits.

### 5.2.2.3 Double-Track Separation with a Second Threshold

The two-threshold technique for double-track separation (or rather “double-pulse separation”) has already been studied in simulation [RIE 97a]. The instrumentation in the X5 test beam now offered us the opportunity to apply the method to real data. This study was performed at the time when the favourite shaping scheme was unipolar with an active baseline restoration. By now this concept has been abandoned (see discussion in Section 4.4.2.2). However, we present these results for reasons of general detector-physical interest.

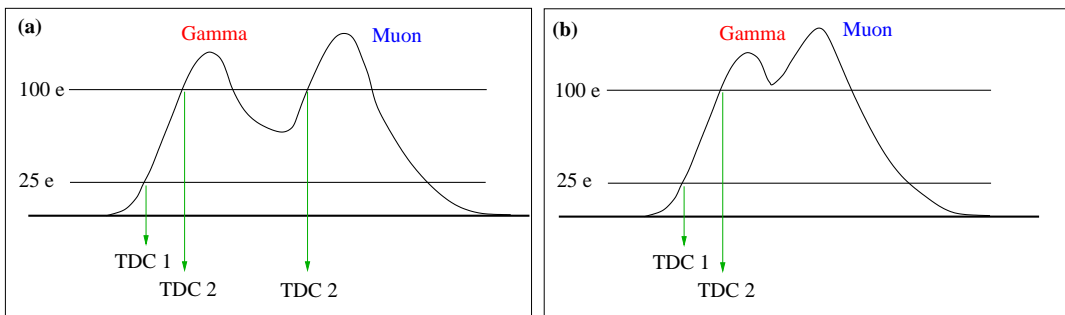


*Figure 5.23: Double track separation with the two-threshold method. In example (a) the hidden muon pulse is reconstructed using the second crossing of the high threshold. Example pulse (b) cannot be separated because the separation time is shorter than the decay time of the gamma pulse.*

The principle of the method is shown in Figure 5.23a, which shows muon pulses arriving very soon after a background pulse (from a gamma, delta-ray or other muon). The muon pulse remains undetected by the lower threshold if it arrives before the background pulse has decayed below that threshold. However, it can still be detected by a higher threshold as shown in Figure 5.23a. If it is too close to the background pulse, it remains masked (Figure 5.23b). At a high threshold of 100 electrons, a muon arriving 100 ns or more after the background pulse has a good chance to be detected. This corresponds to a two-track separation of about 3 mm.

A drawback of the reconstruction with a high threshold is the worse resolution compared to the low threshold: The resolution is  $170\text{ }\mu\text{m}$  at a threshold of 100 electrons instead of  $85\text{ }\mu\text{m}$  at 25 electrons.

In addition, due to the finite rise time of the leading edge the crossing time of the high threshold is systematically shifted with respect to the low-threshold crossing time. But this is no serious problem since we can correct for this systematic effect.

The residual plots in Figure 5.24 illustrate the three mentioned problems: The gap in plot (a) results from the 100 ns minimum separation time. The projection in plot (b) shows the bad resolution and the systematic shift of the reconstructed muon hit radius.

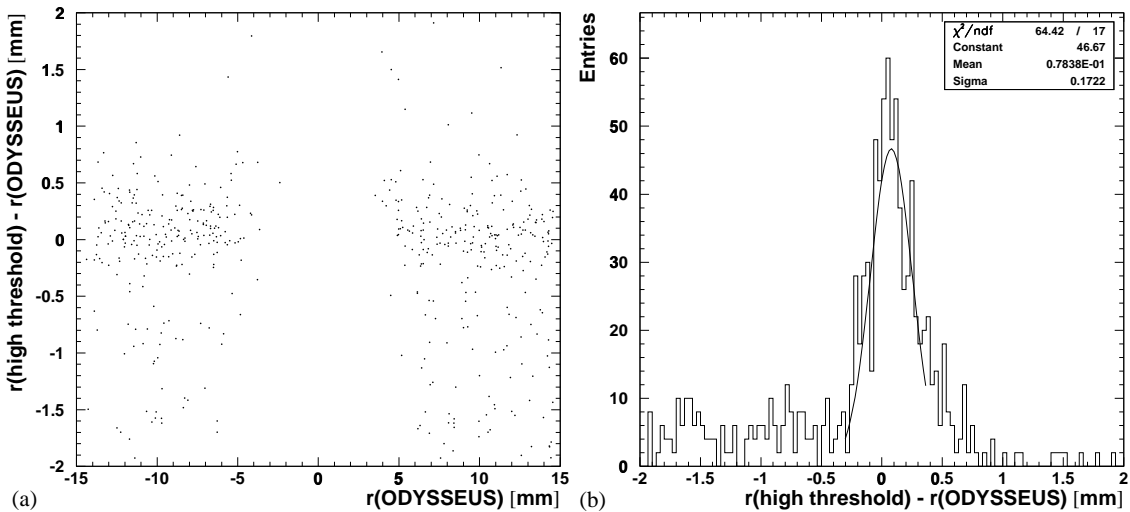


Figure 5.24: Residuals for the second crossing of the 100 electron threshold. Here the background consists of delta-rays only. In (a) the difference between the reconstructed hit radius and the track radius predicted by ODYSSEUS is plotted versus the predicted track radius. (b) is the projection of (a) onto the ordinate.

The read-out concept in the run period with Ar/N<sub>2</sub>/CH<sub>4</sub> (91/4/5) (see Section 5.1.1) allows us to do double track separation with two different sets of information:

- the TDC data: The two thresholds were fixed at  $25\text{ e}^-$  and  $100\text{ e}^-$ .
- the FADC data: They offer the advantage of flexible thresholds (set by software in the analysis).

In both cases the soft tail cancellation was used. ODYSSEUS served as an external tracker. Its information is first needed for determining the r-t relationship, then for the decision whether a hit is a background hit (i.e. whether it arrives more than  $3\sigma_{\text{low threshold}}$  earlier than predicted) and finally for judging whether the reconstruction of a shaded muon was successful, i.e. whether

$$r_{\mu \text{ reconstructed}} - r_{\mu \text{ silicon telescope}} < 3\sigma_{\text{high threshold}}(r) \quad (5.5)$$

To quantify the success of the separation technique we introduce the separation efficiency

$$\eta_{sep} = \frac{\text{separated muons according to (5.5)}}{\text{all muons shaded by background hits}} . \quad (5.6)$$

We studied double track separation for two kinds of background:

- only delta-rays (no external background).
- gamma background and delta-rays.

### a. Separation of Muons and Delta-Rays

We first applied the two-threshold method to data taken without any external background in order to study the possibility of reconstructing muon hits which are shaded by delta-rays.

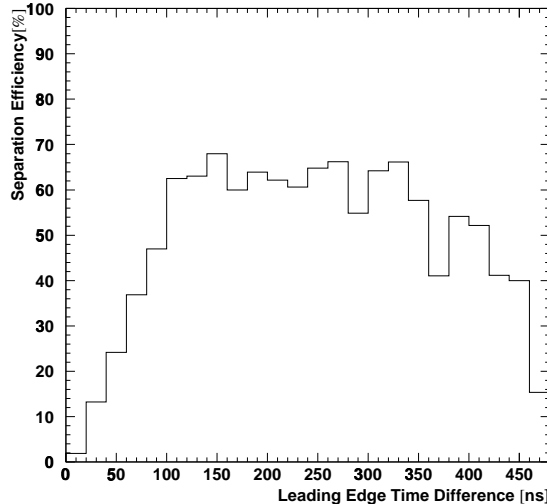


Figure 5.25: Double track separation efficiency for a pure delta-ray background as a function of the leading-edge separation time. The high threshold in this FADC analysis was set to 120 electrons.

In Figure 5.25 the separation efficiency for a high threshold of 120 electrons is plotted as a function of the leading-edge separation time obtained using the silicon telescope information:

$$\Delta t_{\text{leading edge}} = t_{\text{predicted by ODYSSEUS}} - t_{\text{background(low threshold crossing)}} \quad (5.7)$$

As already mentioned above, for  $\Delta t$  smaller than about 100 ns the separation efficiency is bad because in most cases the background pulse has not yet decayed under the high threshold.

The decrease of  $\eta$  at very long separation times can be understood with the following reflection: Delta-rays deposit energy all along their path. To very big  $\Delta t$  only delta-rays with a long range contribute, i.e. only those which have deposited a big amount of energy before being

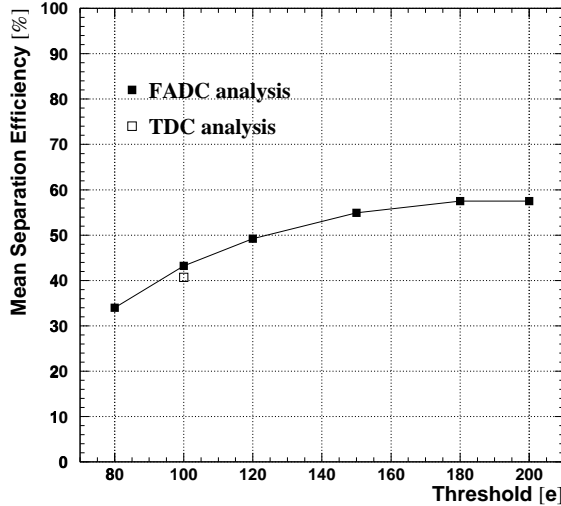


*Figure 5.26: Efficiency for the separation of muons from delta-rays as a function of the high threshold, averaged over all separation times. The low threshold was always at 25 electrons. The solid markers represent the results of the FADC measurements, whereas the open markers have been obtained analyzing the TDC.*

stopped. They produce large and long pulses which often don't decay below the high threshold before the arrival of the muon pulse.

Taking the mean over all  $\Delta t$  for different high thresholds, one obtains the graph in Figure 5.26. If the high threshold is increased, more background pulses decay below the high threshold before the muon pulse arrives, which improves the separation efficiency. Above 180 electrons though, the efficiency levels off as more and more muon signals simply do not reach the second threshold.

### b. Separation of Muons and a Combined Background of Gammas and Delta-Rays

The data for studying the separation of muon and gamma hits were taken with a background rate of 1 kHz/cm. Even at this high gamma background rate about 50 % of the total background is due to delta-rays. Since this intrinsic background is unavoidable in real data, we cannot get a pure gamma background as in simulation [RIE 97a].

In Figure 5.27 the measured and simulated separation efficiency for a high threshold of 120 electrons is plotted as a function of the leading-edge separation time.

Despite the resemblance with the real data, reflecting the qualitatively correct description of the system by the simulation model, a quantitative comparison is difficult, because the conditions were not quite the same:

In the simulation delta-rays are not taken into account. Including them into the model would deteriorate the simulated efficiency, because delta-rays are more difficult to separate than

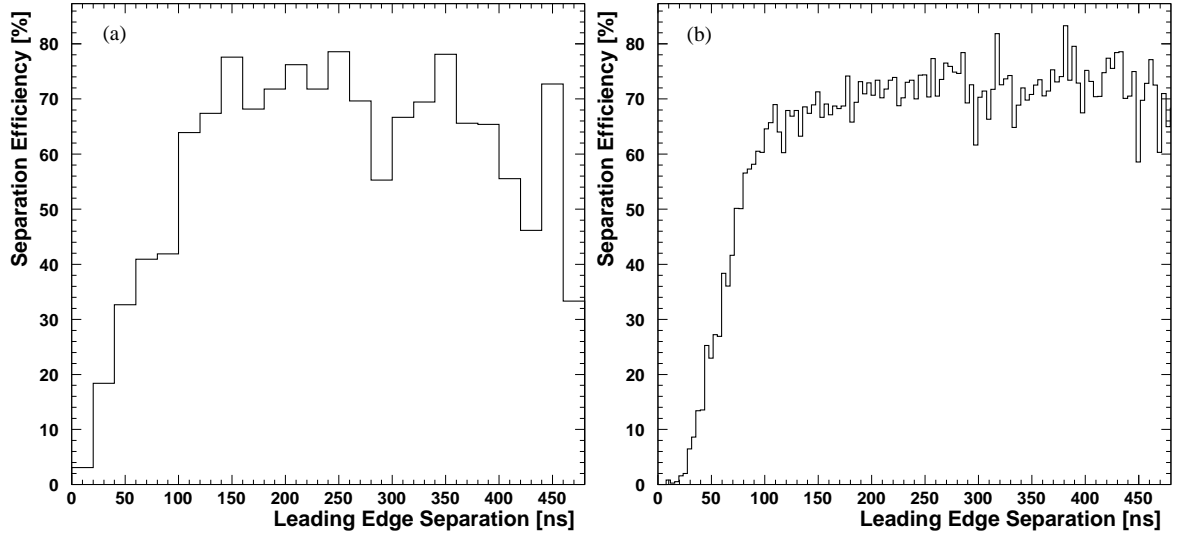


*Figure 5.27: Double track separation efficiency as a function of the leading-edge separation time for a high threshold of 120 electrons. (a) Measurement with external gamma background and intrinsic delta-ray background, (b) simulation with only gamma background [RIE 97a].*

uncorrelated gammas (see a few lines below). The plateau for  $\Delta t > 100$  ns would then be reduced from about 70 % to about 60 % which is lower than the measured level of about 65 %.

The presence of delta-rays in real data explains the deterioration of the separation efficiency for leading-edge separation times greater than 350 ns which is not seen in the simulation neglecting delta-rays.

Figure 5.28 shows the mean separation efficiency as a function of the high threshold. Again the separation efficiency improves with increasing threshold, but only up to about 150 electrons. Above that value hit inefficiencies for the muon pulses at the high threshold become important, leading to a decrease in separation efficiency.

To understand why this effect starts earlier for photons than deltas (cf. Figure 5.26), we have to compare the typical energy deposit of a delta-ray with that of a 662 keV gamma. The 662 keV gammas interact with the chamber gas mainly by Compton scattering. Simulations showed that these Compton electrons deposit on average 36 keV in the tube. The delta-electrons have an average energy of only 60 keV<sup>1</sup> and are therefore strongly ionizing. Their energy is entirely deposited in the tube. Therefore they produce bigger signals than the 662 keV gammas, and muon pulses sitting on the tails of these big delta-ray pulses are more likely to exceed the high threshold than those muon pulses which sit on the smaller tails of gamma pulses.

<sup>1</sup>This value is obtained by integrating the delta-ray energy spectrum  $dN/dE$  [PDG 98] between the following limits: We regard a knock-on electron as a delta-ray if its hit is more than three times the tube resolution off the track, which defines the minimum range of the electron and thus its minimum energy. The maximum delta-ray energy is given by kinematics.

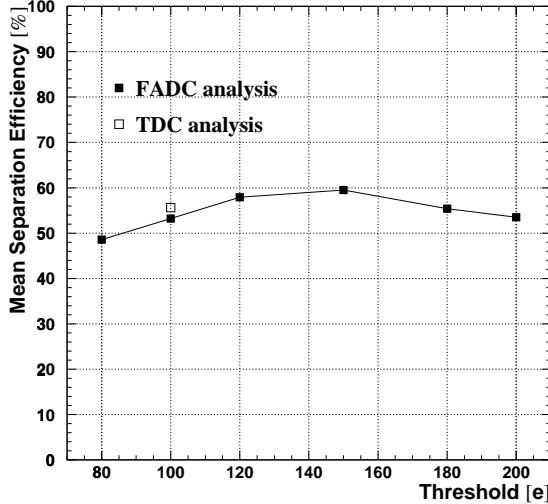


*Figure 5.28: Separation efficiency (muons and 662 keV gammas) as a function of the high threshold. The low threshold was always at 25 electrons. The solid markers represent the results of the FADC measurements, whereas the open markers have been obtained analyzing the TDC's.*

Generally the separation efficiency for delta-ray pulses is lower than for gamma pulses, which can be explained with the strong correlation between a delta-ray and the muon track: Delta-electrons have their origin on the muon track and deposit a big amount of charge already close to the muon track which makes the separation difficult.

### c. Evaluation of Double Track Separation

The results presented above show that in no case more than 65 % of shaded muons can be recovered. This is a rather low yield. Furthermore, to take advantage of all the recorded hit information, pattern recognition has to try all hits at the high threshold and select the “best one”. However, there is also some chance to pick the wrong one which would result in a worse reconstruction efficiency. Another disadvantage is the bad resolution at the high threshold ( $170 \mu\text{m}$ ). In summary, double-track separation turned out not to be very helpful for pattern recognition, which was one reason for the collaboration to renounce the complicated electronics scheme with a second threshold.

### 5.3 Conclusion about the Rate Capability of Drift Tubes

We have demonstrated that MDT's can cope with the expected ATLAS background rates and still fulfil the requirements. However, their behaviour depends on the pulse shaping. Without any baseline restoration in the front-end electronics the baseline is shifted by the equivalent of about  $-9$  electrons at the maximum ATLAS rate and shows fluctuations of the same order of magnitude. The consequence is a time jitter on the leading edges of the signal pulses, which dominates resolution deterioration for linear gases. By introducing big signal undershoots the baseline can be stabilized and the resolution improved.

Resolution is also affected by space charge causing gain drop ( $\rightarrow$  time slewing) and field variations ( $\rightarrow$  fluctuations of the r-t relationship). Simulation showed that the latter effect is dominant for non-linear gas mixtures like Ar/CO<sub>2</sub>. Hence, beside the electronics design, the gas choice has a big impact on the high-rate performance.

The information from a leading-edge charge measurement can be used to correct for time slewing resulting in a resolution around  $80\text{ }\mu\text{m}$  even at the highest rates considered.

As expected the hit efficiency does not suffer significantly from high background rates. The  $3\sigma$ -efficiency however decreases by about 10 % at the maximum rate. This performance degradation is due to gammas shading the muon pulses.

The comparison of measurements and simulations shows a good agreement.

## Chapter 6

# Track Reconstruction with the Maximum Likelihood Method

In the preceding chapters we have given a detailed treatment of the detector-physical aspects of drift tube performance and optimization. It was shown that drift tubes with the chosen working parameters are suited for operation under ATLAS conditions. Now we can pass on to the next stage of preparatory analyses for the ATLAS experiment: the development of techniques for track reconstruction and calibration.

The first issue in this context is a track reconstruction technique which yielded promising results in a test-beam study with a prototype chamber (see also [DEI 98]).

### 6.1 The Least-Squares Track Reconstruction Technique

To reconstruct a muon track through a multilayer of drift tubes, a straight line has to be fitted to the impact circles defined by the threshold-crossing times  $t_i$  of the ionization signals (“drift times”). Traditionally this is done by minimization of

$$\chi^2 = \sum_{i=1}^{N_{\text{hits}}} \frac{[r(t_i) - r_i^{(\text{fit})}]^2}{\sigma_i^2} \quad , \quad (6.1)$$

where  $\sigma_i$  is the resolution of the  $i^{\text{th}}$  tube at the radius  $r_i^{(\text{fit})}$ . The hit radii  $r(t_i)$  are calculated from the r-t relationship and  $r_i^{(\text{fit})}$  is the shortest distance between the reconstructed track  $y = m \cdot z + c$  and the  $i^{\text{th}}$  wire at  $(z_i, y_i)$  (Figure 6.1):

$$r_i^{(\text{fit})} = \frac{|m \cdot z_i + c - y_i|}{\sqrt{1 + m^2}} \quad . \quad (6.2)$$

This approach however is only valid if the drift-time distributions for given radii are Gaussian. The next section will show that this assumption is not always justified.

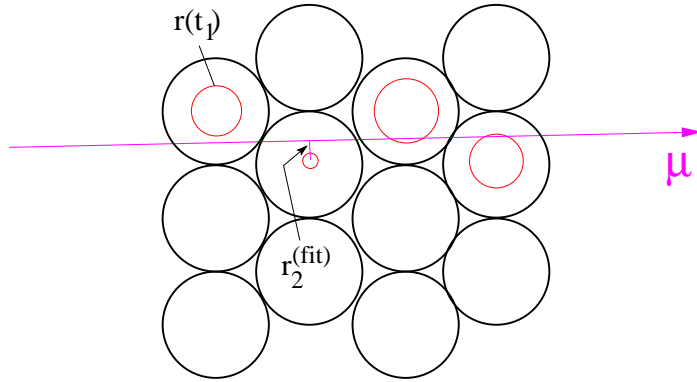


Figure 6.1: Conventional fit of a straight line to the impact circles in a multilayer of drift tubes. The measured drift times are first converted into radii, then the  $\chi^2$  function (6.1) is minimized with respect to the track parameters  $m$  and  $c$ .

## 6.2 Consequences of the Ionization Cluster Statistics

In Section 2.4.1 the ionization charge produced by a muon crossing a tube was explained to be distributed stochastically along the track. This statistical behaviour has consequences for the drift-time distribution at a given distance of a particle track from the anode wire.

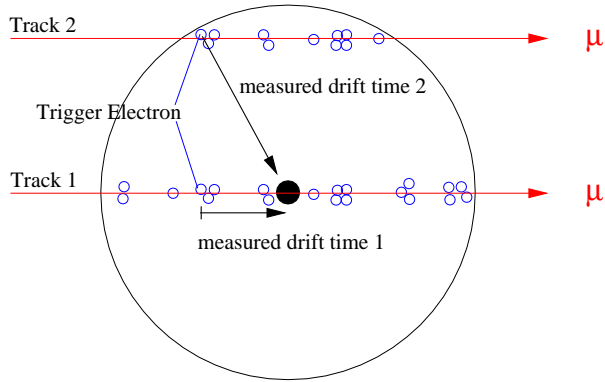


Figure 6.2: Ionization along a track through the anode wire (track 1) and far from the wire (track 2).

As a simple example for the clustering effect let us consider a muon track passing exactly through the anode wire ( $r = 0$ , track 1 in Figure 6.2). Although the track distance to the wire is zero in this case, we will in general measure a non-zero drift time, because we have to wait for a certain number of primary electrons (e.g. 25) before the signal crosses the discriminator threshold. In a rare extreme case we can get a cluster at the wire surface with more than 25 electrons, leading to a zero drift time. On the other hand the cluster containing the 25<sup>th</sup> electron can also be far away from the wire, which is much more frequent for our particular case where the 25<sup>th</sup> electron is most likely to be produced at a distance of about 600  $\mu\text{m}$  from the wire (Figure 6.3a).

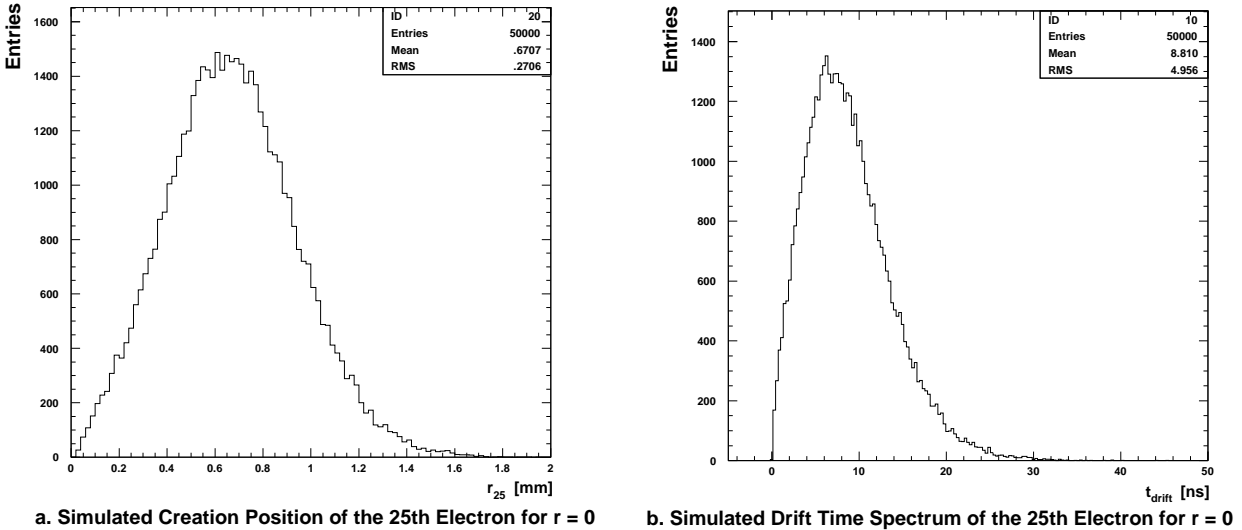


Figure 6.3: Simulation of the clustering effects. For the simulated time spectrum in (b) only the clustering effect is taken into account (no diffusion, noise etc.).

The strong maximum of the cluster size distribution at one electron per cluster yields a long tail in the distribution of the creation position of the 25<sup>th</sup> electron. Passing from this position spectrum (Figure 6.3a) to the corresponding drift-time spectrum (Figure 6.3b) the asymmetry is even enhanced by the high drift velocity near the wire which shifts the peak towards earlier times but does not affect the tail at late times.

The asymmetry is most important for track radii smaller than the typical distance of the 25<sup>th</sup> electron. For tracks further away than about 2 mm the clustering effect becomes less important, because all the electron clusters arrive practically at the same time (Figure 6.2, track 2). Here diffusion dominates the time distribution which becomes Gaussian.

What is the impact of this well-known physical effect on the reconstruction of tracks?

- The first problem arises from the asymmetry of the drift-time distributions for fixed radii near the wire. Conventional methods used to “squeeze” a Gaussian function over the central parts of these distributions. This leads to difficulties in the determination of a Gaussian resolution, which strongly depends on the range around the maximum where the Gaussian is fitted (Section 4.5.2). If this badly defined resolution is then used for a  $3\sigma$  cut, discarding all events in the tails, the reconstruction efficiency will be bad.
- If the track passes closer to the wire than the typical distance of the trigger electron, the mean arrival time of this electron is practically the same as for a track through the wire. In the function  $r(t)$  this shows up as an almost infinite “effective drift velocity”  $v_{\text{eff}} = \frac{dr}{dt}$ . In this domain  $v_{\text{eff}}$  has nothing to do with the drift velocity of the 25<sup>th</sup> electron, because  $r$  is the shortest distance between the track and the wire but no longer the drift distance of the 25<sup>th</sup> electron. The consequence of the almost infinite  $v_{\text{eff}}$  is a very bad sensitivity to the track position.

- Near  $r = 0$  it is not very helpful to define a functional dependence  $t(r)$ . If we take for example the maximum of the measured TDC time distribution at  $r = 0$  as  $t_0$  (and call this “zero drift time”), times  $t < t_0$  have to be artificially set to  $t_0$  in order to avoid non-physical “negative drift times”. By doing so we lose most of the information contained in the measured time.

To avoid these problems, instead of defining a function  $r(t)$  with Gaussian errors we use the full information contained in the time distributions for given  $r$ . For this purpose we measured the shape of the r-t distribution in a test beam using ODYSSEUS, the Silicon microstrip beam telescope, as external reference system. Then we parametrized the conditional probability distribution  $P(t|r)$ <sup>1</sup> for small radial slices.  $P(t|r)$  was used for the construction of a likelihood function. The maximum likelihood method then replaced the usual least  $\chi^2$  method for track fitting. Thus a measured drift time is no longer directly converted into a hit radius. The likelihood fit gets the **time** as an input and yields the track radius, taking correctly into account the tails in the probability distributions.

### 6.3 Experimental Set-up

Our studies are based on data taken in the H8 test beam:

- Spring 1997 test beam with Ar/N<sub>2</sub>/CH<sub>4</sub> (91/4/5): The prototype MDT chamber – a 30 cm long bundle of 16 drift tubes arranged in 4 layers – was placed in the centre of ODYSSEUS (Figure 6.4) where the track prediction accuracy is 5  $\mu\text{m}$  (see Section 3.2). As read-out electronics we used BNL preamplifiers and shapers with a peaking time of 15 ns, Lecroy discriminators with an effective threshold of 25 primary electrons and TMC TDCs [KEK] with a bin width of 781 ps.

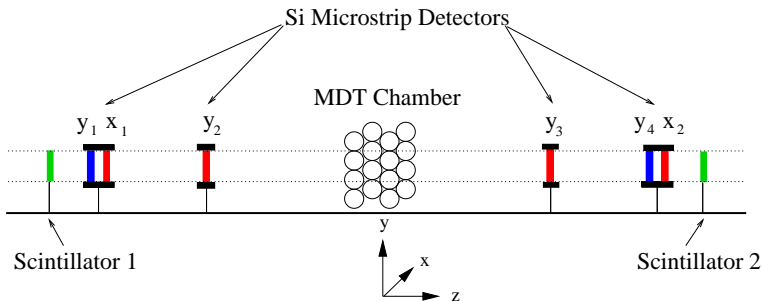


Figure 6.4: Experimental set-up in spring 1997 with Ar/N<sub>2</sub>/CH<sub>4</sub> (91/4/5).

- Autumn 1999 with Ar/CO<sub>2</sub> (93/7): These data have been taken with a BOS prototype. ODYSSEUS was downstream with respect to the chamber (Figure 6.5). The track extrapolation precision at the closest tube was 11  $\mu\text{m}$ . The front-end electronics consisted of BNL preamplifiers, shapers and discriminators; again the standard peaking time of 15 ns

<sup>1</sup> $P(t|r)$  is the probability density for measuring a time  $t$  at a given track radius  $r$ .

and a threshold of 25 primary electrons were applied. KLOE TDCs with 1.042 ns bins served for the hit-time measurement.

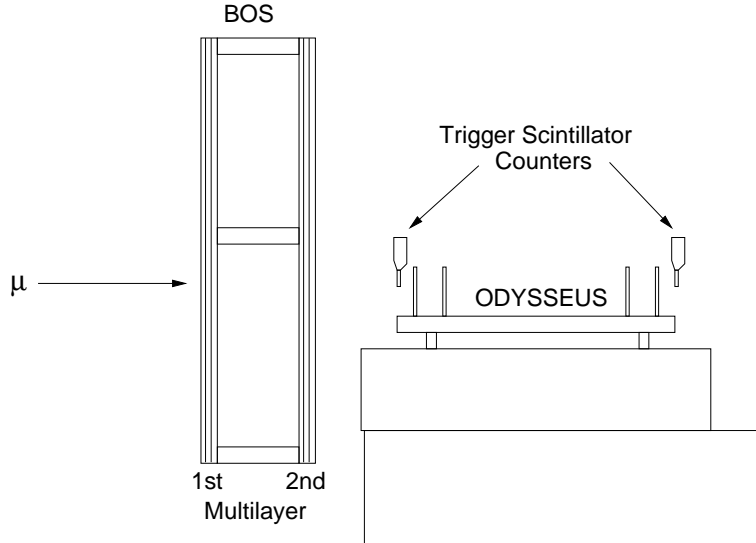


Figure 6.5: Experimental set-up in autumn 1999 with Ar/CO<sub>2</sub> (93/7).

## 6.4 Parametrization of the r-t Relationship

The starting point of our work is an r-t relationship as shown in Figure 6.6. The main band represents the conventional r-t relationship. The entries below the main band are  $\delta$ -rays.

For obtaining the conditional probability distributions  $P(t|r)$  we subdivide the two-dimensional r-t distribution into radial slices, each with a width of 200  $\mu\text{m}$  or smaller. Projection of these slices onto the time axis yields one-dimensional time distributions. However, if we simply projected an entire radial slice, we would not receive a time distribution for a fixed radius but for an interval of radii. This would be the superposition of many individual time distributions which are shifted with respect to each other. The width of such a superposition would be bigger than the width for a fixed radius. We solve this problem by applying the following “centre-of-bin correction”: every measured drift time is shifted to the value which it would have if it were measured at the radius in the centre of the bin:

$$t_{\text{measured}} \mapsto t_{\text{measured}} - t(r_{\text{silicon}}) + t(r_{\text{centre of radial bin}}) \quad (6.3)$$

Theoretically the projected distributions are distorted by another effect: Due to the finite precision of ODYSSEUS’ track prediction some events are attributed to the wrong radial slice. However, the width of the slices is at least 10  $\sigma$  of ODYSSEUS’ resolution, so the contamination from neighbouring bins is negligible.

Figure 6.7a shows an example distribution near the wire. It is very asymmetric. For comparison we also show a distribution for  $r = 5.375$  mm which is rather Gaussian (Figure 6.7b).

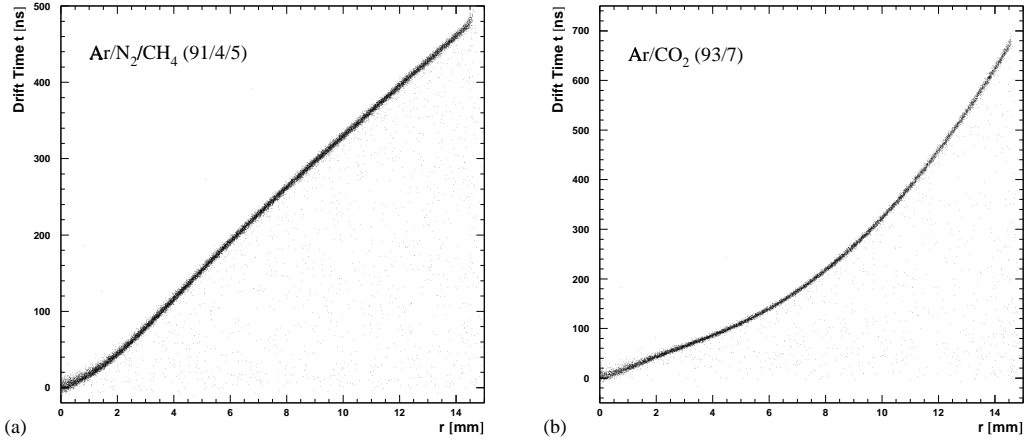


Figure 6.6:  $r$ - $t$  distributions for (a)  $\text{Ar}/\text{N}_2/\text{CH}_4$  (91/4/5), (b)  $\text{Ar}/\text{CO}_2$  (93/7).

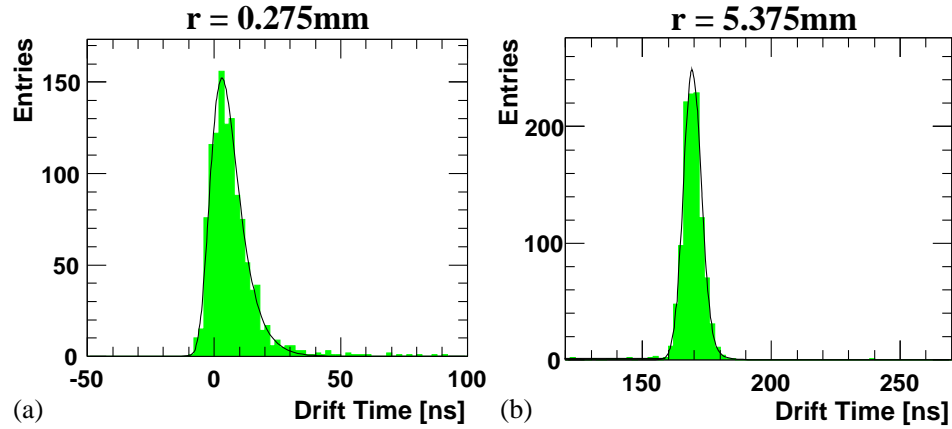


Figure 6.7: Conditional time distributions for  $\text{Ar}/\text{N}_2/\text{CH}_4$  (91/4/5): (a) near the wire, (b) far from the wire. The histograms are the data, the curves are fits of the function (6.5). The left-hand tails are  $\delta$ -rays.

By normalization of the corrected projections we obtain  $P(t|r)$ :

$$\int_{-\infty}^{+\infty} dt P(t|r) = 1 \quad (\text{for all } r \in [0, 15 \text{ mm}]) \quad (6.4)$$

Since the distribution  $P(t|r)$  is by construction well defined for all times  $t$  (including  $t < 0$ ), we no longer introduce a time origin  $t_0 = t(r = 0)$ . Hence the zero of the time scale is arbitrary. We only have to make sure that the time scales are equal for all tubes in a chamber. This can be obtained by fitting Fermi functions to the leading edge of every TDC spectrum [BIS 97, SAM 97].

For track fitting we need a phenomenological parametrization of  $P(t|r)$  which provides a smooth transition from the asymmetric domain at small  $r$  to the Gaussian domain far from the wire. For simplicity and robustness of the fit the number of free parameters should not be too big. Furthermore one would like parameters with an intuitive meaning.

After several attempts we finally found that the following function serves very well:

$$\begin{aligned}
 P(t|r) = & \underbrace{p_1(r) \cdot \frac{1}{p_3(r)} e^{\frac{p_2(r)-t}{p_3(r)} - e^{\frac{p_2(r)-t}{p_3(r)}}}}_{\text{asymmetric part ("Extreme Value Function")}} \\
 + & \underbrace{[1 - p_1(r) - p_4(r) \cdot p_2(r)] \cdot \frac{1}{\sqrt{2\pi} p_3(r)} e^{-\frac{[t-p_2(r)]^2}{2[p_3(r)]^2}}}_{\text{Gaussian part}} \\
 + & \underbrace{p_4(r) \cdot \Theta(p_2(r) - t) \cdot \Theta(t)}_{\delta\text{-ray part}}
 \end{aligned} \tag{6.5}$$

The parameters have the following significance:

$p_1(r)$ : Amount of asymmetric contribution.

$p_2(r)$ : Peak position (corresponding to the conventional  $t(r)$  function).

It is not the mean of the distribution!

$p_3(r)$ : Quantity characterizing the width of the distribution (time resolution).

It is close to, but not equal to the rms!

$p_4(r)$ :  $\delta$ -ray probability density. It is a flat box in time from 0 to the peak  $p_2(r)$ .

Figure 6.7 shows that our parametrization fits the data very well. From these fits we get the parameters  $p_1$ ,  $p_2$ ,  $p_3$  and  $p_4$  for every track radius  $r$ . Their radial variations are given in Figure 6.8 for Ar/N<sub>2</sub>/CH<sub>4</sub> (91/4/5) and in Figure 6.9 for Ar/CO<sub>2</sub> (93/7). The solid lines represent parametrizations of the radial dependences:

$$p_1(r) = f_0 e^{-f_1 r} \tag{6.6}$$

$$p_2(r) = \sum_{i=0}^7 a_i P_i(u) \tag{6.7}$$

$$p_3(r) = s_0 e^{-s_1 r} + s_2 + s_3 r + s_4 r^2 + e^{\frac{r-s_5}{s_6}} \tag{6.8}$$

$$p_4(r) = \sum_{i=0}^5 d_i P_i(u) \tag{6.9}$$

The fitted constants  $f_i$ ,  $a_i$ ,  $s_i$  and  $d_i$  are compiled in Table 6.1.

The parameters  $p_2$  and  $p_4$  involve Legendre polynomials  $P_i(u)$  with  $u \equiv 2 \cdot \frac{r}{r_{\text{tube}}} - 1$ . Compared to ordinary polynomials they have the advantage that due to their orthogonality the stability of the fit result is improved.

As expected, the asymmetry is big near the wire and decreases towards the wall. The qualitative behaviour is the same for both gases studied.

In the parametrization of the width  $p_3(r)$ , the first exponential deals with the poor resolution near the wire, the second with the deterioration in the last 100  $\mu\text{m}$  near the wall where the

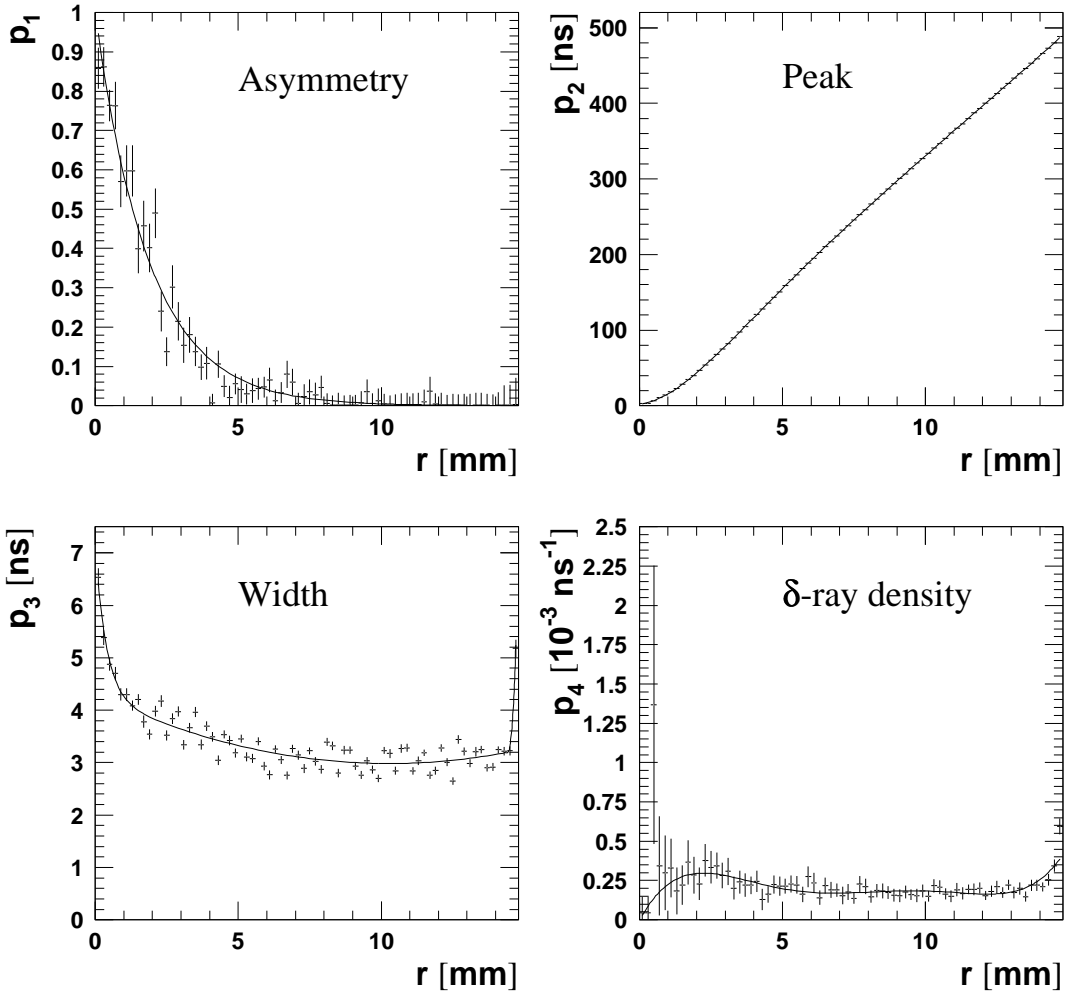


Figure 6.8: Parameters of  $P(t|r)$  as a function of  $r$  for  $\text{Ar}/\text{N}_2/\text{CH}_4$  (91/4/5). The points are the results of fitting function (6.5) for each radial slice. The curves are the fitted functions (6.6 - 6.9). For this plot the radial bin width was  $200 \mu\text{m}$ .

short track length inside the gas volume leads to big charge fluctuations which deteriorate the resolution. Multiplying  $p_3(r)$  with the drift velocity  $v(r) = \left(\frac{dp_2}{dr}\right)^{-1}$  yields approximately the spatial resolution as we know it from Figure 4.13. This relation is not exact because  $p_3(r)$  is not a Gaussian standard deviation, not even the rms.

The  $\delta$ -ray probability density has no strong variation with  $r$ . We see a slight increase within the last millimeter from the wall which is due to the increasing portion of the track inside the Aluminium wall where  $\delta$ -ray production is much more important than in the gas volume.

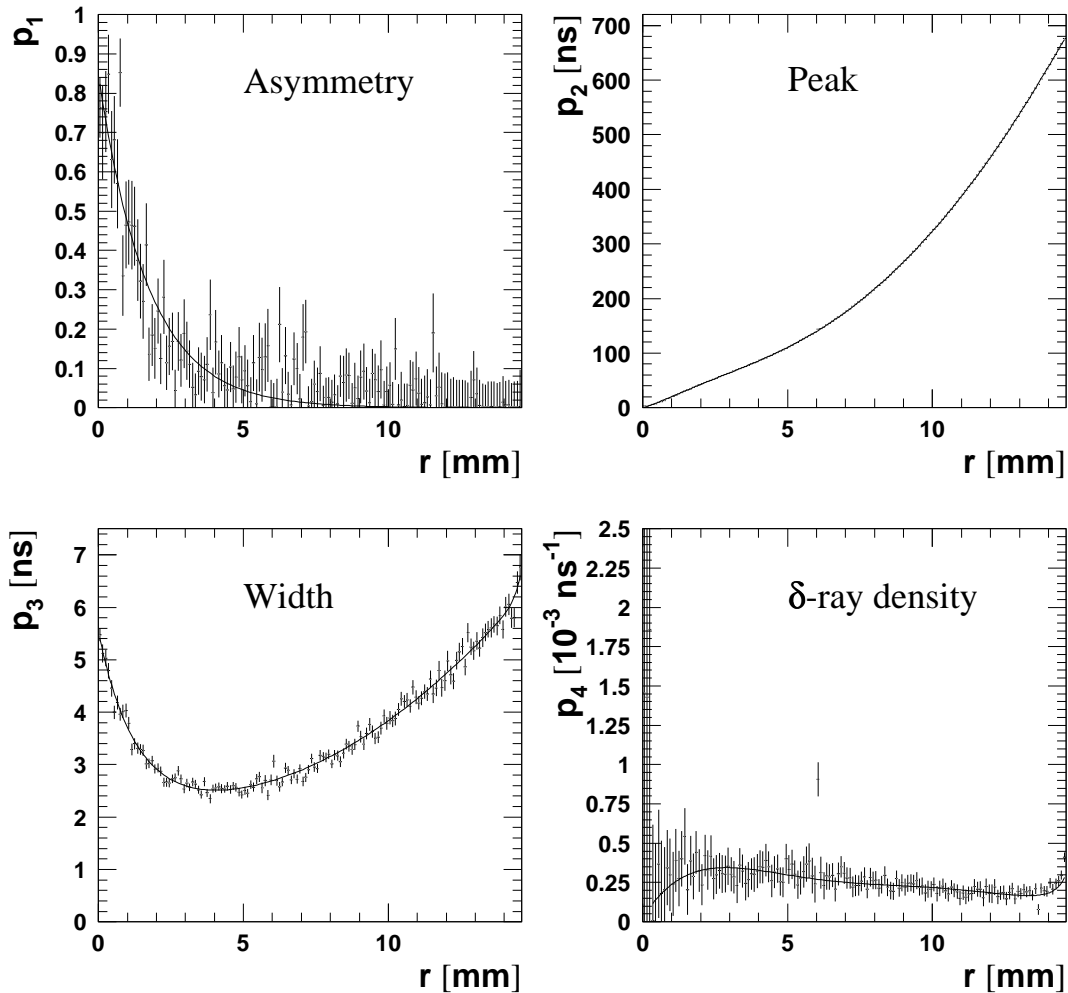


Figure 6.9: Parameters of  $P(t|r)$  as a function of  $r$  for Ar/CO<sub>2</sub> (93/7). For this plot the radial bin width was 100  $\mu$ m.

Approaching  $r = 0$ , the time interval  $[0, p_2(r)]$  where  $\delta$ -ray entries are possible, becomes more and more narrow. Therefore it is difficult to determine the  $\delta$ -ray density in this domain, which explains the huge error bars.

Param.	Gas	Values
$f_i$	I	0.9989 0.5321
	II	0.8480 0.5879
$a_i$	I	237.1 255.4 -2.512 -7.496 9.269 -4.538 1.517 0.2329
	II	241.7 322.6 -103.3 18.42 -6.560 0.3810 1.007 -1.451
$s_i$	I	2.805 2.516 4.286 -0.2538 0.01235 14.65 0.07108
	II	3.041 0.8311 2.485 -0.1250 0.02603 14.72 0.2000
$d_i$	I	0.2052e-3 -0.8766e-5 0.3500e-4 0.1027e-3 -0.4369e-4 0.1092e-3
	II	0.2686e-3 -0.6065e-4 -0.4431e-4 0.1541e-3 -0.3894e-4 0.9484e-4

Table 6.1: Fit constants for the radial parametrizations (6.6 - 6.9). Gas I is Ar/N<sub>2</sub>/CH<sub>4</sub> (91/4/5), gas II is Ar/CO<sub>2</sub> (93/7). The  $f_i$  are dimensionless. The units of the other components are such that  $p_2$  and  $p_3$  are in ns,  $p_4$  in ns<sup>-1</sup>.

### A very Close Look: Tracks through the Avalanche Region

Let us now focus on the peak positions  $p_2(r)$  for very small  $r$ . In the first 200 μm the “r-t relationship” exhibits a peculiarity (Figure 6.10a): approaching  $r = 0$  the most probable drift time rises again. This has nothing to do with an apparent negative drift velocity, but can be understood by considering the avalanche amplification process. Drift electrons created inside the multiplication zone have a shorter path in this zone, and less generations of secondary ionization are produced. Electrons created inside the wire are not multiplied at all. The consequence is that the earliest arriving electrons experience a lower charge amplification. Thus the charge required for exceeding the threshold is achieved for a later primary electron than the nominal one, and the measured time is delayed.

To verify our interpretation of the observed effect, a simulation based on a simple model for the gain reduction was performed:

- For a given radius 50000 tracks were generated.
- Along every track the ionization was modelled using the cluster distance and cluster size distributions as described in Section 2.4.1.
- Every primary electron was amplified according to two different models:
  - The first model assumed a constant gain of  $2 \times 10^4$ .
  - In the second model the gain depended on the creation radius of the primary electron: With Diethorn’s approximation that the Townsend coefficient is proportional to the electric field [DIE 56], the gas gain for an electron created at a radius  $r$  is given by

$$\ln G(r) = \begin{cases} \frac{U \ln 2}{\Delta \Phi} \cdot \frac{\ln \frac{r_{\text{limit}}}{r}}{\ln \frac{b}{a}} & \text{for } r > r_{\text{limit}}, \text{ i.e. outside the avalanche zone} \\ \frac{U \ln 2}{\Delta \Phi} \cdot \frac{\ln \frac{a}{r}}{\ln \frac{b}{a}} & \text{for } r < r_{\text{limit}}, \text{ i.e. inside the avalanche zone} \end{cases} \quad (6.10)$$

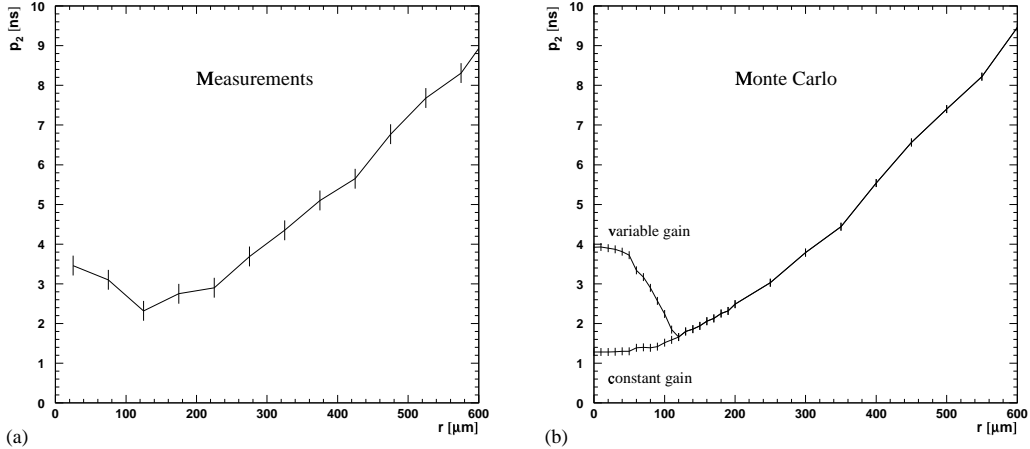


Figure 6.10: Most probable drift time  $p_2(r)$  for very small  $r$ : (a) measurement with Ar/N<sub>2</sub>/CH<sub>4</sub> (91/4/5); the effect was also observed for Ar/CO<sub>2</sub> (93/7); (b) simulation based on a simple model. Since the knowledge about the electron drift velocity near the wire is very unprecise, the simulation can only be in qualitative agreement.

where the Diethorn parameter  $\Delta\Phi$  is the potential difference needed to produce one electron-ion pair. The outer boundary of the avalanche zone  $r_{\text{limit}}$  is determined by the second Diethorn parameter  $E_{\text{min}}$ , i.e. the minimal electric field needed for multiplication:

$$r_{\text{limit}} = \frac{V}{E_{\text{min}} \ln \frac{b}{a}} . \quad (6.11)$$

For Ar/N<sub>2</sub>/CH<sub>4</sub> (91/4/5) the parameters have the values [DEI 96a]:  
 $\Delta\Phi = 55$  V;  $E_{\text{min}} = 45$  kV/cm;  $r_{\text{limit}} = 115$   $\mu\text{m}$ .

- For every primary electron the arrival time at the wire was calculated using an r-t relationship which was modelled to match the measured time distributions for radii greater than 0.5 mm. This model was used since it is impossible to determine the drift time for single electrons from the data. They only give us the threshold-crossing time which is the result of many different smearing effects (clustering, diffusion, noise etc.). Simulations of the single electron drift time on the other hand are far too unprecise near the wire.
- The primary electrons were sorted by the arrival times of their avalanches.
- The charges of the consecutive avalanches were summed up until the threshold charge ( $25\text{ e} \times 2 \times 10^4$ ) was exceeded. The arrival time of the triggering avalanche was recorded as the measured “drift time”.
- The resulting drift-time distributions for both gain models were fitted with the parametrization (6.5) and the parameter  $p_2$  plotted as a function of  $r$  (Figure 6.10b).

Since our model is oversimplified (e.g. no shaping was included) and suffers from lacking knowledge about the actual electron drift velocity, we do not expect a good quantitative agreement with the data. However, the position of the drift time minimum at about  $120\text{ }\mu\text{m}$  is rendered quite well, which demonstrates a good qualitative understanding of the physical effect.

After this digression to the effects very close to the wire we come back to our actual topic: reconstructing tracks through a multilayer of tubes.

## 6.5 The Maximum Likelihood Tracking Method

### 6.5.1 Principle

So far we have explained how to derive the conditional probability distribution  $P(t|r)$  from a measured r-t relationship. In this chapter we will show how this knowledge about the tube response is used for the reconstruction of muon tracks. We will concentrate on the case of a chamber with four layers of tubes as it was available in the spring 1997 test beam.

For this study we only accept so-called “golden events”, i.e. events with exactly one hit in each of the four layers of tubes. Thus every accepted event provides a quadruple  $\{t_1, t_2, t_3, t_4\}$  of drift times.

The principle of track fitting with the maximum likelihood method is the following:

**Maximize the likelihood of the observation  $\{t_1, t_2, t_3, t_4\}$  by varying offset  $c$  and slope  $m$  of the track  $y = mz + c$ .**

The likelihood function  $L$  that has to be maximized is given by the product of the conditional time distributions for the tubes through which the track passes:

$$L = \prod_{i=1}^4 P(t_i|r_i(m, c)) , \quad (6.12)$$

where  $r_i(m, c)$  is the distance between the wire  $i$  and the track  $y = mz + c$ . To avoid correlations between  $m$  and  $c$ , the origin  $z = 0$  has been chosen in the center of the chamber.

### 6.5.2 Technical Procedure

To assure convergence of the likelihood fit we have to provide start values for the fit parameters, i.e. the track offset  $c$  and the slope  $m$ . For this purpose we applied a simple pattern recognition:

The principle is to guess on the hit radii in two out of the four hits by applying a linear function  $r(t) = v_0 t$  (with  $v_0 \approx 30\mu\text{m/ns}$  for Ar/N<sub>2</sub>/CH<sub>4</sub> (91/4/5)) to the measured drift times. These two hit radii leave a four-fold ambiguity about the track candidates (Figure 6.11). Therefore each of the four sets of initial values  $(m_0, c_0)$  is used as a starting point for the maximization of  $L$  (or minimization of  $-\ln L$  as is done in practice).

We have not yet said how many and which pairs of hits we have to test in order to find the most suitable set of initial tracks. The problem is that any of the four hits can belong to a  $\delta$ -ray and have a far too small drift time. The flat  $\delta$ -ray term in the parametrization (6.5) has the

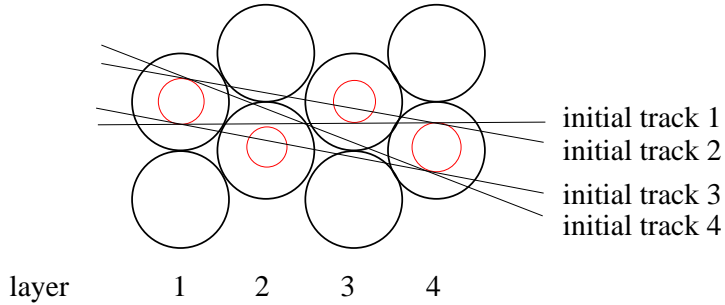


Figure 6.11: The four initial tracks constructed from the hit circles in the first and fourth layer.

effect that hits resulting from  $\delta$ -rays are automatically given the correct statistical weights. No cuts are needed. However, this works only if the initial track is close enough to the true track, such that for the  $\delta$ -ray hit the probability  $P(t|r(m_{\text{initial}}, c_{\text{initial}}))$  is in the low flat  $\delta$ -ray part of the distribution.

With only one  $\delta$ -ray hit the remaining three hits can uniquely determine the track. To guarantee that one of the tested initial tracks is sufficiently close to the true one, we try the four sets of parameters  $(m_0, c_0)$  for each of the following three pairs of tubes: (1, 4), (1, 3), (2, 4). Thus there are  $3 \times 4 = 12$  initial tracks which are optimized by the maximum likelihood fits. Out of the resulting 12 track candidates the one with the least  $-\ln L$  is selected as the real track. Usually this selection is very unambiguous because the likelihood of the second best track is worse by several orders of magnitude.

If two or more hits out of four are caused by  $\delta$ -rays, we have no reliable criterion to distinguish the good hits from the bad ones, because there are usually several possible track candidates with two hits having too small drift times. Therefore with our geometry of only one multilayer these tracks are lost. However, only about 0.3 % of the tracks have more than one  $\delta$ -ray.

Note that the described mechanism for recognizing  $\delta$ -rays does not work with only three layers of tubes. In this case pattern recognition has to use the combined information of both multilayers of a chamber.

## 6.6 Improvements with Respect to Least-Squares Tracking

We now want to judge the quality of our tracking method and compare it with conventional  $\chi^2$  track fitting based on a functional r-t relationship.

After reconstructing a track as described in the previous section, a second track fit is done by  $\chi^2$  minimization as explained in Section 6.1.

Both MDT tracks (from likelihood and  $\chi^2$  method) are compared with the reference track given by the silicon telescope. To quantify the deviations from the reference track we introduce two criteria:

- Offset difference:  $\Delta c = c_{\text{MDT track}} - c_{\text{Sili track}}$
- Slope difference:  $\Delta m = m_{\text{MDT track}} - m_{\text{Sili track}}$

Since improvements are mostly expected near the wires, we distinguish two classes of tracks:

**Class 1:** Tracks with all radii  $r^{(i)} > 2 \text{ mm}$ .

**Class 2:** Tracks with at least one radius  $r^{(i)} < 2 \text{ mm}$ .

In Figure 6.12 the offset difference  $\Delta c$  is plotted versus the reference offset  $c_{\text{Sili track}}$ , in Figure 6.13 the slope difference  $\Delta m$  versus  $c_{\text{Sili track}}$ .

The inefficient zones (gaps) at certain  $c_{\text{Sili track}}$  correspond to tracks passing inside the tube wall in one layer ( $14.6 \text{ mm} \leq r \leq 15 \text{ mm}$ ). These tracks don't fulfill our "golden event" requirement.

For the parts (a) of both figures the tracks were reconstructed by normal  $\chi^2$  minimization without applying any cuts against  $\delta$ -rays which form the diffuse background above and below the main band. The maximum likelihood method (lowest plot (c)) automatically incorporates a correct treatment of tracks with  $\delta$ -rays which now have their entries mostly in the main band. However, this is not the effect we are most interested in, because one can also introduce a pattern recognition improvement to the  $\chi^2$  tracking in order to recover tracks with  $\delta$ -rays. More important for our study are the difficulties that least-squares tracking has with Class 2 tracks: there are steps (evidence for biases) and tails in the band pattern of the upper plots (a) whereas they are strongly reduced in the lower plots (c).

For a fair comparison between  $\chi^2$  and likelihood tracking we have to isolate the biases for Class 2 tracks. This is done by including a  $\delta$ -ray correction into the  $\chi^2$  method: Whenever the modulus of a fit residual  $r_{\text{MDT hit}}^{(i)} - r_{\text{MDT track}}^{(i)}$  in any of the hits is greater than two times the standard deviation of the residual distribution, the fit is repeated with all combinations of three hits out of four. As the middle plots (b) in Figures 6.12 and 6.13 demonstrate, in most cases  $\chi^2$  is smallest for the hit combination which omits the  $\delta$ -ray hit, i.e. the tracks are recovered. Despite this improvement the faults near the wires (Class 2 tracks) are not mended.

A quantitative evaluation of  $\chi^2$  and likelihood tracking is obtained by projecting the two-dimensional histograms in Figures 6.12 and 6.13 on the  $\Delta c$  and  $\Delta m$  axis respectively. This is done separately for Class 1 and 2. Figures 6.14 and 6.15 show the result for  $\Delta c$  and  $\Delta m$  respectively.

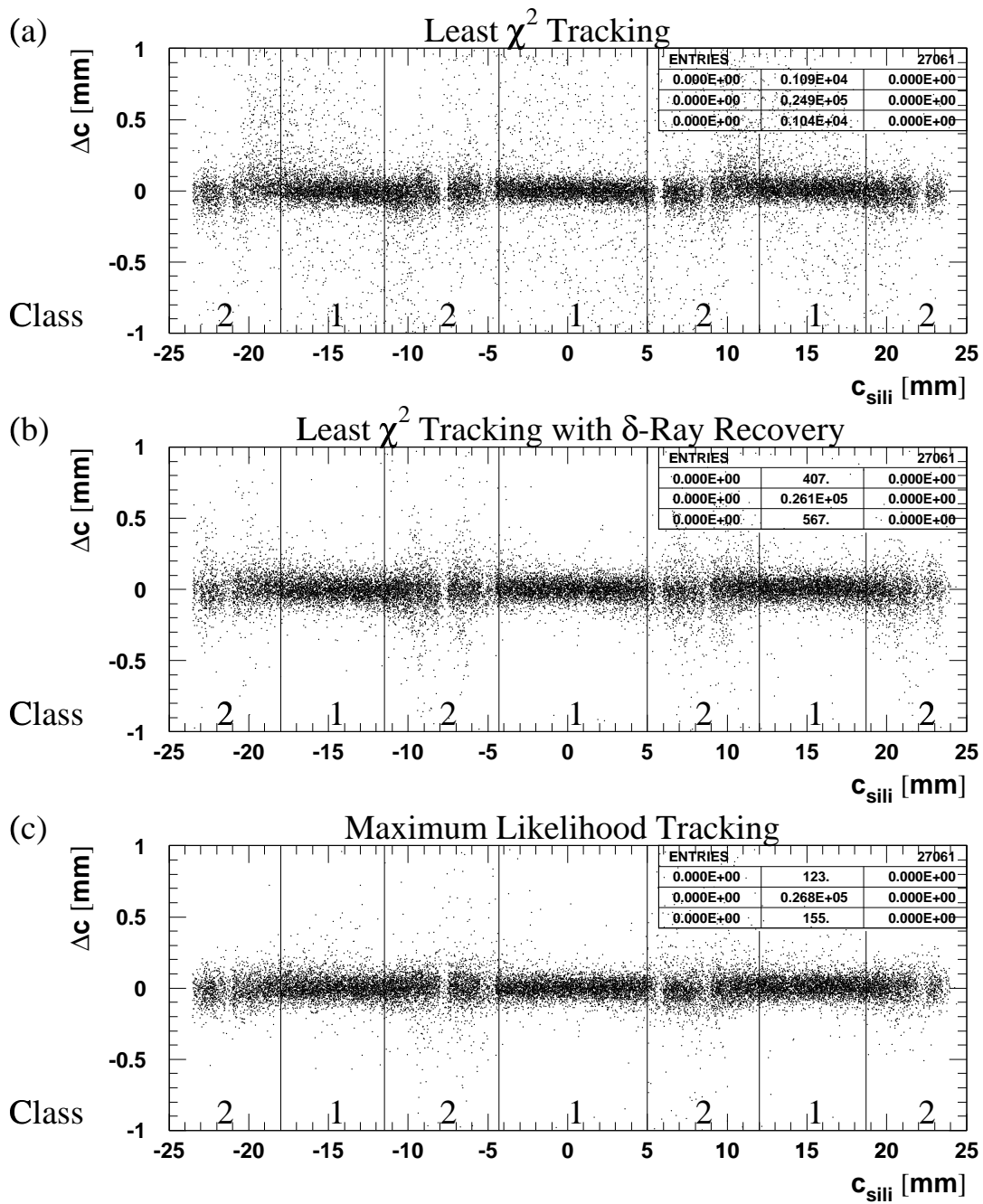


Figure 6.12: Offset difference  $\Delta c$  versus the reference offset  $c_{\text{sili}}$  track. The vertical lines delimit the two classes.

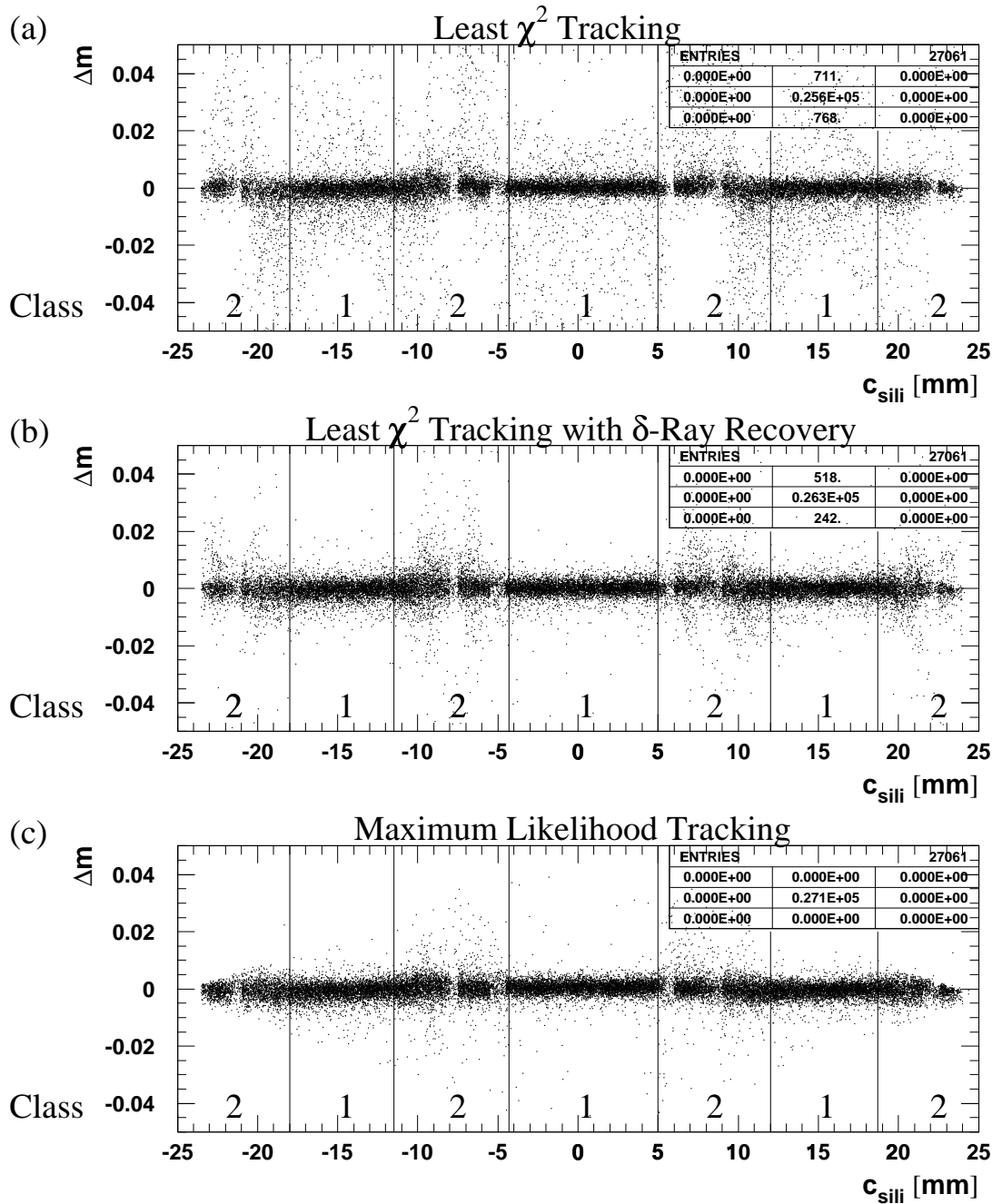


Figure 6.13: Slope difference  $\Delta m$  versus the reference offset  $c_{\text{Sili}}$  track. The vertical lines delimit the two classes.

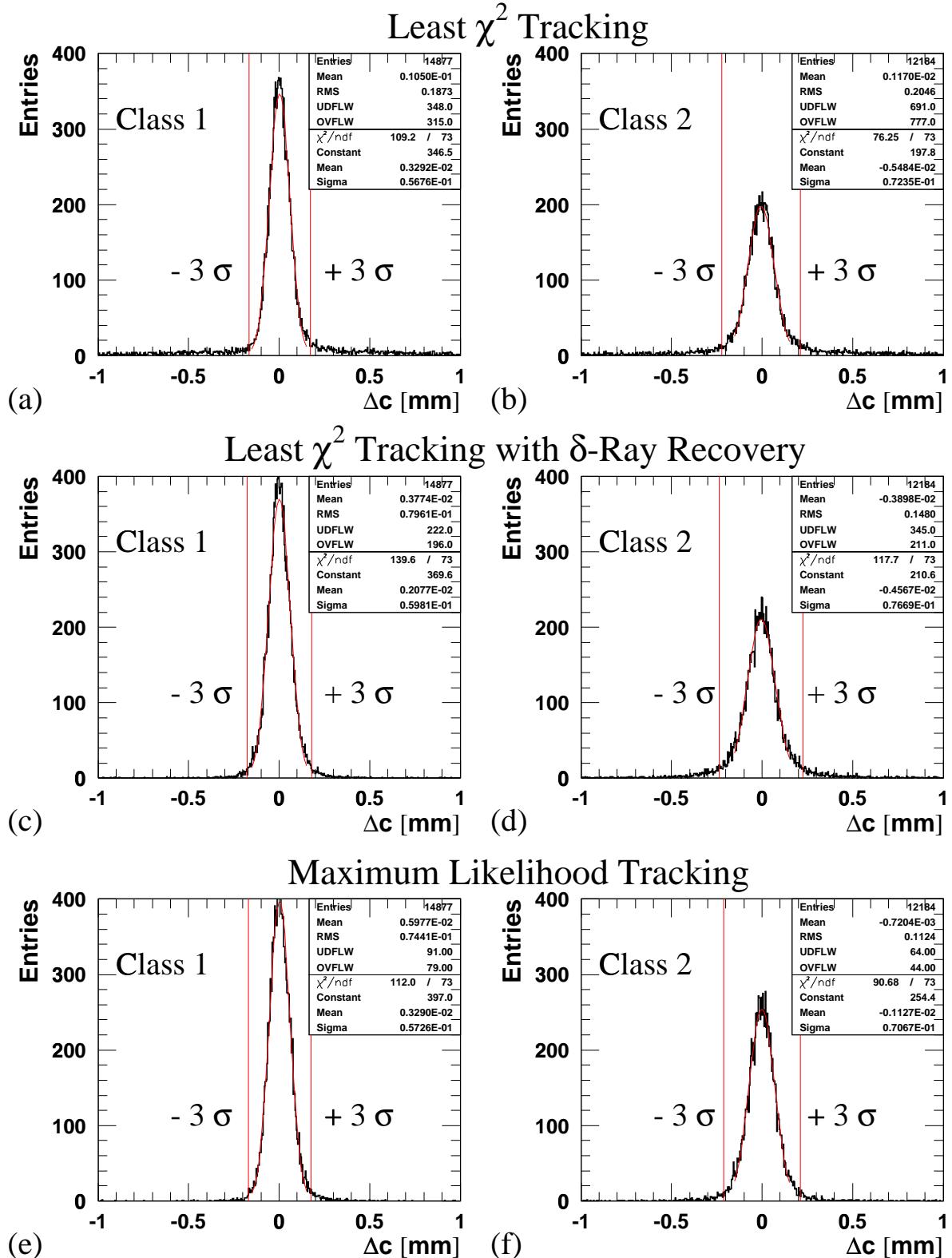


Figure 6.14: Projection of Figure 6.12 on the  $\Delta c$  axis for Class 1 (distributions (a), (c), (e)) and Class 2 (distributions (b), (d), (f)).

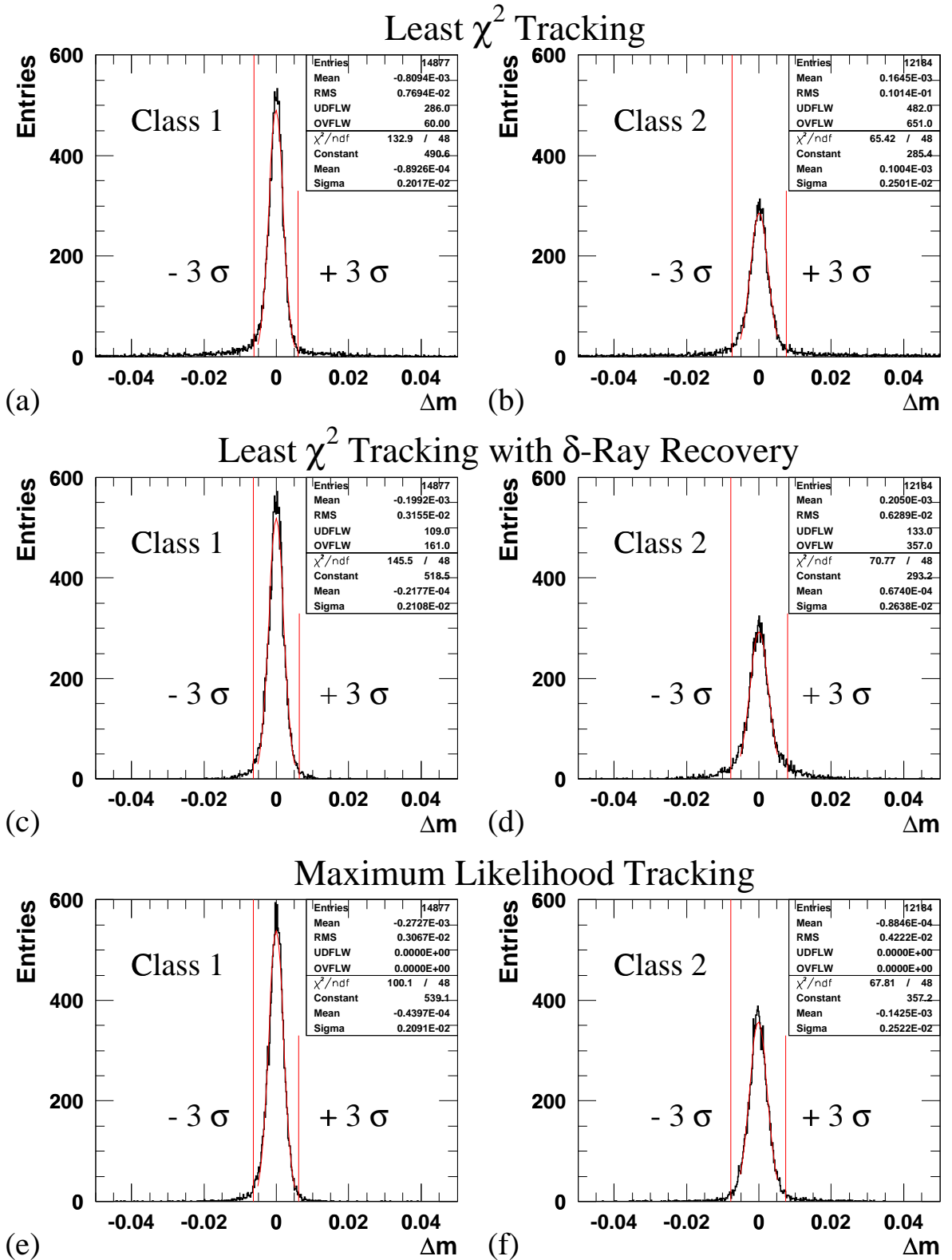


Figure 6.15: Projection of Figure 6.13 on the  $\Delta m$  axis for Class 1 (distributions (a), (c), (e)) and Class 2 (distributions (b), (d), (f)).

A numerical summary about the projected distributions can be found in Tables 6.2 and 6.3. To characterize the widths of the  $\Delta c$  and  $\Delta m$  distributions we give the rms and the  $\sigma$  of a Gauss curve fitted to the central part ( $\pm 3\sigma$ ) of the distributions. The tails are quantified by the  $3\sigma$ -efficiency  $\eta_{3\sigma}$  with

$$\eta_{3\sigma} = \frac{\text{number of entries within } 3\sigma \text{ around the peak}}{\text{total number of entries}} . \quad (6.13)$$

Criterion	Method	$\Delta c$ distribution	$\Delta m$ distribution
rms	$\chi^2$ fit	187.3 $\mu\text{m}$	7.69 mrad
	$\chi^2$ fit with $\delta$ -ray recovery	79.6 $\mu\text{m}$	3.16 mrad
	ML fit	74.4 $\mu\text{m}$	3.07 mrad
$\sigma$	$\chi^2$ fit	(56.8 $\pm$ 0.5) $\mu\text{m}$	(2.02 $\pm$ 0.02) mrad
	$\chi^2$ fit with $\delta$ -ray recovery	(59.8 $\pm$ 0.5) $\mu\text{m}$	(2.11 $\pm$ 0.02) mrad
	ML fit	(57.3 $\pm$ 0.4) $\mu\text{m}$	(2.09 $\pm$ 0.02) mrad
$\eta_{3\sigma}$	$\chi^2$ fit	84.1 %	85.4 %
	$\chi^2$ fit with $\delta$ -ray recovery	94.6 %	94.5 %
	ML fit	96.7 %	96.9 %

Table 6.2: Numerical comparison of the three tracking methods for Class 1 tracks.

Criterion	Method	$\Delta c$ distribution	$\Delta m$ distribution
rms	$\chi^2$ fit	204.6 $\mu\text{m}$	10.14 mrad
	$\chi^2$ fit with $\delta$ -ray recovery	148.0 $\mu\text{m}$	6.29 mrad
	ML fit	112.4 $\mu\text{m}$	4.22 mrad
$\sigma$	$\chi^2$ fit	(72.4 $\pm$ 0.8) $\mu\text{m}$	(2.50 $\pm$ 0.03) mrad
	$\chi^2$ fit with $\delta$ -ray recovery	(76.7 $\pm$ 0.9) $\mu\text{m}$	(2.64 $\pm$ 0.03) mrad
	ML fit	(70.7 $\pm$ 0.7) $\mu\text{m}$	(2.52 $\pm$ 0.03) mrad
$\eta_{3\sigma}$	$\chi^2$ fit	76.9 %	76.8 %
	$\chi^2$ fit with $\delta$ -ray recovery	87.9 %	85.4 %
	ML fit	95.1 %	95.5 %

Table 6.3: Numerical comparison of the three tracking methods for Class 2 tracks.

As expected, for Class 1 (far from all wires) the only significant effect is the reduction of  $\delta$ -ray background passing from normal least-squares tracking to least-squares tracking with  $\delta$ -ray recovery. This is visible in the rms as well as in  $\eta_{3\sigma}$ . Switching from this improved least-squares tracking to maximum-likelihood tracking doesn't yield any further improvements. The Gaussian width of the central peak is comparable for all tracking methods, apart from a small deterioration caused by the  $\delta$ -ray recovery in the  $\chi^2$  method. That procedure shifts events into the peak that have been in the tails before; but these recovered tracks are fitted using only three hits which gives a worse precision.

For Class 2 the Gaussian peak width behaves in a similar way as for Class 1. However, the tails are not only reduced by switching on the  $\delta$ -ray correction in the least-squares tracking, but

also considerably from the improved least-squares tracking to maximum-likelihood tracking: the  $3\sigma$  inefficiency  $1 - \eta_{3\sigma}$  is reduced by a factor 0.4 in the case of  $\Delta c$  and by a factor 0.3 if  $\Delta m$  is considered.

## 6.7 Conclusions about Maximum Likelihood Tracking

Track fitting with the maximum likelihood method naturally incorporates a correct treatment of the non-gaussian errors of the r-t relationship near the wire.

We have shown that compared with least squares fitting the tails are reduced. The effect is particularly important for tracks passing near a wire where the  $3\sigma$ -inefficiencies for maximum-likelihood fits are only 0.3 to 0.4 times the ones for least-squares fits with  $\delta$ -ray correction based on cuts. The maximum likelihood method can handle  $\delta$ -rays without applying any cuts. However, it needs good start values for the track parameters, which requires an efficient pattern recognition.

Since maximum likelihood tracking doesn't need a functional  $t(r)$ - or  $r(t)$ -dependence, no absolute  $t_0$  needs to be introduced and "negative drift times" no longer occur.

For describing the r-t relationship the new method requires two additional parameters, one characterizing the asymmetry of the time distribution for a given track radius, the other one specifying the  $\delta$ -ray probability per unit drift time. Our parametrization of the two-dimensional r-t distribution represents the full knowledge about the response of drift tubes.

So far we have only considered track reconstruction in a single multilayer of tubes. This is a particularly unfavourable situation because pattern recognition and the precision fit rely fully on only four hits. A track fit through a whole chamber, i.e. a superlayer of tubes, or even through the entire ATLAS detector might take advantage from the correlated information from all multilayers. In the next chapter we will investigate whether the non-Gaussian tails in the response function near the wire have any significant impact on momentum resolution and tracking efficiency of the ATLAS muon spectrometer.

# Chapter 7

# Simulation of the Tracking Performance of the ATLAS Muon Spectrometer

This chapter discusses momentum resolution and tracking efficiency of the ATLAS Muon spectrometer and their dependence on the description of the single-tube response. In particular we want to investigate the influence of non-Gaussian drift-time resolution. After an introduction to the simulation tools (Section 7.1) we explain the descriptions of the MDT response for which the performance was tested (Section 7.2). Finally a comparison of momentum resolution, reconstruction efficiency and fake-track probability for the different response descriptions is made (Sections 7.3 and 7.4).

## 7.1 The Simulation Chain

The full chain of the simulation software consists of the following steps:

- Generation of single muons at the ATLAS vertex. For each of the transverse momenta  $10 \text{ GeV}/c$ ,  $30 \text{ GeV}/c$ ,  $100 \text{ GeV}/c$ ,  $300 \text{ GeV}/c$  and  $1 \text{ TeV}/c$  a sample of 4000 single muons was generated at the ATLAS vertex with a flat azimuthal distribution  $\Phi \in [0, 2\pi]$  and a flat distribution of pseudorapidity  $\eta$  extending over the whole range  $[0, 2.7]$  which is covered by the muon spectrometer.
- Every muon was traced through the detector with LHCTOR [CHV 97], a program based on GEANT 3 taking into account the full geometry and magnetic field map of ATLAS. In the muon spectrometer LHCTOR determines for every tube hit the impact radius.
- The impact radii were converted into drift times by the programme MUONBOX [VIR 97]. The drift-tube response for this so-called “digitization” was described by different models. Details about these models will follow in the next section.
- The reconstruction of the muon tracks was also done with MUONBOX. The sagittae of the tracks due to the magnetic field served for the determination of the muon momenta at the entrance of the spectrometer.

- The reconstructed momenta were compared with the true momenta.

## 7.2 Description of the MDT Response

For each hit in a drift tube the track radius is converted into a drift time using the r-t relationship and smeared according to the time resolution of a single drift tube. Before our study this model was very crude: It assumed a linear r-t relationship with a maximum drift time of 500 ns and a Gaussian resolution with an average of 80  $\mu\text{m}$  and a radial dependence like the one measured for Ar/N<sub>2</sub>/CH<sub>4</sub> (91/4/5). In order to achieve a more realistic description of the MDT response, the following effects were added to the digitization:

- Instead of a linear approximation the correct r-t relationship of Ar/N<sub>2</sub>/CH<sub>4</sub> (91/4/5) as measured in test beams was implemented. For a later study an option for Ar/CO<sub>2</sub> (93/7) was also added.
- The time resolution is no longer approximated to be Gaussian. The smearing is now based on the exact time distributions which deviate significantly from the Gaussian shape at drift distances smaller than 2 mm (see Chapter 6).
- The description of the Lorentz effect had been wrong and was corrected: In the old version of the code a constant deviation angle for the drifting electrons was assumed. In reality this angle depends on the electric field which is inversely proportional to the distance from the wire. For Ar/N<sub>2</sub>/CH<sub>4</sub> (91/4/5) the new parametrization of this effect was extracted from the results of test-beam measurements [SAM 97]. As Figure 7.1 demonstrates, the old model differs significantly from the measurements. To verify our basic understanding of the Lorentz effect, we calculated the numerical solution to the equation of motion of a drifting electron in crossed electric and magnetic fields with the approximation of continuous friction:

$$m\ddot{\vec{r}} = e\vec{E}(\vec{r}) + e\dot{\vec{r}} \times \vec{B} - \beta(\vec{r})\dot{\vec{r}} \quad (7.1)$$

where the damping constant  $\beta(\vec{r})$  is approximated to be independent of  $\vec{B}$  and determined from  $r(t)$  at  $\vec{B} = \vec{0}$ . In reality the drift process is much more complicated [BLU 93], but Figure 7.1 shows a fairly good agreement between measurements and calculation up to 0.8 T.

Since for Ar/CO<sub>2</sub> (93/7) no test-beam data with magnetic field were available, the B-field response was simulated with Garfield. It is shown in Figure 7.2.

To study the influence of the individual features of the drift-tube response, they could be separately switched on.

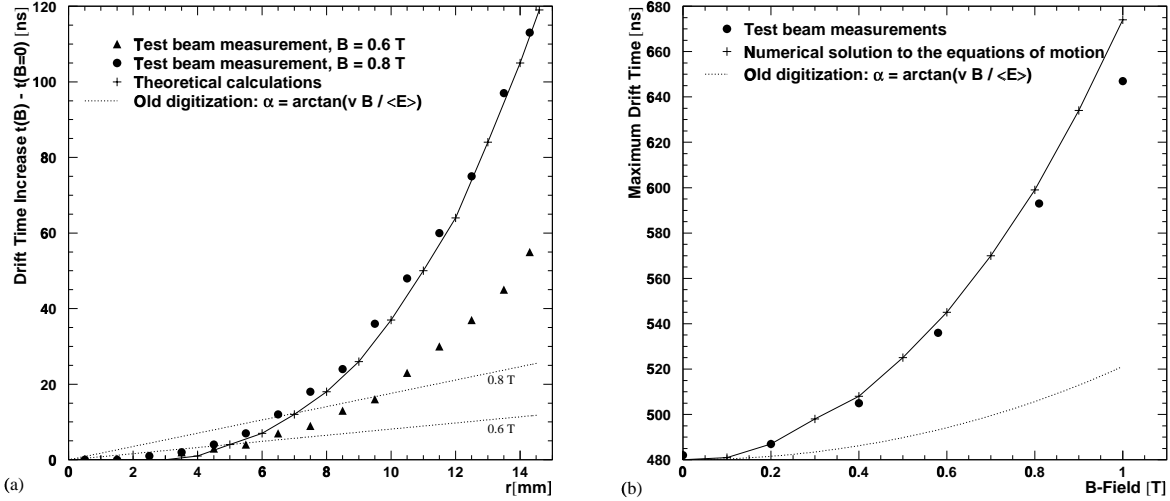


Figure 7.1: (a) Drift-time increase in  $\text{Ar}/\text{N}_2/\text{CH}_4$  (91/4/5) as a function of the muon track radius for  $B = 0.6$  T and  $0.8$  T; (b) maximum drift time as a function of the magnetic field parallel to the wire.

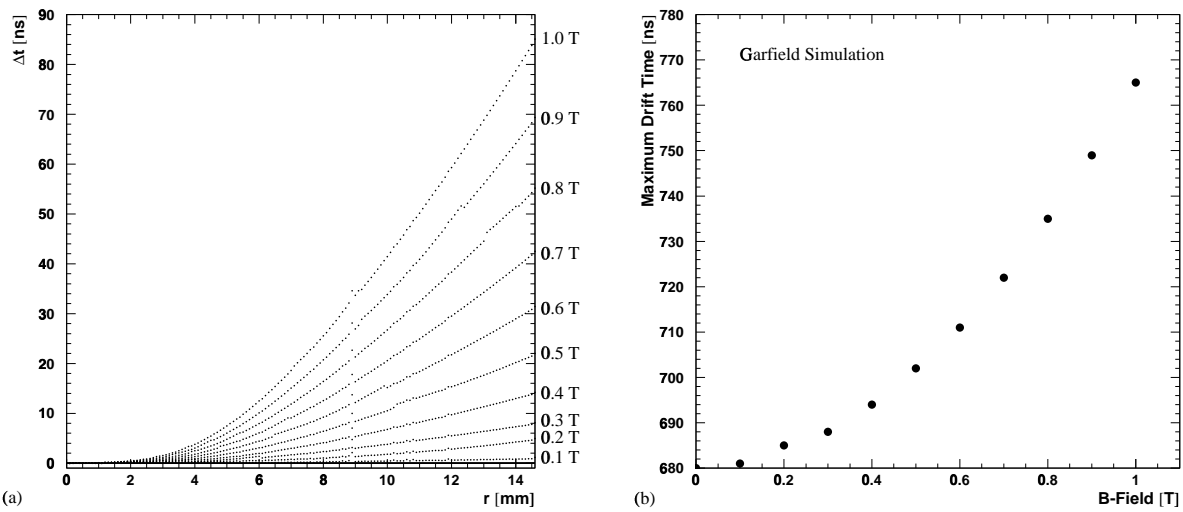


Figure 7.2: (a) Drift-time increase in  $\text{Ar}/\text{CO}_2$  (93/7) as a function of the muon track radius for magnetic fields between 0 and 1 T; (b) maximum drift time as a function of the magnetic field parallel to the wire.

In our simulation the same samples of generated events were digitized with different models for the tube response. These models are defined in Table 7.1:

Model #	1	2	3	4	5	6	7	8	9	10
r(t)	L	L	L	L	R	R	R	R	R	R
Resolution	CG	CG	VG	VG	CG	CG	VG	VG	VA	VA
Lorentz effect	off	on								

L:  $r(t)$  is a straight line with a maximum drift time of 500 ns,

R:  $r(t)$  is realistic as measured for Ar/N<sub>2</sub>/CH<sub>4</sub> (91/4/5),

CG: constant Gaussian resolution of 80  $\mu$ m,

VG: Gaussian resolution varying with  $r$  as measured for Ar/N<sub>2</sub>/CH<sub>4</sub> (91/4/5); mean resolution  $\approx$  80  $\mu$ m.

VA: non-Gaussian resolution varying with  $r$ .

Table 7.1: Models for the drift-tube response.

For the reconstruction the same r-t relationship and resolution were used as for the digitization. The same is true for the parametrization of the Lorentz effect. To take the non-Gaussian resolution function into account, the reconstruction algorithm based on  $\chi^2$  minimization would have to be replaced by a maximum likelihood fit or – equivalently – by a non-parabolic  $\chi^2$  function. However, since we wanted to check first whether the non-Gaussian resolution has any impact at all, we chose a different approach: We kept the Gaussian approximation in the reconstruction and investigated whether the tracking performance deteriorates when in the digitization the non-Gaussian resolution is switched on.

Note that this detailed study was only done for Ar/N<sub>2</sub>/CH<sub>4</sub> (91/4/5). The momentum resolution for Ar/CO<sub>2</sub> (93/7) was simulated later with response model number 10 only.

### 7.3 Momentum Resolution

After fitting the track and the momentum, the reconstructed momentum was compared with the true momentum. Since MUONBOX reconstructs the muon momentum at the entrance of the muon spectrometer, the momentum comparison is done at this position in order to exclude the contribution of energy-loss fluctuations in the calorimeter to the resolution.

Figure 7.3 shows example distributions of  $(p_T^{\text{reconstr.}} - p_T^{\text{true}})/p_T^{\text{true}}$  for generated momenta of 100 GeV/c and 1 TeV/c at the vertex and response model number 10 in the digitization, i.e. using the full knowledge about the tube response. Although these  $\Delta p_T/p_T$  distributions are not Gaussian, an estimate of the momentum resolution can be obtained by fitting a Gaussian function in a range of  $\pm 2$  standard deviations around the peak.

The dependence of the resolution on the transverse momentum is shown in Figure 7.4. These results are based on the most realistic response model (number 10) and were made for the old and the new MDT gas. Owing to the better single tube resolution with Ar/CO<sub>2</sub> (93/7) the momentum resolution is better with this gas. We furthermore distinguish between the even and odd numbered sectors of the spectrometer (cf. Figure 2.2) whose resolutions differ significantly due to the higher field integral  $\int B dl$  in the even sectors which are situated near the coils.

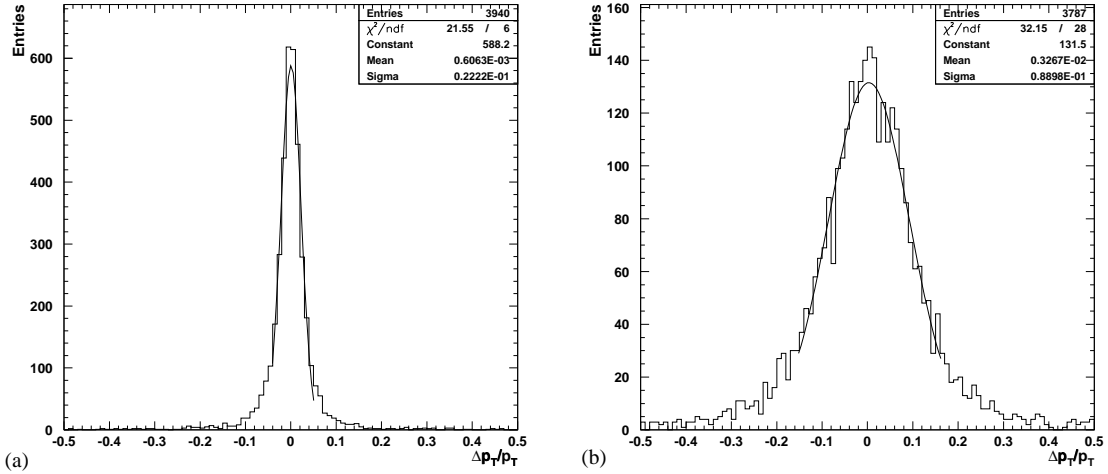


Figure 7.3: Distributions of the difference between reconstructed and true transverse momentum at the entrance of the muon spectrometer, normalized by the true momentum: (a) for  $p_T = 100 \text{ GeV}/c$  at the vertex; (b) for  $p_T = 1 \text{ TeV}/c$  at the vertex. The response model in the digitization was number 10.

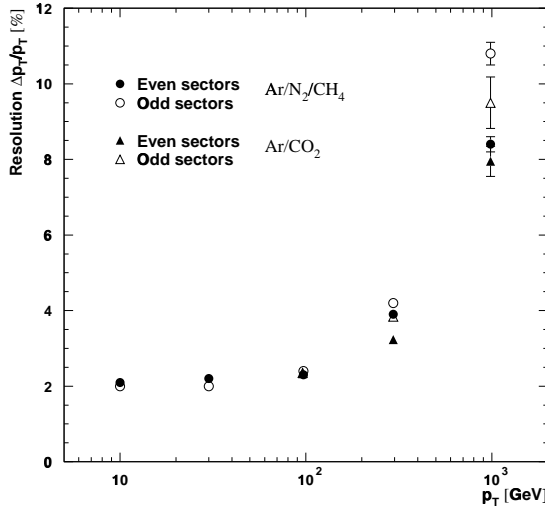


Figure 7.4: Momentum resolution as a function of the transverse momentum at the entrance of the muon spectrometer.

If the drift-tube response has any significant influence on the reconstruction performance, it will be most accentuated at very high momenta where the spectrometer resolution is dominated by the intrinsic detector resolution. For lower momenta on the other hand, detector effects are

blurred by the strong contribution of multiple scattering (cf. Figure 2.4). However, looking at the momentum resolution as a function of the response model (Figure 7.5) no significant effect is visible.

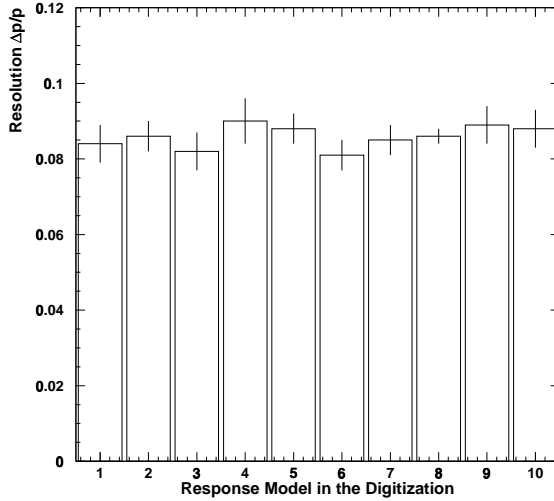


Figure 7.5: Momentum resolution for  $p_T = 1 \text{ TeV}/c$  at the vertex as a function of the response description. The model numbers are defined in Table 7.1.

However, as we pointed out above, the distributions underlying this comparison are not Gaussian and thus the Gaussian width of the central peak suffers from a big systematic uncertainty. This non-Gaussian shape stems from averaging over the highly inhomogeneous resolution in the  $(\eta, \Phi)$  plane (visible in Figures 7.4 and 7.6).

To overcome this problem, we calculate the momentum pull

$$\delta = \frac{(p_T^{\text{reconstr.}} - p_T^{\text{true}})/p_T^{\text{true}}}{\sigma_{\text{theory}}} . \quad (7.2)$$

for every reconstructed muon. Here  $\sigma_{\text{theory}}$  is the resolution which would be theoretically expected for the generated track with the given momentum, direction and position of the muon at the entrance of the muon spectrometer. In practice  $\sigma_{\text{theory}}$  is calculated with a model described in [SCH 95] and [TDR 97b](12.3.2). Basic ingredients of the algorithm are the magnetic field map of the ATLAS detector and a constant Gaussian resolution of  $80 \mu\text{m}$  in every measured track point, i.e. a tube response like in model 6. The contribution of multiple scattering is also taken into account.

The pull distribution has the following advantage: If the theoretical prediction  $\sigma_{\text{theory}}$  is correct for every track, i.e. the measured  $\Delta p_T/p_T$  follows a Gaussian distribution with standard deviation  $\sigma_{\text{theory}}$ , the pull will be distributed according to a standard normal distribution. Indeed, as visible in Figure 7.7, the pull distributions for  $100 \text{ GeV}/c$  and  $1 \text{ TeV}/c$  and response model 6 are rather well fitted by Gaussian functions and have a width close to 1.

Now suppose that there is an important dependence of momentum resolution on the tube response. Then we would expect that unlike the pull distribution for response model 6, the

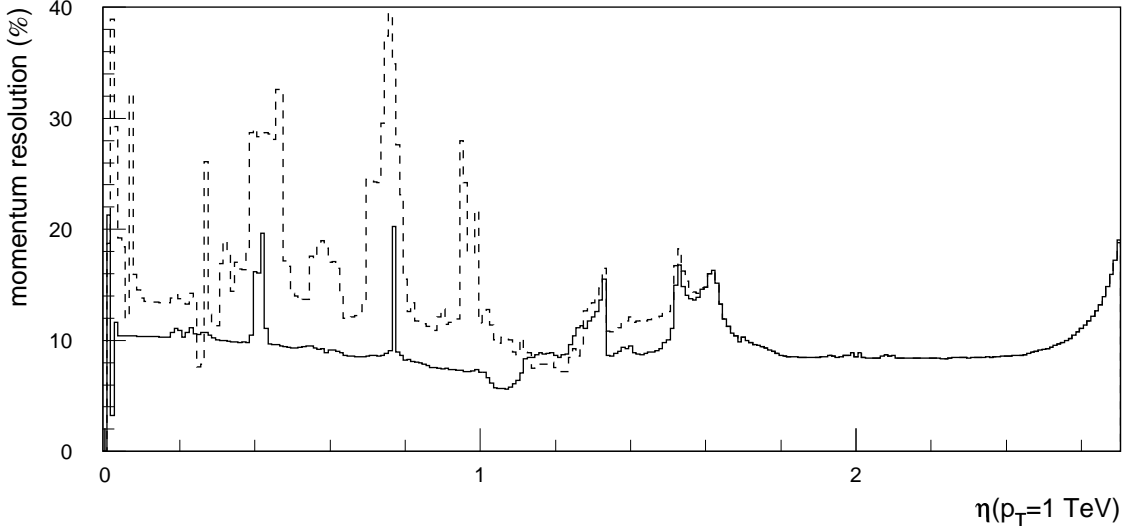


*Figure 7.6:* Momentum resolution for  $p_T = 1 \text{ TeV}/c$  averaged over  $\Phi$  in one ATLAS octant, as a function of  $\eta$  [TDR 99](6.3.3). The dashed curve corresponds to the two octants containing the feet of the ATLAS detector.

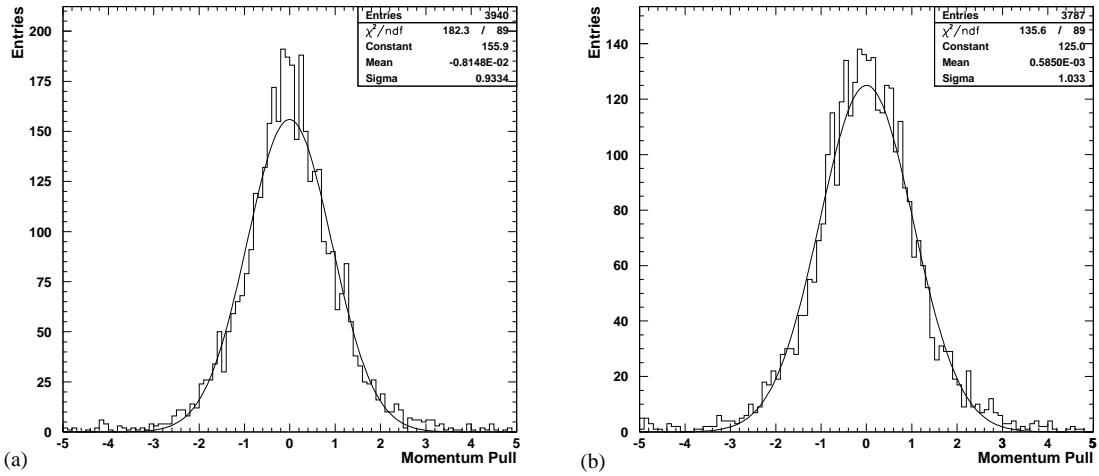


*Figure 7.7:* Momentum pull distributions for response model 6: (a) for  $p_T = 100 \text{ GeV}/c$  at the vertex; (b) for  $p_T = 1 \text{ TeV}/c$  at the vertex.

distribution for the other models would have a significantly different width. However, Figure 7.8 shows that this is not the case. For all response models the widths of the pull distributions are very close to unity.

This result means in particular that the momentum resolution does not deteriorate if a non-

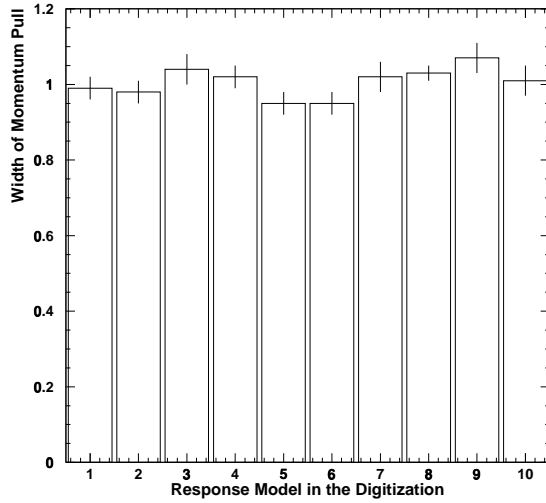


Figure 7.8: Width of the pull distribution for  $p_T = 1 \text{ TeV}/c$  at the vertex as a function of the response description. The model numbers are defined in Table 7.1.

Gaussian time resolution is incorporated in the digitization without taking it into account in the reconstruction. With other words, we could not achieve any resolution improvement by replacing the least-squares fit by a maximum likelihood fit in the track reconstruction. Looking back at the comparison between least-squares and maximum likelihood tracking, this insensitivity to non-Gaussian tails is not even surprising: The conclusion of Section 6.6 was that mainly the reconstruction efficiency depends on this detail of the tube response. Therefore the next section is dedicated to the influence of the tube response on reconstruction efficiency and the probability of reconstructing a fake track.

## 7.4 Reconstruction Efficiency and Fake-Track Probability

The definition of reconstruction efficiency for tracking in ATLAS is more complex than the efficiencies we have considered so far.

A simple quality criterion for a reconstructed muon in ATLAS would be a  $3\sigma$  efficiency on the momentum. However, due to the big amount of background hits in ATLAS it happens that despite a very wrong track the calculated momentum is – by chance – rather correct. Since we are also interested in a correctly fitted track, we follow the convention in [TDR 99](6.3.4.1) and classify reconstructed tracks by a hit quality factor based on Monte Carlo information. It is defined as

$$Q = \frac{\text{hits used for the track fit and really produced by the muon}}{\text{all hits used for the track fit}} . \quad (7.3)$$

A low value of  $Q$  for example indicates that the reconstruction algorithm has chosen many wrong hits (i.e. background or noise) for the track fit. Tracks with a quality factor lower than 10 % are defined as fake tracks.

A “good track” is required to have  $Q > 0.55$ . In addition the reconstructed momentum must be sufficiently close to the true value, such that the momentum pull defined in (7.2) satisfies the condition  $|\delta| < 4$ . The latter criterion is equivalent to a  $4\sigma$  efficiency.

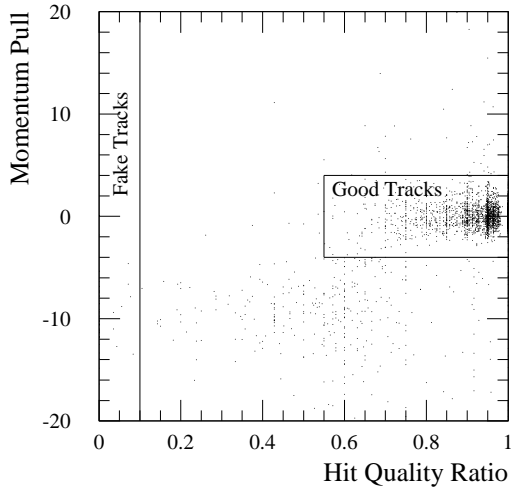


Figure 7.9: Momentum pull versus hit quality factor for  $p_T = 1 \text{ TeV}/c$ .

Figure 7.9 shows the regions for good and fake tracks in the plane defined by the momentum pull  $\delta$  and the hit quality factor  $Q$ . The reconstruction efficiency is defined as the fraction of events which contain at least one good track, whereas the fake-track probability is the average number of fake tracks per event.<sup>1</sup>

The dependence of the reconstruction efficiency and the fake-track probability on the transverse momentum is shown in Figure 7.10. As  $p_T$  increases, more and more electromagnetic showers are produced by the muon via bremsstrahlung and direct pair production. Hits from secondary particles can hide the muon hits and thus lead to wrong drift-time measurements. They also create hits in tubes which are not traversed by the muon. The consequence is an increasing probability for reconstructing a fake track. In the same way the efficiency for finding good tracks decreases.

The efficiency drop for  $p_T < 30 \text{ GeV}/c$  is caused by multiple scattering.

The graphs demonstrate that the reconstruction efficiency does not depend significantly on details of the MDT response description. The only visible but small change occurs when the radial dependence of the resolution is switched on. Introducing non-Gaussian resolution has no effect at all. A close look at single events revealed that due to the big number of measurement points per track the reconstruction algorithm is robust against a few hits with large excursions from the track. As expected, the change from a perfectly linear to a realistic r-t relationship has no consequence either. The same is true for switching on the Lorentz effect. In both cases only the translation between drift times and radii is modified. Since this is done consistently in

<sup>1</sup>Note that we allow for several reconstructed track candidates. If more than one of them are good, the information from other subdetectors will be used to decide which of them is correct.

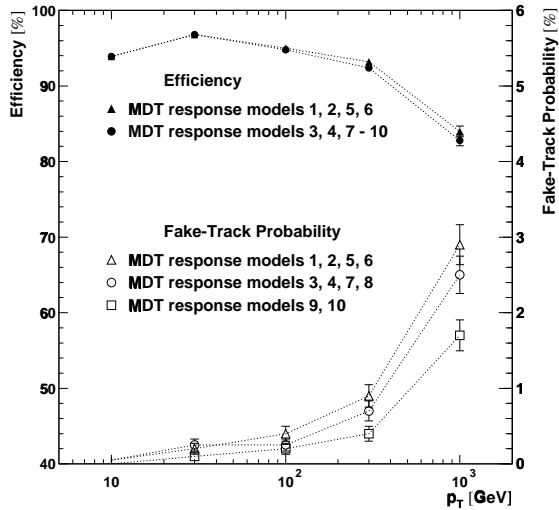


*Figure 7.10: Reconstruction efficiency (left scale) and fake-track probability (right scale) as a function of  $p_T$ . The tube response models defined in Table 7.1 are distinguished as far as allowed by the visibility of the graph. The error bars on the efficiency are based on a binomial distribution for the number of good tracks in a sample of 4000. The errors on the fake-track probability assume a binomial distribution for the number of fake tracks in the total number of tracks found for the sample of 4000 events.*

digitization and reconstruction, the actual track fit does not even notice this change.

The fake-track probability depends on the MDT response (lower graphs in Figure 7.10). The differences occur between the models with constant Gaussian resolution, r-dependent Gaussian resolution and r-dependent non-Gaussian resolution. The more complex the description of the resolution is made, the less is the chance to build up a fake track from background hits. The investigation of events with model-dependent fake tracks showed that this effect concerns mainly events with huge electromagnetic showers in which the real muon track is spoilt by background hits. The details of the mechanism causing the dependence on the shape of the tube resolution function are not understood. We cannot exclude that this effect has its origin in the subtleties of the reconstruction strategy.

## 7.5 Conclusion about the Consequences of Non-Gaussian Resolution

We have seen that neither momentum resolution nor reconstruction efficiency shows any significant deterioration when a non-Gaussian resolution is incorporated into the digitization without taking it into account in the reconstruction. Due to the big number of measurements along a track ( $3 \text{ tubes} \times 2 \text{ multilayers} \times 3 \text{ stations} = 18$ ), the effects of non-Gaussian tails near the wires average out. The reconstruction performance is much more sensitive to pattern recognition difficulties with inefficiencies and background hits.

Consequently one would not draw any significant advantage from replacing in ATLAS the least-squares fitting technique by the maximum-likelihood method.

## Chapter 8

# Calibration of the Space-Time Relationship

In earlier chapters we have reported about test-beam experiments where a high precision silicon tracker was used as external reference system in order to measure the space-time relationship of drift tubes as a function of various operating parameters. This was suited for detailed detector-physical studies. However, in ATLAS no external tracker will be available to calibrate the r-t relationship of MDTs. Since furthermore the response depends on external parameters like temperature, gas density, anode voltage, magnetic field and background rate, it will show temporal and strong spatial variations within the spectrometer. Thus the option of a calibration in the laboratory before chamber installation is excluded, and one had to develop techniques for an in-situ calibration using only the MDTs' own data. This calibration will be repeated as often as necessary.

To be strictly correct, we would have to calibrate the full detector response  $P(t|r)$  as it was discussed in Chapter 6. However, the conclusion from Chapter 7 was that for tracking in ATLAS we do not really need the information about the asymmetry of time distributions near the wire. It is sufficient to approximate the distributions  $P(t|r)$  and  $P(r|t)$  by Gaussians centred at  $t(r)$  and  $r(t)$ , and with widths  $\sigma_t(r)$  and  $\sigma_r(t)$  respectively. In order to minimize biases in the track reconstruction, the function  $r(t)$  should coincide with the **mean** rather than the peak of the correct distribution  $P(r|t)$ .

Up to the present all attempts to calibrate both  $r(t)$  and  $\sigma_r(t)$  simultaneously from the chamber data have failed. Therefore we inject the knowledge about  $\sigma_r(t)$  from test-beam measurements and content ourselves with the calibration of the function  $r(t)$  or the inverse  $t(r)$ , which is already a complicated task.

Techniques for calibrating an r-t relationship have been worked on since the early days of ATLAS preparations, but they had various inherent problems which we set off to analyze and attack with the background of the improved understanding of drift-tube operation.

We distinguish two major classes of techniques:

- The first approach needs nothing more than a drift-time spectrum and is therefore independent of the chamber geometry and track incidence angles. Its drawback is the necessity of an excellent knowledge about the tiniest details of tube response, illumination and wire position with respect to the tube wall. In Section 8.2 substantial extensions of the pre-

decessor technique will be presented. Despite important improvements of the calibration precision, the performance of this approach is still not as good as with the second approach and will mainly serve for determining a good initial  $r(t)$  for the iterative second concept.

- The second approach, called “autocalibration”<sup>1</sup>, uses the correlation of the drift times measured in tubes crossed by a common track. By fitting tracks through a multilayer of tubes the r-t relationship is iteratively improved. The success of this concept depends crucially on the range of track incidence angles and on a good knowledge about the chamber geometry. Furthermore it needs a good start r-t relationship. Our new study (Section 8.3) is focussed on the influence of the track angle on the performance of autocalibration and on the question whether autocalibration has enough information to determine the r-t relationship uniquely. Finally we shall introduce a new technical realization which is designed for making optimal use of all available information.

## 8.1 Required Calibration Precision

To quantify the deviation of the calibrated r-t relationship from the true  $r(t)$  with one number, we introduce the rms deviation

$$\text{rms}(\Delta r) \equiv \sqrt{\frac{1}{t_{\max}} \int_0^{t_{\max}} [r_{\text{calib}}(t) - r_{\text{true}}(t)]^2 dt} . \quad (8.1)$$

To be really free from systematic effects, the deviation of the r-t relationship should be much smaller than the single tube resolution of  $80\,\mu\text{m}$ . In [ATL 94] it has been defined as a goal to achieve a precision which is comparable with the alignment precision of the MDT chambers, i.e. about  $20\,\mu\text{m}$ . This is not a strict limit, but rather an orientation value. In Section 8.3.6.3 we shall see that the intended calibration precision at ATLAS will be limited by the statistics that will be available within a calibration period.

The decisive criterion for the required calibration precision is the influence of  $\text{rms}(\Delta r)$  on the muon momentum resolution. Since significant effects can only be expected at very high momenta, we simulated the momentum resolution of single muons with  $p_T = 1\,\text{TeV}/c$ . The procedure was the same as described in Chapter 7. While the conversion of the Monte Carlo track radii into drift times was done with a realistic tube response, the track reconstruction was based on an r-t relationship that was falsified in all chambers by a function

$$r_{\text{wrong}}(t) - r_{\text{true}}(t) = \text{rms}(\Delta r) \cdot \sqrt{2} \cdot \sin\left(\pi \frac{t}{t_{\max}}\right) . \quad (8.2)$$

This function vanishes at  $t = 0$  and at the maximum drift time  $t_{\max}$ . Its quadratic average over the entire time interval  $[0, t_{\max}]$  is equal to  $\text{rms}(\Delta r)$ . We varied the rms deviation between 0 and  $200\,\mu\text{m}$ . This simulation tests only one specific deviation function which is a pessimistic example: due to its big linear average it can be expected to induce considerable biases on the reconstructed tracks.

---

<sup>1</sup>In the strict sense also the first approach is a kind of autocalibration, which means nothing more than self-calibration, i.e. without external reference detector. We shall however respect the historical convention and reserve the name of autocalibration to the methods based on track fits.

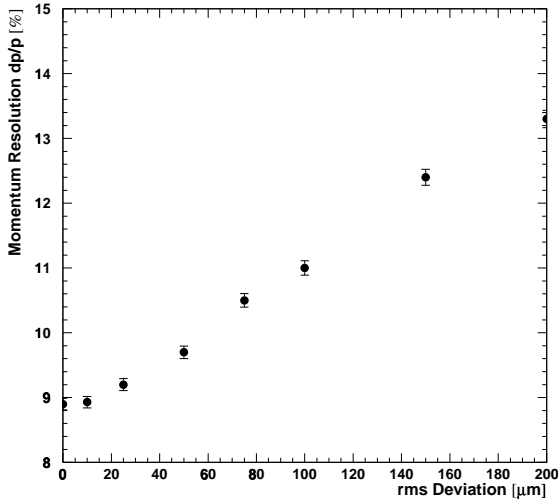


Figure 8.1: Momentum resolution at  $p_T = 1 \text{ TeV}/c$  as a function of the rms deviation of the r-t relationship used for track reconstruction.

Figure 8.1 shows the momentum resolution as a function of  $\text{rms}(\Delta r)$ . If we tolerate a deterioration of momentum resolution up to 1 % of the total momentum resolution due to a wrong r-t relationship, we can afford an  $\text{rms}(\Delta r)$  up to  $60 \mu\text{m}$ . This is a big tolerance which should be kept in mind for the case that autocalibration in ATLAS turns out to suffer from lack of statistics.

## 8.2 Determination of the r-t Relationship from the Drift-Time Spectrum

Several studies have shown that for the correct convergence of autocalibration to the true space-time (r-t) relationship a good start r-t relationship is necessary [SAM 97, CRE 97]. This is especially important with low angular spread of tracks, because then autocalibration cannot uniquely determine the r-t relationship (Sections 8.3.2.2f). It is also important in the presence of a background, where track finding is harder. Furthermore, a good start value saves on computing power needs.

In the past, the following approaches have been used to derive an initial r-t relationship:

- Linear r-t relationship: Even for almost linear gases like Ar / N<sub>2</sub> / CH<sub>4</sub> (91 / 4 / 5) this approximation yields very bad results (up to  $700 \mu\text{m}$  off). For very non-linear gases like Ar / CO<sub>2</sub> mixtures it is several millimeters off.
- Simulation with Garfield [VEE 99]: Garfield together with MAGBOLTZ [BIA] and HEED [SMI 97] provides the best available simulation of the detector response. Its prediction of the r-t relationship is therefore quite accurate (up to  $200 \mu\text{m}$  off). A full simulation

is required to reach this accuracy for each magnetic field value etc. And still there are variations not taken into account such as temperature and water content of the gas.

- Integration Method (see e.g. [BAR 94b]): This approach is based on the data of the MDT itself, and takes into account variations such as water content automatically. However, since it ignores important effects like  $\delta$ -rays, resolution and efficiency, it gives bad results (up to  $450 \mu\text{m}$  off). The details of this method will be discussed in Section 8.2.2.

Figure 8.2 compares the accuracy of these techniques for Ar / N<sub>2</sub> / CH<sub>4</sub> (91 / 4 / 5). We have looked for an improvement on the integration method, whilst retaining its advantage of automatically accounting for local variations in operating conditions. This also retains the full spirit of having a self-calibrating detector, unlike resorting to Garfield; but of course Garfield remains a very good method. The new methods take into account more knowledge of the drift-tube response and give a much better precision than Garfield.

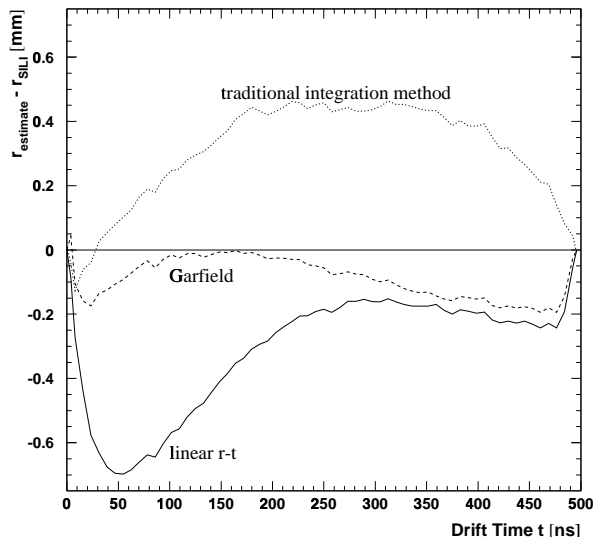


Figure 8.2: Comparison of the performance of three usual techniques for determining a start r-t relationship for autocalibration. The plot shows the difference between the estimated and the true track radius at a given drift time  $t$ .

### 8.2.1 The Composition of a Drift-Time Spectrum

The drift-time spectrum of a drift tube is determined by the radial illumination and the detector response. The latter can be described by  $P(t|r)$ , i.e. the probability of measuring a drift time  $t$  under the condition that the muon track had a minimum distance  $r$  from the wire. In Chapter 6 we have presented a measurement and a parametrization of  $P(t|r)$ .

From the product rule for probabilities we find

$$P(t, r) = P(t|r) \cdot R(r) \quad (8.3)$$

where  $P(t, r)$  is the two-dimensional probability density for having a muon track at a distance  $r$  and measuring a time  $t$  (Figure 6.6).  $R(r)$  is the radial distribution of tracks giving hits in the tube. Marginalization yields the drift-time distribution  $T(t)$ :

$$T(t) = \int_0^\infty P(t, r) dr = \int_0^\infty P(t|r) \cdot R(r) dr . \quad (8.4)$$

This is the basic equation for our following considerations. The choice of  $\infty$  rather than the inner tube radius  $b$  as the upper integration limit was driven by the possibility of getting a  $\delta$ -ray hit from a muon passing through the tube wall. The efficiency drop at the wall is absorbed in  $R(r)$ .

Our task will be to unfold (8.4) and to extract the r-t relationship which is a component of the detector response function  $P(t|r)$ . As we shall see, for simple response functions this inversion problem can be solved exactly, whereas for more realistic descriptions a numerical approach has to be made.

### 8.2.2 Integration Method

Let us first consider the approximation of an ideal detector response, i.e.

$$P(t|r) = \delta(t - \tau(r)) , \quad (8.5)$$

where  $\tau(r)$  is the r-t relationship. Then (8.4) becomes

$$T(t) = \int_0^\infty \delta(t - \tau(r)) \cdot R(r) dr \quad (8.6)$$

$$= \int_0^\infty \delta(r - \rho(t)) \cdot \frac{d\rho}{dt} \cdot R(r) dr \quad (8.7)$$

$$= R(\rho(t)) \cdot \frac{d\rho}{dt} \quad (8.8)$$

Here the (reasonable) assumption has been made that  $\tau(r)$  is monotonous and therefore has an inverse function  $\rho(t) \equiv \tau^{-1}(t)$ , and that  $d\tau/dr$  is never zero: this may be invalid near the wire (see Figure 6.10).

Integration gives

$$\int_0^t T(t') dt' = \int_0^{\rho(t)} R(r) dr . \quad (8.9)$$

The zero-point of the time scale is determined by fitting a Fermi-Dirac function to the leading edge of the drift-time spectrum [BIS 97, SAM 97].

Usually it is assumed that the illumination is homogeneous and the efficiency is 1 from  $r = 0$  to the inner tube radius  $b$ . For the radial hit distribution this means

$$R(r) = \frac{1}{b} \quad \text{if } 0 < r < b \text{ and 0 otherwise.} \quad (8.10)$$

In a beam this is usually a bad approximation. If we still rely on it, (8.9) simplifies to

$$\rho(t) = b \int_0^t T(t') dt' \quad (8.11)$$

For a histogrammed drift-time spectrum  $T(t_i)$  this can be written as a sum over bin contents up to the bin containing  $t$ :

$$\rho(t) = b \sum_{i=1}^n T(t_i) \quad (8.12)$$

Equation (8.12) is the traditional integration method. As we already pointed out in the introduction, it produces an r-t relationship which agrees very badly with the true one. The main reason is that this approach neglects  $\delta$ -rays which have a considerable influence on the shape of the drift-time spectrum. In the following section we refine the model by introducing a correction term for  $\delta$ -rays.

### 8.2.3 Integration Method with $\delta$ -Ray Correction

To take  $\delta$ -rays into account, we modify the perfect detector response (8.5) by adding a constant term  $d$  to the conditional probability density  $P(t|r)$  at drift times  $0 < t < \tau(r)$ . The response function is now given by

$$P(t|r) = [1 - d \cdot \tau(r) \cdot \Theta(\tau(r))] \cdot \delta(t - \tau(r)) + d \cdot \Theta(\tau(r) - t) \cdot \Theta(t) \quad (8.13)$$

where the  $\Theta$ -functions define the cutoff times for the  $\delta$ -ray background. The factor applied to the  $\delta$ -function assures the proper normalization.

Considering the  $\delta$ -ray probability density as constant – independent of  $r$  and  $t$  – is a reasonable approximation. A more detailed treatment is described in Section 8.2.4 where the probability density varies with  $r$ , but this prevents an analytical solution.

Putting (8.13) into the basic equation for the drift-time spectrum (8.4) we get after some simplifications:

$$T(t) = R(\rho(t)) \cdot \frac{d\rho}{dt} \cdot [1 - d \cdot t \cdot \Theta(t)] + d \cdot \Theta(t) \cdot \int_{\rho(t)}^{\infty} R(r) dr \quad (8.14)$$

As in the simple integration method we assume flat illumination and perfect efficiency, hence we use (8.10) for  $R(r)$ . After reorganization we obtain the differential equation

$$\frac{d\rho}{dt} [1 - d \cdot t \cdot \Theta(t)] - \rho(t) \cdot d \cdot \Theta(t) = b \cdot T(t) - b \cdot d \cdot \Theta(t) \quad (8.15)$$

This equation can be solved analytically. The resulting r-t relationship is given by

$$\rho(t) = \frac{b}{1 - d \cdot t \cdot \Theta(t)} \cdot \left[ \int_0^t T(t') dt' - d \cdot t \right] \quad (8.16)$$

Equation (8.16) was applied to H8 test-beam data taken in spring 1997 (cf. Section 6.3). The drift time spectrum of only one tube was used. The  $\delta$ -ray probability density  $d = 0.00024 \text{ ns}^{-1}$  was determined by radially averaging the measured  $p_4(r)$  shown in Figure 6.8. The improvement with respect to the conventional integration method is demonstrated by Figure 8.3: The rms deviation of the reconstructed r-t relationship from the true one is reduced from  $345 \mu\text{m}$  to

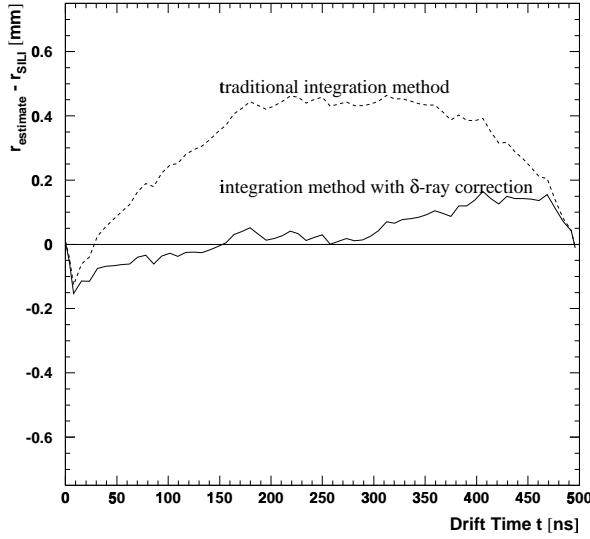


Figure 8.3: Comparison between the simple and the  $\delta$ -ray-corrected integration method for a  $\delta$ -ray probability density  $d = 0.00024 \text{ ns}^{-1}$ . The plot shows the difference between the estimated track radius and the one determined by the r-t relationship measured with the silicon telescope.

$80 \mu\text{m}$ . The assumption of a flat illumination is a very poor approximation for the H8 beam (see Figure 8.4). This is probably a major contribution to the  $80 \mu\text{m}$  rms deviation.

The bad agreement near the wire is not only to blame on the integration methods. The determination of the r-t relationship with the silicon telescope is based on gaussian fits to the distribution of  $r_{\text{hit}} - r_{\text{SILI}}$  in drift-time slices. Near the wire however these residuals are very non-Gaussian and the fits determine the r-t relationship only badly. Therefore also the error of the reference r-t relationship contributes to the deviation.

To improve the precision of the calculated r-t relationship we shall in the following chapter introduce all known details of the detector response into our description.

#### 8.2.4 Unfolding the Detector Response

In both preceding methods, the integral (8.4) could be evaluated, and with simplifying assumptions for  $R(r)$  closed forms for  $\rho(t)$  were obtained. With more realistic responses, the integral (8.4) is difficult to solve analytically and we resort to numerical methods. In the unfolding technique,  $P(t|r)$  and  $R(r)$  are parametrized, and the spectrum  $T(t)$  evaluated by numerical integration of (8.4) with some initial set of parameters. The parameters for resolution, efficiency and  $\delta$ -rays are all taken from silicon telescope measurements. The r-t relationship starts with, say, a straight-line guess. The resulting spectrum is compared to the measured drift-time spectrum  $T_m(t)$  by calculating the following chi-squared:

$$\chi^2 = \sum_{\text{bins i}} \frac{[T_m(t_i) - T(t_i)]^2}{T_m(t_i)} \quad (8.17)$$

Then the parameters for the r-t relationship are varied to minimize  $\chi^2$ .

The drift-time spectrum has contributions from all muons giving a hit: over most of the tube, the hit efficiency is very close to 1, but near the wall it drops rapidly. The efficiency is taken into account by writing  $R$  as a product of the beam profile  $b$  and efficiency  $\eta$ :

$$R(r) = b(r) \cdot \eta(r) \quad (8.18)$$

The beam profile is parametrized by

$$b(r) = \sum_{i=0}^2 b_i y^i \quad \text{with } |y - 5.89 \text{ mm}| = r \quad (8.19)$$

where  $y$  is the position of the muon in the coordinate system used in the data analysis. Since the beam profile is not symmetric about the wire, the integral in (8.4) is carried out separately for the two halves, and then the two contributions are added together. Figure 8.4 shows the measurement of the beam profile with ODYSSEUS, and a fit superposed.

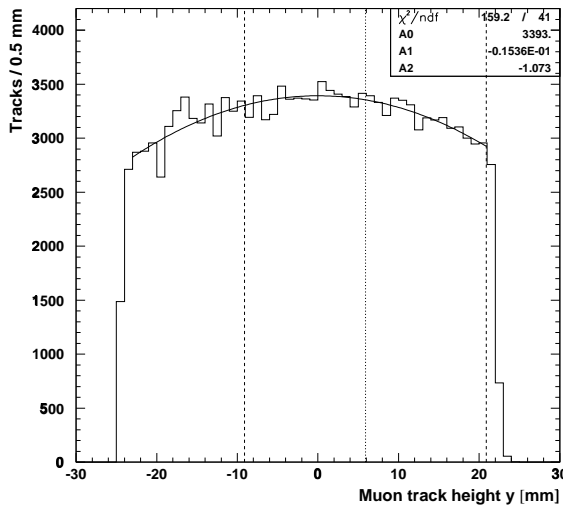


Figure 8.4: Beam profile measured with the silicon telescope with the fit superimposed. The tube covered the region  $(5.89 \pm 15)$  mm as indicated.

The inefficiency (Figure 8.5) can be fitted reasonably well with

$$1 - \eta(r) = \frac{1}{2} \left[ \operatorname{erf} \left( \frac{r - r_{max}}{w} \right) + 1 \right] \quad (8.20)$$

where

$$\operatorname{erf}(x) \equiv \int_0^x \frac{1}{\sqrt{2\pi}} e^{-\frac{(x')^2}{2}} dx' \quad . \quad (8.21)$$

$r_{max}$  is the radius with 50% efficiency which from silicon telescope measurements is very close to the tube inner radius (14.75 mm for the 250  $\mu\text{m}$  thick tubes used for this study, 14.6 mm

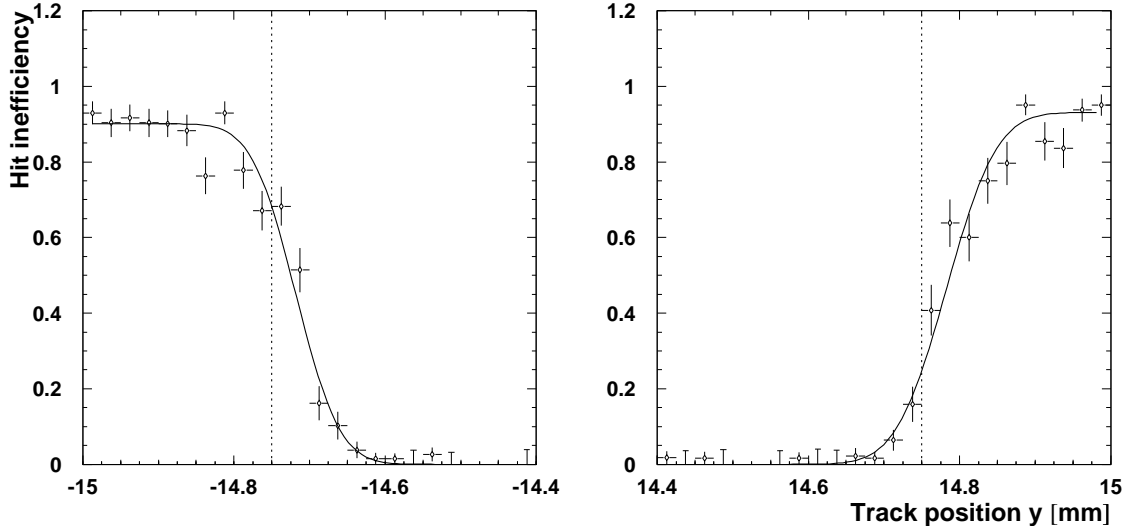


Figure 8.5: Inefficiency as a function of the track position in the regions near the tube walls measured with the silicon telescope. The superposed fit is explained in the text. The vertical lines at  $\pm 14.75$  mm indicate the nominal positions of the inner wall surfaces.

for standard MDT tubes). The parameter  $w$  is a measure of the width of the region where the efficiency drops; a typical value is  $70\ \mu\text{m}$ . In practice  $r_{max}$  is different on opposite sides of the tube due to the wire being off-centre. We have taken the average of the parameter fit values for the two sides.

For the parametrization of  $P(t|r)$  we now use the correct distribution as it was determined in Section 6.4 (see Equations (6.5) to (6.9) and Table 6.1).

The quantities to be determined by the unfolding process are the parameters  $a_i$  of the r-t relationship, i.e. the peak position  $p_2(r)$  of  $P(t|r)$ . To be consistent with the notation used for the integration method, we identify  $\tau(r) = p_2(r)$ . The start values of  $a_i$  for the minimization of the  $\chi^2$  defined in (8.17) are chosen such that  $\tau(r)$  is a straight line. All other coefficients, specifying beam profile, efficiency, resolution, asymmetry and  $\delta$ -ray probability, are taken from the precision measurements and kept constant. The question whether we can realistically assume to know all these fixed parameters at ATLAS without a silicon tracker, will be discussed in Section 8.2.5.

Let us remind that the function  $\tau(r)$  which we have now calibrated, is the peak position of  $P(t|r)$ . For tracking however we need the radial mean of  $P(r|t)$  which for asymmetric distributions is not just the inverse of  $\tau(r)$ . The conversion is done by applying Bayes' theorem

$$P(r|t) = P(t|r) \frac{R(r)}{T(t)} \quad (8.22)$$

and then taking the mean of  $P(r|t)$ .

### 8.2.4.1 Results for Test-Beam Data without Radiation Background

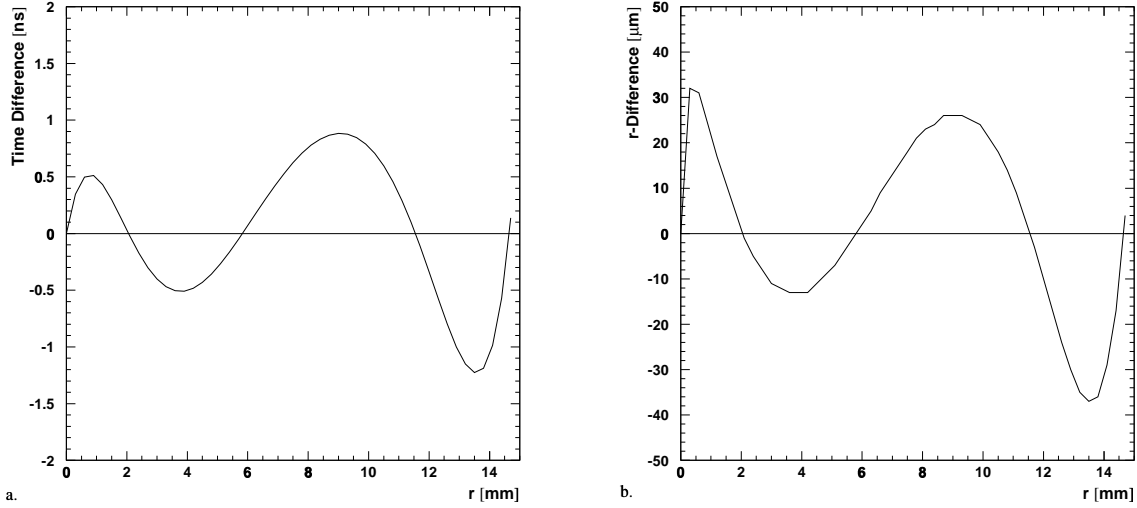


Figure 8.6: a: Difference between unfolded and true  $\tau(r)$ . b: Time difference converted into a radius difference using the local drift velocity.

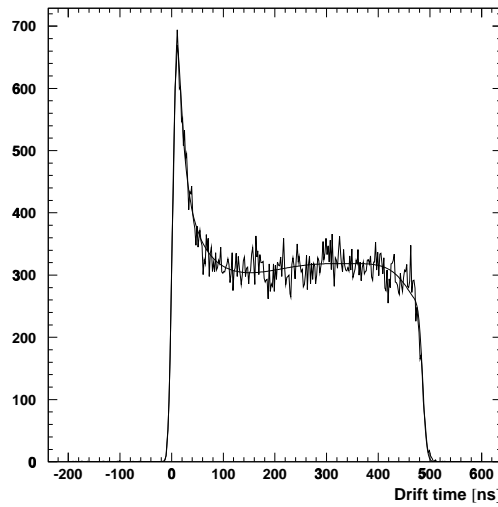


Figure 8.7: The drift-time spectrum used for unfolding  $T_m(t)$ . The smooth curve is the folded spectrum  $T(t)$  with the final parameters.

Like the integration method, also the unfolding technique was applied to the drift-time spectrum of one tube measured in the H8 test-beam. To evaluate the result, the unfolded relationship is compared to the measured one. This is done by calculating  $\tau(r)$  at 0.3 mm steps.

Figure 8.6a shows the time difference of the results. The difference is always less than 1.2 ns, and the rms difference is 0.6 ns. Multiplying the time differences by the local drift velocity yields the radial deviations shown in Figure 8.6b. Figure 8.7 shows the input drift-time spectrum with that resulting from the final values of the parameters. The agreement is excellent.

Figure 8.8 compares the accuracy of the unfolding method with the other techniques. The rms deviations from the true r-t relationships are 345, 80 and 18  $\mu\text{m}$  for the traditional integration, integration with  $\delta$ -ray correction, and unfolding techniques respectively. Clearly the new methods are much more accurate; unfolding is the most accurate method so far, even better than Garfield which has an rms deviation of 109  $\mu\text{m}$ . The accuracy of the result shows that we have a very good understanding of the drift-tube response.

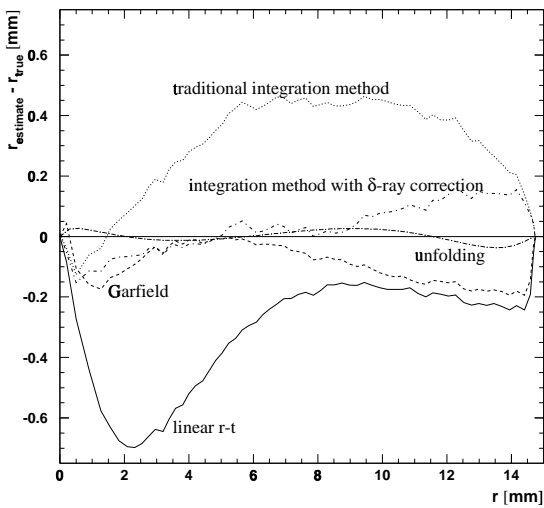


Figure 8.8: Comparison of the accuracies of all described methods for obtaining a first order r-t relationship.

However, we have to admit that the rms precision of 18  $\mu\text{m}$  for the unfolding technique was obtained under very favourable circumstances: By using the drift-time spectrum of only one tube, the task was considerably facilitated because all injected parameters could be precisely measured for this particular tube. At ATLAS a common r-t relationship will be used for all tubes within a calibration zone (Section 8.3.6.3). For the unfolding method this means that the spectra of many tubes have to be superposed and that the radial hit spectrum  $R(r)$ , which is an input to the unfolding method, has to be averaged over all tubes. If the illumination is inhomogeneous or if the wire concentricity differs from one tube to the other, the calibration precision will degrade. In addition, the superposition of several time spectra requires a precise time alignment of these spectra with respect to each other. The best method which is currently available is to fit the leading edge of the time spectrum with a Fermi-Dirac function [BIS 97, SAM 97]. It is difficult to achieve the required precision of better than 300 ps.

For these reasons we applied the method also to a common time-spectrum for a set of eight tubes that were fully or partially covered by the silicon tracker. In this case the rms precision is only 49  $\mu\text{m}$  which is much worse than for a single tube, but still better than the integration method or Garfield.

### 8.2.4.2 Results for Test-Beam Data with Radiation Background

In ATLAS the drift-time spectrum will have a significant background contribution from the high-rate gamma radiation. Figure 8.9 shows a drift-time spectrum measured in the X5 test beam with a gamma count rate of 333 kHz per tube (for the set-up see Chapter 5).

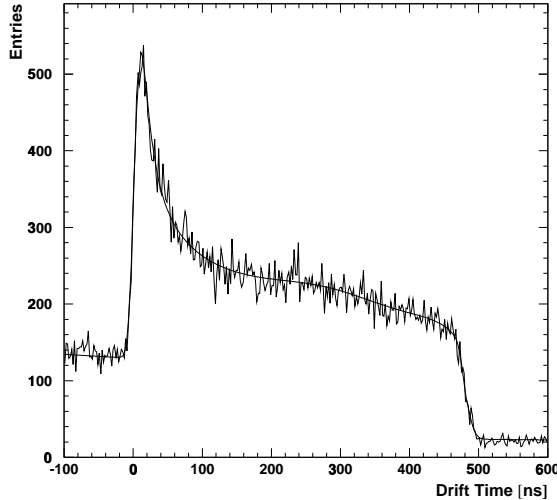


Figure 8.9: The drift-time spectrum used for unfolding  $T_m(t)$  with 333 kHz gamma background. The smooth curve is the folded spectrum  $T(t)$  with the final parameters.

To take the background entries into account for the unfolding, we have to modify Equation 8.4 describing the composition of the measured time spectrum.

The condition for triggering an event was the coincidence of the two  $5 \times 5\text{cm}^2$  scintillators behind and in front of ODYSSEUS and two other scintillators upstream in the beam where the background rate was zero. Therefore we can assume that every trigger was caused by a muon flying through the area defined by ODYSSEUS. We set the trigger time to  $t = t_0$  and the earliest muon arrival time to 0. The probability density to observe a hit at a time  $t$  in a tube which was crossed by a muon, can be written as

$$T(t) = N \cdot \{T_\mu(t) \cdot P(\text{no } \gamma \text{ in } [t_0, t]) + \alpha_0 \cdot T_\gamma(t) \cdot P(\text{no } \mu \text{ in } [t_0, t])\} \quad , \quad (8.23)$$

where  $T_\mu(t)$  is the undisturbed muon drift-time spectrum (8.4) without background and

$$T_\gamma(t) = \lambda e^{-\lambda(t-t_0)} \quad (8.24)$$

the pure time spectrum of the first gamma hit after the trigger.  $N$  is a normalization constant,  $\alpha_0$  a weight factor and  $\lambda$  the gamma count rate of the tube. The probability of not having any gamma hit between the trigger and  $t$  is

$$P(\text{no } \gamma \text{ in } [t_0, t]) = e^{-\lambda(t-t_0)} \quad (8.25)$$

and the probability that the muon hit has not yet arrived at the time  $t$  is

$$P(\text{no } \mu \text{ in } [t_0, t]) = 1 - \int_{t_0}^t dt' T_\mu(t') . \quad (8.26)$$

Thus we obtain

$$T(t) = N \cdot \left\{ T_\mu(t) \cdot e^{-\lambda(t-t_0)} + \alpha_0 \cdot \lambda e^{-\lambda(t-t_0)} \cdot [1 - \int_{t_0}^t dt' T_\mu(t')] \right\} . \quad (8.27)$$

This expression is valid if we know that the muon went through the considered tube. However, since the trigger area covers more than one tube, the muon can also pass through a different tube. To account for this effect, we introduce the probability  $\alpha_1$  that the trigger was caused by a muon passing through the considered tube, and replace  $T_\mu(t)$  in (8.27) by  $\alpha_1 \cdot T_\mu(t)$ :

$$T(t) = N \cdot \left\{ \alpha_1 \cdot T_\mu(t) \cdot e^{-\lambda(t-t_0)} + \alpha_0 \cdot \lambda e^{-\lambda(t-t_0)} \cdot [1 - \int_{t_0}^t dt' \alpha_1 \cdot T_\mu(t')] \right\} . \quad (8.28)$$

How are the additional parameters determined?

- The gamma rate  $\lambda$  can be extracted from the domain  $t < 0$  of the time spectrum, i.e. before the leading edge of the muon entries. It is done by fitting this pure gamma spectrum with  $e^{-\lambda t+c}$  (Figure 8.10).

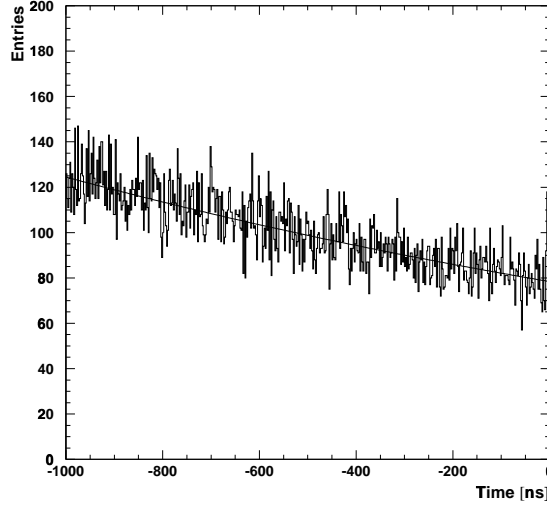


Figure 8.10: The portion of a time spectrum before the leading edge of the muon drift-time spectrum. It is used to fit the parameter  $\lambda$  (see text).

- The weight  $\alpha_0$  is a free parameter and has to be determined by the unfolding procedure.
- $\alpha_1$  can be extracted from the time spectrum:

$$\alpha_1 = 1 - \frac{T(t_{max})}{T(0)} e^{\lambda(t_{max}-t_0)} \quad (8.29)$$

where  $t_{max}$  is the maximum drift time, i.e. the trailing edge of the muon time spectrum. In Figure 8.9 we can see that  $t_{max} \approx 500$  ns.

- The normalization factor  $N$  is fully determined by the other parameters. It assures that  $\int T(t) dt = 1$ .

In summary, there is one free parameter more than in the case without background.

Applying the method to eight tubes that were fully or partially covered by ODYSSEUS, yields the following result: The time spectrum resulting from the fitted values of the free parameters is superimposed on the measured spectrum in Figure 8.9 and shows quite a good agreement. The precision of the unfolded r-t relationship in presence of a gamma background is shown in Figure 8.11. Although the rms deviation of  $85 \mu\text{m}$  is much worse than without background, the unfolded r-t relationship is still acceptable as start for the iterative autocalibration procedure.

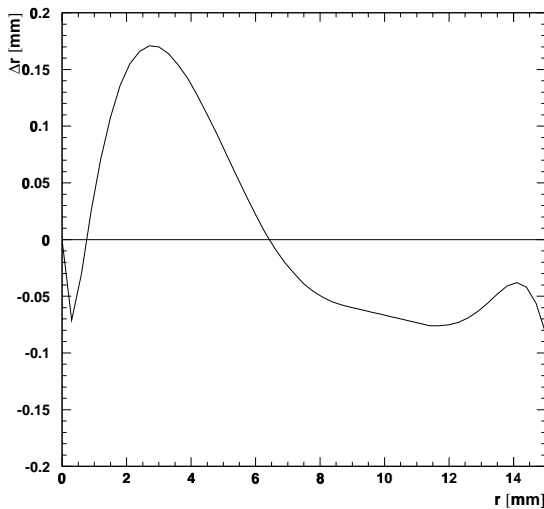


Figure 8.11: Time difference between unfolded and true  $\tau(r)$  converted into a radius difference using the local drift velocity.

### **8.2.5 Applicability in ATLAS**

At ATLAS, drift tubes will be operated at different magnetic fields, temperatures, background rates etc. These change not only the r-t relationship, but the whole response function. In practice we cannot measure the response under all conditions; we shall use a small number of response functions for unfolding the r-t relationship within certain calibration zones. The spectra from all tubes in such a zone ( $\geq 100$  tubes) will be summed after aligning the time axes of all tubes. This means that there will be very high statistics.

The accuracy will depend on how much the response differs from the one used. We expect efficiency, asymmetry and  $\delta$ -ray probability to be rather independant of the conditions; it is mainly the resolution that will be affected. However, away from the wire and wall the drift-time spectrum is rather insensitive to the resolution. This insensitivity prevents us from also extracting the resolution from unfolding.

The problem of uneven illumination in test beams will be much reduced within an auto-calibration zone in ATLAS. The variations of the efficiency function  $\eta(r)$  from one tube to the other will also be considerably reduced. In the prototype chambers used for the test-beam studies the wires had eccentricities of up to  $200\ \mu\text{m}$ , whereas the concentricity specification for the final chambers is  $100\ \mu\text{m}$ .

## 8.3 Autocalibration Using Muon Tracks

So far we have introduced methods for determining the r-t relationship with a precision between 50 and 100  $\mu\text{m}$  precision, which is a good starting point for the iterative high-precision technique of autocalibration.

### 8.3.1 The Principle of Autocalibration

Autocalibration starts with a first-order r-t relationship  $r_{\text{start}}(t)$  which has a systematic deviation  $\epsilon(t)$  from the true relationship  $r_{\text{true}}(t)$ :

$$r_{\text{start}}(t) = r_{\text{true}}(t) + \epsilon(t) \quad (8.30)$$

In the first iteration this start r-t relationship is used to convert the measured drift times  $t_i$  in a multilayer of tubes into hit radii to which then a straight track is fitted. The fitted track serves for obtaining a better estimate for the r-t relationship. In the next iteration the improved r-t relationship replaces  $r_{\text{start}}(t)$  for converting the drift times into radii. Again straight tracks are fitted and used for improving the space-time relationship. This procedure is repeated until the r-t relationship has converged.

**The task of autocalibration is to gain knowledge about the deviation  $\epsilon(t)$  of the start r-t relationship by using the information contained in the fit residuals  $\Delta_i$ :**

$$\Delta_i \equiv r_{\text{start}}(t_i) - r_{i,\text{fit}} \quad (8.31)$$

The index  $i$  designates the tubes hit by the muon (see the illustration in Figure 8.12).  $r_{i,\text{fit}}$  is the shortest distance between the fitted track and wire  $i$ .

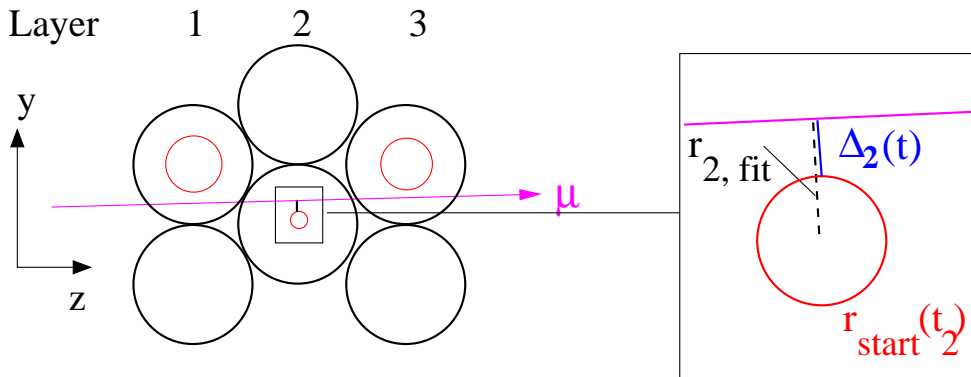


Figure 8.12: Illustration of the definition of the fit residuals, shown for the hit in the second tube layer.

The outlined calibration principle has some important consequences:

- The muon tracks have to be straight lines in a sufficiently good approximation. In ATLAS the muons to be used for autocalibration will have momenta down to 6 GeV/c (lower selection limit of the low  $p_T$  Level 1 muon trigger). Given the magnetic field of up to 1 T, the

deviation of a 6 GeV/c muon track from the straight line is only 16  $\mu\text{m}$  within a multilayer, but 1.5 mm within the superlayer (chamber). This is one reason why autocalibration has to be done for each multilayer separately.

- The r-t relationship must be the same in all tubes used for a track fit. This is another argument restricting us to the separate calibration of every individual multilayer. In the two multilayers of a chamber the r-t relationships are generally unequal due to the inhomogeneous magnetic field and perhaps also due to slightly different gas compositions or temperatures.

Our discussion will start in a general, mathematical way: we first want to find the relation between  $\varepsilon(t)$  and  $\Delta_i$ . This will tell us which information about  $\varepsilon(t)$  is available in  $\Delta_i$ . In particular we are interested in the question whether  $\varepsilon(t)$  can be uniquely inferred from the residuals measured in a sample of tracks. From experiments it is already known that the spread of the track incidence angles plays a crucial role (see e.g. [VIE 96, SAM 97, CRE 97]). Our aim is to explore this issue in a more systematic way.

Based on these insights we shall present two technical realizations of autocalibration and discuss their advantages and disadvantages.

Finally a Monte Carlo study of autocalibration for ATLAS MDT chambers with their particular spread of incidence angles will be described.

### 8.3.2 An Algebraic Approach to Autocalibration

#### 8.3.2.1 The Matrix Equation of Autocalibration

Consider a track fit through  $n$  hits using  $r_{\text{start}}(t)$  to convert the measured drift times  $t_i$  into hit radii. As defined in (8.30),  $r_{\text{start}}(t)$  is wrong by  $\varepsilon(t)$ . Furthermore, each measured drift time has a statistical error

$$\delta t_i = t_i - t_{i,\text{mean}} \quad (8.32)$$

where  $t_{i,\text{mean}}$  is the mean drift time corresponding to the true distance of the track from the wire. This translates into a statistical error on the measured hit radius

$$r_i \equiv r_{\text{start}}(t_i) \quad (8.33)$$

which now has two error contributions:

$$\begin{aligned} r_i &= r_{\text{start}}(t_{i,\text{mean}}) + \frac{dr_{\text{start}}}{dt} \delta t_i \\ &= r_{\text{true}}(t_{i,\text{mean}}) + \varepsilon(t_{i,\text{mean}}) + \frac{dr_{\text{start}}}{dt} \delta t_i \\ &= r_{\text{true}}(t_{i,\text{mean}}) + \varepsilon(t_{i,\text{mean}}) + \delta r_i \end{aligned} \quad (8.34)$$

Since the fit is determined by the hit radii in all tubes crossed by the track, the residual  $\Delta_i$  in a tube  $i$  depends on the deviations  $\varepsilon(t_k)$  and on the statistical errors  $\delta r_k$  in all  $n$  tubes. We express  $\Delta_i$  by a Taylor expansion in  $\varepsilon(t_k)$  and  $\delta r_k$ :

$$\Delta_i = \sum_{k=1}^n \left. \frac{d\Delta_i}{dr_k} \right|_{\varepsilon(t_k)=\delta r_k=0} [\varepsilon(t_k) + \delta r_k] + \mathcal{O}(2) \quad (8.35)$$

Assuming a good start r-t relationship (i.e. a small deviation  $\varepsilon(t_k)$ ) we can drop the higher orders and obtain the matrix equation

$$\Delta_i = \sum_{k=1}^n M_{ik} [\varepsilon(t_k) + \delta r_k] \quad (8.36)$$

where we have defined the matrix elements as

$$M_{ik} \equiv \left. \frac{d\Delta_i}{dr_k} \right|_{\varepsilon(t_k)=\delta r_k=0} . \quad (8.37)$$

The next step is the determination of these matrix elements. From the definitions (8.31), (8.33) and (8.37) follows

$$M_{ik} = \delta_{ik} - \left. \frac{dr_{i,\text{fit}}}{dr_k} \right|_{\varepsilon(t_k)=\delta r_k=0} . \quad (8.38)$$

where  $\delta_{ik}$  is the Kronecker symbol. The distance of the fitted track

$$y = mz + c \quad (8.39)$$

from wire  $i$  is

$$r_{i,\text{fit}} = \frac{|mz_i + c - y_i|}{\sqrt{1+m^2}} , \quad (8.40)$$

where  $(z_i, y_i)$  is the position of wire  $i$ . Now the derivative  $\frac{dr_{i,\text{fit}}}{dr_k}$  in (8.38) can be written as

$$\frac{dr_{i,\text{fit}}}{dr_k} = \frac{\partial r_{i,\text{fit}}}{\partial m} \cdot \frac{\partial m}{\partial r_k} + \frac{\partial r_{i,\text{fit}}}{\partial c} \cdot \frac{\partial c}{\partial r_k} . \quad (8.41)$$

The terms  $\frac{\partial r_{i,\text{fit}}}{\partial m}$  and  $\frac{\partial r_{i,\text{fit}}}{\partial c}$  are calculated from (8.40). The two other terms  $\frac{\partial m}{\partial r_k}$  and  $\frac{\partial c}{\partial r_k}$  can be obtained by implicate differentiation of the  $\chi^2$  minimization equations pertaining to the track fit procedure:

$$\frac{d}{dr_k} \frac{\partial \chi^2}{\partial m} = 0 \quad (8.42)$$

$$\frac{d}{dr_k} \frac{\partial \chi^2}{\partial c} = 0 \quad (8.43)$$

with

$$\chi^2 = \sum_{i=1}^n \frac{1}{\sigma^2(r_i)} [r_i - r_{i,\text{fit}}(m, c)]^2 \quad (8.44)$$

Lengthy algebraic transformations which are displayed in Appendix A finally yield the following expression for the matrix elements:

$$M_{ik} = \delta_{ik} - \text{sgn}(\rho_{i,\text{fit}}) \text{sgn}(\rho_{k,\text{fit}}) \frac{\sum_{l=1}^n \frac{1}{\sigma^2(r_k)\sigma^2(r_l)} (\zeta_i - \zeta_l)(\zeta_l - \zeta_k)}{\left( \sum_{l=1}^n \frac{1}{\sigma^2(r_l)} \zeta_l \right)^2 - \left( \sum_{l=1}^n \frac{1}{\sigma^2(r_l)} \right) \left( \sum_{j=1}^n \frac{1}{\sigma^2(r_j)} \zeta_j^2 \right)} \quad (8.45)$$

with

$$\zeta_i \equiv \frac{1}{\sqrt{1+m^2}}[z_i + m(y_i - c)] = \sqrt{1+m^2}z_i - m\rho_{i,\text{fit}} . \quad (8.46)$$

$\rho_{i,\text{fit}}$  is the signed track radius

$$\rho_{i,\text{fit}} = \frac{mz_i + c - y_i}{\sqrt{1+m^2}} \quad (8.47)$$

$$|\rho_{i,\text{fit}}| = r_{i,\text{fit}} \quad (8.48)$$

$$\text{sgn}(\rho_{i,\text{fit}}) = \begin{cases} +1 & \text{if the track passes above wire } i \\ -1 & \text{if the track passes below wire } i \end{cases} \quad (8.49)$$

(The terms “above” and “below” become evident from Figure 8.12.)

### 8.3.2.2 Autocalibration Constraints for a Given Track

In the previous section we have shown that the fit residuals  $\Delta_i$  for a given track can be expressed as a function of the systematic and statistical errors  $\varepsilon(t_k)$  and  $\delta r_k$  of the hit radii with the matrix equation (8.36). The dimension of the matrix is the number of tubes crossed by the track.

The problem of autocalibration consists in determining  $\varepsilon(t_k)$  from the  $\Delta_i$ . As a first step we want to eliminate the statistical error  $\delta r_k$ . Keeping in mind that the matrix  $M$  depends on  $m$  and  $c$ , we average (8.36) over many tracks with the same slope and intercept, such that  $\langle \delta r_k \rangle$  can be neglected compared to  $\varepsilon(t_k)$ . This results in

$$\langle \Delta_i \rangle = \sum_{k=1}^n M_{ik} \varepsilon(t_k) \quad (8.50)$$

Now the straightforward idea is to invert  $M$  and determine all  $\varepsilon(t_k)$ . However,  $M$  turns out to be singular:

$$\text{rank}(M) = \dim(M) - 2 = n - 2 \quad (8.51)$$

There are only  $n - 2$  independent equations, with the consequence that the linear system of equations is underdetermined. We found an algebraical proof for  $\text{rank}(M) \leq n - 2$  which is given in Appendix B. This is sufficient to demonstrate the singularity. For the general equality we only have empirical evidence. Intuitively the theorem (8.51) can be understood by considering that the straight-line fit correlates the  $n$  components  $\Delta_i$  by fixing two degrees of freedom, namely  $m$  and  $c$ .

To each possible solution  $\varepsilon(t)$  one can add a function  $\xi(t)$  obeying to the homogeneous equation

$$0 = \sum_{k=1}^n M_{ik} \xi(t_k) \quad (8.52)$$

without any change to the observed residuals  $\Delta_i$ .

The physical conclusion from (8.51) is the fact that in general the fit residuals for a given track do not provide enough information to uniquely infer the impact radii at the measured times  $t_i$ .

Later this observation will be generalized to samples of tracks with different intercepts and identical slopes. But before extending the formalism we want to further analyze the amount of information contained in the residuals for a fixed track.

Fortunately, since the r-t relationships of all tubes used for the track fit are required to be equal, there are constraints on the functions of freedom  $\xi(t)$ . We will start with the general treatment of the constraints and then illustrate this complicated matter with some examples.

- Due to the correlation between the drift times in different tubes Equation (8.52) contains information about the shape of possible functions  $\xi(t)$ . See Example 2 further below.
- If two or more of the drift times  $t_i$  are equal, the number of independent variables  $\xi(t_k)$  in (8.52) is reduced and we can replace (8.52) by an equation where the matrix columns corresponding to equal  $\xi(t_k)$  are added:

$$\underbrace{\begin{pmatrix} M_{11} & \dots & M_{1\alpha} & \dots & M_{1\beta} & \dots & M_{1n} \\ \vdots & & & & & & \vdots \\ \vdots & & & & & & \vdots \\ \vdots & & & & & & \vdots \\ \vdots & & & & & & \vdots \\ M_{n1} & \dots & M_{n\alpha} & \dots & M_{n\beta} & \dots & M_{nn} \end{pmatrix}}_{n \text{ columns}} \begin{pmatrix} \xi(t_1) \\ \vdots \\ \xi(t_\alpha) \\ \vdots \\ \xi(t_\beta) \\ \vdots \\ \xi(t_n) \end{pmatrix} = \vec{0} \quad \text{with } t_\alpha = t_\beta \quad (8.53)$$

transforms into

$$\underbrace{\begin{pmatrix} M_{11} & \dots & M_{1\alpha} + M_{1\beta} & \dots & M_{1n} \\ \vdots & & & & \vdots \\ M_{n1} & \dots & M_{n\alpha} + M_{n\beta} & \dots & M_{nn} \end{pmatrix}}_{n-1 \text{ columns}} \begin{pmatrix} \xi(t_1) \\ \vdots \\ \xi(t_\alpha) \\ \vdots \\ \xi(t_n) \end{pmatrix} = \vec{0} \quad (8.54)$$

and so on until all involved  $t_i$  are different.

Suppose we have reduced the number of variables by  $k$ . We now deal with a non-square matrix with  $n$  rows and  $n - k$  columns.

The next step is to triangularize the reduced matrix equation with the Gaussian algorithm. Suppose the lowest  $l$  rows of the resulting upper-right triangular matrix consist only of 0's:

$$\underbrace{\begin{array}{c} n-l \\ l \end{array}}_{\left\{ \begin{array}{c} n-k \\ \hline \end{array} \right\}} \left( \begin{array}{cccccc} M'_{11} & \cdots & \cdots & \cdots & \cdots & M'_{1,n-k} \\ 0 & \ddots & & & & \vdots \\ \vdots & \ddots & \ddots & & & \vdots \\ 0 & \cdots & 0 & M'_{n-l,n-l} & \cdots & M'_{n-l,n-k} \\ 0 & \cdots & \cdots & 0 & \cdots & 0 \\ \vdots & & & \vdots & & \vdots \\ 0 & \cdots & \cdots & 0 & \cdots & 0 \end{array} \right) \begin{pmatrix} \xi(t'_1) \\ \vdots \\ \xi(t'_{n-k}) \end{pmatrix} = \vec{0} \quad (8.55)$$

The variables  $\xi(t'_i)$  ( $i = 1, \dots, n - k$ ) are a subsample of the  $\xi(t_i)$  ( $i = 1, \dots, n$ ) with rearranged indices.

The original matrix (before reducing the variables) had the rank  $n - 2$ , corresponding to 2 rows with only zeroes after triangularization. After the reduction of variables by simple addition of columns the number of zero-rows cannot be smaller than before. Therefore we know that  $l \geq 2$ .  $l > 2$  happens only in a few special cases where more than two columns are added up and yield an additional row of zeroes after triangularization. About  $k$  we know that  $0 \leq k < n$ .

Depending on  $k$  and  $l$  the following cases can occur:

1.  $k = l$ : By dropping the rows with only 0's the triangularized matrix becomes quadratic and non-singular. All  $\xi(t_k)$  have to be zero. In that case the function  $\varepsilon(t)$  is uniquely determined at the drift times  $t_i$ . However, these unique cases are better characterized by the radii  $r$  where  $\varepsilon(t(r)) = 0$ , and not by the drift times at which this occurs<sup>2</sup>. Let us introduce the name “fixpoint” for a triple  $(\alpha, c, r/R)$  with unique autocalibration result. The incidence angle  $\alpha$  is defined such that  $\tan \alpha = m$ , where  $m$  is the track slope.  $c$  is the track intercept and  $R$  the tube radius.

Note that for achieving  $k = l$  we need  $k \geq 2$ , i.e. the number of variables  $\xi(t_k)$  must be reduced by at least 2.

2.  $k < l$ : The system is underdetermined by  $l - k$  degrees of freedom. This number of undetermined degrees of freedom has to be compared with the total number  $n - k$  of different variables  $\xi(t_k)$ . The degree of determination can be quantified by

$$Q \equiv 1 - \frac{l - k}{n - k} = \frac{n - l}{n - k} \quad , \quad (8.56)$$

which ranges between 0 and 1.

---

<sup>2</sup>The radii and incidence angles where autocalibration gives unique results are quantities which only depend on the chamber geometry, whereas the corresponding drift times depend on the individual gas mixtures.

$Q = 1$  characterizes a fixpoint.

$Q = 0$  means that  $\xi(t)$  is arbitrary and not constrained at all. This happens in the case  $\alpha = 30^\circ$ ,  $r < (\sqrt{3} - 1)R$  (see Example 3 further below).

$0 < Q < 1$  means that the system is not uniquely determined, but the set of possible solutions  $\xi(t)$  is constrained.

3.  $k > l$  is unphysical and does not occur. It would correspond to  $n - l$  contradictory equations for  $n - k < n - l$  variables, implying that there is no function  $\varepsilon(t)$  which could produce the observed residuals.

Note that  $n$  is the number of hits on the track, not the number of tube layers! For example a track through a triple layer can cross more than three tubes (mainly at big angles).

Each constraint on the r-t relationship at a radius  $r$  is contributed by one specific track with intercept  $c$  and slope  $m$  (or angle  $\alpha$ ). For a complete characterization of the constraints they would have to be drawn into a three-dimensional diagramme with axes  $\alpha$ ,  $c$  and  $r/R$ , which is hardly feasible. Since in practice the available intercept range is big enough to cover all impact radii in all tube layers whereas the range in  $\alpha$  is limited, the most interesting projection of the  $(\alpha, c, r/R)$ -space is the one onto the  $(\alpha, r/R)$ -plane. In general the degree of determination  $Q$  in a point  $(\alpha, r/R)$  is not unambiguous because there are several tracks with identical  $\alpha$  but different  $c$  giving different amounts of information about the r-t relationship at  $r$  (see Example 6 below). We decided to give for every point in the  $(\alpha, r/R)$ -plane the maximum value  $Q_{\max}(\alpha, r/R) \equiv \max\{Q(\alpha, c, r/R)\}$ . Such constraint diagrammes are displayed in the Figures 8.13 to 8.15. The first of them represents autocalibration for multilayers with three tube layers; the second plot is the analogue for four tube layers. The last figure refers to a common autocalibration for both triple layers of a chamber. These figures have been obtained by a “brute force” search for tracks with identical radii at given incidence angles  $\alpha$ , followed by an algebraic evaluation of the respective matrix equations.

- The circular markers denote the fixpoints.
- The dashed lines at  $\alpha = 30^\circ$  have  $Q = 0$ .
- The points  $(\alpha, r/R)$  lying on the solid lines are defined by tracks where two or more hits have the same drift times (i.e.  $k \geq 1$ ), but where one degree of freedom out of  $n - k > 1$  in the matrix equation remains undetermined: these points have  $l - k = 1$  and thus  $Q = (n - k - 1)/(n - k)$ . The black (darker) lines stand for  $k = 1$  (see also Example 4), the green (lighter) lines for  $k = 2, n \geq 4$  (see also Example 6). The condition  $n - k > 1$  has the purpose to exclude the case  $n - k = l - k = 1$  where the only available degree of freedom is undetermined ( $30^\circ$  case). The value of  $n$  relevant for a point  $(\alpha, r/R)$  can be looked up in the Figures 8.16 and 8.17 for three and four layers respectively.
- The points away from all lines and markers correspond to tracks for which all drift times  $t_i$  are different. They have  $k = 0, l = 2$  and thus  $Q = (n - 2)/n$  which is the worst case apart from the  $30^\circ$  problem with  $Q = 0$ .

For all three multilayer configurations there are almost no constraints at track angles around  $30^\circ$ . This will be geometrically clarified in Example 3 below. Another difficult angular region is around  $0^\circ$  (see Example 2). The region between about  $5^\circ$  and  $22^\circ$  is rather well constrained. Above about  $35^\circ$  the typical number of hits per layer becomes greater than one and the number of hits per track increases. Therefore the chance for having identical drift times in two hits is enhanced, which leads to a high fixpoint density. Increasing the number of tube layers has the same effect.

A bigger number of hits per track has the additional advantage that the degree of determination for the not fully constrained cases increases: For three hits a track passing all tubes at different radii determines the r-t relationship at these radii with  $Q = 1/3$ . For four hits this value increases to  $Q = 1/2$  and for six hits to  $Q = 2/3$ . If two track radii are equal (i.e.  $k = 1$ ) and one degree of freedom is undetermined (i.e.  $l = k + 1 = 2$ ), we get  $Q = 1/2$  for three hits,  $Q = 2/3$  for four hits and  $Q = 4/5$  for six hits.

Figure 8.15 demonstrates that simultaneous autocalibration for all six layers of a chamber would be very advantageous from the point of view of fixpoints. Apart from the difficult region around  $30^\circ$  the density of fixpoints is high. The gap from  $36^\circ$  to  $40^\circ$  in the fixpoint pattern does not constitute a real problem because it is filled by many constraints with one undetermined degree of freedom (like the solid lines in the Figures 8.13 and 8.14). These have  $Q \geq 4/5$ . Unfortunately, as we have explained in Section 8.3.1, a common autocalibration for all six layers of a chamber will not be possible at ATLAS.

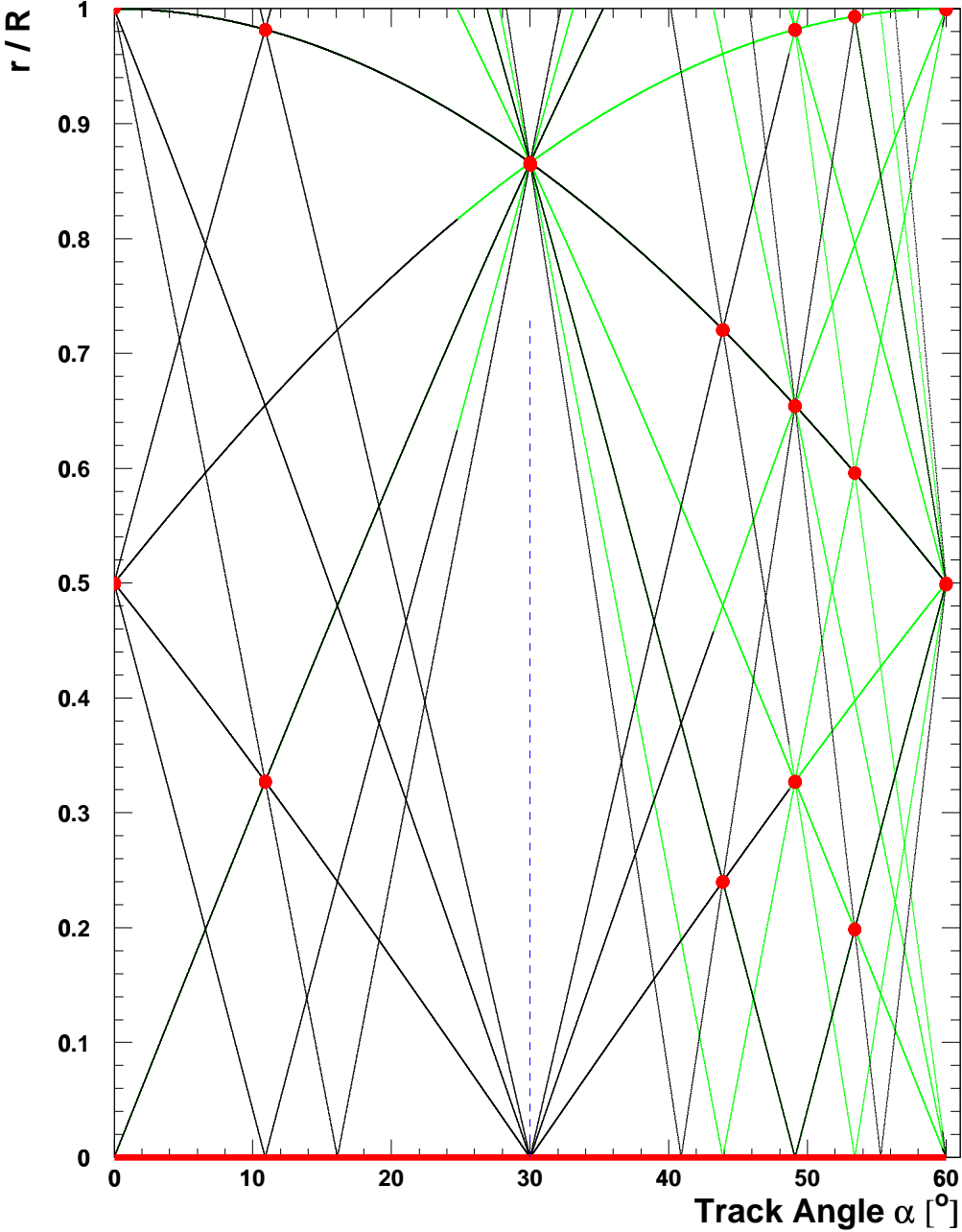
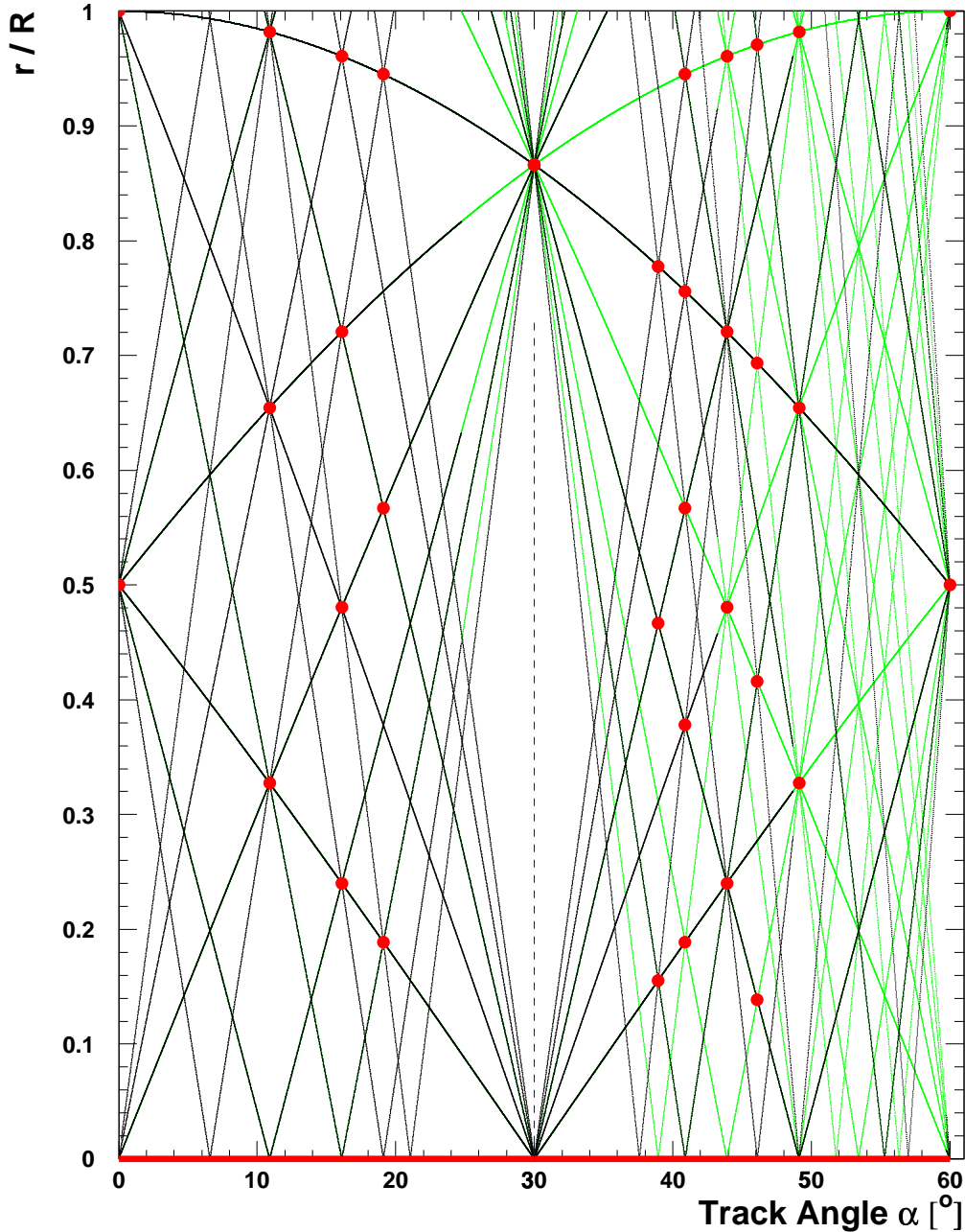


Figure 8.13: Constraints on the result of autocalibration for a multilayer with 3 tube layers. The picture indicates for every track radius  $r$  the maximum achievable degree of determination from tracks with incidence angle  $\alpha$ . The circular markers and the thick line at  $r = 0$  represent fixpoints ( $Q = 1$ ). The explanation why  $r = 0$  is a fixpoint for all angles, is given in Example 5. The solid lines correspond to  $Q = (n - k - 1)/(n - k)$  (1 undetermined degree of freedom): the black (darker) lines stand for  $k = 1$ , the green (lighter) lines for  $k = 2, n \geq 4$ . The dashed line at  $30^\circ$  has  $Q = 0$ . All other points in the plane have  $Q = (n - 2)/n$  (2 undetermined degrees of freedom).



*Figure 8.14: Constraints on the result of autocalibration for a multilayer with 4 tube layers. The circular markers and the thick line at  $r = 0$  represent fixpoints ( $Q = 1$ ). The solid lines correspond to  $Q = (n - k - 1)/(n - k)$ : the black (darker) lines stand for  $k = 1$ , the green (lighter) lines for  $k = 2, n \geq 4$ . The dashed line at  $30^\circ$  has  $Q = 0$ . All other points in the plane have  $Q = (n - 2)/n$ . This figure concerns the MDT stations BIS, BIL, BIR, BEE, EIS, EIL.*

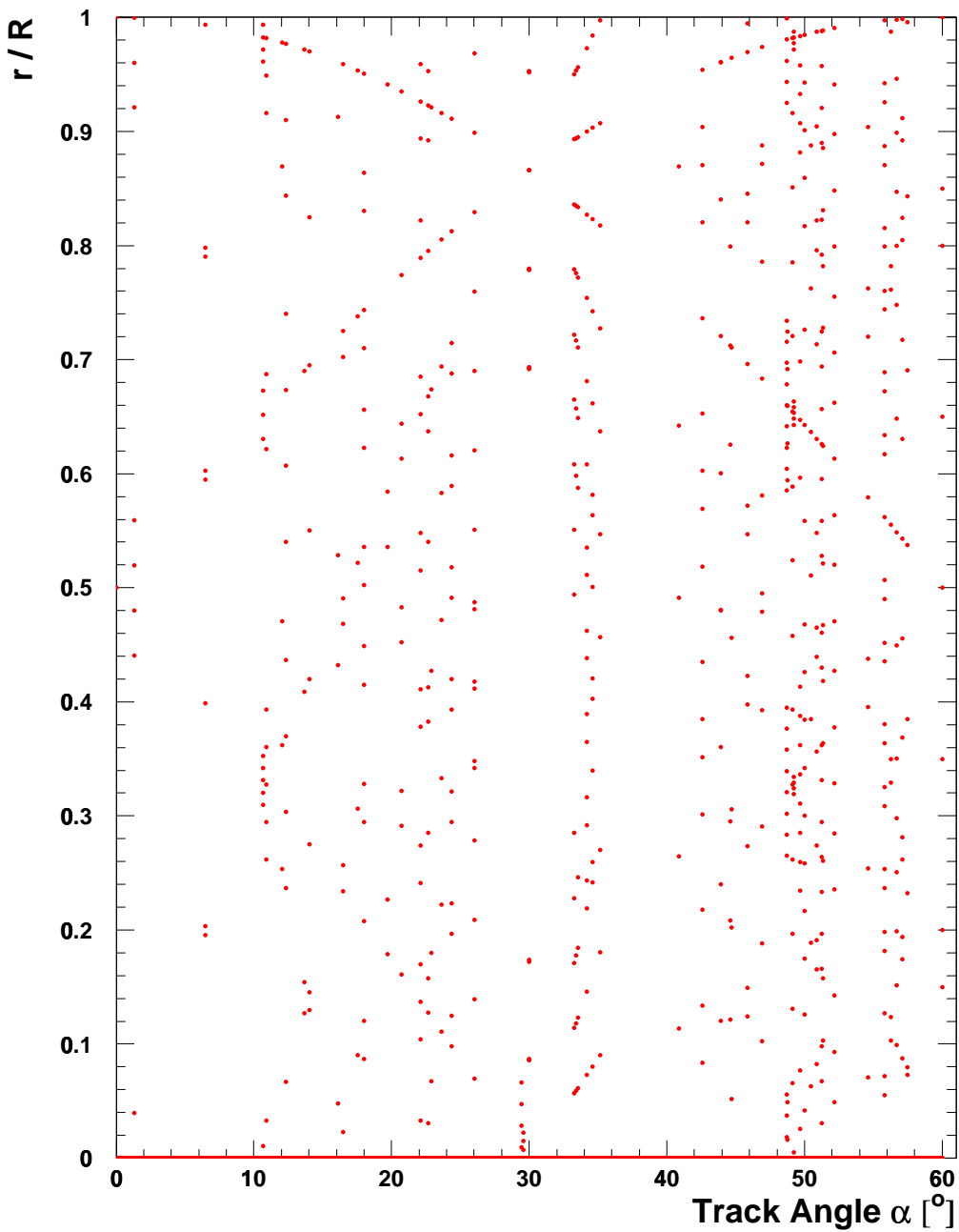


Figure 8.15: Constraints on the result of autocalibration for an entire chamber with two triple layers of tubes (distance between the multilayers: 235 mm). For a better visibility only the fixpoints are shown. The worst case at  $30^\circ$  and  $r < 0.56$  has  $Q = 1/2$ . All other points have  $2/3 \leq Q < 1$ .

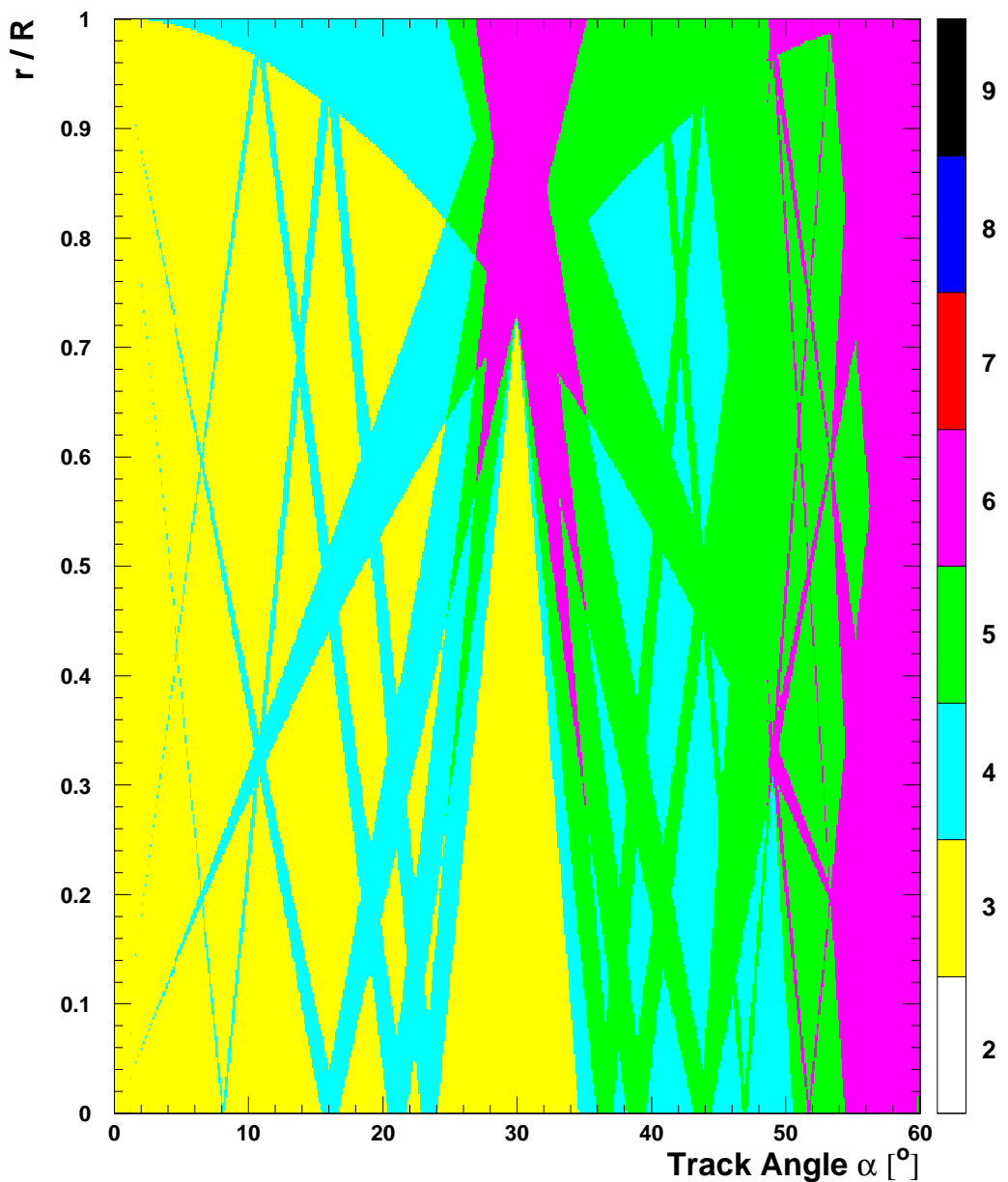


Figure 8.16: Three tube layers: The colour code (or grey scale) gives the number  $n$  of hits on the track with angle  $\alpha$  determining the  $r$ - $t$  relationship at a radius  $r$  with the highest  $Q$ .

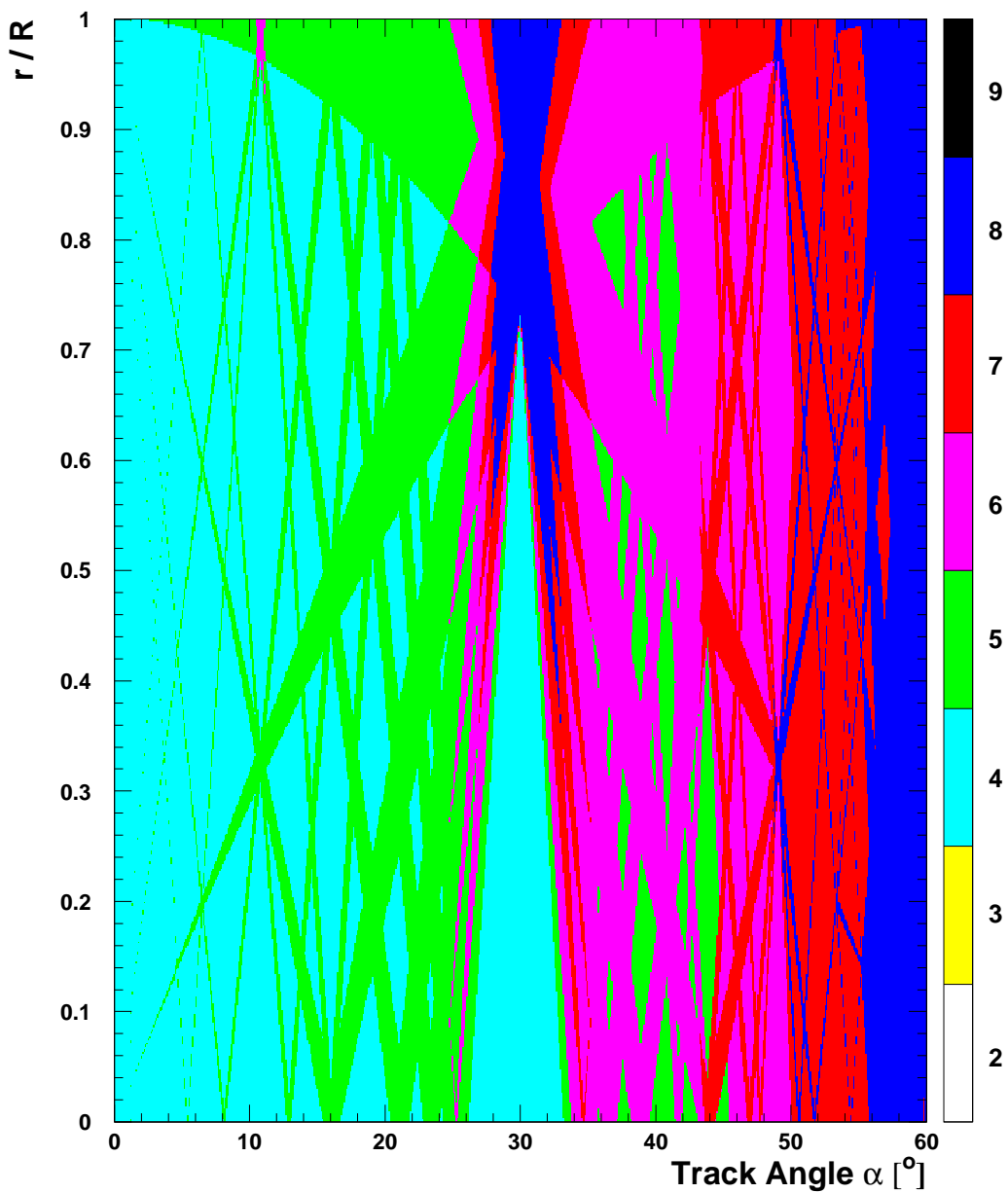


Figure 8.17: Four tube layers: The colour code (or grey scale) gives the number  $n$  of hits on the track with angle  $\alpha$  determining the  $r$ - $t$  relationship at a radius  $r$  with the highest  $Q$ .

### Examples

After the general treatment we now give typical examples for the most important kinds of constraints. This illustration will concentrate on multilayers with three layers of tubes.

#### 1. All track radii are different:

Consider e.g. a track with  $\alpha = 5^\circ$  and a track radius  $r_1 = 0.5R$  in the first layer (Figure 8.18). It has  $n = 3$  hits.

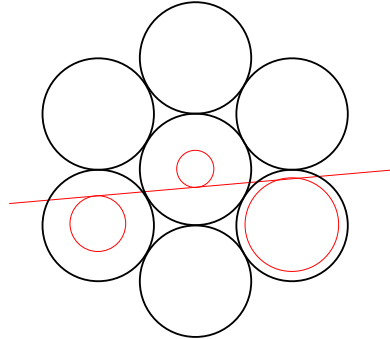


Figure 8.18: Illustration of Example 1. All impact radii are different.  $Q = 1/3$ .

The matrix equation reads

$$\vec{0} = \begin{pmatrix} 0.15013 & 0.31623 & 0.16610 \\ 0.31623 & 0.66610 & 0.34987 \\ 0.16610 & 0.34987 & 0.18377 \end{pmatrix} \begin{pmatrix} \xi(t(0.50R)) \\ \xi(t(0.35R)) \\ \xi(t(0.80R)) \end{pmatrix}$$

Since we cannot reduce the number of variables  $\xi(t(r_i))$ , we get  $k = 0$ . Triangularization yields:

$$\vec{0} = \begin{pmatrix} 0.15013 & 0.31623 & 0.16610 \\ 0 & 0 & 0 \\ 0 & 0 & 0 \end{pmatrix} \begin{pmatrix} \xi(t(0.50R)) \\ \xi(t(0.35R)) \\ \xi(t(0.80R)) \end{pmatrix}$$

The two last rows consisting of zeroes we have  $l = 2$ . Thus the degree of determination is  $Q = \frac{3-2}{3-0} = \frac{1}{3}$ . This means that the r-t relationship can vary freely in any two out of the three involved radii. The third radius (i.e. one out of three) is fixed by the track through the two others.

#### 2. Fixpoint and symmetry for $\alpha = 0^\circ$ :

The matrix equation for  $\alpha = 0^\circ$  is

$$\vec{0} = \begin{pmatrix} 1/6 & 1/3 & 1/6 \\ 1/3 & 2/3 & 1/3 \\ 1/6 & 1/3 & 1/6 \end{pmatrix} \begin{pmatrix} \xi(t(r_1)) \\ \xi(t(R - r_1)) \\ \xi(t(r_1)) \end{pmatrix}$$

Since the impact radii in the first and third tube are equal, we can add the first and the third column of the matrix:

$$\vec{0} = \begin{pmatrix} 1/3 & 1/3 \\ 2/3 & 2/3 \\ 1/3 & 1/3 \end{pmatrix} \begin{pmatrix} \xi(t(r_1)) \\ \xi(t(R - r_1)) \end{pmatrix}$$

After triangularization we obtain

$$\vec{0} = \begin{pmatrix} 1/3 & 1/3 \\ 0 & 0 \\ 0 & 0 \end{pmatrix} \begin{pmatrix} \xi(t(r_1)) \\ \xi(t(R - r_1)) \end{pmatrix}$$

For the special track with  $r_1 = R/2$  (shown in Figure 8.19a) another reduction of variables can be done:

$$\vec{0} = \begin{pmatrix} 2/3 \\ 0 \\ 0 \end{pmatrix} \begin{pmatrix} \xi(t(R/2)) \end{pmatrix}$$

In this case we have  $n = 3$ ,  $k = 2$ ,  $l = 2$  and thus  $Q = 1$ , i.e. a fixpoint.

All other tracks have  $n = 3$ ,  $k = 1$ ,  $l = 2$  and  $Q = 1/2$ . The matrix equation for general  $r_1$  yields a symmetry condition for  $\xi(t(r))$ :

$$0 = \xi(t(r_1)) + \xi(t(R - r_1)) \quad .$$

$\xi(t(r))$ , i.e. the function by which the calibrated r-t relationship may be wrong, has to be antisymmetric about the fixpoint at  $r = R/2$  (like the two example functions in Figure 8.19b).

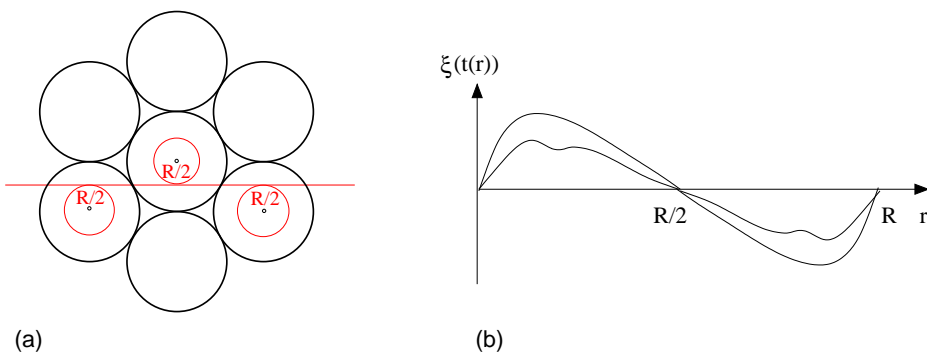


Figure 8.19: (a) Illustration of the hit pattern for Example 2. (b) Two freedom functions  $\xi(t(r))$  allowed by tracks with  $\alpha = 0^\circ$ .

### 3. The problem at $\alpha = 30^\circ$ :

Tracks passing a triple layer of tubes at an angle of  $30^\circ$  can cross three or six tubes, depending on the track intercept (Figure 8.20).

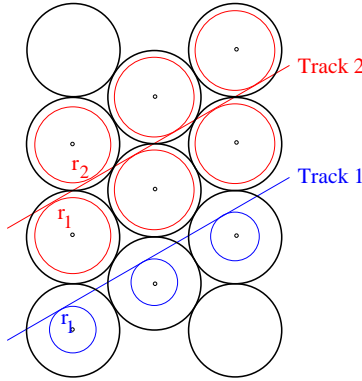


Figure 8.20: Hit pattern for Example 3: track 1 doesn't provide any information about the r-t relationship; track 2 defines a fixpoint at  $r \approx 0.866 R$ .

Let us first look at the case with  $n = 3$ . These tracks pass all tubes on the same side of the wires and at identical impact radii  $r_i = r_1$ . This happens if  $r_1 < (\sqrt{3} - 1)R$  (symbolized by the dashed line in Figure 8.13). A representative is track 1 in the figure. The corresponding matrix equation

$$\vec{0} = \begin{pmatrix} 1/6 & -1/3 & 1/6 \\ -1/3 & 2/3 & -1/3 \\ 1/6 & -1/3 & 1/6 \end{pmatrix} \begin{pmatrix} \xi(t(r_1)) \\ \xi(t(r_1)) \\ \xi(t(r_1)) \end{pmatrix}$$

can be reduced by adding all three columns:

$$\vec{0} = \begin{pmatrix} 0 \\ 0 \\ 0 \end{pmatrix} \left( \begin{array}{c} \xi(t(r_1)) \\ \xi(t(r_1)) \\ \xi(t(r_1)) \end{array} \right)$$

Obviously this equation doesn't provide any constraint on  $\xi(t(r_1))$ . We have  $k = 2$ ,  $l = 3$  and thus  $Q = 0$ . This dilemma is also easy to understand intuitively: All measured drift times are equal (in the limit of perfect resolution or infinite statistics). Whatever r-t relationship is used, it will attribute the same radius to all hits, and the fit residuals will be zero.

In the case  $n = 6$  which happens for  $r_1 > (\sqrt{3} - 1)R$  the situation is better (track 2 in the figure):

$$\vec{0} = \begin{pmatrix} 0.47619 & 0.38095 & -0.23810 & 0.09524 & 0.04762 & -0.19048 \\ 0.38095 & 0.70476 & 0.20952 & -0.12381 & 0.03810 & 0.04762 \\ -0.23810 & 0.20952 & 0.81905 & 0.15238 & -0.12381 & 0.09524 \\ 0.09524 & -0.12381 & 0.15238 & 0.81905 & 0.20952 & -0.23810 \\ 0.04762 & 0.03810 & -0.12381 & 0.20952 & 0.70476 & 0.38095 \\ -0.19048 & 0.04762 & 0.09524 & -0.23810 & 0.38095 & 0.47619 \end{pmatrix} \begin{pmatrix} \xi(t(r_1)) \\ \xi(t(r_2)) \\ \xi(t(r_1)) \\ \xi(t(r_2)) \\ \xi(t(r_1)) \\ \xi(t(r_2)) \end{pmatrix}$$

$$\vec{0} = \begin{pmatrix} 0.28571 & 0.28571 \\ 0.62857 & 0.62857 \\ 0.45714 & 0.45714 \\ 0.45714 & 0.45714 \\ 0.62857 & 0.62857 \\ 0.28571 & 0.28571 \end{pmatrix} \begin{pmatrix} \xi(t(r_1)) \\ \xi(t(r_2)) \end{pmatrix}$$

$$\vec{0} = \begin{pmatrix} 0.28571 & 0.28571 \\ 0 & 0 \\ 0 & 0 \\ 0 & 0 \\ 0 & 0 \\ 0 & 0 \end{pmatrix} \begin{pmatrix} \xi(t(r_1)) \\ \xi(t(\sqrt{3}R - r_1)) \end{pmatrix}$$

At  $r = \frac{1}{2}\sqrt{3}R \approx 0.866 R$  we find a fixpoint. At the other radii  $Q = 1/2$ .

#### 4. One pair of identical radii:

Consider a track with  $\alpha = 5^\circ$  and track radii  $r_1 = r_2 = 0.42 R$ ,  $r_3 = 0.72 R$  (Figure 8.21).

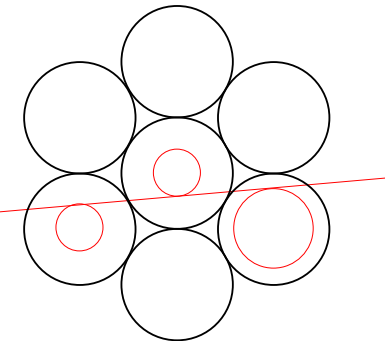


Figure 8.21: Illustration of Example 4 ("single pair").  $Q = 1/2$ .

In the matrix equation

$$\vec{0} = \begin{pmatrix} 0.15013 & 0.31623 & 0.16610 \\ 0.31623 & 0.66610 & 0.34987 \\ 0.16610 & 0.34987 & 0.18377 \end{pmatrix} \begin{pmatrix} \xi(t(r_1)) \\ \xi(t(r_1)) \\ \xi(t(r_3)) \end{pmatrix}$$

we can add the first two columns and get after triangulation:

$$\vec{0} = \begin{pmatrix} 0.46635 & 0.16610 \\ 0 & 0 \\ 0 & 0 \end{pmatrix} \begin{pmatrix} \xi(t(r_1)) \\ \xi(t(r_3)) \end{pmatrix}$$

This system has one undetermined degree of freedom:  $l = 2$ ,  $k = 1$ ,  $n = 1$ ; thus  $Q = 1/2$ . Consequently the points  $(5^\circ, 0.42)$  and  $(5^\circ, 0.72)$  sit on black solid lines in Figure 8.13.

##### 5. One pair of identical radii with fixpoint at $r = 0$ :

A peculiar situation happens if the track goes through the wire of an inner layer, like in Figure 8.22. The radii in the adjacent tubes are then equal and allow the reduction of the matrix equation.

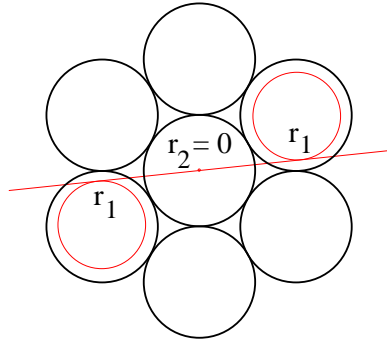


Figure 8.22: Illustration of Example 5 ("centred pair").  $Q = 1/2$ .

$$\begin{aligned} \vec{0} &= \begin{pmatrix} 1/6 & \pm 1/3 & -1/6 \\ \pm 1/3 & 2/3 & \mp 1/3 \\ -1/6 & \mp 1/3 & 1/6 \end{pmatrix} \begin{pmatrix} \xi(t(r_1)) \\ \xi(t(0)) \\ \xi(t(r_1)) \end{pmatrix} \\ \vec{0} &= \begin{pmatrix} 0 & \pm 1/3 \\ 0 & 0 \\ 0 & 0 \end{pmatrix} \begin{pmatrix} \xi(t(r_1)) \\ \xi(t(0)) \end{pmatrix} \end{aligned}$$

The consequence is that  $\xi(t(r_1))$  is completely unconstrained whereas at  $r = 0$  there is a fixpoint. It would be worthwhile checking whether this feature can be used to solve the  $t_0$ -problem, i.e. the determination of the absolute starting point of the drift-time scale.

##### 6. Two pairs of identical radii without fixpoint:

We now want to convince ourselves that reduction by two variables does not necessarily give rise to fixpoints. An example is shown in Figure 8.23a, where the track radii in the two outer hits and those in the two inner hits are equal. Now the calibrated r-t relationship can be wrong at both involved radii in a correlated way such that instead of the true

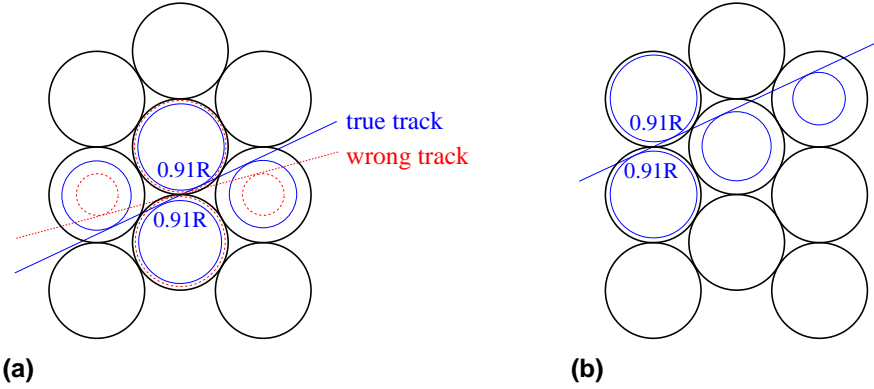


Figure 8.23: Hit pattern for Example 6: (a) “double pair” without fixpoint; the solid line and hit radii represent the true event geometry; the dotted radii correspond to a wrong  $r$ - $t$  relationship leading to the dotted track. (b) Alternative track determining  $r = 0.91 R$  with  $Q = 2/3$  instead of  $Q = 1/2$  like the track in (a).

track (solid line in the figure) another track (e.g. the dotted line) is reconstructed without any influence on the  $\chi^2$  of the fit. In the matrix formalism the situation for  $\alpha = 25^\circ$ ,  $r_1 = 0.73 R$ ,  $r_2 = 0.91 R$  looks as follows:

$$\vec{0} = \begin{pmatrix} 0.28379 & 0.37551 & -0.12449 & -0.21621 \\ 0.37551 & 0.71621 & 0.21621 & -0.12449 \\ -0.12449 & 0.21621 & 0.71621 & 0.37551 \\ -0.21621 & -0.12449 & 0.37551 & 0.28379 \end{pmatrix} \begin{pmatrix} \xi(t(r_1)) \\ \xi(t(r_2)) \\ \xi(t(r_2)) \\ \xi(t(r_1)) \end{pmatrix}$$

$$\vec{0} = \begin{pmatrix} 0.06758 & 0.25102 \\ 0.25102 & 0.93242 \\ 0 & 0 \\ 0 & 0 \end{pmatrix} \begin{pmatrix} \xi(t(r_1)) \\ \xi(t(r_2)) \end{pmatrix}$$

$$\vec{0} = \begin{pmatrix} 0.06758 & 0.25102 \\ 0 & 0 \\ 0 & 0 \\ 0 & 0 \end{pmatrix} \begin{pmatrix} \xi(t(r_1)) \\ \xi(t(r_2)) \end{pmatrix}$$

With  $n = 4$ ,  $l = 3$  and  $k = 2$  we find the degree of determination  $Q = 1/2$ .

The point  $(25^\circ, 0.91)$  is better determined by another track, parallel to the first one but with a different  $c$ . That other track which is shown in Figure 8.23b has  $k = 1$  and  $Q = 2/3$ . Since Figure 8.13 gives for every point the highest possible  $Q$ , points like  $(25^\circ, 0.91)$  are labelled by a black solid line corresponding to  $k = 1$  and not by a green line for  $k = 2$ .

Let us summarize these technical considerations in simpler words:

So far we have examined the constraints that an individual track contributes to the result of autocalibration. It was shown that only for a few tracks with particular angles and at some discrete radii the calibrated  $r$ - $t$  relationship is uniquely determined by the measured track fit

residuals. Other, less stringent constraints allow deviations of the r-t relationship, but keep them limited by imposing certain conditions on their shape. Requiring smoothness and monotony for  $r(t)$  enhances the practical importance of these partial constraints.

However, the fixpoint plots show that the individual constraints are not sufficient to obtain an r-t relationship which is correct over the full radial range. The obvious solution is to combine tracks with different angles, each of them contributing its own constraints.

### 8.3.2.3 Autocalibration Constraints Combining Different Tracks

If the only attainment of combining different tracks were a simple collection of the individual fixpoints, the situation would be rather desperate, particularly for three layers: For example, even within the large angular range from  $0^\circ$  to  $11^\circ$  we would only have three fixpoints and some partial constraints leaving room for deviations. The good news of the following considerations is that a sample of different tracks contains more information than just a linear superposition of the previously derived constraints. Even tracks with identical slopes but different intercepts bear astonishing correlations.

The treatment will start with a general derivation of the additional constraints from combining tracks. Afterwards the full information contained in a sample of tracks with identical slope but the entire range of intercepts will be analyzed. The final step will be the correlation of different track angles.

#### a. Fixpoints of Higher Order

Let us assume that we have  $N$  different tracks. Each track  $i$  has  $n_i$  hits with impact radii  $r_{ij}$  ( $j = 1, \dots, n_i$ ) and measured drift times  $t(r_{ij})$ . We now merge the individual matrix equations

$$M_i \vec{\xi}_i = \vec{0} \quad (i = 1, \dots, N) \quad (8.57)$$

where

$$\vec{\xi}_i \equiv \begin{pmatrix} \xi(t(r_{i1})) \\ \vdots \\ \xi(t(r_{in_i})) \end{pmatrix} \quad (8.58)$$

to one common equation:

$$\underbrace{\begin{pmatrix} M_1 & O & \dots & O \\ O & \ddots & & \vdots \\ \vdots & & \ddots & O \\ O & \dots & O & M_N \end{pmatrix}}_{\mathcal{M}} \begin{pmatrix} \vec{\xi}_1 \\ \vdots \\ \vec{\xi}_n \end{pmatrix} = \vec{0} \quad (8.59)$$

The common matrix has the properties

$$\dim(\mathcal{M}) = \sum_{i=1}^N n_i \quad (8.60)$$

$$\text{rank}(\mathcal{M}) = \sum_{i=1}^N n_i - 2N \quad (8.61)$$

In a similar way as with the normal fixpoints we can try to achieve uniqueness by looking for identical radii. This time however, identical radii are also relevant if they appear in different tracks. Again we assume that the number of independent variables  $\xi(t(r_{ij}))$  can be reduced by  $k$ , and after triangularization of the matrix the number of zero-rows is  $l$ . If  $k = l$  we have found a new fixpoint. Note that due to (8.60) and (8.61) we need  $k \geq 2N$ . A fixpoint created by correlating  $N$  tracks will be called “fixpoint of  $N^{\text{th}}$  order”.

The mechanism will be illustrated by the discussion of some interesting cases:

### b. Correlation of Tracks with Identical Slope

Consider the two tracks in Figure 8.24. They have a common incidence angle of  $16.1^\circ$ . Their impact radii in the first tube are  $r_1 = 0.24 R$  and  $r_2 = 0.72 R$  respectively. For the two tracks together only these two different impact radii occur.

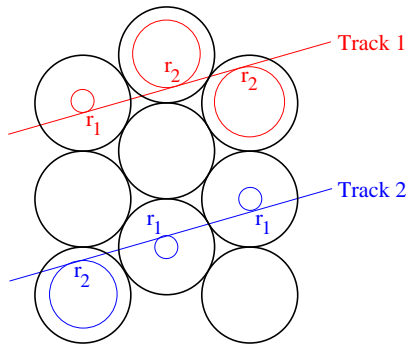


Figure 8.24: Creation of a second-order fixpoint by correlating the information of track 1 and track 2.

The common matrix equation for this two-track system is

$$\begin{pmatrix} 0.11468 & -0.27523 & -0.16055 & 0 & 0 & 0 \\ -0.27523 & 0.66055 & 0.38532 & 0 & 0 & 0 \\ -0.16055 & 0.38532 & 0.22477 & 0 & 0 & 0 \\ 0 & 0 & 0 & 1/6 & -1/3 & -1/6 \\ 0 & 0 & 0 & -1/3 & 2/3 & 1/3 \\ 0 & 0 & 0 & -1/6 & 1/3 & 1/6 \end{pmatrix} \begin{pmatrix} \xi(t(r_1)) \\ \xi(t(r_2)) \\ \xi(t(r_2)) \\ \xi(t(r_2)) \\ \xi(t(r_1)) \\ \xi(t(r_1)) \end{pmatrix} = \vec{0}$$

Due to the equal impact radii we can add the columns 1, 5, 6 and the columns 2, 3, 4:

$$\begin{pmatrix} 0.11468 & -0.43578 \\ -0.27523 & 1.04587 \\ -0.16055 & 0.61009 \\ -1/2 & 1/6 \\ 1 & -1/3 \\ 1/2 & -1/6 \end{pmatrix} \begin{pmatrix} \xi(t(r_1)) \\ \xi(t(r_2)) \end{pmatrix} = \vec{0}$$

Triangularization and suppression of the zero-rows yields

$$\begin{pmatrix} 0.11468 & -0.43578 \\ 0 & -0.39749 \end{pmatrix} \begin{pmatrix} \xi(t(r_1)) \\ \xi(t(r_2)) \end{pmatrix} = \vec{0},$$

which is non-singular! This implies that there are two second-order fixpoints at  $r_1 = 0.24R$  and  $r_2 = 0.72R$  for the angle  $16.1^\circ$ .

This is a particularly simple example where only two tracks are required. Most other new fixpoints have a higher order. A combinatorical consideration reveals that each point on a solid line for  $\alpha < 27.7^\circ$  in Figure 8.13 is a fixpoint of order  $\leq 16$ : At each angle in that range there is a set of  $N \leq 16$  tracks for which only  $N$  different impact radii occur. The resulting matrix equation turns out to be non-singular. Intuitively this mechanism can be understood considering that the tracks corresponding to the points on the solid lines have only one undetermined degree of freedom which can be compensated by information from other tracks.

However, in practice fixpoints of high order are not as useful as fixpoints of lower order: Since a high-order fixpoint relies on the equality of radii in many tracks, the statistical effects due to the finite single hit resolution become important and lead to a dilution of these constraints.

We have made a systematic search for fixpoints up to the fourth order, i.e. by looking for correlations between up to four tracks with the same angle. We restricted ourselves to the most critical case of three tube layers and to an angular range from  $0^\circ$  to  $45^\circ$ . The result is illustrated in Figure 8.25. We found that at every angle where at least two lines of partial constraint cross each other, there are fixpoints of order  $\leq 4$ .

Up to the present these insights are purely empirical. We have no theorem determining the order of a fixpoint from first principles.

#### Intermediate Conclusion:

At this stage we know all constraints for a given track angle, provided that the available tracks have enough spread in their intercept to cover the full radial range of the tubes in all layers. Figure 8.25 shows that in addition to the fundamental fixpoints discussed in the previous section there are fixpoints of higher order, generated by correlation of tracks with different intercepts.

However, even with these new constraints a single track angle is not sufficient for a unique autocalibration result.

The next step is to look for correlations between tracks with different slopes.

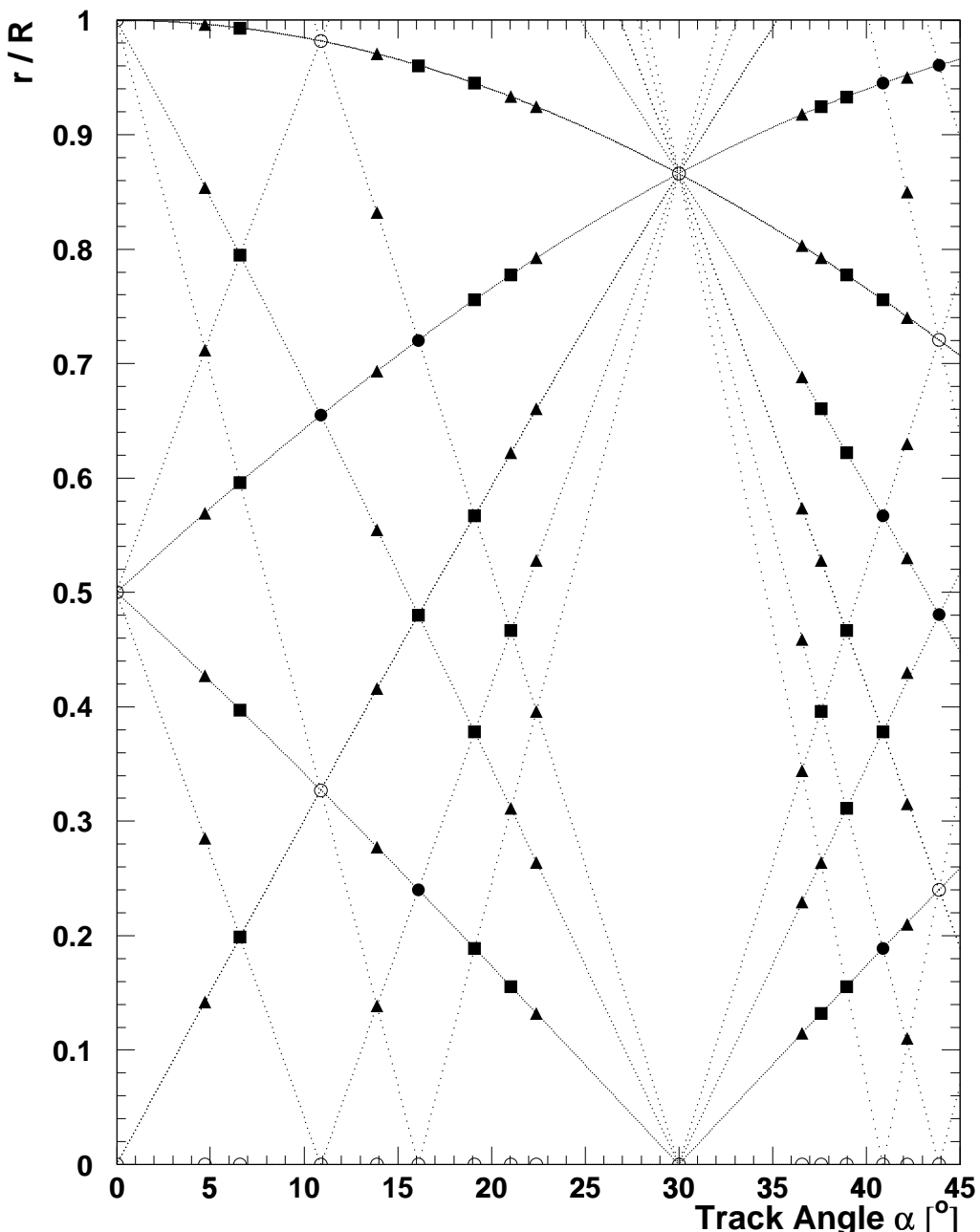


Figure 8.25: Fixpoints for three tube layers up to the fourth order:  $\circ$ : 1<sup>st</sup> order;  $\bullet$ : 2<sup>nd</sup> order;  $\blacksquare$ : 3<sup>rd</sup> order;  $\blacktriangle$ : 4<sup>th</sup> order. The dotted lines correspond to the lines in Figure 8.13. They represent fixpoints of order  $\leq 16$ .

### c. Correlation of Tracks with Different Slopes

#### α. “Recycling” of Fixpoints

The first examples will show that the information from two ordinary (first order) fixpoints can be combined to give rise to new fixpoints: Figure 8.26a shows a track with  $\alpha = 5.8^\circ$  and impact radii  $r_1 = 0.67R$ ,  $r_2 = 0.33R$  and  $r_3 = 0.5R$ . At  $r_3$  there is a fixpoint for  $\alpha = 0^\circ$  (Section 8.3.2.2, Example 2), at  $r_2$  for  $10.89^\circ$ . Since the track under consideration is fixed by  $r_2$  and  $r_3$ , the r-t relationship is now also fixed at  $r_1$ . We refrain from giving the explicit matrix calculation because it doesn't provide any new knowledge compared to the previous examples which were discussed in full detail.

A second example is given in Figure 8.26b:  $r_1 = 0$  is fixed by all tracks through the wire in an inner tube layer (Section 8.3.2.2, Example 5);  $r_3 = 0.5R$  is a fixpoint for  $\alpha = 0^\circ$ . Therefore  $r_2 = 0.74R$  is determined by a track with  $\alpha = 8.3^\circ$  connecting the radii  $r_1$  and  $r_3$ .

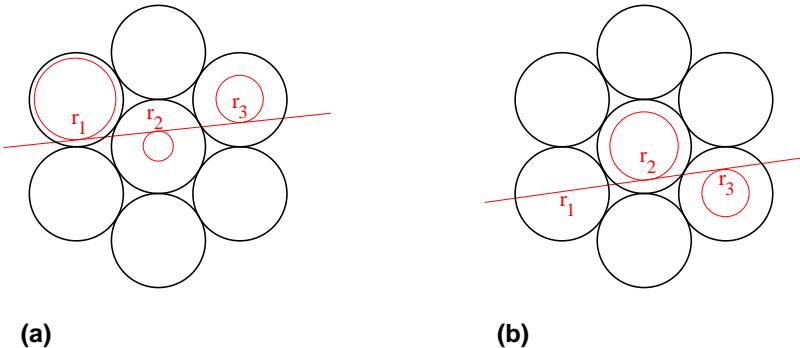


Figure 8.26: Examples for “fixpoint recycling”: (a) A track with  $\alpha = 5.8^\circ$  through the fixpoints  $r_2 = 0.33R$  and  $r_3 = 0.5R$  defines the r-t relationship at  $r_1 = 0.67R$ . (b) The track with  $\alpha = 8.3^\circ$  through  $r_1 = 0$  and  $r_3 = 0.5R$  fixes the third radius  $r_2 = 0.74R$ .

This “recycling” mechanism yields fixpoints of third order: We need two tracks defining the ordinary fixpoints and one track connecting them with each other.

#### β. Correlations of Tracks without own Fixpoints

The two tracks drawn in Figure 8.27 have very different incidence angles and do not define any fixpoints on their own. Nevertheless the combined matrix equation has a unique solution for  $\xi(t(0.24R))$  and  $\xi(t(0.72R))$ .

The condition for observing this correlation is the availability of tracks with incidence angles of  $0^\circ$  and  $16.1^\circ$ . At ATLAS very few chambers will dispose of such a wide angular range.

Up to the third order we did not find many representatives of this class of fixpoints.

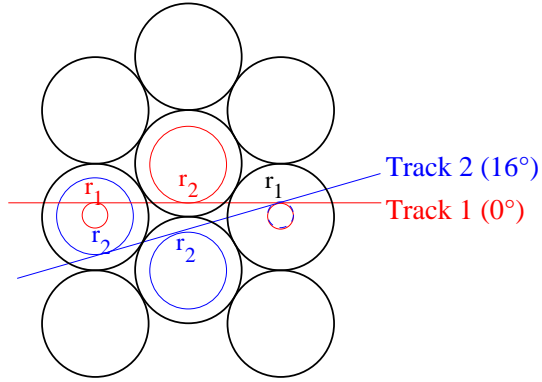


Figure 8.27: Example for the creation of second order fixpoints by correlating a track at  $0^\circ$  and a track at  $16.1^\circ$ . The impact radii are  $r_1 = 0.24R$  and  $r_2 = 0.72R$ .

### γ. Evaluation of Higher Order Fixpoints

A complete search for the fixpoints of order  $> 1$  is very difficult because for many of them a high number of tracks with sometimes very different angles has to be correlated. We have not found any algorithm determining the full set. However, the practical importance of fixpoints from tracks with very different angles is small anyway because at ATLAS the angular spread of muon tracks will be very limited (cf. Appendix C).

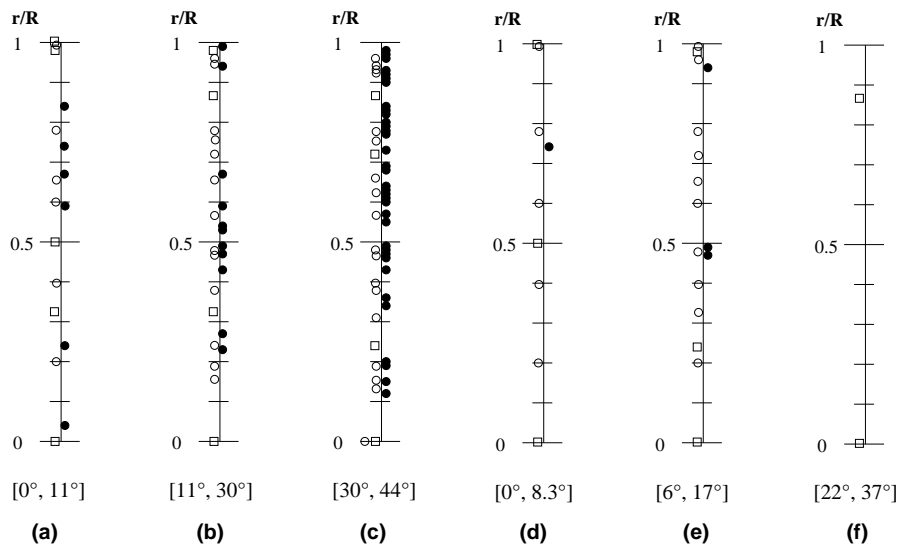


Figure 8.28: Fixpoints up to the third order for three layers. The solid circles on the right hand side of the radial axes indicate the positions of fixpoints from correlations between tracks with different angles. All markers on the left hand side correspond to fixpoints contributed by the individual angles. The primary fixpoints are symbolized by open squares, the secondary and tertiary ones by open circles.

More relevant are the sets of fixpoints that are available for a given angular range. In Figure 8.28 we have collected all the fixpoints up to the third order which we found in the intervals between angles with primary fixpoints ( $[0^\circ, 11^\circ]$ ,  $[11^\circ, 30^\circ]$  and  $[30^\circ, 44^\circ]$ ) and in some narrower intervals around angles with primary fixpoints ( $[0^\circ, 9^\circ]$ ,  $[6^\circ, 17^\circ]$  and  $[22^\circ, 37^\circ]$ ). Note that these fixpoints require the presence of the entire interval. Most of them are generated by the “recycling” mechanism and disappear when the angles with primary fixpoints are not available. This is well visible comparing diagrams (a) and (d) or – in an even more impressive way – comparing (c) and (f). If the angular interval around  $30^\circ$  is narrower than  $[21^\circ, 38^\circ]$ , the only remaining fixpoint is the primary one at  $(\alpha, r/R) = (30^\circ, 0.866)$ .

### 8.3.3 Autocalibration Methods and their Performance

Up to this point we have investigated the principle capabilities of autocalibration. The constraints discussed in the previous section constitute the complete information provided by the measured track residuals. We have shown that even by mixing tracks with a wide range of angles the r-t relationship is not fixed at every radius. Hence in the strict mathematical sense the result of autocalibration is not unambiguous. However, in practice we need to know the r-t relationship only at a finite number of drift times, usually every 10 ns. Therefore we have some hope that the density of constraints is high enough for a practically unique determination of  $r(t)$ . Before investigating this question in a Monte Carlo study of autocalibration at ATLAS, we shall focus on technical realizations of the autocalibration principle.

We shall first look at the classical autocalibration technique and ask how it takes advantage of the available information. Afterwards we shall tackle the challenge of finding an algorithm making maximum use of the autocalibration constraints.

#### 8.3.3.1 The Conventional Autocalibration Technique

As we have said in the short introduction at the beginning of Section 8.3, autocalibration is an iterative method. In every iteration  $i$  the current estimate  $r^{(i)}(t)$  for  $r_{\text{true}}(t)$  serves for a track fit, then the residuals (8.31) are measured and used to determine a correction to the current r-t relationship.

In the classical method the residuals from a track fit are histogrammed as a function of the drift time. However, for a given track the residuals in the individual tube layers are different and cannot be merged in one common histogramme: the track fit is most determined by the hits in the outer layers. This means that for a given deviation of the current r-t relationship from the true one, the residuals are biggest in the inner tubes<sup>3</sup>. Therefore conventional autocalibration only uses the residuals in one of the inner tube layers, i.e.  $\Delta_2$  in the case of three layers and  $\Delta_2$  or  $\Delta_3$  in the case of four layers. These residuals are then averaged over many tracks within about 50 drift-time slices and directly applied as correction to the current estimate  $r^{(i)}(t)$ :

$$r^{(i+1)}(t) = r^{(i)}(t) - \langle \Delta_2(t) \rangle \quad (8.62)$$

with  $r^{(0)}(t) = r_{\text{start}}(t)$ .

---

<sup>3</sup>These facts are fully expressed by the matrix equation (8.50). Here we have only put some of its aspects into simpler words.

The algorithm sequence (track fit  $\rightarrow$  histogramming  $\Delta_2$  versus  $t_2$   $\rightarrow$  correction of  $r(t)$ ) is repeated until the  $(t_2, \Delta_2)$ -distribution is a flat band centred at zero (Figure 8.29).

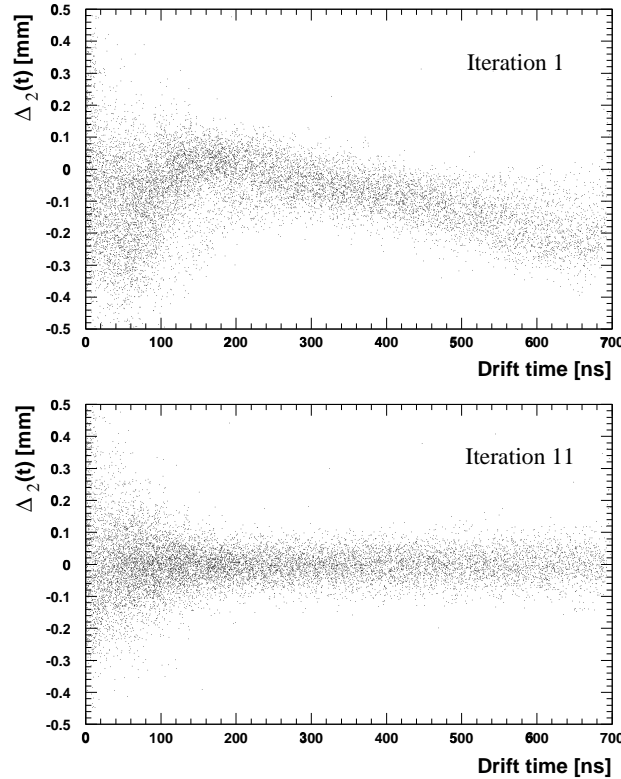


Figure 8.29: Residuals in the middle tube layer versus drift time in that layer. (a) at the first iteration; (b) at the 11<sup>th</sup> iteration. This autocalibration was done for the angular range of the chamber BML 4 ( $[24^\circ, 33^\circ]$ ).

With the notation of the matrix formalism this approach is equivalent to the assumption

$$\langle \Delta_2(t_2) \rangle = \varepsilon(t_2) \quad (8.63)$$

instead of the correct matrix equation

$$\langle \Delta_i(t_i, \alpha) \rangle = \sum_{k=1}^n M_{ik}(\alpha) \varepsilon(t_k) \quad (8.64)$$

Apparently the assumption (8.63) is a very strong approximation. It has the following consequences:

- The information contained in the residuals is not correctly used.
- One aspect of the information is completely ignored: The residuals are only distinguished by the drift time  $t_2$ , while their angular dependence is not taken into account.

- In the case of three hits it is justified to only use  $\Delta_2$  because according to Eq. (8.51) for a track with  $n = 3$  hits there is only  $n - 2 = 1$  independent residual. We would preserve the full information by exploiting

$$\langle \Delta_2(t_2, \alpha) \rangle = \sum_{k=1}^3 M_{2k}(\alpha) \varepsilon(t_k) .$$

On the other hand, for  $n > 3$  information is lost if only the residual in one tube is analyzed. In the four-layer case there have been attempts to scale the residuals of different layers with respect to each other in order to fill them into a common histogramme. However, the scale factors derived at  $\alpha = 0^\circ$  failed for other angles, which is no big surprise considering the angular dependence of the matrix.

Later (Section 8.3.6.2) we shall see that these problems result in a rather slow convergence if the typical incidence angle of the tracks is in a range with poor constraints and if the angular spread is low. In those cases also the final calibration precision suffers.

Looking at the oversimplification passing from (8.64) to (8.63), it is even surprising that the conventional autocalibration technique converges at all. Our attempt of explanation is the following:

For simplicity we assume  $n = 3$  and focus on the residual in the middle tube. By ignoring the angular dependence of the residuals the old autocalibration averages the matrix elements over the angle:

$$\langle \Delta_2(t_2, \alpha) \rangle_\alpha = \sum_{k=1}^3 \langle M_{2k}(\alpha) \rangle_\alpha \varepsilon(t_k) \quad (8.65)$$

A detailed analysis of the angular dependence of  $M_{2k}$  reveals that the non-diagonal elements do not always vary smoothly with  $\alpha$ . When the slope is changed such that in layer  $k$  a different tube is hit, the non-diagonal element  $M_{2k}$  changes sign, while the diagonal elements don't do so. Thus, if the angular spread is big, the non-diagonal elements average out:

$$\langle \Delta_2(t_2, \alpha) \rangle_\alpha \stackrel{\text{wide spread in } \alpha}{\approx} \langle M_{22}(\alpha) \rangle_\alpha \varepsilon(t_2) \quad (8.66)$$

Now the basic mistake in the assumption of the old technique is the missing factor  $\langle M_{22}(\alpha) \rangle_\alpha$  which can be compensated by a bigger number of iterations. An example is given in Figure 8.30 where the distributions of the matrix elements  $M_{21}$ ,  $M_{22}$  and  $M_{23}$  are shown for the large angular range  $[0^\circ, 25^\circ]$  as it is available at the ATLAS chamber BOL 1. Under such favourable conditions the algorithm converges rather fast and yields a good precision.

For low angular spread the non-diagonal elements remain important, as is visible in Figure 8.31 for the range  $[24^\circ, 33^\circ]$ . We shall see that for such low spreads conventional autocalibration has difficulties.

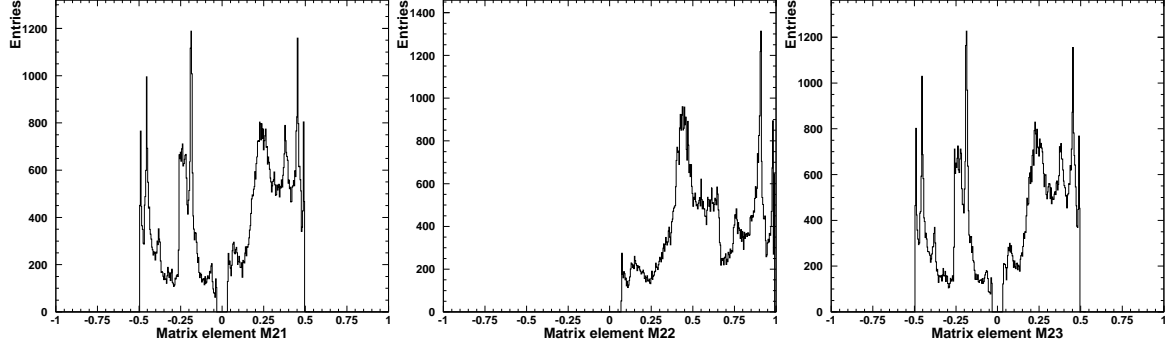


Figure 8.30: Distribution of the matrix elements  $M_{21}$ ,  $M_{22}$  and  $M_{23}$  for the angular range of tracks through BOL 1 ( $[0^\circ, 25^\circ]$ , see Appendix C).

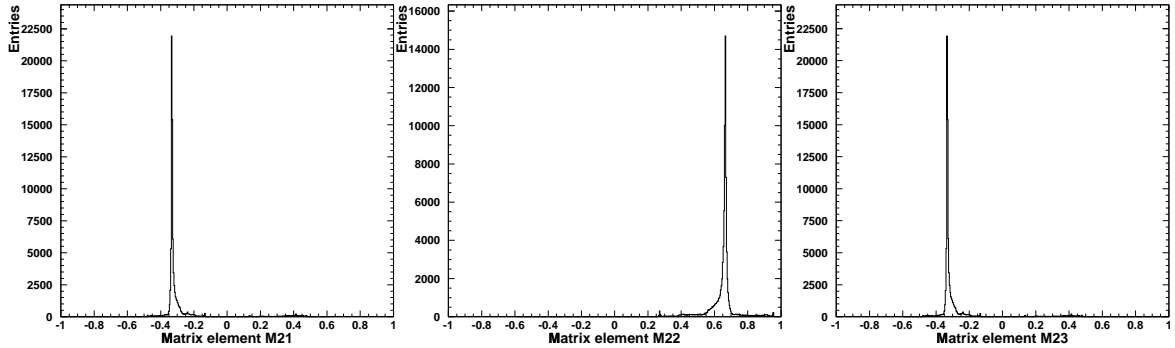


Figure 8.31: Distribution of the matrix elements  $M_{21}$ ,  $M_{22}$  and  $M_{23}$  for the angular range of tracks through EOL 6 ( $[24^\circ, 33^\circ]$ , see Appendix C).

### 8.3.3.2 Fitting the Global Matrix Equation

Confronted with the disadvantages of the conventional autocalibration, we have developed an alternative technique with the design goal of making optimum use of all available information in the residuals. This new method is closely related to the global matrix equation (8.59) for a sample of different tracks, discussed in connection with the higher-order fixpoints. The difference is that instead of the homogeneous equation for the freedom function  $\xi(t)$  we now exploit the inhomogeneous equation involving  $\vec{\varepsilon}(t_i)$  and  $\Delta_i$ :

$$\underbrace{\begin{pmatrix} M_1 & O & \dots & O \\ O & \ddots & & \vdots \\ \vdots & & \ddots & O \\ O & \dots & O & M_N \end{pmatrix}}_{\mathcal{M}} \begin{pmatrix} \vec{\varepsilon}_1 + \delta \vec{r}_1 \\ \vdots \\ \vec{\varepsilon}_N + \delta \vec{r}_N \end{pmatrix} = \begin{pmatrix} \vec{\Delta}_1 \\ \vdots \\ \vec{\Delta}_N \end{pmatrix} \quad (8.67)$$

$M_i$  ( $i = 1, \dots, N$ ) are the matrices belonging to the  $N$  individual tracks in the considered sample. Like in the old autocalibration technique the tracks are fitted using a start r-t relationship which deviates from the true r-t relationship by the function  $\varepsilon(t)$ . The deviations at the impact radii of a track  $i$  with  $n_i$  hits are given by the vector

$$\vec{\varepsilon}_i \equiv \begin{pmatrix} \varepsilon(t(r_{i1})) \\ \vdots \\ \varepsilon(t(r_{in_i})) \end{pmatrix} . \quad (8.68)$$

Furthermore there are statistical errors

$$\vec{\delta r}_i \equiv \begin{pmatrix} \delta r_{i1} \\ \vdots \\ \delta r_{in_i} \end{pmatrix} \quad (8.69)$$

on the hit radii which we no longer neglect because the rows in (8.67) represent individual tracks, not the average over many tracks with given  $m$  and  $c$ . After the fit every track has a residual vector

$$\vec{\Delta}_i \equiv \begin{pmatrix} \Delta_{i1} \\ \vdots \\ \Delta_{in_i} \end{pmatrix} . \quad (8.70)$$

The matrices  $M_i$  for every track are estimated from the fit result  $(m, c)$  using Eq. (8.45).

An algebraic inversion of (8.67) to obtain  $\varepsilon(t)$  is not possible:

- Due to the unknown statistical terms  $\delta r_i$  there is no exact solution  $\varepsilon(t)$ .
- Even if we neglect  $\delta r_i$  and reduce the number of columns with the scheme explained in Section 8.3.2.3, the matrix remains singular in general. We cannot rely on the hypothetically possible case that an extremely good angular spread provides enough constraints for a unique determination of  $\varepsilon(t)$  for all  $t$  occurring in the considered sample of tracks.

We still found a viable solution for extracting maximum information from (8.67):

- For track reconstruction it is sufficient to know the r-t relationship and hence  $\varepsilon(t)$  in time bins of about 10 ns width. Therefore we can discretize  $\varepsilon(t)$  in 70 time slices and thus reduce the dimension of the vector  $\vec{\varepsilon}$  to 70. Consequently the global matrix has 70 columns. If several drift times of one track end up in the same time bin, the matrix columns corresponding to these hits are summed.
- For an application in practice it is appropriate to keep in mind that every track has only  $n_i - 2$  independent residuals and matrix rows. We can therefore reduce the number of rows to process from  $N_{\text{tot}} \equiv \sum_{i=1}^N n_i$  to  $N_{\text{ind}} \equiv \sum_{i=1}^N (n_i - 2)$  by only keeping independent rows.

- By virtue of the two reduction steps the full matrix  $\mathcal{M}$  with dimension  $N_{\text{tot}} \times N_{\text{tot}}$  is replaced by a smaller matrix  $\tilde{\mathcal{M}}$  with dimension  $N_{\text{ind}} \times 70$ . The resulting matrix equation looks like the following:

$$\underbrace{\tilde{\mathcal{M}}}_{\substack{\text{70 time bins}}} \begin{pmatrix} \varepsilon(t_1) \\ \vdots \\ \varepsilon(t_{70}) \end{pmatrix} = \begin{pmatrix} \Delta_1 \\ \vdots \\ \Delta_{N_{\text{ind}}} \end{pmatrix} - \begin{pmatrix} D_1 \\ \vdots \\ D_{N_{\text{ind}}} \end{pmatrix} \quad (8.71)$$

where we have arranged the contributions from statistical errors (i.e. the independent rows of  $\mathcal{M} \cdot (\delta \vec{r}_1, \dots, \delta \vec{r}_N)^T$ ) in the terms  $D_i$  on the right side.

- Without statistical errors the 70 components  $\varepsilon(t_i)$  would obey to

$$\tilde{\mathcal{M}} \begin{pmatrix} \varepsilon(t_1) \\ \vdots \\ \varepsilon(t_{70}) \end{pmatrix} = \begin{pmatrix} \Delta_1 \\ \vdots \\ \Delta_{N_{\text{ind}}} \end{pmatrix} \quad (8.72)$$

Since we do have errors, we determine the  $\varepsilon(t_i)$  by minimizing

$$\chi^2 \equiv \sum_{i=1}^{N_{\text{ind}}} \frac{1}{\sigma^2(\Delta_i)} \left[ \Delta_i - \sum_{k=1}^{70} \tilde{\mathcal{M}}_{ik} \varepsilon(t_k) \right]^2 \quad (8.73)$$

with

$$\sigma(\Delta_i) = \sqrt{\sum_{k=1}^{70} [\tilde{\mathcal{M}}_{ik} \sigma(r_k)]^2} \quad (8.74)$$

where  $\sigma(r_k)$  is the spatial tube resolution at the radius  $r_k$  corresponding to the time  $t_k$ .

- As an alternative to the variation of all 70 components  $\varepsilon(t_i)$  in the fit, we parametrized  $\varepsilon(t)$  with a sum of sine functions:

$$\varepsilon(t) = \sum_{l=1}^{20} p_l \sin(l \pi \frac{t}{t_{\max}}) \quad . \quad (8.75)$$

This allowed us to reduce the number of fit parameters from 70 to 20. The chosen parametrization function has the property of vanishing at  $t = 0$  and  $t = t_{\max}$  which is reasonable because the start r-t relationship can be chosen to match in these two points. The advantage of the parametrization is a reduction of computing time while the precision was observed to remain unaffected.

This new method uses the full information from the individual matrix equations. Section 8.3.6.2 will demonstrate that it has the advantage of very fast convergence: With good angular spread only two iterations are needed. Furthermore, for low angular spread and angles around 30° the precision of the calibrated r-t relationship is significantly better than with the conventional method.

### 8.3.4 Autocalibration Tests in Monte Carlo – The Procedure

To judge the performance of the two autocalibration techniques, we performed a Monte Carlo study. This has several advantages with respect to using data from test beams:

- The distribution of incidence angles, i.e. our main point of interest, can be varied at will. In test beams on the other hand only very limited angular ranges can be achieved by rotating the prototype chambers with respect to the beam. A free choice of the angular distribution is particularly important for studying autocalibration at ATLAS (Section 8.3.6.2).
- Individual components of the tube response can be switched on and off.
- The problems of autocalibration can be isolated from other difficulties: In real data analysis we suffer from  $t_0$  problems, wire displacements, misalignment etc. which mix with the effects to be investigated.

The tests were done in the following way:

1. Generation of tracks through a multilayer with ideal geometry (no wire displacements). The number of tube layers per multilayer could be chosen. The distribution of track intercepts was flat within an interval whose width was such that in every layer at least one tube was fully illuminated. The angular distribution could be custom-designed.
2. The track impact radius in every crossed tube was converted into a drift time using the full response function  $P(t|r)$  for Ar/CO<sub>2</sub>.
3. A start r-t relationship was used to convert the drift times into hit radii.
4. Tracks were fitted to the hit radii.
5. The r-t relationship was corrected according to either the old or the new method.
6. The steps 3 to 5 were iterated until our convergence criterion was fulfilled: We expect a statistical precision of the order  $(\sigma/\sqrt{N} \sim 100\text{ }\mu\text{m}/\sqrt{N})$ , where  $\sigma$  is the single tube resolution and  $N$  the number of tracks. Therefore we considered the calibration as converged when the rms change of the r-t relationship between subsequent iterations was smaller than this expected precision. For 10000 tracks the convergence criterion is  $1\text{ }\mu\text{m}$ .
7. The final r-t relationship was compared to the true one used in step 2. The calibration precision was quantified by the rms deviation defined in (8.1).

### 8.3.5 Comment on Autocalibration near the Wire

In Chapter 6 we discussed the asymmetry of the time distributions  $P(t|r)$  for impact radii  $r < 2\text{ mm}$  and the consequences for track reconstruction. To treat the domain near the wire correctly, a maximum-likelihood track fit involving the full knowledge about the tube response is necessary. In principle this is also true for autocalibration. However, the likelihood technique reconstructs the track radii directly from the drift times without introducing hit radii. Thus there are no residuals to which the matrix formalism could be applied. A genuine “maximum-likelihood

autocalibration” would require a completely new concept which we decided to postpone unless it would prove to be inevitable.

It turned out that autocalibration with ordinary least-squares fits can give satisfactory results even at small radii:

After a Monte Carlo autocalibration we have to compare the final r-t relationship with the correct  $r_{\text{true}}(t)$  from the event generation. But how should  $r_{\text{true}}(t)$  be defined in terms of  $P(t|r)$ ? Up to now we have always taken the peak position  $p_2(r)$  as  $t(r)$ ; correspondingly  $r(t)$  was defined as the inverse function  $\rho(t) \equiv (p_2^{-1})(t)$ . Unfortunately this definition is inadequate for autocalibration because both autocalibration techniques converge to the mean radius  $\langle r(t) \rangle = \int r P(r|t) dr$  for a given time  $t$  rather than to  $\rho(t)$ . If we define  $r_{\text{true}}(t) \equiv \rho(t)$ , there is a systematic deviation at low drift times (Figure 8.32a). If on the other hand  $\langle r(t) \rangle$  is taken as reference, the deviation disappears (Figure 8.32b).

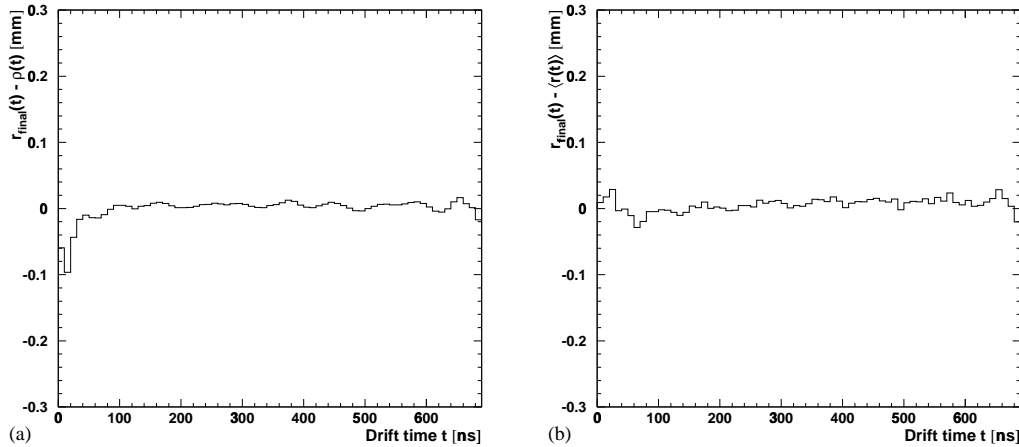


Figure 8.32: Comparison of the autocalibration result with the “true” r-t relationship  $r_{\text{true}}(t)$ . Two definitions of  $r_{\text{true}}(t)$  were tried: (a)  $r_{\text{true}}(t) \equiv \rho(t)$  (peak position); (b)  $r_{\text{true}}(t) \equiv \langle r(t) \rangle$ . This autocalibration with the new method was based on 100000 tracks with the angular spread of the chamber BOL 1.

Of course, comparing the calibrated r-t relationship with  $\langle r(t) \rangle$  instead of  $\rho(t)$  does not solve the fundamental problem of asymmetric time distributions near the wire. Individual tracks reconstructed with the least-squares method will still have biases if their drift times are just converted into the corresponding  $\langle r(t) \rangle$ . However, since we know asymmetry  $p_1(r)$  and resolution  $p_3(r)$  from test beams, it will be possible to construct the full  $P(t|r)$  from the autocalibrated  $\langle r(t) \rangle$ .

In other words, autocalibration determines one component of  $P(t|r)$ , namely the mean radius as a function of  $t$ . The other components of the response must be injected from external knowledge.

### 8.3.6 Autocalibration at ATLAS

In this section we shall analyze the performances of the two autocalibration techniques applied to the track-angle distributions as they will be present in the individual ATLAS chambers. The main aim of the study is to know whether the angular spread is sufficient to calibrate the r-t relationship with an rms precision better than  $20\mu\text{m}$ . We are also interested in the statistics required for calibrating an r-t relationship. This will allow us to estimate the time needed for collecting enough data for a calibration of the entire muon spectrometer.

#### 8.3.6.1 Determination of the Angular Spread in ATLAS MDT Chambers

The general Monte Carlo procedure was already described in Section 8.3.4. However, we still need to determine the distribution of track incidence angles for every MDT chamber in ATLAS.

In Section 8.3.1 we have reasoned that for autocalibration at ATLAS all muons with transverse momenta above  $6\text{ GeV}/c$  will be usable in the sense of having a track curvature which can be neglected within a multilayer. Since this lower limit coincides with the threshold of the low  $p_T$  level 1 muon trigger, all muonic events selected by the ATLAS trigger strategy can be used.

To measure the distributions of track incidence angles in all different chambers, a full detector simulation with the programme DICE was done. At the ATLAS vertex 24000 single muons were generated with transverse momenta above  $6\text{ GeV}/c$  distributed according to the inclusive muon cross-section shown in Figure 2.5b. Due to the strong decrease of the cross-section with increasing  $p_T$  we introduced an upper cut-off at  $60\text{ GeV}/c$ . The pseudo-rapidity distribution of the generated muons was flat in  $[-2.7, 2.7]$  (cf. Figure 2.5a).

To reduce the required number of muons for this simulation, we took advantage of the eight-fold azimuthal symmetry of the muon spectrometer (see Figure 2.2): equivalent chambers at the same radial and longitudinal position but in different octants were not distinguished. The results for all chamber types together with drawings specifying their locations in the detector are shown in Appendix C.

Generating all muons at the vertex is an approximation which is not fully valid for the muons from pion and kaon decays which take place mainly in the calorimeter. If these muons came from significantly different directions, the total angular spread would increase. To investigate this suspicion, we simulated 4000 events of the class  $b\bar{b} \rightarrow \mu X$  with at least one muon above  $6\text{ GeV}/c$ . In the hadronization phase many pions and kaons are formed and decay into soft muons. The resulting angular spread turned out not to be significantly different from the one obtained with muons generated at the vertex.

#### 8.3.6.2 Precision of Autocalibration for all MDT Chambers

For every type of MDT chambers 10000 tracks were generated with an angular distribution according to the histograms in Appendix C. As start r-t relationship a Garfield prediction with an rms deviation of about  $140\mu\text{m}$  was chosen rather than an unfolded  $r(t)$  in order not to treat the most optimistic case.

Before summarizing the performance of autocalibration for all types of MDT chambers we focus on two examples:

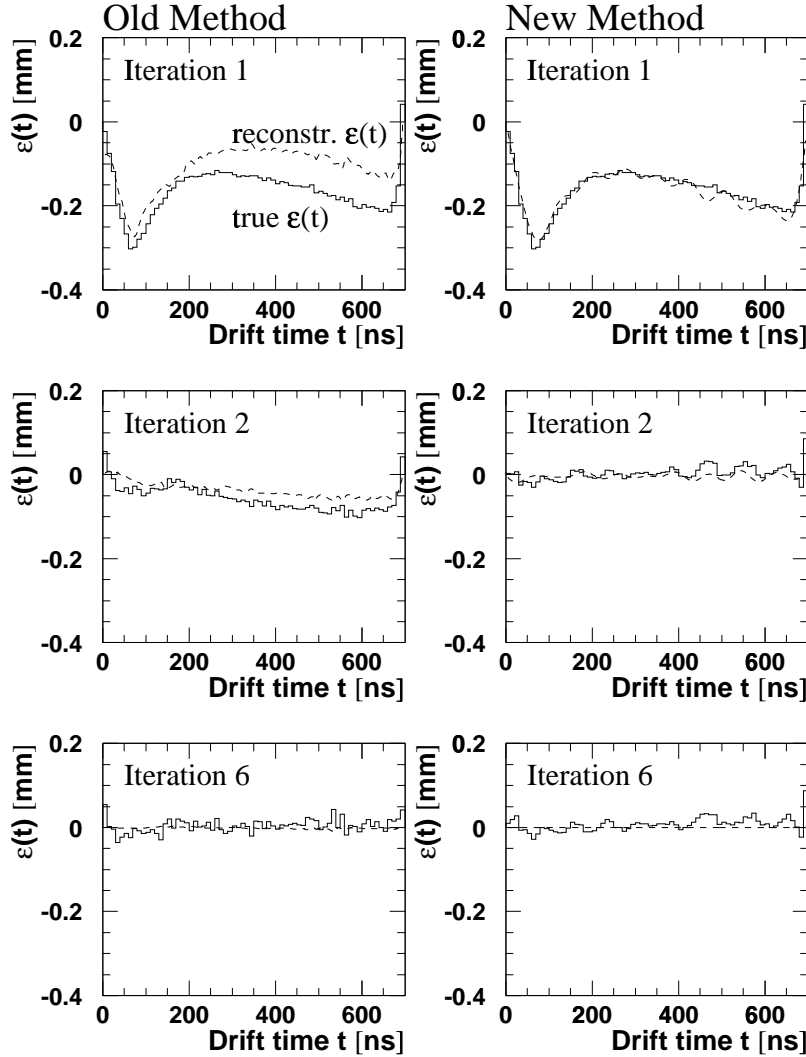


Figure 8.33: True and reconstructed deviation  $\varepsilon^{(i)}(t) = r^{(i)}(t) - r_{\text{true}}(t)$  after the iterations  $i = 1, 2, 6$  of an autocalibration for BOL 1 chambers. The left-hand plots are for the old method, the right-hand plots for the new method. For iteration 1 the true  $\varepsilon^{(1)}(t)$  characterizes the start  $r$ - $t$  relationship.

1. BOL 1 has a very wide angular spread in a range with sufficient constraints:  $\alpha \in [0^\circ, 25^\circ]$  (see Appendix C).
2. EOL 6 has only angles in a narrow range around  $30^\circ$ :  $\alpha \in [24^\circ, 33^\circ]$ .

Figure 8.33 shows the deviation  $\varepsilon^{(i)}(t)$  of the current  $r^{(i)}(t)$  from  $r_{\text{true}}(t)$  at the iterations  $i = 1, 2, 6$  for the chamber BOL 1. The solid lines represent the real  $\varepsilon(t)$ , while the dashed lines

stand for the estimate from autocalibration. The latter are the corrections which are applied to  $r^{(i)}(t)$  at the end of the current step. The left-hand plots show the performance of conventional autocalibration while the right-hand plots give the results of the new method. Apparently for this advantageous angular spread both methods converge rather quickly. This is even more clearly visible in Figure 8.34a where the rms deviation (defined in Eq. (8.1)) is drawn as a function of the iteration number.

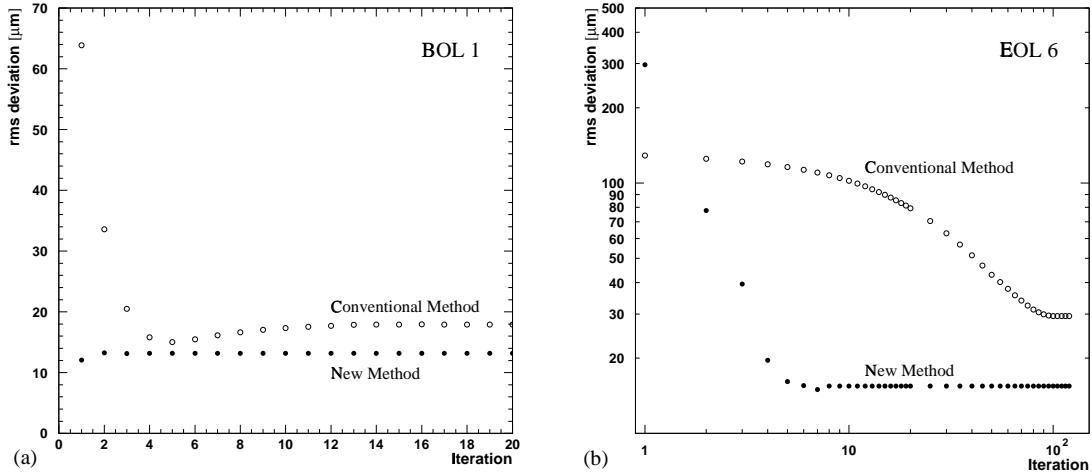


Figure 8.34: RMS deviation of the calibrated  $r$ - $t$  relationship as a function of the iteration number: (a) for the chambers BOL 1 ( $\alpha \in [0^\circ, 25^\circ]$ ); (b) for the chambers EOL 6 ( $\alpha \in [24^\circ, 33^\circ]$ ).

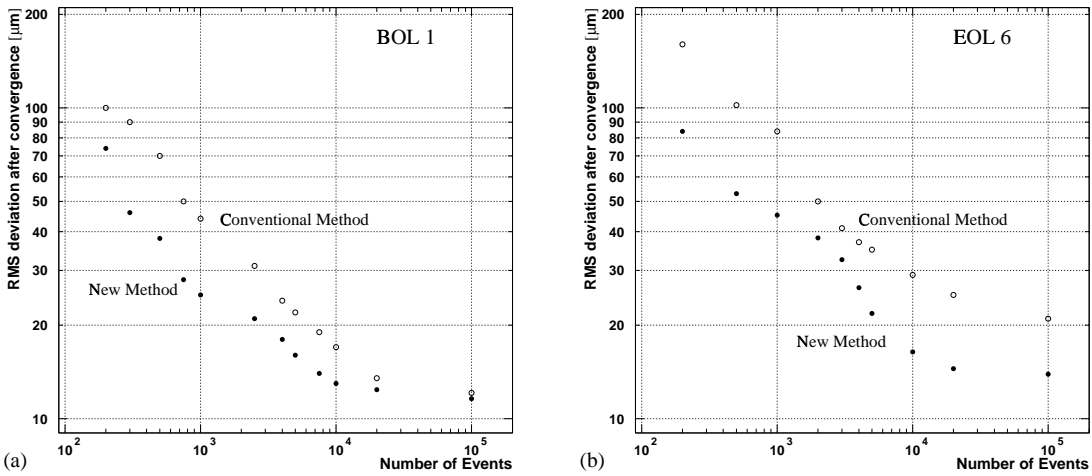


Figure 8.35: RMS deviation of the final  $r$ - $t$  relationship as a function of the number of events: (a) for the chambers BOL 1 ( $\alpha \in [0^\circ, 25^\circ]$ ); (b) for the chambers EOL 6 ( $\alpha \in [24^\circ, 33^\circ]$ ).

The new method reaches the optimum already in the first iteration whereas the classical

technique needs five iterations. Both methods have the peculiar behaviour of finally converging at a level which is slightly worse than the optimum. In both cases the precision is better than 20  $\mu\text{m}$ .

The difference between the two techniques is much more accentuated in the second example (Figure 8.34b) where the incidence angles range in a narrow interval with few constraints. Here the new method converges to a precision of 16  $\mu\text{m}$  within six iterations whereas the old method has big problems to converge at all. In this pathological case our convergence criterion is not very adequate: After 46 iterations the subsequent  $r^{(i)}(t)$  differ by less than a micron. At this point the precision is 41  $\mu\text{m}$ . However, the r-t relationship keeps improving very slowly with steps below a micron. The optimum of 30  $\mu\text{m}$  is only achieved after 97 iterations.

Note that the two examples presented are extreme cases. Usually the new method converges within 1 to 3 iterations, whereas the classical algorithm needs 5 to 10 steps.

We also wanted to know how many events are needed for a satisfactory calibration precision. Figure 8.35 shows the rms deviation of the final r-t relationship as a function of the statistics. For a precision better than 20  $\mu\text{m}$  the BOL 1 chambers with excellent angular spread need about 3000 events if the new method is applied and 6000 if we do classical autocalibration. For very bad angular spread (e.g. chamber EOL 6) about 7000 tracks are necessary with the new method whereas the old method comes close to 20  $\mu\text{m}$  only if 100000 tracks are available.

The final precision and the necessary number of iterations for all types of ATLAS MDT chambers are summarized in Table 8.1. The following concluding observations can be made:

- With good angular spread both methods give similar precision. For one chamber type out of 79 the old technique is better by a fraction of a micron, for all the others the new method is superior. The distributions of the final rms deviations are plotted in Figure 8.36.
- The number of iterations needed is histogrammed in Figure 8.37. The new method needs typically two iterations. For the classical method typically five iterations are sufficient if the angular spread is good.
- The advantage of the new method is particularly accentuated if the incidence angles lie predominantly in the interval [22°, 37°]. Note that in this interval there is only one fixpoint up to the third order! Apparently the new method makes better use of higher-order constraints. The difference between the two techniques is best visible at the following chambers where at least one method yields a precision worse than 20  $\mu\text{m}$ :

Station	angular range (95 % interval)	rms(old method)	rms(new method)
BIL 3	23.5° – 36.5°	32 $\mu\text{m}$ (27 it.)	12 $\mu\text{m}$ (2 it.)
BIR 3	23° – 37°	27 $\mu\text{m}$ (29 it.)	14 $\mu\text{m}$ (3 it.)
EIS 2	24.5° – 32.5°	39 $\mu\text{m}$ (34 it.)	14 $\mu\text{m}$ (4 it.)
EIL 3	27.5° – 32.5°	no convergence	39 $\mu\text{m}$ (11 it.)
EEL 1	25° – 38°	30 $\mu\text{m}$ (42 it.)	13 $\mu\text{m}$ (2 it.)
EML 4	24° – 38°	28 $\mu\text{m}$ (26 it.)	12 $\mu\text{m}$ (2 it.)
EOS 6	20° – 32°	21 $\mu\text{m}$ (28 it.)	13 $\mu\text{m}$ (3 it.)
EOL 5	22.5° – 29.5°	33 $\mu\text{m}$ (29 it.)	14 $\mu\text{m}$ (3 it.)
EOL 6	24.5° – 32.5°	41 $\mu\text{m}$ (46 it.)	16 $\mu\text{m}$ (8 it.)

The indicated angular range represents intervals centred about the mean and containing 95 % of all entries. It is difficult to characterize these irregular angular distributions with

only two numbers. The behaviour of autocalibration is determined by the full distribution (see Appendix C).

The new technique can calibrate 78 out of 79 chamber types with an rms precision better than  $20\mu\text{m}$  if for each calibration 10000 tracks are available. With the old method 9 chamber types have a precision worse than  $20\mu\text{m}$ .

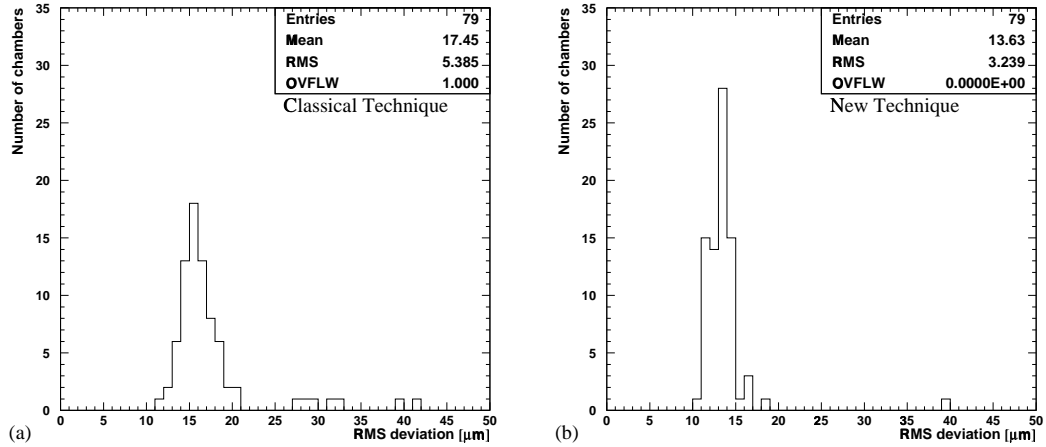


Figure 8.36: Distributions of the rms deviation of the calibrated r-t relationship. (a) represents the classical method, (b) the new method.

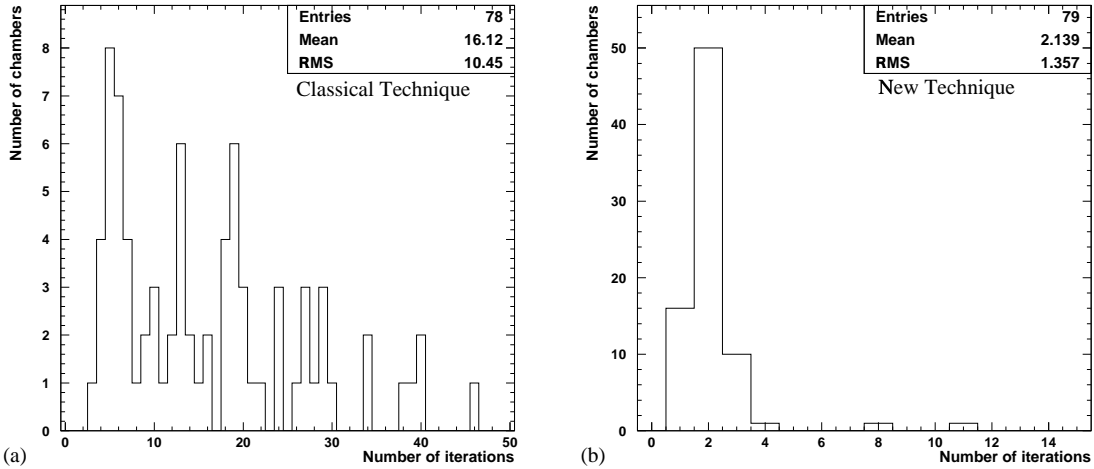


Figure 8.37: Distributions of the number of iterations needed for convergence with 10000 tracks. (a) represents the classical method, (b) the new method.

Station	Location index along $z$ (Barrel) or $r$ (End-Cap)							
	1	2	3	4	5	6	7	8
BIS	14.1 (9)	14.7 (13)	19.7 (29)	16.1 (18)	14.4 (7)	14.1 (12)	14.4 (6)	14.2 (13)
	11.6 (2)	13.9 (2)	13.8 (2)	11.5 (2)	13.7 (1)	11.5 (1)	12.8 (2)	12.4 (1)
BIL	16.2 (5)	17.1 (18)	31.6 (27)	13.9 (14)	13.4 (7)	13.9 (6)		
	14.0 (2)	11.2 (2)	11.9 (2)	11.9 (2)	10.6 (2)	13.3 (1)		
BMS	15.8 (5)	17.6 (19)	15.5 (24)	15.5 (16)	15.3 (5)	11.4 (4)		
	12.6 (1)	14.6 (2)	13.2 (2)	12.7 (2)	11.4 (1)	11.6 (2)		
BML	16.2 (6)	15.9 (20)	18.6 (22)	14.4 (11)	15.1 (5)	15.2 (6)		
	13.4 (2)	14.5 (3)	13.4 (3)	13.8 (3)	13.9 (1)	14.3 (2)		
BOS	14.1 (4)	18.1 (18)	16.9 (21)	14.8 (9)	12.8 (4)	13.0 (7)		
	13.3 (2)	13.1 (1)	13.2 (2)	14.0 (2)	12.1 (2)	11.5 (1)		
BOL	17.9 (7)	15.9 (12)	15.7 (19)	14.8 (19)	16.1 (5)	13.7 (6)		
	13.2 (2)	12.7 (1)	14.0 (2)	12.7 (2)	14.5 (1)	11.9 (1)		
BIR	18.9 (15)	14.5 (5)	15.3 (20)	27.3 (29)	15.3 (18)	15.2 (6)	15.1 (6)	
	15.6 (3)	13.2 (1)	14.2 (2)	13.9 (3)	14.2 (2)	11.6 (2)	12.9 (2)	
BEE	13.8 (3)	12.9 (4)						
	11.9 (1)	12.2 (1)						
EIS	15.5 (10)	39.1 (34)						
	12.5 (2)	13.5 (4)						
EIL	16.0 (13)	16.6 (40)	failed	16.5 (24)				
	14.6 (2)	11.5 (2)	39.1 (11)	12.8 (2)				
EES	15.0 (38)	17.7 (19)						
	14.0 (3)	14.2 (2)						
EEL	29.0 (40)	17.5 (30)						
	12.9 (2)	11.5 (2)						
EMS	18.8 (13)	16.3 (15)	16.9 (16)	18.3 (27)	16.5 (27)			
	16.8 (2)	13.4 (2)	16.5 (3)	13.5 (2)	13.1 (2)			
EML	15.5 (13)	17.2 (8)	15.7 (39)	28.0 (26)	14.3 (19)			
	13.4 (2)	13.9 (2)	12.9 (2)	11.6 (2)	13.6 (2)			
EOS	20.8 (34)	16.6 (5)	15.5 (10)	17.9 (10)	19.8 (20)	20.9 (28)		
	18.2 (3)	14.4 (1)	14.2 (2)	14.1 (2)	13.9 (3)	13.0 (3)		
EOL	18.1 (24)	16.1 (5)	17.5 (13)	14.7 (19)	32.7 (29)	41.4 (46)		
	13.5 (2)	12.7 (2)	13.2 (2)	13.7 (2)	13.5 (3)	16.3 (8)		

Table 8.1: RMS deviation of the autocalibrated  $r$ - $t$  relationship in microns for all types of ATLAS MDT chambers. In every double row the upper number refers to the conventional method, the lower number to the new technique. The number of iterations needed for convergence is indicated in brackets. The convergence criterion is that subsequent  $r$ - $t$  relationships have an rms difference smaller than  $1\mu\text{m}$ . Every calibration was done with 10000 events. For the BIR chambers the location indices must be reduced by 1. They start with 0 for the chambers centred at  $z = 0$ .

### 8.3.6.3 Autocalibration Zones and the Time Required for a Calibration

The last question we want to tackle in this work concerns the feasibility of autocalibration at ATLAS in terms of the time needed to collect enough data for calibrating the entire muon spectrometer with the required precision of  $20\mu\text{m}$ . In this context it is important to know that no specific calibration runs are foreseen and thus we ought to be able to do calibration with normal physics data.

The objective target for the calibration frequency is on the level of one per day in order to follow climatical changes and long-term variations of gas composition, operating voltage etc. Whether we actually need such frequent calibrations remains to be seen in experience.

The calibration time involves the following issues:

- The rate of muons recorded by the ATLAS data acquisition.
- The number of tracks needed to calibrate one r-t relationship.
- The number of different r-t relationships in the whole spectrometer.

We will now discuss these items in more detail:

#### a. The Rate of Muons available for Calibration

According to [TDR 97b](12.2) the estimated single-muon rate after the Level 1 trigger stage ranges between 2 kHz with the high- $p_T$  trigger and 23 kHz with the low- $p_T$  trigger. However, the subsequent trigger stages (Level 2 and Event Filter) reduce the final event rate to 100 Hz. The question whether each of these events will contain a muon, depends on the selection criteria at the last trigger levels. So far no final decision on these criteria has been taken, and reliable numbers on the fraction of muonic events are not available. This topic will need more studies and discussions in the collaboration.

For the time being we shall make the simple assumption that all final events contain one muon. The fact that many events will have several muons, allows for other events having none at all. **Thus the assumed muon rate is 100 Hz.**

#### b. The Number of Tracks needed to Calibrate one r-t Relationship

In Figure 8.35 we have presented two examples for the dependence of the calibration precision on the number of muon tracks used. We have seen that depending on the spread of the incidence angles and depending on the autocalibration method, 3000 to 7000 events are needed to obtain an r-t relationship whose deviation from the true one has an rms smaller than  $20\mu\text{m}$ . However, earlier autocalibration studies with test-beam data have shown that at least 10000 events are needed in real life. This is due to additional problems like wire displacements and errors in the determination of  $t_0$  (the absolute start point of the drift-time scale), which were not included in the Monte Carlo model. **For our estimate we assume that 10000 tracks are needed to calibrate one r-t relationship.**

**c. The Number of Different r-t Relationships in ATLAS**  
**- Definition of Autocalibration Zones**

In the introduction to autocalibration (Section 8.3.1) we have pointed out that every multilayer of tubes will have to be calibrated separately. But this segmentation is not even enough: Owing to the inhomogeneity of the magnetic field every multilayer will have to be subdivided in autocalibration zones. The size of the zones must be chosen such that the rms uncertainty of  $r(t)$  due to spatial variations of the magnetic field is less than the tolerance of  $20\mu\text{m}$ .

The aim of this paragraph is to define rules for determining autocalibration zones and to obtain a crude estimate for their total number in ATLAS.

As a first ingredient we need the variation of the drift time with the magnetic field. Let us consider a drift tube in a magnetic field  $\vec{B} = B \vec{e}_B$  with arbitrary orientation. We write the radial electric field as  $\vec{E} = E \vec{e}_r$ . In [BLU 93](Section 2.1) it was shown that the electron drift velocity  $\vec{v}$  is given by

$$\vec{v} = -\frac{e}{m}\tau E \frac{1}{1 + \omega^2\tau^2} [\vec{e}_r + \omega\tau\vec{e}_r \times \vec{e}_B + \omega^2\tau^2(\vec{e}_r \cdot \vec{e}_B)\vec{e}_B] \quad (8.76)$$

where  $\omega = \frac{e}{m}B$  is the cyclotron frequency and  $\tau$  the average time between collisions with atoms;  $m$  is the electron mass and  $e$  the elementary charge. In every point of the electron trajectory the Lorentz angle  $\psi_L$  between the drift velocity  $\vec{v}$  and  $-\vec{E}$  is

$$\psi_L(r, B) = \arctan \left[ \frac{e}{m} \tau(r) B \frac{\sin \alpha(r)}{\sqrt{1 + (\frac{e}{m} \tau(r) B)^2 \cos^2 \alpha(r)}} \right] \quad (8.77)$$

where we have introduced the angle  $\alpha$  between the electric and the magnetic field:

$$\alpha = \arccos(\vec{e}_r \cdot \vec{e}_B) \quad (8.78)$$

Note that due to the radial electric field in a tube we are confronted with the difficulty that even in a homogeneous B-field the angle  $\alpha$  will – in general – change along the drift trajectory and therefore depend on  $r$ . In the case of orthogonal fields (8.77) reduces to the more familiar expression

$$\psi_L(r, B) = \arctan \left[ \frac{e}{m} \tau(r) B \right] \quad (8.79)$$

For our discussion we shall keep the general formula (8.77). The total drift distance  $s$  is obtained by integrating the infinitesimal track sections  $\frac{dr'}{\cos[\psi_L(r', B)]}$  between the wire ( $r' = 0$ ) and the track radius  $r_0$ :

$$s = \int_0^{r_0} \frac{dr'}{\cos[\psi_L(r', B)]} \quad (8.80)$$

Using the modulus of the drift velocity

$$v(r, B) = \frac{e}{m}\tau(r)E(r) \cos[\psi_L(r, B)] \quad (8.81)$$

we get the drift time

$$\begin{aligned} t(r_0, B) &= \int_0^s \frac{ds'}{v(r(s'), B)} = \int_0^{r_0} \frac{dr'}{v(r', B) \cos[\psi_L(r', B)]} = \int_0^{r_0} \frac{dr'}{\frac{e}{m}\tau(r')E(r')\cos^2[\psi_L(r', B)]} \\ &= \int_0^{r_0} \frac{dr'}{\frac{e}{m}\tau(r')E(r')} (1 + \tan^2[\psi_L(r', B)]) \end{aligned} \quad (8.82)$$

Inserting (8.77) yields

$$t(r_0, B) = t(r_0, 0) + \frac{e}{m} \int_0^{r_0} dr' \frac{\tau(r')}{E(r')} B^2 \frac{\sin^2 \alpha(r')}{1 + (\frac{e}{m} \tau(r') B)^2 \cos^2 \alpha(r')} \quad (8.83)$$

Defining the effective magnetic field as

$$B_{\text{eff}}(r) \equiv B \frac{\sin \alpha(r)}{\sqrt{1 + (\frac{e}{m} \tau(r) B)^2 \cos^2 \alpha(r)}} \quad (8.84)$$

we obtain

$$t(r_0, B) = t(r_0, 0) + \frac{e}{m} \int_0^{r_0} dr' \frac{\tau(r')}{E(r')} B_{\text{eff}}^2(r') \quad . \quad (8.85)$$

We are now in the unpleasant situation that the effective B-field, i.e. the field strength which is relevant for the drift time, changes during the drift. Let us try to obtain an approximate value for  $B_{\text{eff}}$  which doesn't depend on  $r$ .

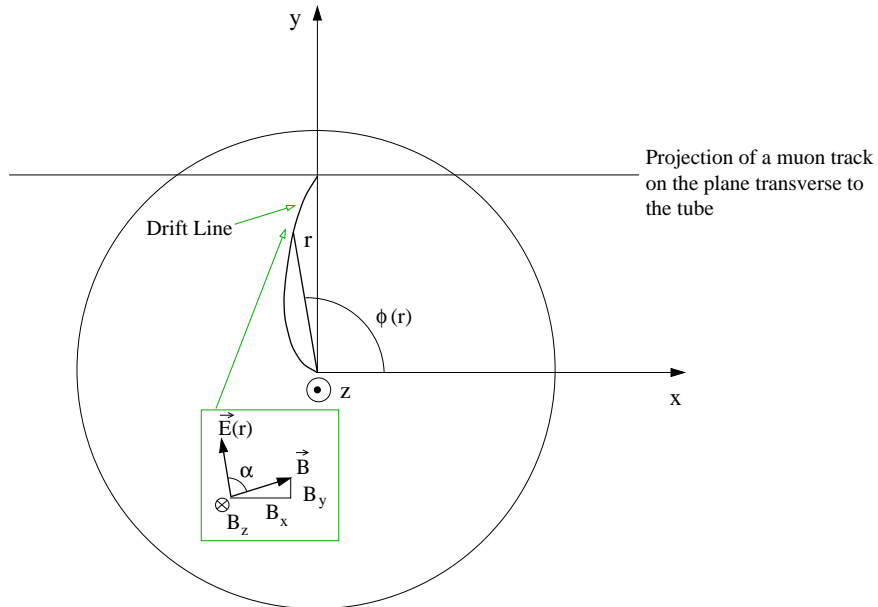


Figure 8.38: Trajectory of a drift electron for a non-zero magnetic field component  $B_z$ . The figure illustrates the geometry and notation used in the text.

In the referential frame shown in Figure 8.38 we can express  $\cos \alpha(r)$  by the magnetic field components and the azimuth  $\phi(r)$  of a drift electron at the radius  $r$ :

$$\vec{e}_r(r) = \begin{pmatrix} \cos \phi(r) \\ \sin \phi(r) \\ 0 \end{pmatrix} \quad \vec{e}_B = \frac{1}{B} \begin{pmatrix} B_x \\ B_y \\ B_z \end{pmatrix} \quad (8.86)$$

$$\cos \alpha(r) = \vec{e}_r(r) \cdot \vec{e}_B = \cos \phi(r) \frac{B_x}{B} + \sin \phi(r) \frac{B_y}{B} \quad (8.87)$$

$$\sin \alpha(r) = \sqrt{1 - \left[ \cos^2 \phi(r) \frac{B_x^2}{B^2} + \sin^2 \phi(r) \frac{B_y^2}{B^2} + 2 \sin \phi(r) \cos \phi(r) \frac{B_x B_y}{B^2} \right]} \quad (8.88)$$

Thus

$$B_{\text{eff}}(r) = B \frac{\sqrt{1 - \left[ \cos^2 \phi(r) \frac{B_x^2}{B^2} + \sin^2 \phi(r) \frac{B_y^2}{B^2} + 2 \sin \phi(r) \cos \phi(r) \frac{B_x B_y}{B^2} \right]}}{\sqrt{1 + \left( \frac{e}{m} \tau(r) B \right)^2 \left[ \cos^2 \phi(r) \frac{B_x^2}{B^2} + \sin^2 \phi(r) \frac{B_y^2}{B^2} + 2 \sin \phi(r) \cos \phi(r) \frac{B_x B_y}{B^2} \right]}} \quad (8.89)$$

We shall now consider which field components are important at ATLAS: The component  $B_z$  is oriented parallel to the wire and hence azimuthal in ATLAS. Given the toroidal geometry of the ATLAS field, this component is dominant. The component  $B_x$  is oriented parallel to the projection of the muon track on the plane transverse to the tube. It only contributes significantly in chambers near the coils in the Barrel (e.g. BIS, BIL) where this component is radial in the global ATLAS frame. The third component  $B_y$  – oriented parallel to the ATLAS beam line – is usually small compared to  $B_z$  and  $B_x$ . In the following we shall assume

$$B^2 \approx B_z^2 + B_x^2 \quad \text{and} \quad B_y \approx 0 \quad . \quad (8.90)$$

Now (8.89) simplifies to

$$B_{\text{eff}}(r) \approx B \frac{\sqrt{1 - \cos^2 \phi(r) \frac{B_x^2}{B^2}}}{\sqrt{1 + \left( \frac{e}{m} \tau(r) B \right)^2 \cos^2 \phi(r) \frac{B_x^2}{B^2}}} = B \frac{\sqrt{\frac{B_z^2}{B^2} + \sin^2 \phi(r) \left( 1 - \frac{B_x^2}{B^2} \right)}}{\sqrt{1 + \left( \frac{e}{m} \tau(r) B \right)^2 \cos^2 \phi(r) \left( 1 - \frac{B_x^2}{B^2} \right)}} \quad (8.91)$$

The azimuth  $\phi(r)$  of the drift electrons is determined by the magnetic field component  $B_z$  (along the wire). The Lorentz angle in the x–y plane at  $B_z = 0.5 \text{ T}$  is drawn in Figure 8.39a as a function of  $r$ . Based on this Lorentz angle a sample of electron drift trajectories was simulated with GARFIELD for Ar/CO<sub>2</sub> (93/7). Figure 8.39b demonstrates that at  $B_z = 0.5 \text{ T}$  the drift direction is still predominantly radial.

With simulated trajectories  $\phi(r)$  starting from a muon track at  $r_0 = 14.6 \text{ mm}$  and  $\phi(r_0) = 90^\circ$  we calculated  $B_{\text{eff}}$  as a function of  $r$  for different values of  $B_z$  and  $B = \sqrt{B_x^2 + B_z^2} = 1 \text{ T}$ . In Figure 8.40 we notice that  $B_{\text{eff}}$  is very close to  $\sqrt{B_x^2 + B_z^2}$ . The strongest deviation is 8% and occurs at very low radii if  $B_x = B_z = \frac{1}{\sqrt{2}}B$ , i.e. if the angle between  $\vec{B}$  and the wire is  $45^\circ$ . Since the drift time (8.85) involves the square of  $B_{\text{eff}}(r)$ , we calculated the quadratic radial average  $\sqrt{\langle B_{\text{eff}}^2(r) \rangle_r}$ . In the extreme case  $B_x = B_z = \frac{1}{\sqrt{2}}B$  we found  $\sqrt{\langle B_{\text{eff}}^2(r) \rangle_r} = 0.98 \sqrt{B_x^2 + B_z^2}$ .

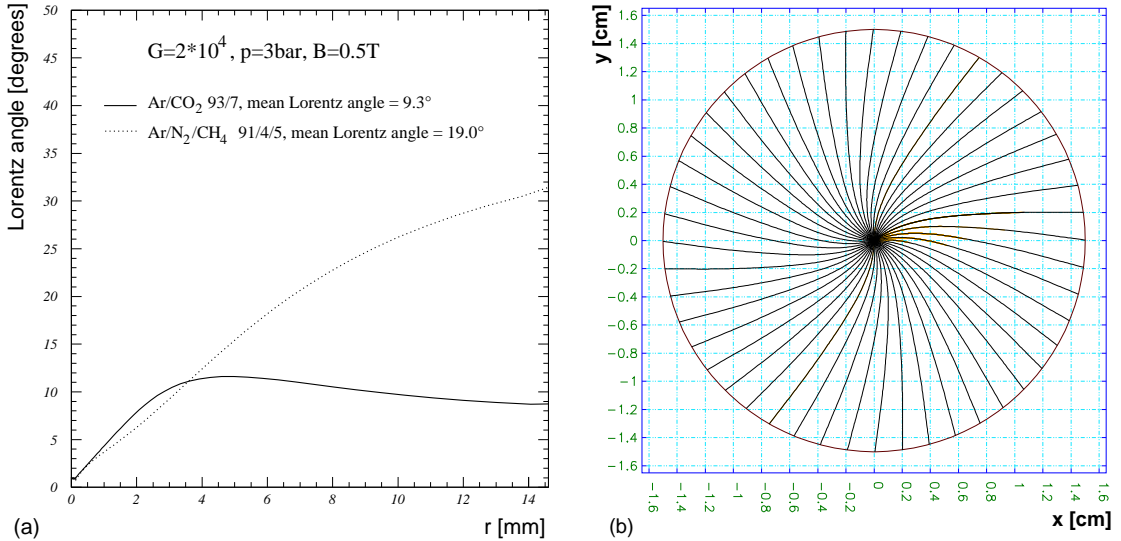


Figure 8.39: (a) Lorentz angle as a function of  $r$  at  $B_z = 0.5$  T for the gases Ar/N<sub>2</sub>/CH<sub>4</sub> (91/4/5) and Ar/CO<sub>2</sub> (93/7) (taken from [ALE 99b]). (b) Drift lines for Ar/CO<sub>2</sub> (93/7) at  $B_z = 0.5$  T, simulated with GARFIELD.

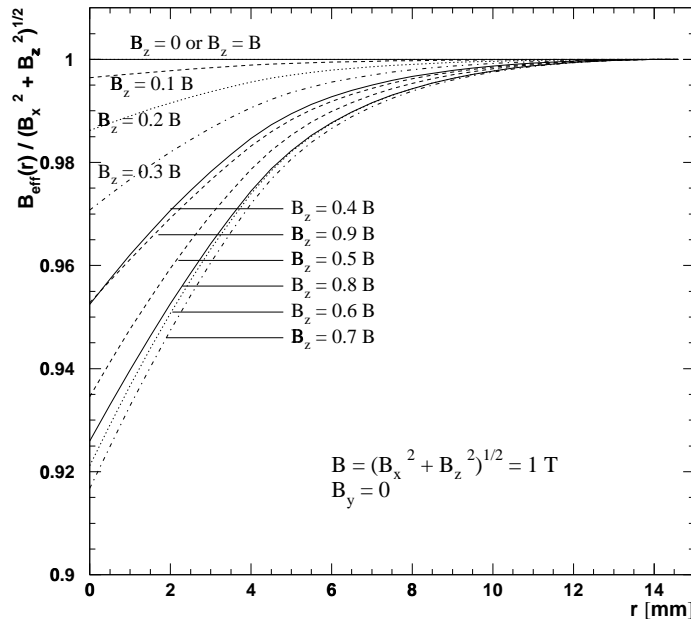


Figure 8.40: The ratio between the effective magnetic field  $B_{\text{eff}}$  (8.91) and  $\sqrt{B_x^2 + B_z^2}$  for  $B = 1$  T,  $B_y = 0$  and different values of  $B_z$ .

Therefore we can make the approximation<sup>4</sup>

$$B_{\text{eff}}(r) \approx \sqrt{B_x^2 + B_z^2} \quad \text{for all } r. \quad (8.92)$$

In Equation (8.85) expressing the drift time with magnetic field we can now consider  $B_{\text{eff}}$  as constant and move it out of the integral:

$$t(r_0, B) \approx t(r_0, 0) + B_{\text{eff}}^2 \frac{e}{m} \int_0^{r_0} dr' \frac{\tau(r')}{E(r')} \quad (8.93)$$

The increase of the drift time

$$\Delta t(r, B_{\text{eff}}) \equiv t(r, B_{\text{eff}}) - t(r, 0) \quad (8.94)$$

has a quadratic dependence on  $B_{\text{eff}}$ . This result is well confirmed by a Garfield simulation:

Figure 8.41 shows  $\Delta t(r, B_{\text{eff}})$  as a function of  $r$  for different  $B_{\text{eff}}$ . For this diagramme the magnetic field was parallel to the wire:  $B = B_{\text{eff}} = B_z$ . We also verified that a field  $B = B_x$  and a field with  $B_x = B_z = \frac{1}{\sqrt{2}}B$  give the same result within Garfield's precision (2 ns).

For every field strength the radial dependence of  $\Delta t(r, B_{\text{eff}})$  was fitted with an empirical parametrization:

$$\Delta t(r, B_{\text{eff}}) = \sum_{k=1}^3 q_k(B_{\text{eff}}) r^{2+k} \quad (8.95)$$

As predicted by Eq. (8.93) all three parameters  $q_k$  show a quadratic dependence on  $B_{\text{eff}}$  (Figure 8.42):

$$q_k(B_{\text{eff}}) = \alpha_k B_{\text{eff}}^2 \quad (k = 1, \dots, 3) \quad (8.96)$$

Thus we have

$$\Delta t(r, B_{\text{eff}}) = \sum_{k=1}^3 \alpha_k r^{2+k} B_{\text{eff}}^2 \quad (8.97)$$

where we identify

$$\gamma(r) \equiv \sum_{k=1}^3 \alpha_k r^{2+k} = \frac{e}{m} \int_0^r dr' \frac{\tau(r')}{E(r')} \quad . \quad (8.98)$$

---

<sup>4</sup>This approximation was also made in [TDR 97b](Section 10.1.2). However, starting from (8.84) and (8.85) its validity is not immediately obvious. The condition  $B_y \ll B$  is important. The field configuration  $B_x = B_y = \frac{1}{\sqrt{2}}T$ ,  $B_y = 0.2$  T yields  $\sqrt{\langle B_{\text{eff}}^2(r) \rangle_r} = 0.95\sqrt{B_x^2 + B_z^2}$ , i.e. a 5 % deviation.

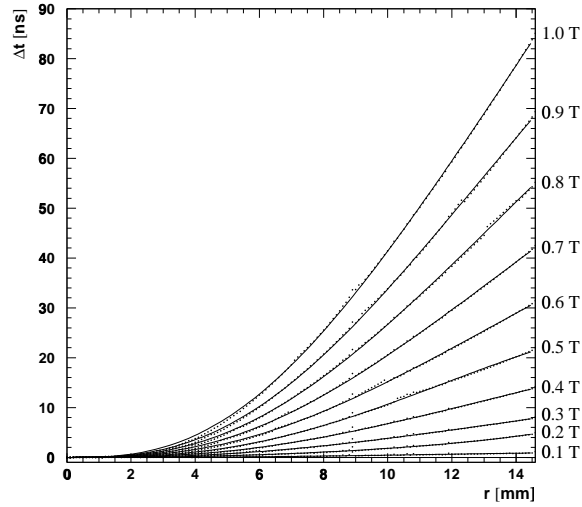


Figure 8.41: Drift-time increase  $\Delta t(r, B_{\text{eff}})$  as a function of the radius  $r$  for different strengths of the field  $B_{\text{eff}}$  parallel to the wire. The simulation results were parametrized according to (8.95).

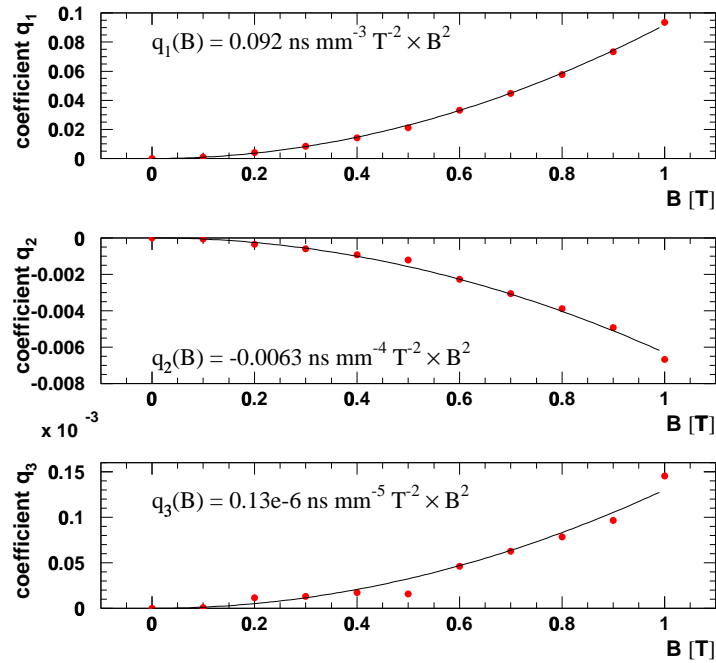


Figure 8.42: The coefficients  $q_1$  to  $q_3$  of the parametrization (8.95) in Figure 8.41 are drawn as a function of the magnetic field  $B_{\text{eff}}$  parallel to the wire and fitted with parabolae.

For the determination of the autocalibration zones we consider two scenarii:

**Scenario I: One common  $r(t)$  for the entire zone:** With this approach the zone size must be chosen so small that the changes in  $r(t)$  induced by the field variations are smaller than  $20\mu\text{m}$ . Suppose that the effective magnetic field in an autocalibration zone has the mean value  $B_{\text{eff}}$  and an rms variation  $\delta B_{\text{eff}}$ . The rms variation of the drift time for a given radius is then given by

$$\delta t(r, B_{\text{eff}}) = \sum_{k=1}^3 \alpha_k r^{2+k} \delta(B_{\text{eff}}^2) . \quad (8.99)$$

To obtain a typical value for this variation we take the radial average between 0 and the tube radius  $R$ :

$$\delta t(B_{\text{eff}}) \equiv \langle \delta t(r, B_{\text{eff}}) \rangle_r = \sum_{k=1}^3 \alpha_k \frac{1}{3+k} R^{2+k} \delta(B_{\text{eff}}^2) . \quad (8.100)$$

Inserting the values for  $\alpha_k$  from Figure 8.42 we find

$$\delta t(B_{\text{eff}}) = 28.7 \text{ ns/T}^2 \cdot \delta(B_{\text{eff}}^2) \quad (8.101)$$

By multiplication with the average drift velocity  $\langle v \rangle \approx 20.4 \mu\text{m/ns}$  we can convert the time variation into an approximate spatial uncertainty

$$\delta r(B_{\text{eff}}) = \langle v \rangle \delta t(B_{\text{eff}}) = 586 \mu\text{m/T}^2 \cdot \delta(B_{\text{eff}}^2) \quad (8.102)$$

Since  $\delta r(B_{\text{eff}})$  is required not to exceed  $20\mu\text{m}$ , the rms variations of the squared magnetic field within a zone are limited to

$$\delta(B_{\text{eff}}^2) \leq 0.034 \text{ T}^2 \quad (8.103)$$

With the approximation that the distribution of  $B_{\text{eff}}^2$  within a zone is flat, the rms variation  $\delta(B_{\text{eff}}^2)$  can be easily converted into an interval size for  $B_{\text{eff}}^2$ :

$$B_{\text{eff max}}^2 - B_{\text{eff min}}^2 = \sqrt{12} \delta(B_{\text{eff}}^2) \leq 0.12 \text{ T}^2 \quad (8.104)$$

The three-dimensional magnetic field map of the ATLAS detector allows us to calculate  $B_{\text{eff}}^2$  throughout every chamber. Applying the criterion for the size of the  $B_{\text{eff}}^2$  intervals one can finally count the number of autocalibration zones needed in every chamber. To give an example, Figure 8.43 shows the profile of  $B_{\text{eff}}^2$  in the inner multilayer of a BIL 1 chamber. The 11 zones are distinguished by the colour/grey-scale. The full collection of linear and quadratic B-field profiles for all chambers can be found in [DEI 00b].

The results for all chambers are presented in Table 8.2. Summing up all the individual numbers we find a total of 13100 zones.

Multilayer	Location index along $z$ (Barrel) or $r$ (End-Cap)							
	1	2	3	4	5	6	7	8
BIS	inner outer	$3 \times 1 (16)$ $3 \times 1 (16)$	$3 \times 1 (16)$ $2 \times 2 (16)$					
	BIL	inner outer	$11 \times 1 (16)$ $11 \times 1 (16)$					
BMS	inner outer	$3 \times 1 (14)$ $5 \times 1 (14)$						
	BML	inner outer	$1 \times 1 (16)$ $1 \times 1 (16)$					
BOS	inner outer	$5 \times 1 (16)$ $1 \times 1 (16)$	$3 \times 2 (16)$ $1 \times 1 (16)$					
	BOL	inner outer	$3 \times 1 (16)$ $1 \times 1 (16)$					
BIR	inner outer	$3 \times 1 (2)$ $2 \times 1 (2)$	$3 \times 1 (4)$ $2 \times 1 (4)$					
	BEE	inner outer		$7 \times 2 (16)$				
EIS	inner outer	$1 \times 1 (16)$ $1 \times 1 (16)$	$1 \times 1 (16)$ $1 \times 1 (16)$					
	EIL	inner outer	$1 \times 1 (16)$ $1 \times 1 (16)$	$1 \times 1 (16)$ $1 \times 1 (16)$	$1 \times 1 (16)$ $1 \times 1 (16)$	$7 \times 6 (16)$ $7 \times 6 (16)$		
EES	inner outer	$13 \times 9 (16)$ $13 \times 9 (16)$	$11 \times 3 (16)$ $11 \times 3 (16)$					
	EEL	inner outer	$10 \times 2 (16)$ $10 \times 2 (16)$	$5 \times 1 (16)$ $5 \times 1 (16)$				
EMS	inner outer	$1 \times 1 (16)$ $1 \times 1 (16)$						
	EML	inner outer	$1 \times 1 (16)$ $1 \times 1 (16)$					
EOS	inner outer	$1 \times 1 (16)$ $1 \times 1 (16)$						
	EOL	inner outer	$1 \times 1 (16)$ $1 \times 1 (16)$					

Table 8.2: For every type of MDT multilayer the number of autocalibration zones is indicated assuming scenario I. Apart from BIS 8 and BEE 1,2 all chambers have two multilayers: “inner” designates the multilayer closer to the interaction point. The notation  $a \times b (c)$  means that there are  $c$  multilayers of this type in ATLAS; each one is divided into  $a$  zones along the tubes and  $b$  zones perpendicular to them. For the BIR chambers the location indices must be reduced by 1. They start with 0 for the chambers centred at  $z = 0$ .

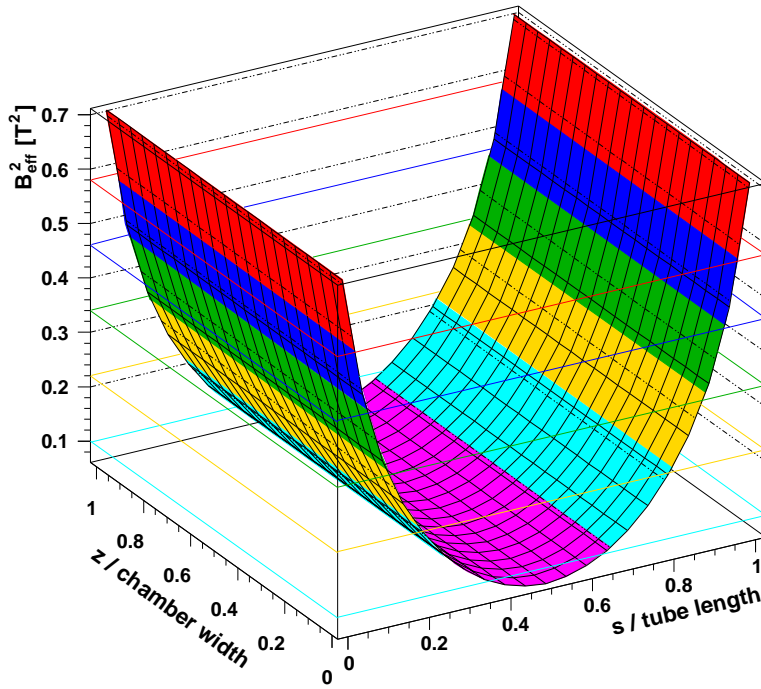


Figure 8.43: This picture shows the profile of  $B_{\text{eff}}^2$  in the inner multilayer of a BIL 1 chamber. The  $s$ -coordinate is parallel to the wires, i.e. azimuthal in ATLAS; the  $z$ -coordinate is perpendicular to the wires and parallel to the ATLAS beam line. Both coordinates are normalized to the width or length of the BIL 1 chamber. Due to the toroidal geometry of the field the variations along  $z$  are very small. The colour/grey-scale indicates a possible arrangement of 11 autocalibration zones according to scenario I with a maximum width of  $0.12 \text{ T}^2$  in  $B_{\text{eff}}^2$  space.

**Scenario II: First-order B-field correction for  $r(t)$  within a zone:** In this scenario we make use of the fact that we have some knowledge about the variation of the drift time with the magnetic field. In a first-order approach we assume that the derivative  $\frac{dt}{dB}$  is known, but not the absolute level of  $t(r, B)$ <sup>5</sup>. Furthermore, in ATLAS the magnetic field will be known with very high precision (about 4 mT). Thus it is sufficient to calibrate in every zone the r-t relationship  $t(r, \langle B \rangle)$  corresponding to the mean magnetic field  $\langle B \rangle$ . The individual r-t relationship  $t(r, B)$  at a field  $B$  is then approximated by a first order expansion:

$$t_{\text{approx}}(r, B) = t(r, \langle B \rangle) + (B - \langle B \rangle) \left[ \frac{dt}{dB} \right]_{\langle B \rangle} \quad (8.105)$$

Expressing  $t(r, B)$  as  $t(r, 0) + \gamma(r)B^2$  (from Eq. (8.97) and (8.98)) results in

$$t_{\text{approx}}(r, B) = t(r, 0) + \gamma(r)\langle B \rangle^2 + (B - \langle B \rangle)2\gamma(r)\langle B \rangle \quad (8.106)$$

The deviation of  $t_{\text{approx}}(r, B)$  from  $t(r, B)$  is then

$$t_{\text{approx}}(r, B) - t(r, B) = 2\gamma(r)B\langle B \rangle - \gamma(r)\langle B \rangle^2 - \gamma(r)B^2 = -\gamma(r)(B - \langle B \rangle)^2 \quad (8.107)$$

The criterion that the radial uncertainty must not be bigger than 20 μm provides now a lower and an upper limit for the field  $B$  in a zone with mean field  $\langle B \rangle$ :

$$20 \mu\text{m} \geq \langle v \rangle |\langle t_{\text{approx}}(B_{\min/\max}) - t(B_{\min/\max}) \rangle| = \langle v \rangle \langle \gamma \rangle (B_{\min/\max} - \langle B \rangle)^2 \quad (8.108)$$

where all means are taken over the radius. Finally the maximum size of the magnetic field interval in a zone is given by

$$B_{\max} - B_{\min} \leq 2 \sqrt{\frac{20 \mu\text{m}}{\langle v \rangle \langle \gamma \rangle}} = 0.37 \text{ T} \quad (8.109)$$

Note that this scenario yields intervals in the linear B-space, whereas the first scenario sets boundaries on  $B^2$ .

Like in the first scenario we can now use the magnetic field map of ATLAS to count the number of zones needed for every chamber. Table 8.3 presents the result. The total number of zones is 3628, slightly less than a third of the number from scenario I. This demonstrates that autocalibration can take big advantage from prior knowledge about the field dependence of the drift time.

---

<sup>5</sup>From now on we omit the subscript “eff” at the magnetic field. Nevertheless  $B$  stands always for  $B_{\text{eff}}$ .

Multilayer	Location index along $z$ (Barrel) or $r$ (End-Cap)							
	1	2	3	4	5	6	7	8
BIS	inner outer	1×1 (16) 1×1 (16)						
BIL	inner outer	3×1 (16) 3×1 (16)						
BMS	inner outer	1×1 (14) 1×1 (14)						
BML	inner outer	1×1 (16) 1×1 (16)						
BOS	inner outer	3×1 (16) 1×1 (16)						
BOL	inner outer	1×1 (16) 1×1 (16)						
BIR	inner outer	1×1 (2) 1×1 (2)	1×1 (4) 1×1 (4)					
BEE	inner outer							
		3×1 (16)	3×1 (16)					
EIS	inner outer	1×1 (16) 1×1 (16)	1×1 (16) 1×1 (16)					
EIL	inner outer	1×1 (16) 1×1 (16)	1×1 (16) 1×1 (16)	1×1 (16) 1×1 (16)	3×2 (16) 3×2 (16)			
EES	inner outer	3×2 (16) 3×2 (16)	3×2 (16) 3×2 (16)					
EEL	inner outer	4×2 (16) 4×2 (16)	1×1 (16) 1×1 (16)					
EMS	inner outer	1×1 (16) 1×1 (16)						
EML	inner outer	1×1 (16) 1×1 (16)						
EOS	inner outer	1×1 (16) 1×1 (16)						
EOL	inner outer	1×1 (16) 1×1 (16)						

Table 8.3: For every type of MDT multilayer the number of autocalibration zones is indicated assuming scenario II. The notation is the same as in Table 8.2.

#### d. Synthesis: Estimate of the Time for Collecting enough Muons

The time required to collect enough muon tracks for the calibration of the entire muon spectrometer can be estimated with the formula

$$\text{Time needed} = \frac{(\text{number of zones}) \times (\text{tracks per zone})}{(\text{muon rate}) \times (\text{zones crossed by one track})} . \quad (8.110)$$

Inserting the numbers from the preceding paragraphs and taking into account that every track crosses at least six multilayers and thus six zones, we obtain:

$$\text{Time needed} = \frac{(\text{number of zones}) \times 10000}{100 \text{ s}^{-1} \times 6} . \quad (8.111)$$

**Scenario I:** 13100 zones  $\Rightarrow$  Time needed  $\approx 60$  hours

**Scenario II:** 3628 zones  $\Rightarrow$  Time needed  $\approx 16$  hours

This result demonstrates that the aim of about one calibration per day can be achieved with a good knowledge about  $\frac{dt}{dB}$ . On the other hand, if no such knowledge were available and the r-t relationship were considered as constant within a zone, a calibration would take almost three days.

At this point we want to stress that the above estimate is meant to give us an idea about the order of magnitude of the achievable calibration frequency. The numbers can be wrong by a factor 2-3. The main uncertainty lies in the expected muon rate.

There are several conceivable approaches to reduce the time requirement:

- We have seen that using the knowledge about the drift-time variation  $\frac{dt}{dB}$  we can linearly correct the r-t relationship within a calibration zone. This allows us to increase the zone size such that for many chambers one single zone is sufficient. By improving the knowledge about  $t(r, B)$  one could perform higher-order corrections and thus increase the zone size in the few chambers with very strong field variations (e.g. in all EES types). To put this approach into practice, we would need a series of high-precision test-beam measurements of  $t(r, B)$  with a silicon telescope as reference.
- In a similar way other systematic effects (e.g. the dependence on temperature, gas composition and voltage) could be measured. This would allow us to apply further calculative corrections to the r-t relationship (see also [ALE 99b]). The calibration frequency could be reduced.
- The  $20 \mu\text{m}$  requirement was defined in a rather arbitrary way (cf. Section 8.1). It could be rethought. By loosening this specification we would need less tracks per r-t relationship. Furthermore the zone size could be increased.
- If the recorded muon rate turns out to be too low, a dedicated muon-calibration level 2 trigger could be created. By selecting only muonic events and writing out only the muon data one might be able to increase the read-out speed beyond 100 events per second.

# Chapter 9

## Summary

We have carried out a muon test beam programme for understanding and optimizing the properties of Monitored Drift Tube Chambers which will be used in the ATLAS Muon Spectrometer. The silicon microstrip tracker ODYSSEUS with its  $7\text{ }\mu\text{m}$  intrinsic precision in each of the six detector planes proved to be a very convenient tool for the determination of single tube resolution and efficiency and for the verification of muon tracks fitted through MDT prototype chambers.

The first outcome of the experiments was a set of operating parameters for the drift tubes which satisfies all requirements defined by the ATLAS physics programme whilst assuring a reliable service over the scheduled ten years of running LHC. To keep ageing effects small, ATLAS drift tubes are operated with the non-hydrocarbonic gas mixture Ar/CO<sub>2</sub>(93/7). The disadvantage of this gas is the strong dependence of the drift velocity on the reduced electric field  $E/p$  resulting in an instability of the r-t relationship against variations of operating parameters. This problem will have to be mastered by regularly measuring all variations of environmental parameters like temperature and gas composition in order to apply calculative corrections.

The combination of the low gas gain of  $2 \times 10^4$  with the pressure of 3 bar is the result of a common optimization of life time and resolution.

The choice of anode wires with  $50\text{ }\mu\text{m}$  was driven by resolution optimization: For thicker wires the resolution deteriorates while for even thinner wires there is no further improvement.

Even at the maximum background radiation rate in ATLAS (1.5 kHz/cm or 300 kHz /tube including a safety factor 5) where electronics and space-charge effects deteriorate the tube performance, a mean resolution of  $80\text{ }\mu\text{m}$  can be achieved. This is sufficient to obtain the desired momentum resolution better than 10 % at transverse muon momenta around 1 TeV. However, the test-beam experiments with gamma background underlined that satisfactory performance requires front-end electronics with an appropriate shaping scheme in order to stabilize the signal baseline. Another prerequisite is the application of time-slewing corrections compensating the effects of time jitter due to space-charge.

The hit efficiency does not significantly suffer from background radiation: Even at the highest rates it is greater than 99.9 %. The  $3\sigma$ -efficiency on the other hand deteriorates considerably because muon hits can be hidden by gamma hits. At the maximum rate in ATLAS only 85 % of all hits are reconstructed within  $3\sigma$  from the track. This is the factor limiting the efficiency of pattern recognition.

---

Precision measurements of the drift-tube response with the silicon tracker revealed that clustering effects in the primary ionization along particle tracks entail asymmetric drift-time distributions for impact radii smaller than 2 mm. The maximum-likelihood method incorporates the exact shape of these distributions into the track fitting procedure. A positive side effect is the automatic recovery of tracks with one delta-ray. If tracks are reconstructed through a single multilayer of tubes, the maximum-likelihood technique reduces the tails in the slope and intercept deviations down to 30 – 40 % of the amounts for least-squares tracking. However, in global track fits through all 18 multilayers traversed by a muon on its way through the ATLAS Muon Spectrometer the effects of non-Gaussian resolution near the wires average out. In this case the tracking performance is dominated by pattern recognition problems. It is therefore not worthwhile replacing in ATLAS the  $\chi^2$  minimization technique by maximum-likelihood fits.

The precise description of the drift-tube response turned out to be also useful for the determination of the space-time relationship from the drift-time spectrum. By unfolding the drift-time spectrum the r-t relationship can be calibrated with an rms precision of  $50 \mu\text{m}$ , which is good enough for using the result as a start r-t relationship for the iterative autocalibration procedure based on straight track fits.

An algebraic investigation of the autocalibration principle exhibited a strong dependence of the calibration reliability on the range of track incidence angles. For track angles around  $30^\circ$  the result of autocalibration is very poorly constrained. The calibration precision suffers particularly if mainly angles in the interval  $[22^\circ, 37^\circ]$  contribute. This happens for 9 out of 79 chamber types in ATLAS. In these pathological cases the classical autocalibration technique applied to samples of 10000 tracks yields an rms calibration precision worse than  $20 \mu\text{m}$  because the little amount of information contained in the track fit residuals is not even optimally used. We have developed an improved autocalibration method which is based on a matrix formalism. It was designed to take optimum advantage of all available information. With this method even the difficult  $30^\circ$  chambers can be calibrated with a precision better than  $20 \mu\text{m}$  (apart from one exception). In all other cases the precision of the new method is only slightly better than that of the old technique, but less iterations are needed.

Due to the inhomogeneous magnetic field in ATLAS autocalibration will have to be done in spatial zones whose size will be determined by the variations of the magnetic field. The resulting uncertainty of the r-t relationship is required not to exceed  $20 \mu\text{m}$ . If within each zone only one fixed r-t relationship is to be used, the total number of zones amounts to about 13000. Assuming that a single r-t relationship can be calibrated with 10000 tracks and that every ATLAS event contains at least one muon with a momentum above  $6 \text{ GeV}/c$ , the entire muon spectrometer can be calibrated within 60 hours of normal data taking. This scenario however is too pessimistic because we can perform test-beam measurements to acquire some knowledge about the variation of the drift time with the magnetic field. Then within each zone a first-order B-field correction can be applied to the drift times before the calibration. Thus the number of zones can be reduced to about 3600, and the data needed for a calibration will be collected within only 16 hours, allowing us to follow eventual diurnal variations of temperature, gas composition and other parameters.

In the remaining five years before the first run of LHC the collaboration should put even more effort into an extensive test-beam programme for measuring the dependence of the drift time on as many operating parameters as possible. The more prior knowledge we can inject, the less work will have to be done in the individual calibrations during data-taking, saving computing time as well as man-power for the exciting challenges of ATLAS particle physics.

## Appendix A

# Derivation of the Autocalibration Matrix Elements

According to Equations (8.37) and (8.38) the matrix elements are given by

$$M_{ik} = \left. \frac{d\Delta_i}{dr_k} \right|_{\varepsilon(t_k)=\delta r_k=0} = \delta_{ik} - \left. \frac{dr_{i,\text{fit}}}{dr_k} \right|_{\varepsilon(t_k)=\delta r_k=0}, \quad (\text{A.1})$$

where

$$r_{i,\text{fit}} = \frac{|mz_i + c - y_i|}{\sqrt{1 + m^2}} \quad (\text{A.2})$$

is the distance of the fitted track  $y = mz + c$  from wire  $i$  with the position  $(z_i, y_i)$ . We write the derivative  $\frac{dr_{i,\text{fit}}}{dr_k}$  as

$$\frac{dr_{i,\text{fit}}}{dr_k} = \frac{\partial r_{i,\text{fit}}}{\partial m} \cdot \frac{\partial m}{\partial r_k} + \frac{\partial r_{i,\text{fit}}}{\partial c} \cdot \frac{\partial c}{\partial r_k} \quad . \quad (\text{A.3})$$

and must now calculate the four partial derivatives in that expression.

For convenience we first recall some definitions and abbreviations:

$$\zeta_i = \sqrt{1 + m^2} z_i - m \rho_{i,\text{fit}} \quad , \quad (\text{A.4})$$

$$|\rho_{i,\text{fit}}| = r_{i,\text{fit}} \quad (\text{A.5})$$

$$\text{sgn}(\rho_{i,\text{fit}}) = \begin{cases} +1 & \text{if the track passes above wire } i \\ -1 & \text{if the track passes below wire } i \end{cases} \quad (\text{A.6})$$

In addition we define

$$s_i \equiv \text{sgn}(\rho_{i,\text{fit}}) \quad . \quad (\text{A.7})$$

From (A.2) we obtain by simple differentiation:

$$\frac{\partial r_{i,\text{fit}}}{\partial m} = \frac{1}{1+m^2} [\text{sgn}(\rho_{i,\text{fit}}) z_i \sqrt{1+m^2} - r_{i,\text{fit}} m] = \frac{1}{1+m^2} s_i \zeta_i \quad (\text{A.8})$$

$$\frac{\partial r_{i,\text{fit}}}{\partial c} = \frac{1}{\sqrt{1+m^2}} s_i \quad (\text{A.9})$$

The other two terms are determined by minimizing

$$\chi^2 = \sum_{i=1}^n \frac{1}{\sigma^2(r_i)} [r_i - r_{i,\text{fit}}(m, c)]^2 \quad (\text{A.10})$$

with respect to  $m$  and  $c$  in the track fit:

$$0 \stackrel{!}{=} \frac{\partial \chi^2}{\partial m} = - \sum_{i=1}^n \frac{2}{\sigma^2(r_i)} [r_i - r_{i,\text{fit}}] \frac{\partial r_{i,\text{fit}}}{\partial m} \quad (\text{A.11})$$

$$0 \stackrel{!}{=} \frac{\partial \chi^2}{\partial c} = - \sum_{i=1}^n \frac{2}{\sigma^2(r_i)} [r_i - r_{i,\text{fit}}] \frac{\partial r_{i,\text{fit}}}{\partial c} \quad (\text{A.12})$$

Inserting (A.8) and (A.9) we get

$$0 = \sum_{i=1}^n \frac{1}{\sigma^2(r_i)} [r_{i,\text{fit}} - r_i] s_i \zeta_i \quad (\text{A.13})$$

$$0 = \sum_{i=1}^n \frac{1}{\sigma^2(r_i)} [r_{i,\text{fit}} - r_i] s_i \quad (\text{A.14})$$

Now we differentiate (A.13) and (A.14) with respect to  $r_k$ :

$$0 = \sum_{i=1}^n s_i \left\{ -\frac{2}{\sigma^3(r_i)} \frac{d\sigma}{dr} \delta_{ik} [r_{i,\text{fit}} - r_i] \zeta_i + \frac{1}{\sigma^2(r_i)} \left[ \left( \frac{dr_{i,\text{fit}}}{dr_k} - \delta_{ik} \right) \zeta_i + (r_{i,\text{fit}} - r_i) \frac{d\zeta_i}{dr_k} \right] \right\} \quad (\text{A.15})$$

$$0 = \sum_{i=1}^n s_i \left\{ -\frac{2}{\sigma^3(r_i)} \frac{d\sigma}{dr} \delta_{ik} [r_{i,\text{fit}} - r_i] + \frac{1}{\sigma^2(r_i)} \left[ \frac{dr_{i,\text{fit}}}{dr_k} - \delta_{ik} \right] \right\} \quad (\text{A.16})$$

Insertion of (A.3) and

$$\begin{aligned} \frac{d\zeta_i}{dr_k} &= \left[ z_i \frac{m}{\sqrt{1+m^2}} - \rho_{i,\text{fit}} - \zeta_i \frac{m}{1+m^2} \right] \frac{\partial m}{\partial r_k} - \frac{m}{\sqrt{1+m^2}} \frac{\partial c}{\partial r_k} \\ &= -\frac{1}{1+m^2} \rho_{i,\text{fit}} \frac{\partial m}{\partial r_k} - \frac{m}{\sqrt{1+m^2}} \frac{\partial c}{\partial r_k} \end{aligned} \quad (\text{A.17})$$

yields the equations

$$\begin{aligned} 0 &= \sum_{i=1}^n \left\{ \frac{\partial m}{\partial r_k} \frac{1}{\sigma^2(r_i)} \frac{1}{1+m^2} [\zeta_i^2 + (r_i - r_{i,\text{fit}}) r_{i,\text{fit}}] \right. \\ &\quad + \frac{\partial c}{\partial r_k} \frac{1}{\sigma^2(r_i)} \frac{1}{\sqrt{1+m^2}} [\zeta_i + s_i(r_i - r_{i,\text{fit}})] \\ &\quad \left. - \frac{1}{\sigma^2(r_i)} \delta_{ik} s_i \zeta_i + \frac{2}{\sigma^3(r_i)} \delta_{ik} s_i \zeta_i (r_i - r_{i,\text{fit}}) \frac{d\sigma}{dr} \right\} \end{aligned} \quad (\text{A.18})$$

$$\begin{aligned} 0 &= \sum_{i=1}^n \left\{ \frac{\partial m}{\partial r_k} \frac{1}{\sigma^2(r_i)} \frac{1}{1+m^2} \zeta_i \right. \\ &\quad + \frac{\partial c}{\partial r_k} \frac{1}{\sigma^2(r_i)} \frac{1}{\sqrt{1+m^2}} \\ &\quad \left. - \frac{1}{\sigma^2(r_i)} \delta_{ik} s_i + \frac{2}{\sigma^3(r_i)} \delta_{ik} s_i (r_i - r_{i,\text{fit}}) \frac{d\sigma}{dr} \right\} \end{aligned} \quad (\text{A.19})$$

Writing (A.18) and (A.19) in the form

$$0 = A_k \frac{\partial m}{\partial r_k} + B_k \frac{\partial c}{\partial r_k} + C_k \quad (\text{A.20})$$

$$0 = D_k \frac{\partial m}{\partial r_k} + E_k \frac{\partial c}{\partial r_k} + F_k \quad (\text{A.21})$$

with

$$A_k = \sum_{i=1}^n \frac{1}{\sigma^2(r_i)} \frac{1}{1+m^2} [\zeta_i^2 + (r_i - r_{i,\text{fit}}) r_{i,\text{fit}}] \quad (\text{A.22})$$

$$B_k = \sum_{i=1}^n \frac{1}{\sigma^2(r_i)} \frac{1}{\sqrt{1+m^2}} [\zeta_i + s_i(r_i - r_{i,\text{fit}})] \quad (\text{A.23})$$

$$C_k = \sum_{i=1}^n \left[ -\frac{1}{\sigma^2(r_i)} \delta_{ik} s_i \zeta_i + \frac{2}{\sigma^3(r_i)} \delta_{ik} s_i \zeta_i (r_i - r_{i,\text{fit}}) \frac{d\sigma}{dr} \right] \quad (\text{A.24})$$

$$D_k = \sum_{i=1}^n \frac{1}{\sigma^2(r_i)} \frac{1}{1+m^2} \zeta_i \quad (\text{A.25})$$

$$E_k = \sum_{i=1}^n \frac{1}{\sigma^2(r_i)} \frac{1}{\sqrt{1+m^2}} \quad (\text{A.26})$$

$$F_k = \sum_{i=1}^n \left[ -\frac{1}{\sigma^2(r_i)} \delta_{ik} s_i \zeta_i + \frac{2}{\sigma^3(r_i)} \delta_{ik} s_i \zeta_i (r_i - r_{i,\text{fit}}) \frac{d\sigma}{dr} \right] \quad (\text{A.27})$$

we recognize that we have to deal with a linear system of equations which we can resolve for  $\frac{\partial m}{\partial r_k}$  and  $\frac{\partial c}{\partial r_k}$ :

$$\frac{\partial m}{\partial r_k} = \frac{C_k E_k - B_k F_k}{B_k D_k - A_k E_k} \quad (\text{A.28})$$

$$\frac{\partial c}{\partial r_k} = \frac{A_k F_k - C_k D_k}{B_k D_k - A_k E_k} \quad (\text{A.29})$$

Since (A.1) requires the derivatives to be evaluated at  $\varepsilon(t_k) = \delta r_k = 0$ , we have to set

$$r_i = r_{i,\text{fit}} \quad (\text{A.30})$$

in the coefficients  $A_k$  to  $F_k$ . Thus we obtain

$$\frac{\partial m}{\partial r_k} \Big|_{\varepsilon(t_k)=\delta r_k=0} = (1 + m^2) s_k \frac{\sum_{l=1}^n \frac{1}{\sigma^2(r_k)\sigma^2(r_l)} (\zeta_l - \zeta_k)}{\left( \sum_{l=1}^n \frac{1}{\sigma^2(r_l)} \zeta_l \right)^2 - \left( \sum_{l=1}^n \frac{1}{\sigma^2(r_l)} \right) \left( \sum_{j=1}^n \frac{1}{\sigma^2(r_j)} \zeta_j^2 \right)} \quad (\text{A.31})$$

$$\frac{\partial c}{\partial r_k} \Big|_{\varepsilon(t_k)=\delta r_k=0} = \sqrt{1 + m^2} s_k \frac{\sum_{l=1}^n \frac{1}{\sigma^2(r_k)\sigma^2(r_l)} \zeta_l (\zeta_k - \zeta_l)}{\left( \sum_{l=1}^n \frac{1}{\sigma^2(r_l)} \zeta_l \right)^2 - \left( \sum_{l=1}^n \frac{1}{\sigma^2(r_l)} \right) \left( \sum_{j=1}^n \frac{1}{\sigma^2(r_j)} \zeta_j^2 \right)} \quad (\text{A.32})$$

Finally we can collect the terms (A.8), (A.9), (A.31) and (A.32) in (A.3), then (A.1) gives us the result:

$$M_{ik} = \delta_{ik} - \text{sgn}(\rho_{i,\text{fit}}) \text{sgn}(\rho_{k,\text{fit}}) \frac{\sum_{l=1}^n \frac{1}{\sigma^2(r_k)\sigma^2(r_l)} (\zeta_i - \zeta_l) (\zeta_l - \zeta_k)}{\left( \sum_{l=1}^n \frac{1}{\sigma^2(r_l)} \zeta_l \right)^2 - \left( \sum_{l=1}^n \frac{1}{\sigma^2(r_l)} \right) \left( \sum_{j=1}^n \frac{1}{\sigma^2(r_j)} \zeta_j^2 \right)} \quad (\text{A.33})$$

## Appendix B

# Proof of $\text{rank}(M) \leq \dim(M) - 2$ for the Autocalibration Matrix $M$

Let  $M$  be the autocalibration matrix as given in (8.45). It has the dimension  $n$ .

We will show that  $M$  has only  $n - 2$  linearly independent rows  $\vec{M}_i$ . For this purpose it is sufficient to prove the equation

$$\vec{0} = \sum_{i=1}^n s_i w_i (\zeta_j - \zeta_i) \vec{M}_i \quad \forall j \in \{1, \dots, n\} \quad (\text{B.1})$$

where we have introduced the abbreviations

$$s_i \equiv \text{sgn}(\rho_i) \quad (\text{B.2})$$

$$w_i \equiv \frac{1}{\sigma^2(r_i)} \quad (\text{B.3})$$

Equation (B.1) is equivalent to

$$\vec{M}_k = \sum_{i \in \{1, \dots, n\} \setminus \{k\}} s_i s_k \frac{w_i}{w_k} \frac{\zeta_j - \zeta_i}{\zeta_j - \zeta_k} \vec{M}_i \quad \forall j, k \in \{1, \dots, n\}, j \neq k \quad (\text{B.4})$$

which means that any row  $\vec{M}_k$  can be expressed by a linear combination of all other rows except one to which we have given the index  $j$ . The contribution of  $\vec{M}_j$  vanishes. Other contributions cannot be zero because by geometry  $i \neq j \Rightarrow \zeta_i \neq \zeta_j$ . With other words,  $\vec{M}_k$  is a linear combination of  $n - 2$  other rows, which is what we want to show.

To ease the manipulations with (B.1), we first multiply it by

$$D \equiv \left( \sum_{l=1}^n w_l \zeta_l \right)^2 - \left( \sum_{l=1}^n w_l \right) \left( \sum_{j=1}^n w_j \zeta_j^2 \right) \quad (\text{B.5})$$

and work on the right side of (B.1) for the  $k^{\text{th}}$  column. In the first step we replace  $M_{ik}$  by the explicit expression (8.45):

$$\begin{aligned}
 & \sum_{i=1}^n D s_i w_i (\zeta_j - \zeta_i) M_{ik} = \\
 &= \sum_i \delta_{ik} s_i w_i (\zeta_j - \zeta_i) \left[ \left( \sum_{\alpha} w_{\alpha} \zeta_{\alpha} \right)^2 - \left( \sum_{\alpha} w_{\alpha} \right) \left( \sum_{\alpha} w_{\alpha} \zeta_{\alpha}^2 \right) \right] \\
 &+ \sum_i w_k w_i s_k (\zeta_j - \zeta_i) \left[ \sum_{\alpha} w_{\alpha} \zeta_{\alpha}^2 + \sum_{\alpha} w_{\alpha} \zeta_i \zeta_k - (\zeta_i + \zeta_k) \sum_{\alpha} w_{\alpha} \zeta_{\alpha} \right]
 \end{aligned}$$

Now all we have to do is to transform this expression until it yields zero:

$$\begin{aligned}
 & \sum_{i=1}^n D s_i w_i (\zeta_j - \zeta_i) M_{ik} = \\
 &= s_k w_k (\zeta_j - \zeta_k) \left[ \sum_{\alpha} w_{\alpha}^2 \zeta_{\alpha}^2 + 2 \sum_{\alpha > \beta} w_{\alpha} w_{\beta} \zeta_{\alpha} \zeta_{\beta} - \sum_{\alpha, \beta} w_{\alpha} w_{\beta} \zeta_{\beta}^2 \right] \\
 &+ s_k w_k \sum_i w_i (\zeta_j - \zeta_i) \sum_{\alpha} w_{\alpha} (\zeta_{\alpha}^2 + \zeta_i \zeta_k - \zeta_i \zeta_{\alpha} - \zeta_k \zeta_{\alpha}) \\
 &= s_k w_k \left\{ (\zeta_j - \zeta_k) \left[ \sum_{\alpha} w_{\alpha}^2 \zeta_{\alpha}^2 + 2 \sum_{\alpha > \beta} w_{\alpha} w_{\beta} \zeta_{\alpha} \zeta_{\beta} - \sum_{\alpha} w_{\alpha}^2 \zeta_{\alpha}^2 - \sum_{\alpha > \beta} w_{\alpha} w_{\beta} \zeta_{\beta}^2 - \sum_{\alpha > \beta} w_{\alpha} w_{\beta} \zeta_{\alpha}^2 \right] \right. \\
 &\quad \left. + \zeta_j \sum_{\alpha, \beta} w_{\alpha} w_{\beta} [\zeta_{\alpha}^2 + \zeta_k (\zeta_{\beta} - \zeta_{\alpha}) - \zeta_{\alpha} \zeta_{\beta}] - \sum_{\alpha, \beta} w_{\alpha} w_{\beta} \zeta_{\beta} [\zeta_{\alpha}^2 + \zeta_k (\zeta_{\beta} - \zeta_{\alpha}) - \zeta_{\alpha} \zeta_{\beta}] \right\} \\
 &= s_k w_k \left\{ -(\zeta_j - \zeta_k) \sum_{\alpha > \beta} w_{\alpha} w_{\beta} (\zeta_{\alpha} - \zeta_{\beta})^2 + \zeta_j \zeta_k \sum_{\alpha, \beta} w_{\alpha} w_{\beta} (\zeta_{\beta} - \zeta_{\alpha}) + \zeta_j \sum_{\alpha, \beta} w_{\alpha} w_{\beta} \zeta_{\alpha} (\zeta_{\alpha} - \zeta_{\beta}) \right. \\
 &\quad \left. - \zeta_k \sum_{\alpha, \beta} w_{\alpha} w_{\beta} \zeta_{\beta} (\zeta_{\beta} - \zeta_{\alpha}) - \sum_{\alpha, \beta} w_{\alpha} w_{\beta} \zeta_{\beta} \zeta_{\alpha} (\zeta_{\alpha} - \zeta_{\beta}) \right\} \\
 &= s_k w_k \left\{ -(\zeta_j - \zeta_k) \sum_{\alpha > \beta} w_{\alpha} w_{\beta} (\zeta_{\alpha} - \zeta_{\beta})^2 + \zeta_j \sum_{\alpha > \beta} w_{\alpha} w_{\beta} \zeta_{\alpha} (\zeta_{\alpha} - \zeta_{\beta}) + \zeta_j \sum_{\alpha > \beta} w_{\alpha} w_{\beta} \zeta_{\beta} (\zeta_{\beta} - \zeta_{\alpha}) \right. \\
 &\quad \left. - \zeta_k \sum_{\alpha > \beta} w_{\alpha} w_{\beta} \zeta_{\beta} (\zeta_{\beta} - \zeta_{\alpha}) - \zeta_k \sum_{\alpha > \beta} w_{\alpha} w_{\beta} \zeta_{\alpha} (\zeta_{\alpha} - \zeta_{\beta}) \right\} \\
 &= s_k w_k (\zeta_j - \zeta_k) \left\{ - \sum_{\alpha > \beta} w_{\alpha} w_{\beta} (\zeta_{\alpha} - \zeta_{\beta})^2 + \sum_{\alpha > \beta} w_{\alpha} w_{\beta} \zeta_{\alpha} (\zeta_{\alpha} - \zeta_{\beta}) - \sum_{\alpha > \beta} w_{\alpha} w_{\beta} \zeta_{\beta} (\zeta_{\alpha} - \zeta_{\beta}) \right\} \\
 &= 0
 \end{aligned}$$

q.e.d.

## Appendix C

# The Distributions of Track Incidence Angles for ATLAS Chambers

On the following pages for all types of ATLAS chambers the distributions of track incidence angles are displayed.

Their positions in the detector can be looked up in the Figures C.1 for the small sectors and C.2 for the large sectors. A transverse cut through the spectrometer defining the sectors is given in Figure 2.2.

The chamber names have the following meaning:

- First letter: B = barrel, E = end-cap.  
The letter ‘F’ for ‘forward’ was replaced by ‘E’ but is still present in the drawings. In this work we write ‘E’.
- Second letter: I = inner, M = middle, O = outer, E = extra (special chambers).
- Third letter: S = small sector, L = large sector.
- Some exceptional chambers don’t fit into this nomenclature scheme: BIR (barrel chambers below the rails, see [TDR 97b]), BEE (visible in Figure C.1).
- The number after the three letters specifies the location of the chamber along  $|z|$  (in the barrel) or along  $r$  (in the end-cap). The distinction between positive and negative  $z$  (forward/backward direction along the beam) needs an additional parameter.  
Examples: BIS 1 designates the BIS chambers closest to the middle plane  $z = 0$  of the detector. EOS 6 labels the outermost EOS chambers.

Due to the eight-fold azimuthal symmetry of the ATLAS detector we did not distinguish the chambers by their octant.

Some angular distributions exhibit two peaks (e.g. BOL). They are due to muons with positive and negative charge respectively.

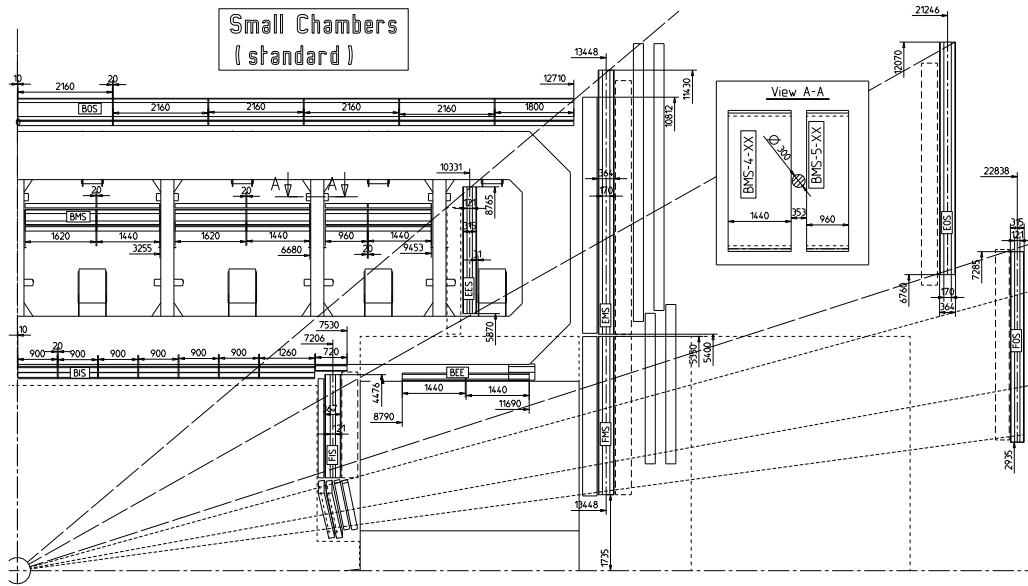


Figure C.1: Longitudinal cut through a small sector of the muon spectrometer.

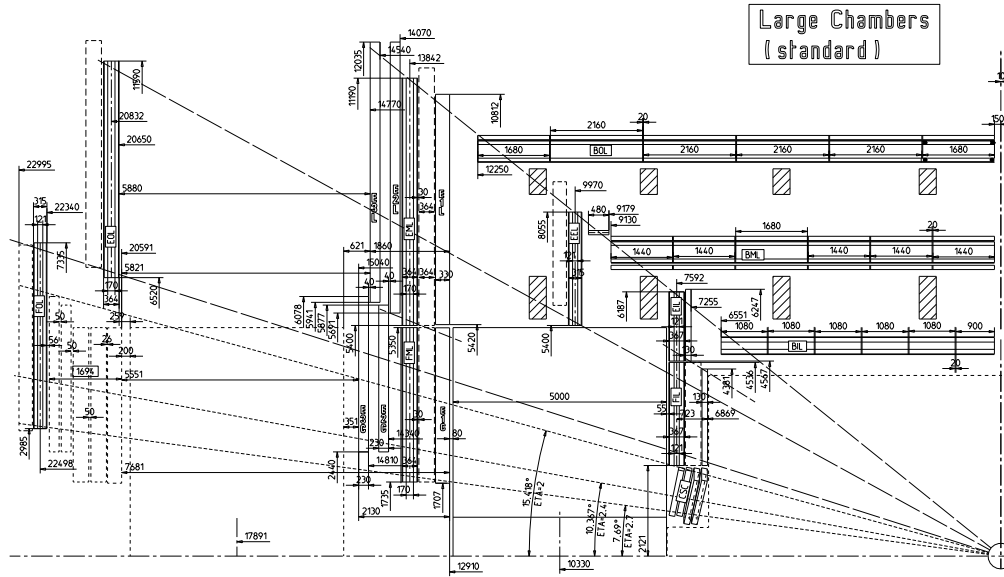
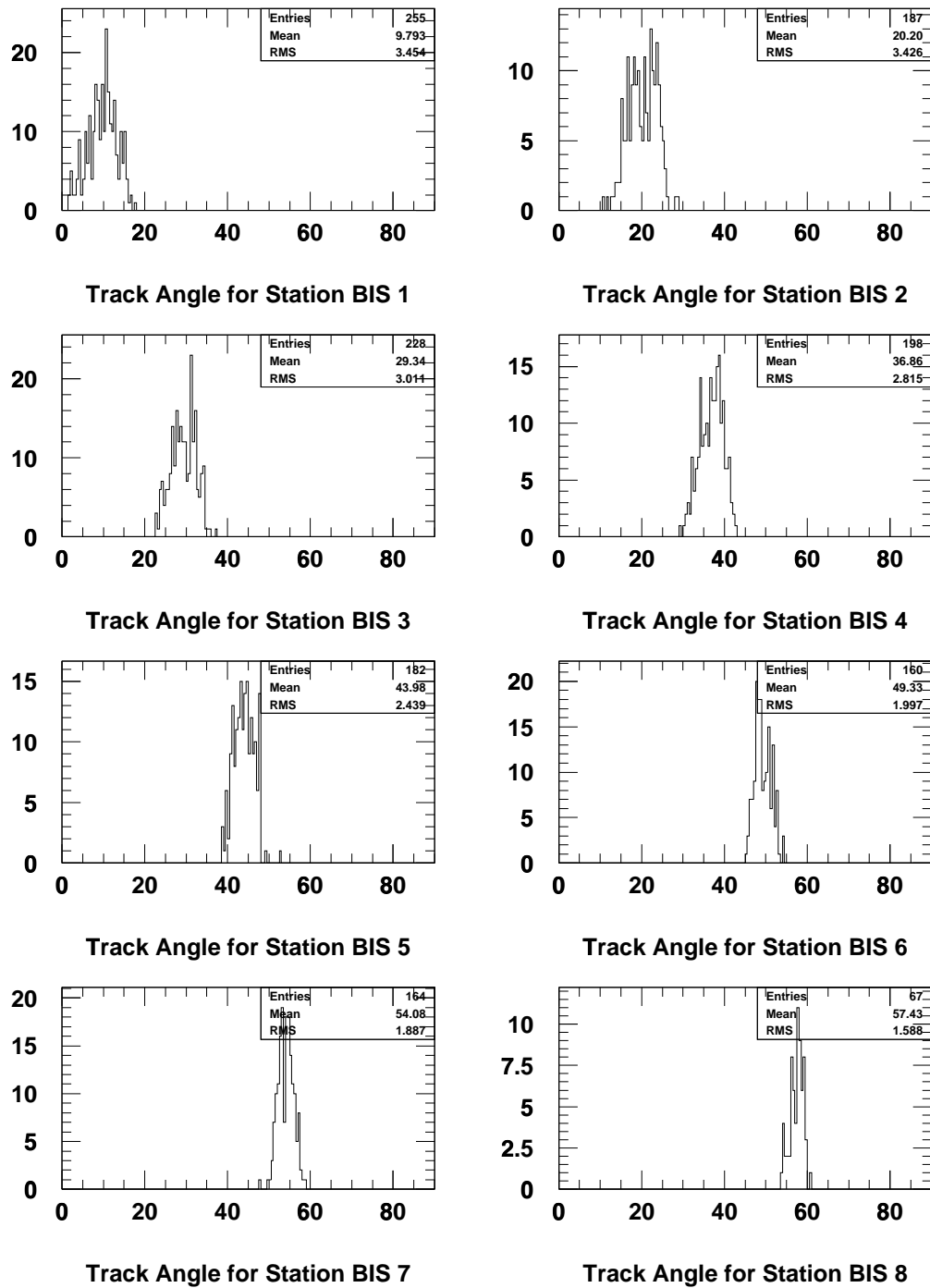
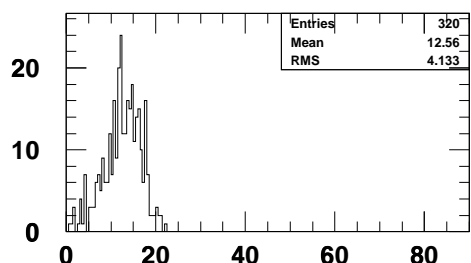
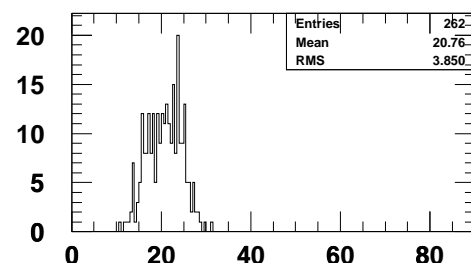


Figure C.2: Longitudinal cut through a large sector of the muon spectrometer.

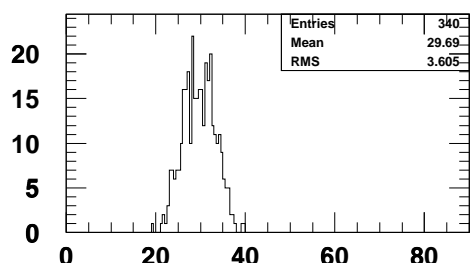




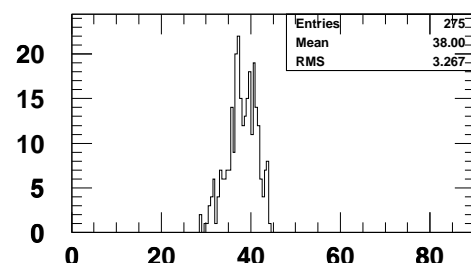
Track Angle for Station BIL 1



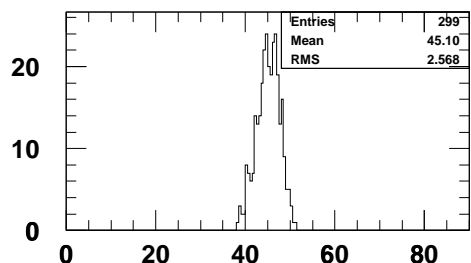
Track Angle for Station BIL 2



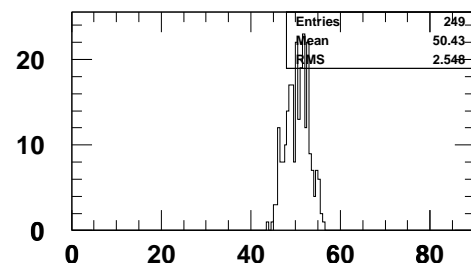
Track Angle for Station BIL 3



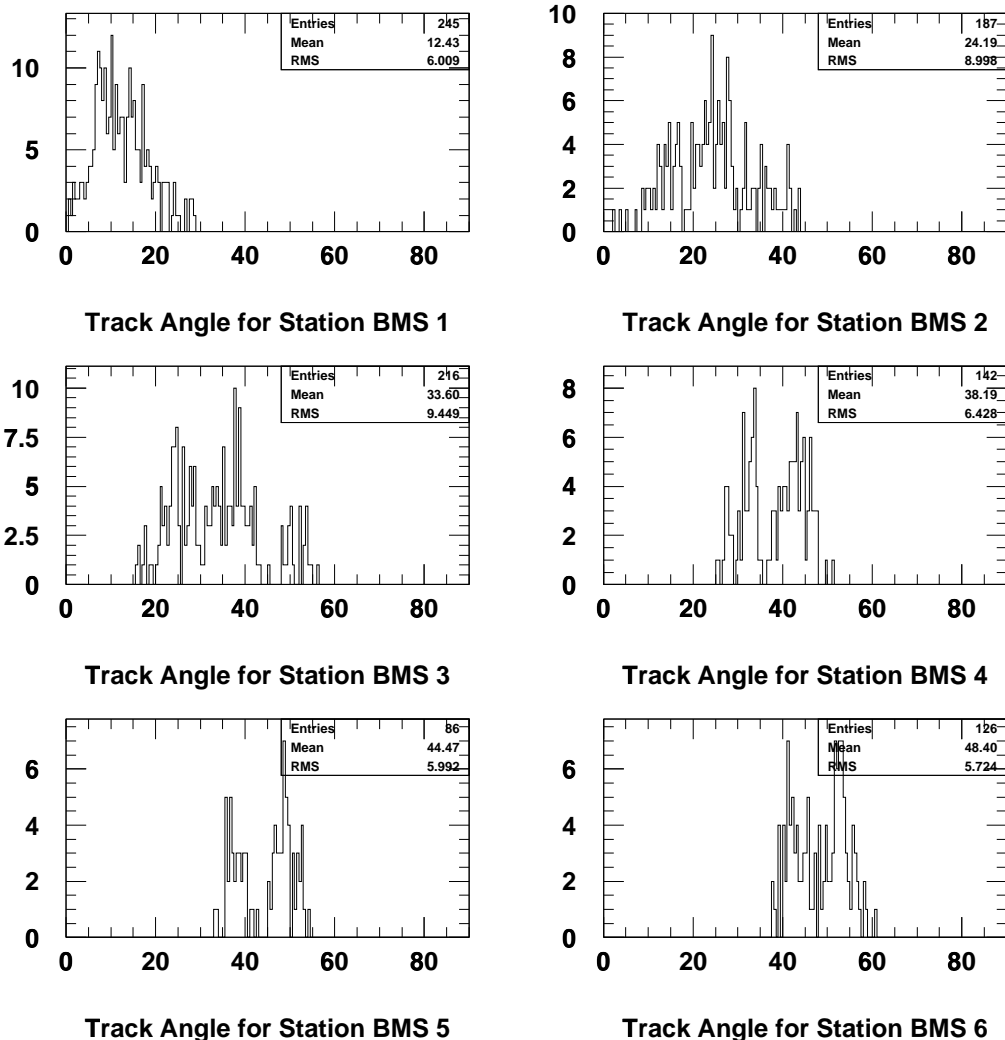
Track Angle for Station BIL 4

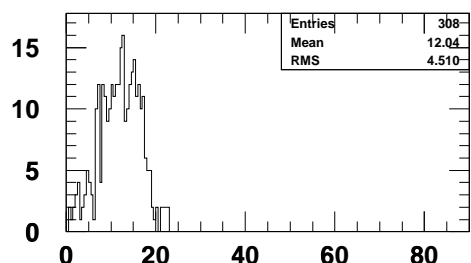


Track Angle for Station BIL 5

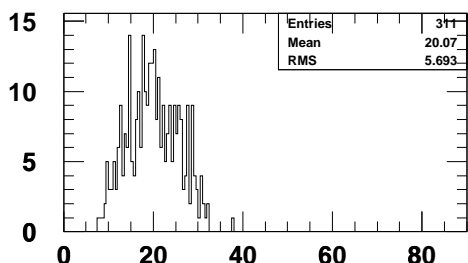


Track Angle for Station BIL 6

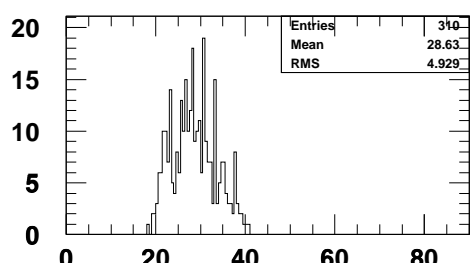




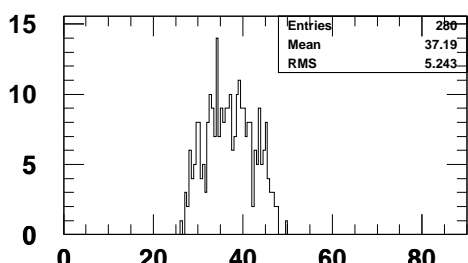
Track Angle for Station BML 1



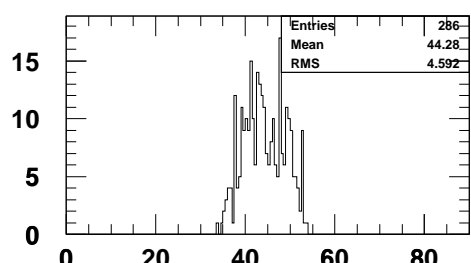
Track Angle for Station BML 2



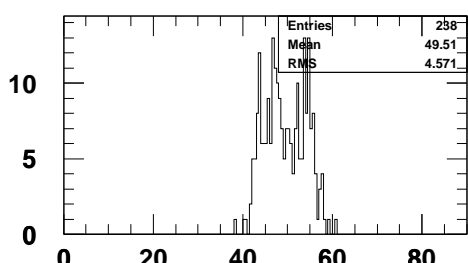
Track Angle for Station BML 3



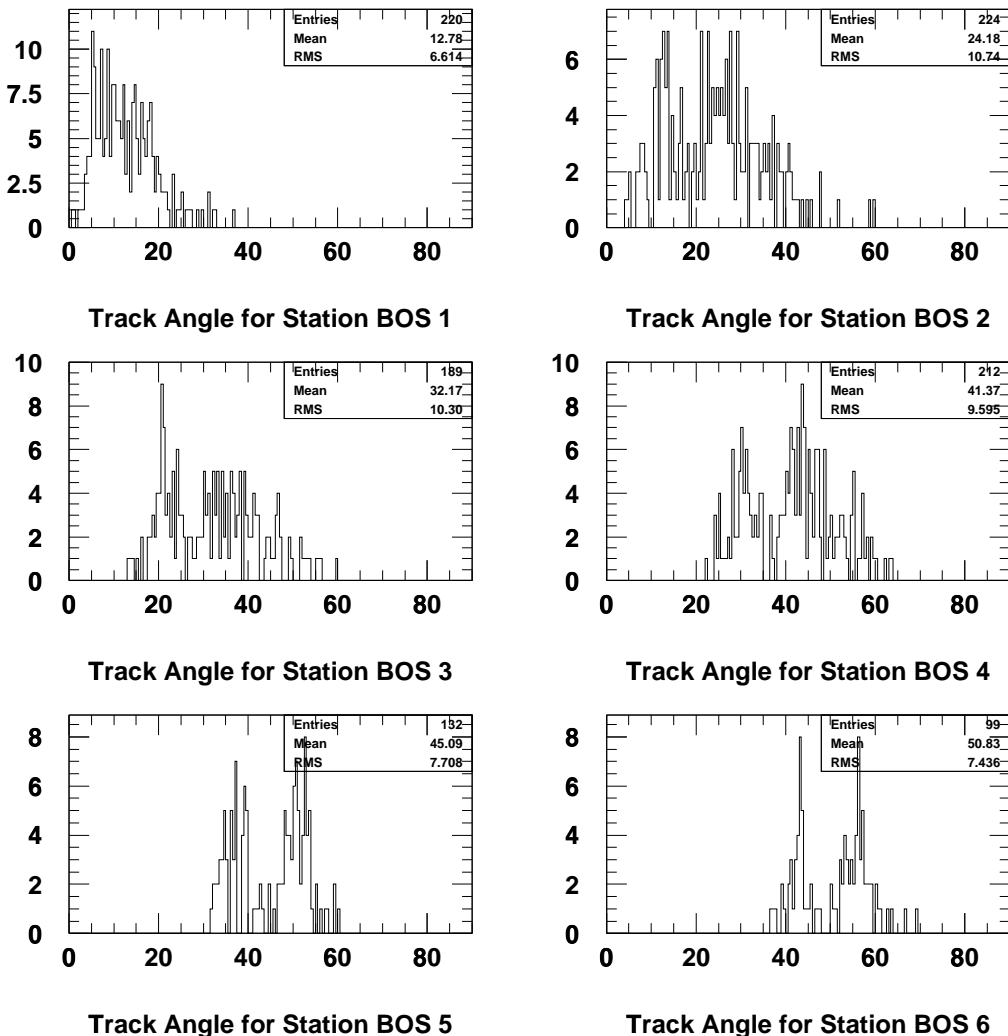
Track Angle for Station BML 4

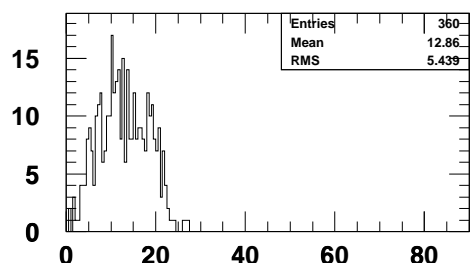


Track Angle for Station BML 5

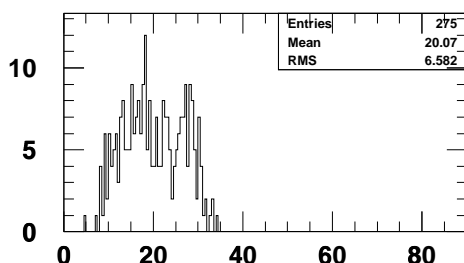


Track Angle for Station BML 6

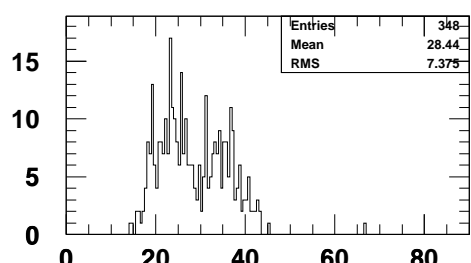




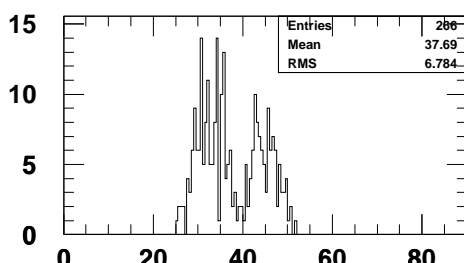
Track Angle for Station BOL 1



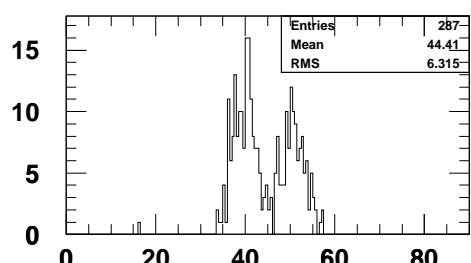
Track Angle for Station BOL 2



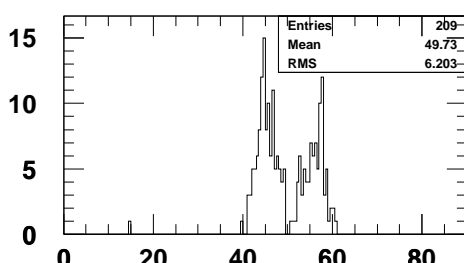
Track Angle for Station BOL 3



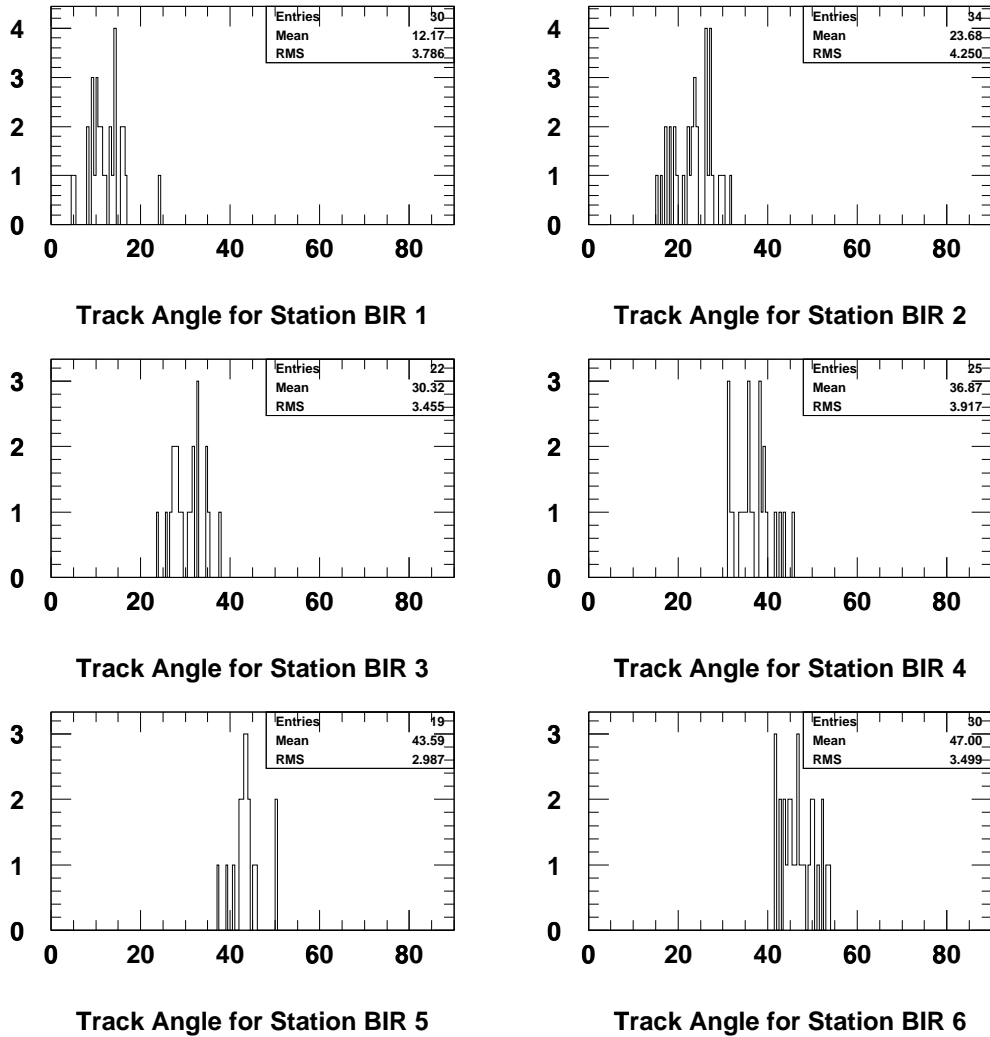
Track Angle for Station BOL 4



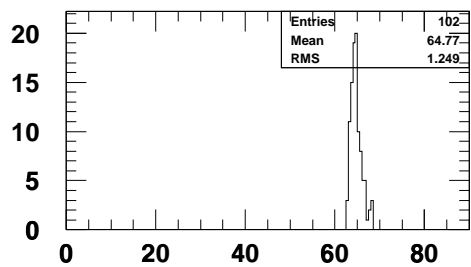
Track Angle for Station BOL 5



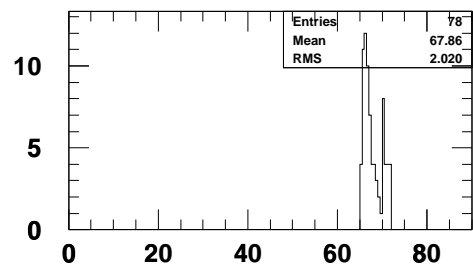
Track Angle for Station BOL 6



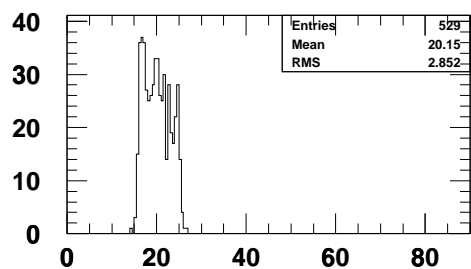
The station BIR 0 does not get any hits with the simulation software used (DICE 3.21). From the chamber position and geometry (radial position of the chamber centre:  $r = 5.8\text{ m}$ ; position of chamber centre along the beam direction:  $z = 0$ ; chamber width:  $\Delta z = 0.54\text{ m}$ ) one can infer the approximate angular range of  $[-5^\circ, +5^\circ]$ .



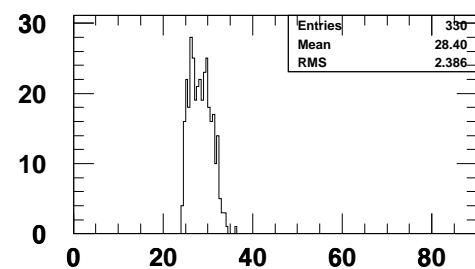
Track Angle for Station BEE 1



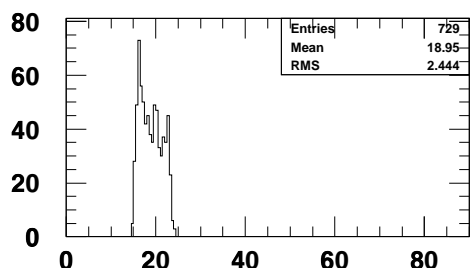
Track Angle for Station BEE 2



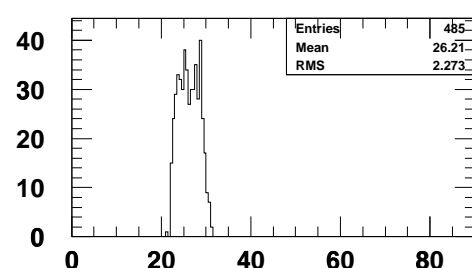
Track Angle for Station EIS 1



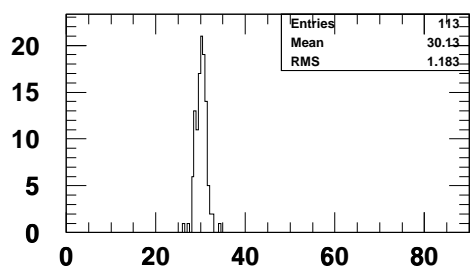
Track Angle for Station EIS 2



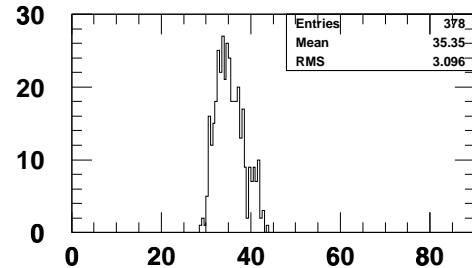
Track Angle for Station EIL 1



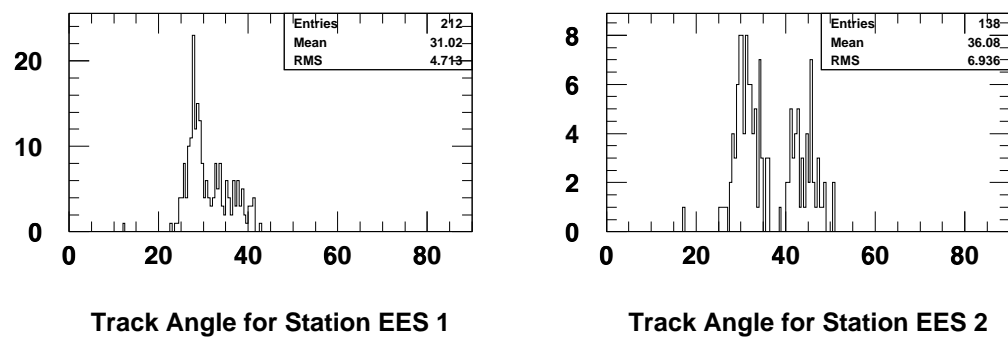
Track Angle for Station EIL 2

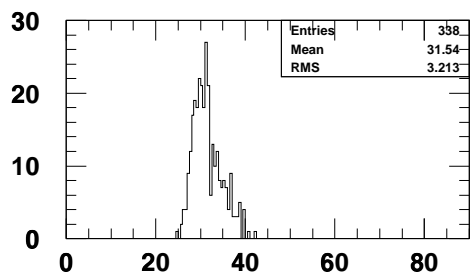


Track Angle for Station EIL 3

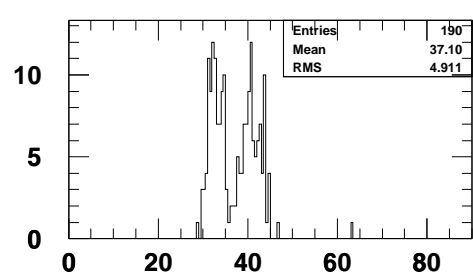


Track Angle for Station EIL 4

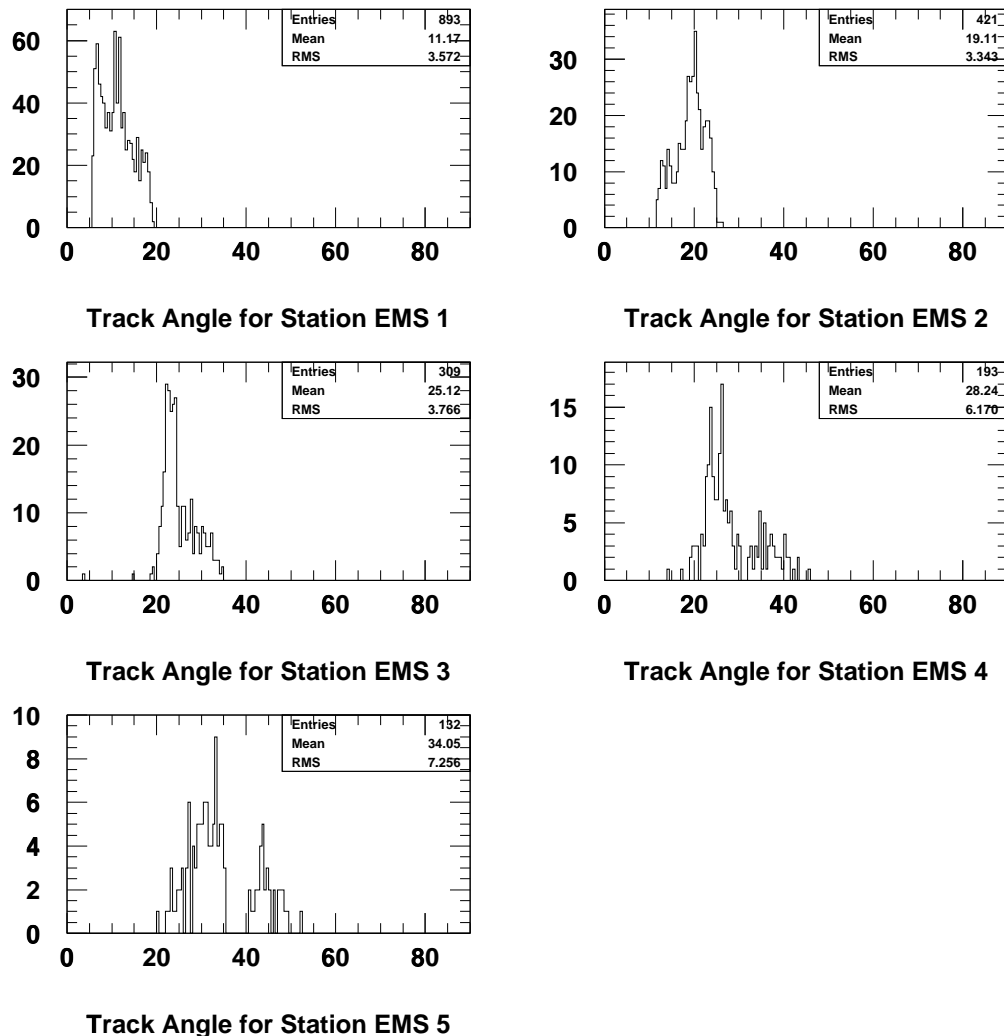


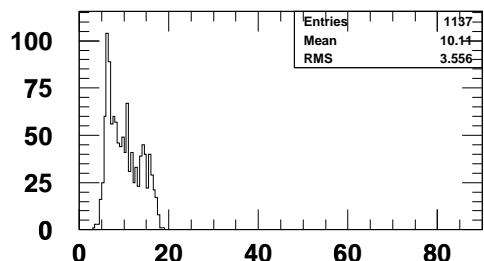


Track Angle for Station EEL 1

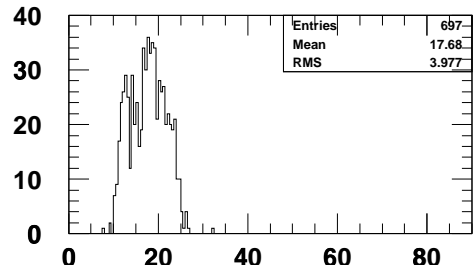


Track Angle for Station EEL 2

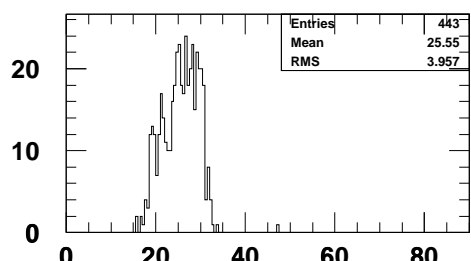




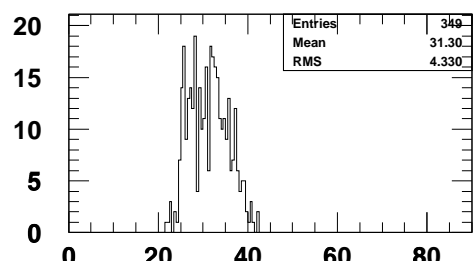
Track Angle for Station EML 1



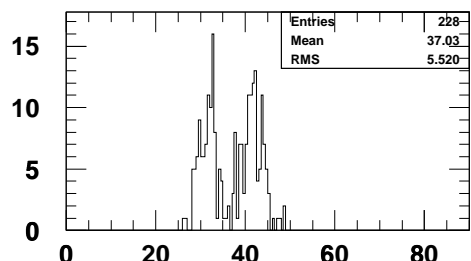
Track Angle for Station EML 2



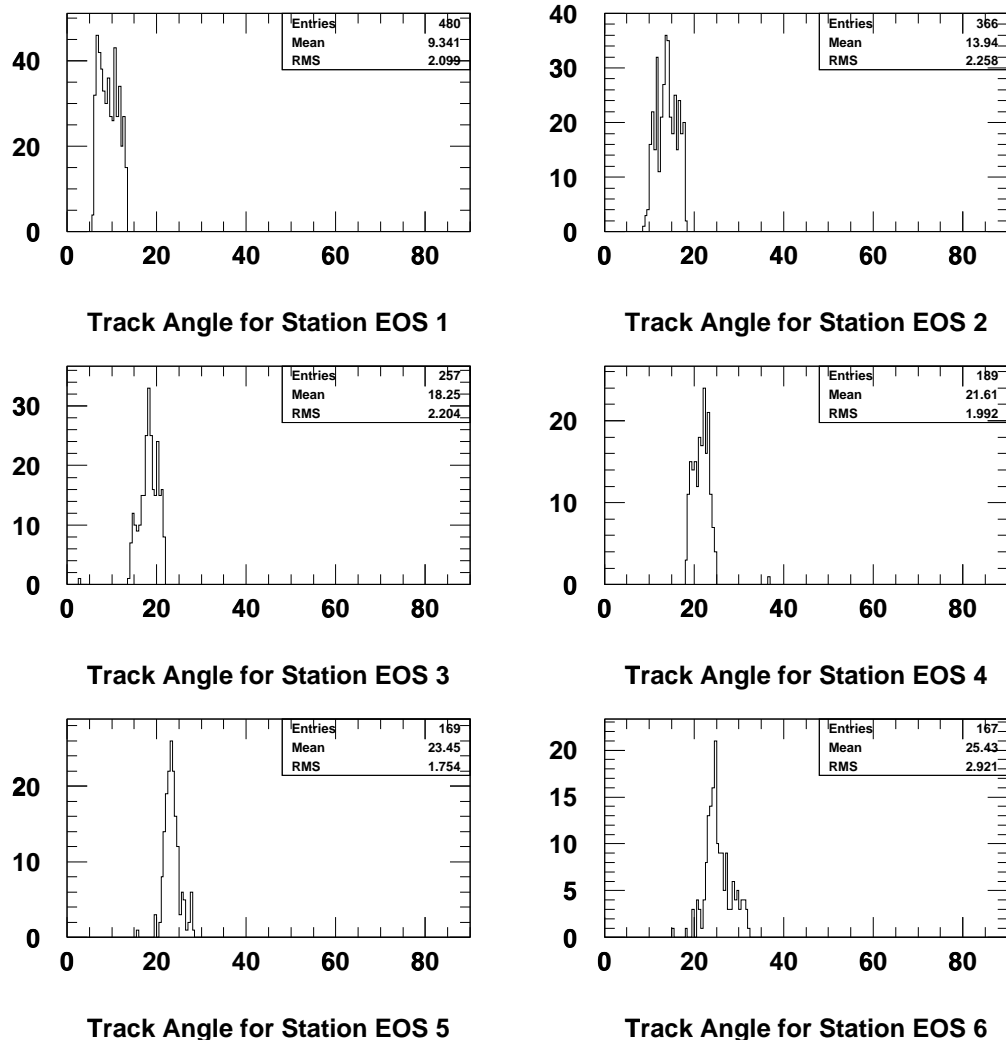
Track Angle for Station EML 3

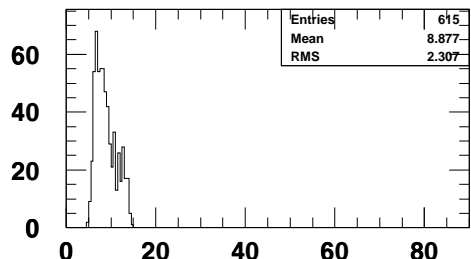


Track Angle for Station EML 4

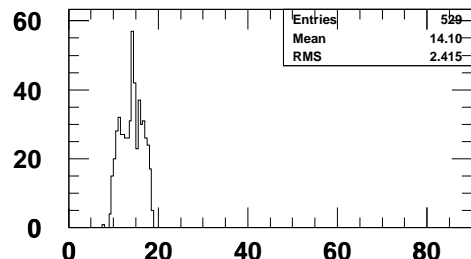


Track Angle for Station EML 5

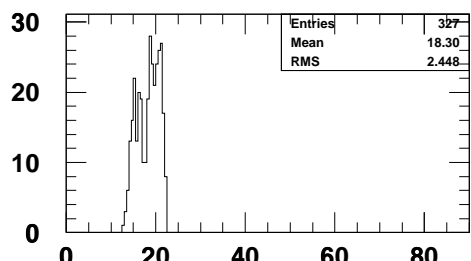




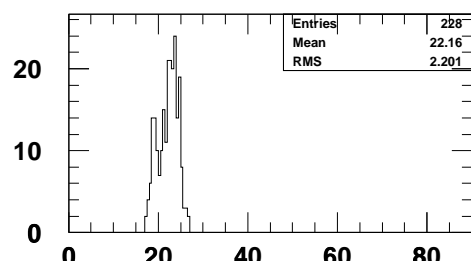
Track Angle for Station EOL 1



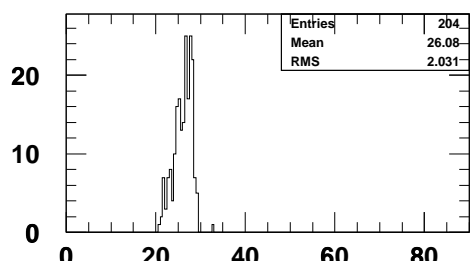
Track Angle for Station EOL 2



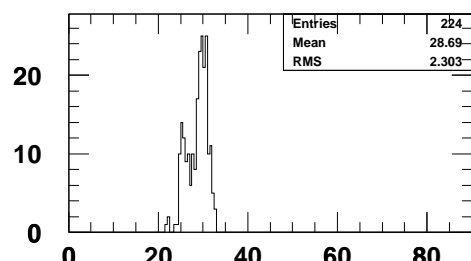
Track Angle for Station EOL 3



Track Angle for Station EOL 4



Track Angle for Station EOL 5



Track Angle for Station EOL 6

# Bibliography

- [ALE 98a] M. Aleksi, M. Deile et al.: MDT Performance in a High Rate Background Environment, ATLAS Note ATL-MUON-98-258, CERN 1998
- [ALE 98b] M. Aleksi, W. Riegler: Non-Linear MDT Drift Gases like Ar/CO<sub>2</sub>, ATLAS Note ATL-MUON-98-268, CERN 1998
- [ALE 99a] M. Aleksi, M. Deile et al.: Rate Effects in High-Resolution Drift Chambers, CERN-EP/99-101 (1999), NIM A 446/3 (2000), pp. 435-443
- [ALE 99b] M. Aleksi: Performance of the ATLAS Muon Spectrometer, PhD Thesis, CERN 1999
- [ALI 95] ALICE Collaboration: ALICE Technical Proposal, CERN/LHCC 95-71, 1995
- [ATL 94] ATLAS Collaboration: ATLAS Technical Proposal, CERN/LHCC 94-43, LHCC/P2, 1994.
- [BAR 94a] S. Baranov et al.: Gamma Sensitivity of Pressurized Drift Tubes, ATLAS Note ATL-MUON-94-036, CERN 1994
- [BAR 94b] S. Baranov et al.: Autocalibration method for determination of drift time – space relation for HPDT, ATLAS Note ATL-MUON-94-040, CERN 1994
- [BEL 83] E. Belau et al.: Charge Collection in Silicon Strip Detectors, NIM 214 (1983) 253-260
- [BIA] S. Biagi: MAGBOLTZ, a program to compute gas transport parameters, Version 1.16, CERN.
- [BIS 97] A. Biscossa et al.: The First Full-Scale Prototype of a BIL MDT Chamber for the ATLAS Muon Spectrometer, ATLAS Note ATL-MUON-97-136, CERN 1997
- [BLU 93] W. Blum, L. Rolandi: Particle Detection with Drift Chambers, Springer Verlag, 1993.
- [BNL 73] Common base preamplifier IO354-2 and shaping amplifier IO532-01, Instrumentation Division, Brookhaven National Laboratory, Upton, New York, 1973.
- [BOY 95] I.R. Boyko et al.: Investigation of the ratio between streamer and proportional signals in drift tubes, ATLAS Note ATL-MUON-95-088, CERN 1995.

- [BOY 97] I.R. Boyko et al.: MDT Gamma Response, ATLAS Note ATL-MUON-97-194, CERN 1997.
- [CAE 94] CAEN 2-Channel C-RAMS, Mod. V 550, Technical Information Manual, September 1994
- [CHE 93] A. Cheplakov et al.: Muon Rates in ATLAS, ATLAS Note ATL-MUON-93-21, CERN 1993
- [CHL 93] G.A. Chelkov et al.: Investigation of spectral efficiency of pressurized drift tubes for detection of neutrons in the energy range between 5 ev and 200 keV, ATLAS Note ATL-MUON-93-31, CERN 1993
- [CHV 97] L. Chevalier: LHCTOR: A stand alone Geant Program for simulation of the ATLAS spectrometer, ATLAS Note ATL-MUON-97-147 in preparation.
- [CMS 94] CMS Collaboration: CMS Technical Proposal, CERN/LHCC 94-43, 1994
- [CRE 97] P. Creti, M. Deile et al.: Testbeam Results from the Calypso MDT Chamber, ATLAS Note ATL-MUON-97-196, 1997.
- [DEI 96a] M. Deile: Optimierung der Operationsparameter von Hochdruckdriftrohren für ATLAS, diploma thesis, LMU Munich 1996
- [DEI 96b] M. Deile et al.: Charge Division and Intrinsic Pulse Shaping in Drift Tubes, ATLAS Note ATL-MUON-96-105, CERN 1996
- [DEI 96c] M. Deile et al.: Test Beam Studies of the Gas Mixtures ... for Drift Tubes, ATLAS Note ATL-MUON-96-122, CERN 1996
- [DEI 97] M. Deile, N.P. Hessey: Density Control of MDT Gas, ATLAS Note ATL-MUON-97-203, CERN 1997
- [DEI 98] M. Deile et al.: MDT Track Fitting with the Maximum Likelihood Method, ATLAS Note ATL-MUON-98-240, CERN 1998
- [DEI 99] M. Deile, J. Dubbert, N.P. Hessey, A. Staude: ODYSSEUS – a Silicon Telescope for Test Beam Experiments, System Description and User Manual for the Data Analysis, ATLAS Communication ATL-COM-MUON-99-015, CERN 1999
- [DEI 00a] M. Deile et al.: Dependence of Drift Tube Performance on the Anode Wire Diameter, CERN-EP-2000-039, NIM A 449/3 (2000), pp. 528-536
- [DEI 00b] M. Deile: Linear and quadratic profiles of the effective magnetic field for all ATLAS MDT chambers, available on:  
[http://www.etp.physik.uni-muenchen.de/atlas/psfiles/atlas\\_bfieldmaps](http://www.etp.physik.uni-muenchen.de/atlas/psfiles/atlas_bfieldmaps)
- [DIE 56] W. Diethorn: A methane proportional counter system for natural radiocarbon measurements, USAEC Report NY06628 (1956)

- [DEN 90] D. Denegri: Standard Model Physics at the LHC, Proceedings of the Large Hadron Collider Workshop (Aachen 1990), CERN 90-10, ECFA 90-133, Vol. 1, p.56
- [DUB 96] J. Dubbert, Bestimmung der Ortsauflösung von Hochdruckdriftrohren für das Myon-Spektrometer des ATLAS-Experimentes, diploma thesis, LMU Munich, August 1996
- [GOR 00] A. Gordeev et al.: CSC Performance at High Background Rates, ATLAS Note ATL-MUON-2000-005, CERN 2000
- [HYA 83] B. Hyams et al.: A Silicon Counter Telescope to study short-lived Particles in High-Energy Hadronic Interactions, NIM 205 (1983) 99-105
- [IDE 94] The VA circuit, Integrated Detector & Electronics AS, Veritasveien 9, N-1322 Høvik, <http://www.ideas.no>
- [KAD 91] J.A. Kadyk: Wire Chamber Ageing, NIM A 300 (1991)
- [KEK] KEK, National Laboratory for High Energy Physics, Japan
- [KOL 97] M. Kollefrath et al.: MDT Ageing Studies using Different Cathodes, ATLAS Note ATL-MUON-97-176, CERN 1997
- [KOR 99] O. Kortner, M. Deile et al.: Results of the Analysis of the August 1998 Material Runs with Silicon Telescope, ATLAS Note ATL-MUON-99-009, CERN 1999
- [LEO 94] W.R. Leo: Techniques for Nuclear and Particle Physics Experiments, Springer 1994
- [LHB 98] LHCb Collaboration: LHCb Technical Proposal, CERN/LHCC 98-4, 1998
- [PAS 00] V. Paschhoff, M. Spegel: Ageing studies for the ATLAS MDT's using Ar-CO<sub>2</sub> 90-10, ATLAS Note ATL-MUON-2000-004, CERN 2000
- [PAU 90] F. Pauss: Beyond the Standard Model in pp Collisions, Proceedings of the Large Hadron Collider Workshop (Aachen 1990), CERN 90-10, ECFA 90-133, Vol. 1, p.118
- [PDG 98] Particle Data Group: Review of Particle Physics, The European Physical Journal, Springer 1998
- [POL 94] V.A. Polychronakos, A Proposal to Use the Cathode Strip Chambers for the ATLAS Forward Muon System, ATLAS Note ATL-MUON-94-038, CERN 1994
- [REW 86] P. Rewiersma: The L3 Wire-Amplifier, Type NH19-6112, NIKHEF 1986.
- [RIE 97a] W. Riegler: Limits to Drift Chamber Resolution, PhD Thesis, CERN 1997
- [RIE 99a] W. Riegler, M. Aleksa, M. Deile et al.: Resolution Limits of Drift Tubes, CERN-EP/99-99 (1999), NIM A 443/1 (2000), pp. 156-163
- [RIE 99b] W. Riegler, M. Aleksa, M. Deile et al.: Front-End Electronics for Drift Tubes in a High-Rate Environment, CERN-EP/99-100 (1999), NIM A 446/3 (2000), pp. 555-559

- [RIE 99c] W. Riegler, M. Aleksi: Bipolar versus Unipolar Shaping of MDT Signals, ATLAS Note ATL-MUON-99-003, CERN 1999
- [SAM 97] T. Sammer: Autokalibration von Driftrohrkammern für das ATLAS-Myon-spektrometer, diploma thesis, LMU Munich, May 1997
- [SCH 95] Ph. Schune, C. Guyot, M. Virchaux: Momentum resolution of the ATLAS muon spectrometer, ATLAS Note ATL-MUON-95-065, CERN 1995
- [SHA 97] J. Shank et al.: Studies of  $A^0$ ,  $Z'$  and  $W'$  Production and Detection with the ATLAS Muon Detector, ATLAS Note ATL-MUON-97-161, CERN 1997
- [SMI 97] I. Smirnov: HEED, program to compute energy loss of fast particles in gases, Version 1.01, CERN
- [SPE 98] M. Spegel: On the Lifetime of Proportional Counters, PhD Thesis, CERN 1998
- [SPI 95] M. Spira et al.: Higgs Boson Production at the LHC, CERN-TH/95-30 (1995)
- [TDR 96] ATLAS Collaboration: Calorimeter Performance Technical Design Report, CERN/LHCC 96-40, December 1996.
- [TDR 97a] ATLAS Collaboration: Inner Detector Technical Design Report, CERN/LHCC 97-16 and 97-17, April 1997.
- [TDR 97b] ATLAS Collaboration: Muon Spectrometer Technical Design Report, CERN/LHCC 97-22, June 1997.
- [TDR 99] ATLAS Collaboration: Detector and Physics Performance Technical Design Report, CERN/LHCC 99-14, May 1999.
- [VEE 99] R. Veenhof: GARFIELD, a drift chamber simulation program, Version 6.31, CERN 1999. on-line documentation:  
<http://consult.cern.ch/writeups/garfield/>
- [VIE 96] G. Viehhauser: Detector Physics of the ATLAS precision muon chambers, PhD Thesis, CERN 1996
- [VIR 97] M. Virchaux et al.: Muonbox – a full 3D tracking programme for Muon reconstruction in the ATLAS Spectrometer, ATLAS Note ATL-MUON-97-198 in preparation
- [VIT 98] P. Vitulo: private communication, information available on the WWW page:  
<http://www1.pv.infn.it/vitulo/testbeam/simulation.html>

# Acknowledgements

In experimental particle physics the single physicist is like an ant. Together with others he can realize sophisticated projects, but on his own he is lost. Therefore I feel obliged to thank all those who accompanied my activities in physics during the last four years.

In the very first place I am grateful towards my supervisor, Prof. Arnold Staude, for all the support and encouragement he gave me during the last four years. I profited a lot from his almost permanent availability for discussing difficulties and results. His physical intuition was an excellent test bench for the verification of surprising results. If he tells you “this contradicts the principles of nature”, you can be almost certain that after a week of calculations you will end up confirming his suspicion.

Prof. Dorothee Schaile, the chairwoman of our department, helped with constructive suggestions and comments to my reports in the group’s seminar. I appreciate her incentives to speed up my activities by keeping the main target in mind rather than getting lost in too many details. Furthermore, it was her merit to create a friendly ambience in the group, which eased survival in the lonesome desert of Garching’s institute district. Here I also want to thank all the other chevaliers of the Garching coffee table for various kinds of help or support, and be it just a relaxing chat from time to time. Otto Schaile, Rudi Lutter and Klaus Steinberger made work easier by giving quick and efficient assistance in computing problems. And what would we do without the cordiality, humour and helpfulness of our secretary Herta Franz?

Since the earliest days of my diploma thesis I have been working together with Nigel Hessey. He supervised me when I had first arrived at CERN without any idea about working in experimental particle physics. I (hopefully) learned a lot from him. Even after his departure to NIKHEF we pursued some common projects. Also I will never forget our (sometimes extremely cold) ski trips on top of the Jura ridge.

With my test-beam colleagues Werner Riegler, Martin Alekса, Chuck Gruhn, Thomas Sammer and Sven Kircher I shared some tough times but also a lot of fun. When a system was finally working, the joy usually didn’t end in the experimental hall but was exported to Charlie’s (St. Genis) or to one of the numerous austro-parties which I enjoyed a lot. In this context I also want to thank Edda Gschwendtner, Sophie L’Huillier, Helmut Vincke and the other members of the austrian gang for various private activities which made me look forward to every stay at CERN.

Without the technical support and expertise from Horst Herbert and Konrad Bussmann our experiments would not have been successful. The same is true for Gerhard Lutz and Rainer Richter from the MPI semiconductor laboratory and for CERN’s semiconductor detector specialists Alan Rudge, Robert Boulter, Ogmundur Runolfsson and Kaspar Mühlemann. Their help was vital for keeping ODYSSEUS alive who had the awkward habit to fall seriously ill especially during the tight periods of data-taking.

Rob Veenhof was always very helpful with all sorts of questions about GARFIELD. The promptness of his replies is exemplary for the sector of software support.

Many thanks to Thomas Trefzger who introduced me into the art of enduring stoically the bugs – sorry, I meant to say ‘features’ – of huge, badly commented software packages. Being my office neighbour in Garching he was the first target for my frustration and regularly had to calm down my “Grant” (bavarian for ‘anger’) when once again programme XXXX crashed after 4000 events or produced empty output files or ...

Great assistance in understanding and modifying LHCTOR and MUONBOX was given by Marc Virchaux, Jean-François Laporte and Laurent Chevalier. Merci beaucoup pour l’accueil chaleureux à Saclay!

# Curriculum Vitae

23. June 1970	Born in Munich, Germany.
1976 – 1980	Primary school in Ebersberg (near Munich).
1980 – 1989	Secondary school (“Gymnasium Grafing” near Munich).
June 1989	A-levels (“Abitur”) with distinction (mark 1.0); major courses: Mathematics and Latin.
June 1989 – September 1990	National service: alternative service at the lutheran parish of Grafing.
November 1990 – July 1996	Studies of physics at the University of Munich LMU; Permanent scholarship from the State of Bavaria for exceptional success at secondary school and in a special examination.
September 1993 – June 1994	Studies of physics, astrophysics and geophysics at the Université de Paris XI (Orsay) with an additional european scholarship (“Erasmus”) for one year. Examination results in astrophysics and applied physics were recognized as parts of the diploma in Munich.
March 1995 – February 1996	Diploma thesis at CERN about “Optimization of the Operating Parameters of Pressurized Drift Tubes for ATLAS”, supervised by Prof. Dr. Arnold Staude.
July 1996	Diploma of physics with distinction (mark 1.0).
since September 1996	Scientific employee at the LMU; Doctoral thesis in the ATLAS Experiment, supervised by Prof. Dr. Arnold Staude.
May – June 1997	European Summer School of High-Energy Physics in Menstrup (Denmark).